Doctoral theses at NTNU, 2021:168

Tina Bergh

Electron microscopy of intermetallic phases in aluminium-steel joints

Doctoral thesis

NTNU
Norwegian University of Science and Technology
Thesis for the Degree of
Philosophiae Doctor
Faculty of Natural Sciences
Department of Physics

NTNU
Norwegian University of
Science and Technology

Tina Bergh

Electron microscopy of intermetallic phases in aluminium-steel joints

Thesis for the Degree of Philosophiae Doctor

Trondheim, May 2021

Norwegian University of Science and Technology
Faculty of Natural Sciences
Department of Physics

NTNU
Norwegian University of
Science and Technology

NTNU
Norwegian University of Science and Technology

Thesis for the Degree of Philosophiae Doctor

Faculty of Natural Sciences
Department of Physics

ISBN 978-82-326-6011-7 (printed ver.)
ISBN 978-82-326-5276-1 (electronic ver.)
ISSN 1503-8181 (printed ver.)
ISSN 2703-8084 (online ver.)

Doctoral theses at NTNU, 2021:168

Printed by NTNU Grafisk senter

Abstract

Joints that combine the light weight of aluminium (Al) alloys with the high strength of steels, can be beneficial in structural components. For instance, in automobiles, Al-steel joints can enable improvement of the strength-to-weight distribution and contribute to reduce the fuel consumption and the greenhouse gas emission. However, Al-steel welding poses several challenges, due to the large differences in the thermo-physical properties, such as the melting point, between Al alloys and steels. In addition, Al alloys are sensitive to thermo-mechanical treatment and typically develop a soft zone during welding. Moreover, the elevated temperatures reached during welding typically lead to formation and growth of intermetallic phases along the bonded interface. These phases are hard and brittle, and they are typically detrimental to the properties of the joint. The overall goal of this work was to characterise the interface microstructure in selected Al-steel joints, to contribute to better understanding of the underlying bonding mechanisms and the performance of the joints. The main focus was placed on the formed interfacial intermetallic phase layers. In sound joints, the interfacial layers typically have thicknesses on the nanometre or micrometre scale. Electron microscopy provides the required spatial resolution to study such layers. The main tool in this work was transmission electron microscopy, which enables acquisition of a broad range of complementary signals that can be used to characterise the specimen both in terms of morphology, chemical composition and crystal structure with a spatial resolution down to atomic scale.

In one of the studied joints, the interfacial layer was only a few tens of nanometres thick and therefore posed extra challenges for characterisation. For this specimen, scanning electron diffraction was used, which involves scanning a nanometre-sized probe across the specimen and collecting diffraction patterns at each probe position. This yields a four dimensional dataset that, combined with data analysis, enables the local crystallography to be assessed. However, overlap of crystals is a recurring challenge with analysis of such data. Two methods to segment the signals associated with individual crystals were explored in this thesis. The first segmentation approach was based on virtual dark field imaging, where diffraction contrast images are created by integrating the intensity within a region in the diffraction patterns, with respect to probe position. The second was based on non-negative matrix factorisation, which is a data matrix decomposition method that can be used to extract the individual parts constituting a non-negative dataset. By applying the two approaches to a demonstration dataset of partly overlapping magnesium oxide nanoparticles, it was found that both could be used for nanocrystal segmentation if artefacts were considered carefully. The segmentation approaches were also applied to datasets from an Al-steel joint fabricated by hybrid metal extrusion & bonding.

To overcome the challenges associated with Al-steel welding, methods that enable bonding with lower heat input have been developed during the last decades, including the patented solid state welding method hybrid metal extrusion & bonding. This method is based on continuous extrusion of an Al filler material that is squeezed in between the metals to be joined. The addition of filler material is combined with large plastic deformation to yield a flexible

low temperature method, which is suitable for Al-steel welding. A second generation Al-steel joint was studied that showed tensile strengths comparable to that achieved with competing joining methods. The underlying bonding mechanism was found to be a combination of microscale mechanical interlocking and formation of a discontinuous interfacial nanoscale Al-iron-silicon (Al-Fe-Si) layer. Analysis of scanning electron diffraction data indicated that the layer contained the cubic α_c-Al-(Fe,Mn)-Si phase.

After the promising results for Al-steel joints, the possibility of using the hybrid metal extrusion & bonding method for multi-material joining was explored. A four-metal Al-copper-steel-titanium (Al-Cu-steel-Ti) demonstration joint was characterised. Electron microscopy studies again revealed microscale mechanical interlocking and formation of interfacial intermetallic phase layers at the bonded interfaces. The Al-steel interface showed adequate bonding and an interfacial Al-Fe-Si(-Cu) layer $\sim$0.1-1 µm thick. In bonded areas, the Al-Cu interface was covered by a $\sim$0.5 µm thick layer mainly composed of the phases θ-Al_2Cu and γ_1-Al_4Cu_9. However, some Al-Cu regions suffered from lack of bonding and porosity, due to an insufficient supply of filler material. The Al-Ti interface was covered by a $\sim$50 nm thick Al-Ti-Si layer, and the Al-Ti region showed excellent tensile properties with ductile fracture running through the Al during testing. Overall, the hybrid metal extrusion & bonding method showed great prospects for multi-metal welding primarily due to its flexibility and the low process temperature.

The formation and growth of interfacial intermetallic phases were also studied in a more fundamental sense to gain insight into the influence of alloying elements. Joints between an Al-magnesium-Si (Al-Mg-Si) alloy and a stainless steel containing chromium (Cr) and nickel (Ni), were made by roll bonding, and the joints were heat treated to promote interdiffusion and growth of intermetallic phases. The formed phases were characterised in terms of morphologies, chemical compositions, crystal structures and mechanical properties. The alloying elements Si, Mn, Cr and Ni led to a decrease in the growth rate of the total interfacial intermetallic phase layer. The phase layers were mainly identified to be composed of τ_1-$FeNiAl_9$, α_c-Al-(Fe,Cr,Mn)-Si, θ-Fe_4Al_{13} and η-Fe_2Al_5, arranged from the Al to the steel side.

Joints made by the fusion welding method cold metal transfer, were also studied. The intermetallic phases α_c-Al-(Fe,Mn)-Si, θ-Fe_4Al_{13} and η-Fe_2Al_5 were again identified and characterised in terms of morphologies, compositions and crystal structures. In addition, the interfacial intermetallic phase layer was subjected to phase and orientation mapping by indexing of electron backscatter diffraction data. The findings agreed well with the results obtained from the joints made with the other two methods and with observations reported in literature.

There are still questions that remain to be answered, especially concerning the initial formation and growth of interfacial intermetallic phase layers at the nanoscale. New insights can possibly be obtained by combining *in-situ* heating experiments with electron microscopy techniques. Some proof-of-concept *in-situ* heating experiments that were conducted in this work are discussed, and specific challenges are highlighted that should be considered prior to performing *in-situ* heating experiments aimed at studying phenomena related to interdiffusion. Overall, this thesis advocates the importance of electron diffraction techniques in the study of interfacial intermetallic phase layers in Al-steel joints. Scanning electron diffraction techniques offer possibilities to characterise a wide range of materials, especially with the advent of direct electron detectors, and these opportunities should be seized in future studies.

Preface

This thesis has been submitted to the Norwegian University of Science and Technology (NTNU) as a part of the fulfilment of the requirements for the degree of Philosophiae doctor (PhD). The work was conducted from August 2016 to March 2021, mainly at the Department of Physics, NTNU. The main supervisor was Ass. Prof. Per Erik Vullum, Department of Physics, NTNU. Prof. Randi Holmestad, Department of Physics, NTNU, and Ass. Prof. Ida Westermann, Department of Materials Science and Engineering, NTNU, were co-supervisors.

The project was a part of the centre for research-based innovation *SFI Manufacturing*, which was financially supported by industrial partners together with the *Research Council of Norway* (RCN) under project number 237900. Within SFI Manufacturing, this project was a part of research area 1: *multi-material products and processes* and work package 1.2: *multi-material products of dissimilar metallic materials*.

The infrastructure within the *TEM Gemini Centre*, Department of Physics, NTNU Trondheim, was primarily employed. The TEM Gemini Centre is a part of the *Norwegian Centre for TEM* (NORTEM), that was financially supported by the RCN under project number 197405. In addition, instrumentation within the cleanroom facility *NTNU NanoLab* was used, which was financially supported by the RCN under the project *Norwegian Micro- and Nano-Fabrication Facility* (NorFab) with number 245963/F50. Instrumentation within the *Electron microscopy lab* at the Department of Materials Science and Engineering, NTNU Trondheim, was also employed.

This thesis is divided into three main parts, and the research is presented in the form of an article collection. The first part gives an introduction to the research conducted, states the objectives and scope and presents the required background knowledge on the materials and joining methods studied, as well as the principles behind the experimental techniques used. In the second part, the main findings are summarised and discussed, future work is proposed and the main conclusions are given. The conducted research is presented in the form of scientific publications included in the third part.

Publication list

Papers included in this thesis

Paper I — Nanocrystal segmentation in scanning precession electron diffraction data
T. Bergh, D.N. Johnstone, P. Crout, S. Høgås, P.A. Midgley, R. Holmestad, P.E. Vullum, A.T.J. van Helvoort
Journal of Microscopy (2020) **279** 158-167

Paper II — Microstructural and mechanical characterisation of a second generation hybrid metal extrusion & bonding aluminium-steel butt joint
T. Bergh, L. Sandnes, D.N. Johnstone, Ø. Grong, F. Berto, R. Holmestad, P.A. Midgley, P.E. Vullum
Materials Characterization (2021) **174** 110761

Paper III — Microstructure and tensile properties of a multi-material aluminium-copper-steel-titanium butt joint made in one pass by hybrid metal extrusion & bonding
T. Bergh, H. Fyhn, L. Sandnes, J. Blindheim, Ø. Grong, R. Holmestad, F. Berto, P.E. Vullum
To be submitted

Paper IV — On intermetallic phases formed during interdiffusion between aluminium alloys and stainless steel
T. Bergh, S.M. Arbo, A.B. Hagen, J. Friis, J. Blindheim, I. Ringdalen, M.Z. Khalid, R. Holmestad, I. Westermann, P.E. Vullum
To be submitted

Paper V — On interfacial intermetallic phase layers in cold metal transfer aluminium-steel joints made with an Al-Si-Mn alloy as filler material
T. Bergh, H.W. Ånes, R. Aune, S. Wenner, R. Holmestad, X. Ren, P.E. Vullum
Unpublished work

Papers not included in this thesis

Paper A — Influence of thermomechanical processing sequence on properties of A6082-IF steel cold roll bonded composite sheet
S.M. Arbo, T. Bergh, H. Solhaug, I. Westermann, B. Holmedal
Procedia Manufacturing (2018) **15** 152-160

Paper B — Relationship between Al-Ni intermetallic phases and bond strength in roll bonded steel-aluminum composites with nickel interlayers
S.M. Arbo, T. Bergh, B. Holmedal, P.E. Vullum, I. Westermann
Metals (2019) **9** 827

Paper C — β- and δ-Al-Fe-Si intermetallic phase, their intergrowth and polytype formation
H. Becker, T. Bergh, P.E. Vullum, A. Leineweber, Y. Li
Journal of Alloys and Compounds (2019) **780** 917-929

Paper D — Effect of Mn and cooling rates on α-, β- and δ-Al–Fe–Si intermetallic phase formation in a secondary Al–Si alloy
H. Becker, T. Bergh, P.E. Vullum, A. Leineweber, Y. Li
Materialia (2019) **5** 100198

Paper E — An analytical framework for modelling intermetallic compound (IMC) formation and optimising bond strength in aluminium-steel welds
Ø. Grong, L. Sandnes, T. Bergh, P.E. Vullum, R. Holmestad, F. Berto
Material Design & Processing Communications (2019) **1** 3

Paper F — Interface microstructure and tensile properties of a third generation aluminium-steel butt weld produced using the hybrid metal extrusion & bonding (HYB) process
L. Sandnes, T. Bergh, Ø. Grong, R. Holmestad, P.E. Vullum, F. Berto
Materials Science and Engineering A (2021) **809** 140975

Code contributions

pyxem/pyxem: pyxem 0.10.0
D.N. Johnstone, P. Crout, J. Laulainen, S. Høgås, B. Martineau, T. Bergh, S. Smeets, ...; *Zenodo* (2019) 10.5281/zenodo.3533653

pyxem/pyxem-demos: pyxem-demos 0.10.0
D.N. Johnstone, P. Crout, S. Høgås, T. Bergh, J. Laulainen, S. Smeets; *Zenodo* (2019) 10.5281/zenodo.3533670

kikuchipy/kikuchipy: kikuchipy 0.2.2
H.W. Ånes, T. Bergh; *Zenodo* (2020) 10.5281/zenodo.3842021

Datasets

Scanning precession electron diffraction data of partly overlapping magnesium oxide nanoparticles
T. Bergh; *Zenodo* (2019) 10.5281/zenodo.3382873

Scanning electron diffraction tilt series data of an aluminium-steel interface region
T. Bergh, D.N. Johnstone, C.S. Allen; *Zenodo* (2020) 10.5281/zenodo.3938898

Acknowledgements

I have been lucky to work with several people during the last four years, and I am grateful for all the collaborations and the fruitful discussions. First, I would like to thank my main supervisor Per Erik Vullum for giving me this opportunity, for all the guidance, and for teaching me many tips and tricks in the lab. I am also very grateful for the help from my co-supervisor Randi Holmestad, who has in many ways been an extra main supervisor. You have both given me a lot of freedom and have always supported and encouraged me. Moreover, I would like to express my gratitude towards the people in SFI Manufacturing and the industrial partners.

I have enjoyed working with and have learned a lot from Siri Marthe Arbo and my co-supervisor Ida Westermann, who have given valuable input from the metallurgists' perspective. Thank you for the interesting specimens and the many useful discussions. To Lise Sandnes, Øystein Grong and Filippo Berto, I have greatly appreciated our collaboration and would like to thank you for providing highly relevant specimens, for promptly responding to questions, and for being extremely enthusiastic and encouraging.

To Antonius (Ton) van Helvoort, I am very grateful for the guidance you gave and the enthusiasm you spread both as my supervisor during my master thesis and during the last four years. Thank you also for introducing me to the collaborators Duncan Johnstone, Phillip Crout and Paul Midgley, from whom I have learnt a lot regarding data analysis and preparation of manuscripts. Especially, I would like to thank Duncan Johnstone for performing experiments, showing me around and giving constructive criticism. I am also very grateful to have worked with Hursanay Fyhn, who has inspired with her ability to work efficiently and with drive. To Simon Høgås and Eirik Opheim, thank you for sharing good ideas and raising interesting questions, and for always being eager to tackle new challenges. Furthermore, I would like to thank Håkon Ånes for many motivating discussions and all the help. I would like to give special thanks to Hanka Becker, Anette Brocks Hagen, Sigurd Wenner, Jesper Friis, Muhammad Zeeshan Khalid, Inga Ringdalen, Bjørn Holmedal, Ragnhild Aune and Xiaobo Ren, for the collaborations.

My gratitude extends to the engineers in the TEM group, Bjørn Soleim and Ragnhild Sæterli. Thank you for giving me training, for running the lab facilities in a smooth way, and for taking all concerns seriously and promptly responding to issues. I am thankful to everyone in the TEM group for the open and positive environment, the low threshold for asking questions, and the eagerness to help. I would like to thank Adrian, Julie, Jonas S, Aleksander, Emil, Elisabeth, Inger-Emma, Christoph, Dipanwita, Håkon, and many others who have resided in or near the B4 corridor, for sharing the PhD experience, both at and outside of work.

My friends both inside and outside of the PhD-life-bubble also deserves to be mentioned, though they are too many to state by name. A special thank you to Sandra, Solveig, Trygve, Øyvind and Nita, for all the support and time spent together, and to my friends from nano. I am grateful to my family, and to my parents especially, for always challenging me to think critically and take responsibility from an early age, for always expressing their support and being there when help is appreciated. The last and biggest thank you goes to Jonas, who has helped me in so many aspects of life during the past four years, and who made it all seem much more cheerful and meaningful.

Thank you all for everything, and I wish you the very best in the future.

Acronyms

4D	four dimensional
AS	advancing side
bcc	body centred cubic
(V)(A)BF	(virtual) (annular) bright field
BM	base material
BSE	backscattered electron
CBED	convergent beam electron diffraction
CCD	charge coupled device
CMT	cold metal transfer
(V)(A)DF	(virtual) (annular) dark field
DFT	density functional theory
DP	dual phase
EBSD	electron backscatter diffraction
EELS	electron energy loss spectroscopy
(S)(P)ED	(scanning) (precession) electron diffraction
EDS	X-ray energy dispersive spectroscopy
(S)(T)EM	(scanning) (transmission) electron microscopy
EZ	extrusion zone
fcc	face-centered cubic
FIB	focused ion beam
FM	filler material
FOLZ	first order Laue zone
FSW	friction stir welding
GMAW	gas metal arc welding
HAADF	high angle annular dark field
HAZ	heat affected zone
HOLZ	higher order Laue zone
HR	high resolution
(A)HSS	(advanced) high strength steel
HYB	hybrid metal extrusion & bonding
IF	interstitial free
IMP	intermetallic phase
MIG	metal inert gas
NBD	nanobeam electron diffraction
NMF	non-negative matrix factorisation
PCA	principal component analysis
RB	roll bonding
RED	rotation electron diffraction
ROI	region of interest
RS	retreating side
SAED	selected area electron diffraction
SE	secondary electron
SOLZ	second order Laue zone
SSSS	supersaturated solid solution
SVD	singular value decomposition
TMAZ	thermo-mechanically affected zone
UTS	ultimate tensile strength
ZOLZ	zero order Laue zone

Contents

Part I

Background

Chapter 1

Introduction

1.1 Motivation

The overall motivation for this project is connected to challenges faced by the manufacturing industry. Manufacturing companies must answer increasing demands to improve product performance and functionality. In the last decades, greenhouse gas emissions and global warming concerns have risen in line with increasing population and living standards. Manufacturing industries therefore also face requirements of reducing the environmental impact. In answering the ever-growing demands, products that are composed of only one single material fall short. It is necessary to fabricate multi-materials or hybrid structures that are composed of two or more dissimilar materials joined together [1]. With multi-material structures, the individual properties of the parent materials can be jointly utilised, and the material properties can be tailored for each independent structural component. Such structures enable improvement of performance and functionality and/or reduction of weight and cost [2]. In particular, using materials with diverse properties increase the lightweighting potential significantly [3].

Lightweighting is especially important in vehicle manufacturing and transportation industries that continuously face stricter regulations on fuel efficiency. One common lightweighting strategy is to re-evaluate the material selection and substitute high density materials with high strength lower density materials where possible. As an example, in automobile constructions, steels have dominated for about a century, after taking over from woods [4]. Figure 1.1 presents an Ashby diagram that shows strength versus density for common engineering materials [5]. As expected, it can be seen that woods lie at the bottom left of the diagram, while metal alloys cover a broad range of properties and generally have high strengths and high densities. Table 1.1 lists key physical parameters for the common metals aluminium (Al), titanium (Ti), iron (Fe) and copper (Cu), where it can be seen that the density of Al is about three times lower than the density of Fe [6]. By value, Al is one of the top five largest export products of Norway. In its pure state, Al is relatively soft, but by adding $\sim$1 wt.% of alloying elements and performing thermo-mechanical treatment, high strength and lightweight Al alloys can be fabricated. In addition, Al alloys typically have good corrosion resistance and formability, and high electrical and thermal conductivity. It has been stated that by using Al alloys in vehicles, a weight reduction of up to 50% can be achieved without compromising safety [7, 8]. Due to the many advantages of Al alloys, their use in automobiles has been rising recently. Already in 1994, Audi developed the Audi A8 with a car body frame, named the 'spaceframe', entirely made of Al alloys, which enabled a 40% weight reduction compared to a corresponding steel body [9, 10].

Apart from using lower density materials, downsizing is another common lightweighting strategy. Research is ongoing to develop advanced steels with higher specific strengths [12], which offer an alternative to lightweighting by using Al alloys. It must also be mentioned that when it comes to the total environmental footprint, there is a trade-off in the user phase for when the use of Al alloys are more environmentally friendly than steels in vehicle bodies [13]. Existing

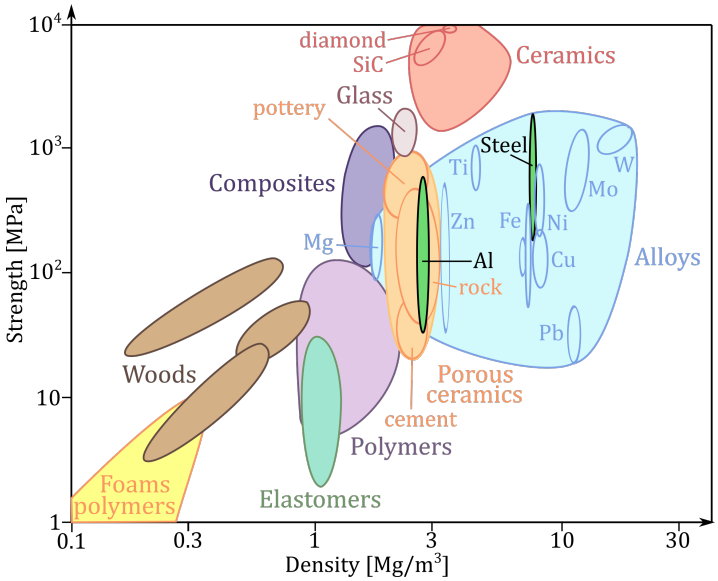

Figure 1.1: Ashby chart showing strength versus density for common engineering materials. For metal alloys the yield strength is shown. Adapted from Figure 6 in [5].

Table 1.1: Physical properties of pure Al, Ti, Fe and Cu. Note that the thermal conductivity is given for temperatures in the range of $20-100$°C, the thermal expansion for $0-100$°C, and the electrical resistivity at 20°C. Adapted from [6], but with crust compositions extracted from [11].

Property	Unit	Al	Ti	Fe	Cu
Atomic number	-	13	22	26	29
Relative mass	u	26.98	47.90	55.85	63.55
Relative density	$\mathrm{g\,cm^{-3}}$	2.70	4.51	7.87	8.96
Elastic modulus	GPa	70	120	211	130
Specific modulus	$\mathrm{GPa\,/\,g\,cm^{-3}}$	26	26	27	14
Melting point	°C	660	1678	1535	1083
Thermal conductivity	$\mathrm{W\,m^{-1}\,K^{-1}}$	238	26	78	397
Thermal expansion	$\mathrm{10^{-6}K^{-1}}$	23.5	8.9	12.1	17.0
Electrical resistivity	$\mu\Omega\,\mathrm{cm}$	2.67	54	10.1	1.69
Crust composition	wt.% or ppm*	8	4010*	4	25*

production lines and infrastructure favour continued use of steel, and Al alloys are in general both more cost and energy expensive than steels. Fortunately, the electricity production is mainly based on hydropower in Norway. Further, Al alloys can be produced by recycling of scrap material, which only requires a fraction of the energy, typically 5% [14]. The competition between the use of steels and Al alloys has set the scene for a materials lightweighting race, which recently has intensified due to the growing demand for electric vehicles where weight plays a crucial role. The materials race has been described by news articles in the last decade with titles such as "For lightweight cars, a materials race" [15], "Material wars - who's going to win the automotive metals race?" [16] and "The battle of the bodies: steel vs. aluminium in automotive production" [17]. There are several indications that the future is multi-material products. One example is the "Super Light Car" project where 35 car manufacturers together

developed a multi-material body-in-white solution that consisted of 53% Al alloys, 36% steel, 7% magnesium (Mg) alloys and 4% plastics, and that allowed a 37% weight saving [18].

To realise the use of multi-material products, cost-effective, robust and flexible dissimilar material joining methods are needed, and such methods are key to innovative and sustainable manufacturing. For instance, it was written in a manual of 2015 by the European Aluminium Association that [19]: "With respect to the automotive market, the most important task is joining aluminium to steel. Consequently, this problem is also the main driving force to develop new, improved joining methods for dissimilar materials." Traditionally, mechanical joining methods, such as riveting, screwing and clinching, have been used to join dissimilar metals. However, the strength of welded joints is often higher than what can be achieved with mechanical or adhesively bonded joints [20]. Unfortunately, dissimilar metal welding is in general highly challenging due to the large differences in thermo-physical properties between the metals to be welded. For Al alloys and steels, the large differences in melting point, thermal conductivity and thermal expansion (Table 1.1), make Al-steel welding near impossible with traditional fusion welding techniques where the metals are melted. Also, Al alloys are sensitive to thermo-mechanical treatment and develop soft *heat affected zones* (HAZs) during welding, which can limit the mechanical properties of the joints. Moreover, Fe has low solid solubility in Al [21], so that the two metals will not mix continuously when bonded. Rather, intermetallic Al-Fe phases will grow at the bonded interface depending on the alloying elements present and the thermo-mechanical treatment history [22]. These phases are inherently brittle and limit the properties of the joints, especially if they form thick *intermetallic phase* (IMP) layers along the Al-steel interfaces [23, 24].

To overcome the challenges associated with Al-steel welding, low temperature welding methods can be employed, including in particular solid-state welding methods. Solid-state welding methods comprise a versatile range of welding methods that typically gives high strength joints [25]. An example of a traditional solid state welding method is *roll bonding* (RB). Further, welding methods have been developed during the last decades that enable metallurgical bonding at lower temperatures than traditional fusion welding methods, such as the fusion welding method *cold metal transfer* (CMT) [26] and the solid-state welding method *friction stir welding* (FSW) [27]. FSW utilises high plastic deformation to join various metal alloys, and it has been used successfully to join Al and steel. For instance, in 2012 the Honda Motor Company used friction stir welding to fabricate a car front subframe of Al and steel, which was 25% lighter compared to a conventional steel subframe [28]. *Hybrid metal extrusion & bonding* (HYB) is another solid-state welding method that uses large plastic deformation to allow bonding at low temperatures [29, 30]. HYB is based on continuous extrusion of an Al filler material that is squeezed into the gap between the metals to be joined. The continuous extrusion of Al filler material is a unique feature of HYB, which make this welding method more flexible and versatile than other solid-state methods. The method was invented in Trondheim, Norway, and the company HyBond AS was founded based on the HYB technology and has the vision of further developing and industrialising the HYB process [31].

To enable further development of Al-steel joining methods and fabrication of improved Al-steel joints, characterisation of the joints is crucial. In Al-steel joints, the IMP layer that typically forms along the bonded interface can be detrimental, as mentioned previously. Thus, it is crucial to characterise both the mechanical properties of the joints and their IMP layers to explain the performance of the joints. In sound joints, the IMP layers typically have thicknesses in the range from the micrometre to the nanometre scale. Obtaining the required spa-

tial resolution to study these layers is not possible with conventional visible light microscopy, where the wavelength of the light used to form magnified images is on the order of a few hundreds of nanometres. However, fast electrons have a wavelength several magnitudes smaller, and electron microscopes can be used to study materials with a spatial resolution down to the atomic scale. In *electron microscopy* (EM), fast electrons are impinged onto the specimen, and the various electron-matter interactions that subsequently take place give rise to a broad range of complementary signals that can be recorded. The specimen can be characterised in terms of for instance morphology, chemical composition, and crystal structure [32, 33], which is important in the characterisation of the IMP layers. Therefore, the main characterisation technique used in this work was EM, and in particular *transmission EM* (TEM). Altogether, the main motivation for this project was associated with the demand for characterisation of Al-steel joints with focus on the IMP layers formed, and the use and development of EM techniques that make such characterisation possible.

1.2 Objectives and scope

This PhD work is a part of the Norwegian research centre SFI Manufacturing, which has the vision of showing that "sustainable and advanced manufacturing is possible in high cost countries, with the right products, technologies and humans involved" [34]. Within SFI Manufacturing, this PhD project lies under research area 1: "multi-material products and processes", for which the overall objective is "to develop the ability to optimize material choice, multi-materials geometry and processes simultaneously".

The main goal of this project has been to characterise the microstructure of the interface regions in selected joints to gain better understanding of the underlying bonding mechanisms and the performance of the joints, with the main focus placed on the formed IMP layers. To reach the overall goal, EM techniques were to be used and developed. Summarised point-wise, the objectives were to:

- assess the bonding mechanisms in selected joints,
- characterise the formed IMP layers in terms of morphology, crystal structure and composition,
- use and develop EM methods central in the characterisation of the IMP layers,
- contribute to better understanding of how alloying elements and heat treatments affect the interfacial IMP layers formed, and
- contribute to better understanding of the microstructure-property relationship in joints.

The scope of this work was naturally limited, and the focus was placed on a few central topics. Most importantly, the work concerned only microstructural characterisation of the interface regions in selected Al-steel joints. The selected joints were fabricated by collaborators using the three welding techniques: HYB, RB and CMT. Development of the joining techniques was not a topic of this work. Further, the interface characterisation was done with TEM as the main tool, and the focus was placed on the formed IMPs, while detailed characterisation of the parent materials was not performed. The work was experimental in nature, and use and/or development of modelling tools or theoretical frameworks were outside the scope. Insight gained from the interface microstructural characterisation should ultimately be connected to insight gained from characterisation of bulk specimens, which was done by collaborators. There the focus was placed on mechanical properties, including hardness and tensile strength, and characterisation of other properties, such as corrosion resistance and electrical conductivity, was not included here.

Chapter 2

Materials — Aluminium-steel joints

This chapter provides the necessary background to understand the materials that were characterised in this work. First, the fundamental metallurgy of Al and its alloys is in focus. A brief general description of strengthening mechanisms of metal alloys is also given. The next section aims to provide a short overview over steels, and related microstructures and strengthening mechanisms. After the background on Al alloys and steels, joining methods that can be used to bond them together are described, with the focus placed on the welding methods central in this work. Subsequently, an overview over known Al-Fe-silicon (Si) IMPs is presented, and solid state interdiffusion is explained in short. Finally, interfacial Al-Fe(-Si) IMP layers that have been reported to grow in Al-steel joints are elaborated on briefly. The influence of alloying elements on the formation and growth of IMP layers, and the mechanical properties of the joints are discussed, based on findings reported in the literature.

2.1 Aluminium and its alloys

The properties of Al can be altered significantly by alloying and thermo-mechanical treatment. These property changes result from the introduction of various defects into the Al crystal lattice and changes in the Al grain structure and texture. This section gives a brief introduction into crystal defects and strengthening mechanisms in metal alloys in general, in addition to describing key concepts of Al alloys. To begin with, classification of Al alloys is explained, before main takeaways regarding thermo-mechanical processing routes and strengthening mechanisms are described.

2.1.1 Classification

Al has a *face-centred cubic* (fcc) crystal structure. In nature, Al readily reacts with oxygen (O) to form various types of Al oxides, and the Earth's crust contains 15 wt.% Al_2O_3, compared to 62 wt.% SiO_2 and 6 wt.% Fe_2O_3 [11]. The most economical natural source of Al is bauxite, a sedimentary rock formed after millions of years of surface weathering of rocks in (semi-)tropical regions [35]. Bauxite consists of several forms of hydrated Al oxides, typically amounting for $30-60$%, together with Fe, Si and Ti oxides and various impurities. The first step in Al production is to produce alumina, Al_2O_3, from bauxite ore. Typically, this process also yields insoluble waste residue consisting of Fe, Ti and Si oxides, denoted "red mud". The subsequent production of metallic Al from alumina can be achieved by electrolytic reduction, which is extremely energy expensive. Al alloys are then prepared by melting and mixing Al metal together with the alloying elements in a furnace before casting, which yields *primary alloys*. Al alloys can also be produced by recycling of scrap material, which gives Al alloys referred to as *secondary alloys*. Production of secondary alloys demands only a fraction of the energy required for primary Al production, typically 5% [14]. However, a challenge in recycling is to limit the amount of trace elements that may significantly influence the properties, and to obtain the correct amount of alloying elements.

Al alloys are typically grouped into two main categories; cast and wrought alloys, often denoted AC and AW, respectively. Casting is a process where a liquified metal is allowed to consolidate in a mould. A *cast alloy* is produced directly into the finished shape during casting. Production of a *wrought alloy* however, includes a working process involving plastic deformation, such as rolling, extrusion, drawing or forging. Wrought alloys amounts for $75-80$% of all Al alloy products, and a few hundred types of wrought alloys are available commercially [6]. These are denoted using a four digit system, where the first digit stands for the main alloying element(s). Main alloying elements include Cu, Mg, manganese (Mn), Si and zinc (Zn) [36]. Typically, other elements are also added, such as chromium (Cr), lithium (Li), scandium (Sc), silver (Ag) and Ti [14]. The second digit indicates possible modifications, and the two last digits are either identifiers for a specific alloy or signifies the Al purity. Table 2.1 lists the eight main wrought Al alloy series, together with their key characteristics. In addition, both cast and wrought Al alloys are also categorised as heat-treatable or non-heat-treatable, depending on whether they can be hardened by heat treatment or not.

Table 2.1: The eight main wrought Al alloy series according to the four digit classification system. The main alloying elements and the heat-treatability are listed. Typical *ultimate tensile strength* (UTS) values and typical characteristics are given, together with some example applications. The information has been extracted from [14, 36, 37].

Series	Main element(s)	Heat-treatable	Typical UTS [MPa]	Typical characteristics	Example applications
1xxx	None	No	$100-200$	Good conductivity, exceptional formability, good weldability and good corrosion resistance	Electrical conductors, chemical equipment, foil, architecture and cooking utensils
2xxx	Cu	Yes	$200-450$	High strength, also at elevated temperatures	Aerospace
3xxx	Mn	No	$100-300$	Good corrosion resistance and formability	Cans, utensils and heat exchangers
4xxx	Si	Yes and no	$150-400$	Good weldability	Filler wires and forged pistons
5xxx	Mg	No	$100-350$	Good corrosion resistance, toughness and weldability	Marine, military, construction and automotive
6xxx	Mg and Si	Yes	$100-400$	Excellent extrudability	Structural and automotive
7xxx	Mg and Zn	Yes	$200-700$	High strength	Military and aerospace
8xxx	Miscellaneous	Yes and no	$100-400$	Miscellaneous	Nuclear, automotive and aerospace

2.1.2 Thermo-mechanical treatment

Thermo-mechanical treatment involves both heat and plastic deformation, and is crucial to obtain the desired properties of most Al alloys. Each alloy is given a suffix letter that states its treatment condition, where the letter T is given for heat treated alloys. For such alloys, a subsequent digit is included that specifies the heat treatment, and these are shown in Table 2.2. As can be seen, processing of a specific Al alloy typically involves several stages. Here, processing steps are explained in the form of a generic production route for a typical $6xxx$ (Al-Mg-Si) extrusion alloy that is hot worked and then heat treated to T6 condition. A sketch of the temperature-time profile is depicted in Figure 2.1(a).

Table 2.2: Temper designations for heat treated Al alloys. Adapted from [36].

Temper	Treatment
T1	cooled after elevated temperature shaping and naturally aged
T2	cooled after elevated temperature shaping, cold worked and naturally aged
T3	solution heat treated, cold worked and naturally aged
T4	solution heat treated and naturally aged
T5	cooled after elevated temperature shaping and artificially aged
T6	solution heat treated and artificially aged
T7	solution heat treated and over-aged (stabilised)
T8	solution heat treated, cold worked and artificially aged
T9	solution heat treated, artificially aged and cold worked
T10	cooled after elevated temperature shaping, artificially aged and cold worked

First, the alloy is cast above the melting point. During solidification of the cast, *constituent particles* form that are often referred to as constituent phases or primary particles or only as IMPs. These are coarse foreign phase particles that solidify before Al via interdendritic decomposition [14]. As the Al dendrites solidify, solute is rejected into the liquid between the dendrite arms, which leads to a gradient of composition that is referred to as microsegregation [37].

Homogenisation is the next step, and here the alloy is held at a high temperature right below the eutectic. This enhances diffusion so that a large amount of solute is dissolved and microsegregation is eliminated [37]. During this process, *dispersoids*, also called secondary particles, form by solid state precipitation of elements that diffuse slowly and have modest solubilities [14]. Dispersoids are well distributed within the Al matrix, hence their name, and typically have dimensions on the order of $\sim 50 - 500$ nm. A sketch showing dispersoids and a constituent particle embedded within Al is shown in Figure 2.1(b).

After homogenisation, the example $6xxx$ alloy is pre-heated and hot worked by extrusion, as can be seen in Figure 2.1(a). During *extrusion*, a billet is pressed through a die so that its cross-sectional area is significantly reduced. In this process, the billet is subjected to high temperatures and substantial plastic deformation. The extensive plastic deformation during working typically introduces line defects known as *dislocations* that will be introduced in the next section. However, due to the high temperature during hot working, *recovery* may happen. That is annihilation and rearrangement of dislocations, which lower the elastic strain energy of the material, without motion of high angle grain boundaries [38]. The recovery occurring during hot working is dynamic and progresses as the material is deformed, as opposed to static recovery that happens during annealing of a cold worked material. Recovery is a multi-step process that eventually leads to subgrain formation and growth. *Subgrains* are crystalline regions divided by low-angle grain boundaries. Further, *recrystallisation* can occur, which is formation and growth of new grains with low dislocation densities [38]. More information on dislocations will be given in the next section, while the reader is referred to [38] for more information on recovery and recrystallisation. If the specimen is kept at elevated temperatures, *grain growth* may progress so that large grains with low strain energy grow at the expense of smaller ones to reach a configuration which lowers the grain boundary energy [38]. To obtain a higher strength alloy, it is most often advantageous to suppress recrystallisation and grain growth, and this can be accomplished with the presence of dispersoids [14]. In total, the processes taking place during working alter the dislocation density and grain structure, which both are parameters that influence the strength, as will be discussed in the next section.

After extrusion the alloy may be solution heat treated[1] to dissolve solutes and create a nearly homogeneous *supersaturated solid solution* (SSSS) [37]. This is followed by *quenching*, i.e. rapid cooling, to maintain the SSSS and to quench in vacancies, i.e. empty lattice sites. The vacancies aid solute diffusion and facilitate heterogeneous nucleation of precipitates during subsequent heat treatment. Afterwards, the alloy is *naturally aged*, i.e. stored at room temperature and/or *artificially aged* at an elevated temperature. During natural ageing, solutes in the SSSS gather to form clusters, and during artificial ageing these grow into nanoscale particles called *precipitates*. The precipitates typically evolve through various stages and transform from metastable phases into stable phases after sufficient heat treatment time. This evolution depends strongly on the alloy composition [39, 40]. For Al-Mg-Si alloys, the precipitation sequence has been found to be [41–43];

$$\text{SSSS} \rightarrow \text{solute clusters} \rightarrow \text{Guinier-Preston zones} \rightarrow \beta'' \rightarrow \beta', \text{U}_1, \text{U}_2, \text{B'} \rightarrow \beta, \text{Si}. \tag{2.1}$$

Guinier-Preston zones are ordered regions that form before precipitates. During ageing, these zones are replaced by a sequence of semi-coherent metastable phases, and coherency with the Al matrix is gradually lost as the precipitates evolve [39]. β'', β', U_1, U_2 and B' are all metastable precipitates and the last β-Mg_2Si phase is the final equilibrium precipitate. A simple schematic drawing of example precipitates is shown in Figure 2.1(b). Precipitates grow along specific directions in the Al crystal lattice and reach dimensions typically on the order of $\sim 1-100$ nm. They give the main contribution to the strength of heat treatable Al alloys, and for a specific alloy there is a specific heat treatment schedule that leads to peak hardness, which lies in between underaged and overaged conditions. An *underaged* alloy has not been aged sufficiently to reach peak hardness, while an *overaged* alloy has been aged past peak hardness. However, in general several strengthening mechanisms contribute collectively.

2.1.3 Strengthening mechanisms

A material that is subjected to an applied stress deforms, meaning that it changes in size and/or shape. For elastic deformation, the original shape and size are recovered after the external stress has subsided. For plastic deformation, the induced shape and size changes still persist after unloading. The *yield strength* of a material is its capacity to endure an applied load without deforming plastically. This is most commonly measured by tensile testing, where a specimen is stretched at a constant rate, and the applied uniaxial load and the specimen elongation are recorded [45]. From the recorded data, a load versus displacement curve can be presented, or converted to a stress-strain curve. Engineering strain is given by $\epsilon = \Delta L/L_0$, where ΔL is the change in specimen length and L_0 is the initial length [45]. Engineering stress is given by $\sigma = F/A_0$, where F is the applied load and A_0 is the initial cross-sectional area normal to the force direction [45]. Schematic engineering stress-strain curves are shown in Figure 2.2 for both a ductile and a brittle material. During tensile testing, a specimen first undergoes elastic deformation. In this regime, the stress is proportional to the strain, as given by Hooke's law: $\sigma = E\epsilon$, where E is the *Young's modulus* [45]. Elastic deformation continues up to a limit, after which plastic deformation occurs. The elastic-plastic transition is often hard to pinpoint. By convention the yield stress, σ_y, is determined by the intersection of the stress-strain curve with a line parallel to the elastic region of the curve, where the line is given a specified strain offset, often 0.2% [45]. From the yield point, the applied stress continues to increase, mainly due to work hardening, until the *ultimate tensile strength* (UTS), σ_u, is reached.

[1] Note that solution heat treatment is not necessarily done after extrusion, since high temperatures are reached during extrusion that may act similar to a solution heat treatment.

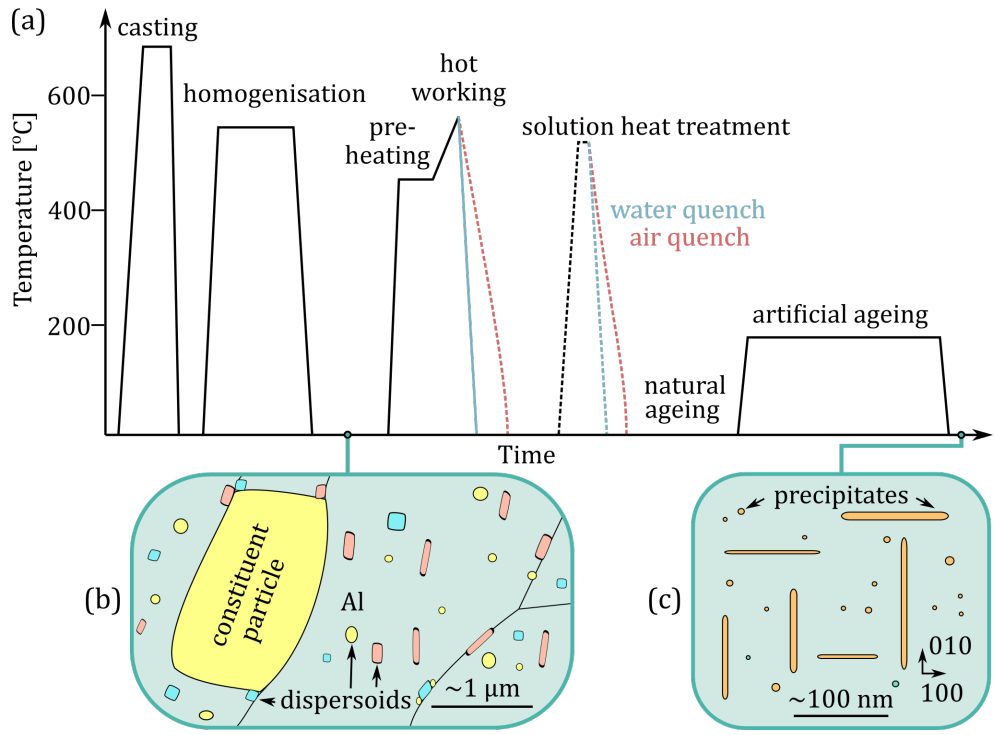

Figure 2.1: Illustration of thermo-mechanical treatment for an age-hardenable $6xxx$ Al-Mg-Si extrusion alloy. **(a)** Typical schematic temperature-time profile for an alloy that is homogenised, extruded and age hardened. Adapted from [44]. Drawings showing foreign phase particles embedded within Al; **(b)** a constituent particle and dispersoids, and **(c)** precipitates. The various colours indicate phases with distinct chemical compositions.

The UTS is the maximum applied stress that the material can withstand before deformation becomes localised. A brittle material undergoes limited plastic deformation and fractures almost immediately after reaching the UTS. A ductile material on the other hand, undergoes extensive plastic deformation and necking before fracture, as shown in Figure 2.2. After the onset of necking, the work hardening cannot compete with the reduction in cross-sectional area, so that the applied stress decreases until fracture.

When Al deforms plastically, the deformation is not simply a result of breaking of atomic bonds. In fact, if that was the case, the strength would be significantly higher. Instead, plastic deformation happens as a result of propagation of line defects in the crystal lattice that are called *dislocations*[2]. Dislocations are divided into two main categories in the ideal extreme case; edge and screw dislocations, although a general and curved dislocation has a mixed character that varies along its length. An edge dislocation in a simple cubic material is illustrated to the bottom left in Figure 2.3. Associated with the edge dislocation is a long-range stress field that is compressive at the side of the inserted half plane and tensile at the opposite side. Any dislo-

[2]Note that plastic deformation occurs also by twinning in some materials [46, 47]. Since Al has a high stacking fault energy, stacking faults and twins scarcely form [14]. Thus, only dislocation motion is considered here.

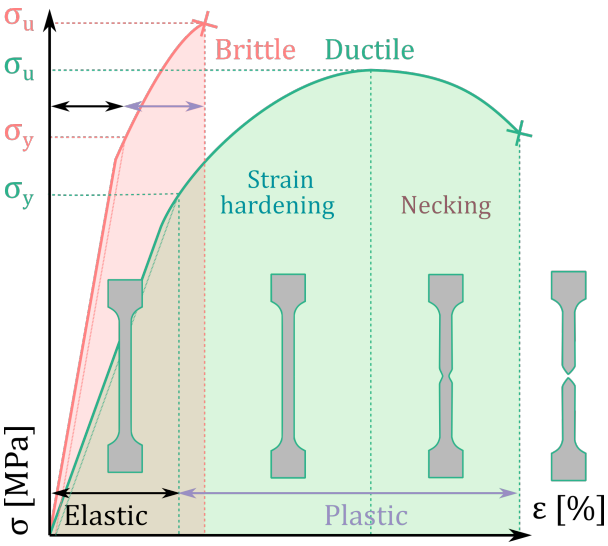

Figure 2.2: Schematic engineering stress-strain curve for a brittle and a ductile material. Adapted from [45]. The elastic and plastic deformation regimes are indicated, and the yield stress, σ_y, and the UTS, σ_u, are marked. The insets show elongation, necking and fracture of a schematic tensile specimen of a ductile material. The area under the curve (coloured) signifies the material toughness, i.e. the energy absorbing ability.

cation can be described by the displacement vector known as the Burgers vector, $\vec{b}$, and by the dislocation line vector, $\vec{t}$. The Burgers vector is the vector that joins the start and end position of the constructed Burgers circuit, as shown in Figure 2.3, which for an ideal edge dislocation is $\vec{b} = \frac{1}{2}[110]$ in a fcc crystal [46]. An edge dislocation can move by reorganisation of bonds so that it glides along a plane known as the slip plane. The *slip plane* is the plane that contains both the dislocation line vector and the Burgers vector, i.e. $\{111\}$ in this case [46]. The stress required to initiate slip in a specific metal is often approximated to a constant characteristic value referred to as the critical resolved shear stress, τ_c [47]. The resolved shear stress is the value of the shear stress resolved on the slip plane in the slip direction. The critical resolved shear stress, τ_c, is connected to the yield stress by $\sigma_y = \tau_c M$, where M is the Taylor factor that accounts for texture and load condition, typically around 3 [46]. An edge dislocation can also move out of its slip plane by a mechanism known as climb, and a screw dislocation can move to another equivalent slip plane by cross-slip, but these topics are not covered here. The reader is referred to [46, 47] for further information on dislocations.

Since plastic deformation is a result of dislocation movement in Al, strengthening can be achieved by introducing crystal defects that interact with and hinder propagation of dislocations. In general, crystal defects are categorised into four main groups; point, line, planar and bulk defects. Amongst the point defects, vacancies and solute atoms are the most important. A solute atom is a foreign element that is incorporated into the crystal lattice either by occupying a lattice position at the expense of a host atom, which is known as a *substitutional solute*, or by taking a position in between lattice points, which is known as an *interstitial solute*. These point defects are shown schematically in Figure 2.3. Around a solute atom there is a displacement field mainly due to the mismatch in atomic radius between the solute atom and the matrix atoms. This field may interact with the displacement field associated with a dislocation, so that a higher stress must be applied for it to glide, resulting in *solute strengthening* [46]. The increase in yield stress by solute strengthening, increases with the solute concentration [48].

When it comes to line defects, dislocations have already been introduced. Dislocations repel each other if the compressive regions of their stress fields overlap. They attract each other

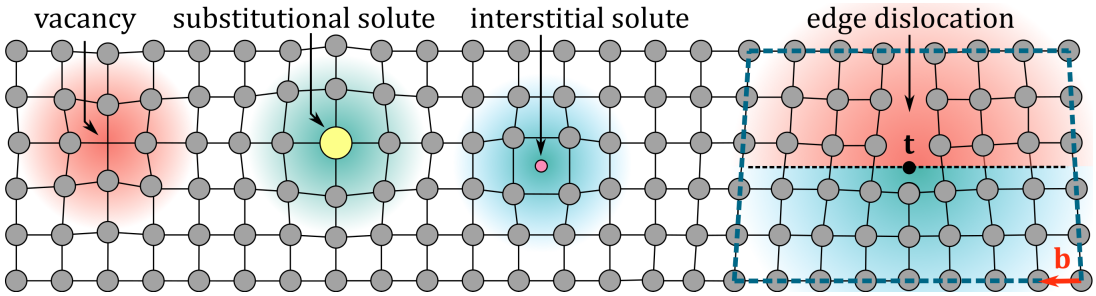

Figure 2.3: Illustration of defects in a simple cubic crystal lattice. Inspired by [35]. Atom positions are illustrated with grey circles. Compressive and tensile displacement fields are illustrated with blue and red gradients, respectively. For the edge dislocation, the line vector, $\vec{t}$, that goes into the paper plane, and the Burgers vector, $\vec{b}$, are shown. Also, the slip plane is marked by the black dashed line and the Burgers circuit by the blue broken rectangle.

if the compressive part of the stress field of one of them overlaps with the tensile part of the stress field of the other [46]. Simply put, a moving dislocation must overcome the force exerted by an adjacent dislocation to bypass it, so that higher dislocation density gives yielding at higher applied stress. Therefore, dislocations contribute to the yield stress by: $\sigma_d \propto \sqrt{\rho}$, where ρ is the total dislocation density [46]. There are two main contributions to the dislocation density. Geometrically necessary dislocations are those required to accommodate strain gradient fields due to geometrical constraints of the crystal lattice, e.g. due to bending. During plastic deformation, an amount of the applied work can be stored in the material via creation of dislocations independent of any geometrical constraints, and these dislocations are referred to as statistically stored dislocations. The increase in dislocation density obtained via plastic deformation leads to an increase in strength and is referred to as *work hardening* or strain hardening.

Grain boundaries are important planar defects in this context, since Al is generally polycrystalline. A *grain boundary* is a boundary separating regions with distinct crystallographic orientation. Often there is a discontinuity of slip systems between grains [45]. This means that dislocations cannot continuously glide between grains, but rather tend to pile up near the grain boundary. These dislocations often exert repulsive forces on one another, which leads to stress build-up. If the stress exceeds a threshold, dislocation sources in the adjacent grain are stimulated, so that the yielding process propagates between grains [46]. The shear stress at the front of a dislocation pile-up is proportional to the number of dislocations in the pile-up [49]. Since less dislocations can pile-up inside a smaller grain, the yield stress is higher the smaller the grain size [49]. Also, a fine grained material has a larger total area of grain boundaries that hinder dislocation movement. Thus, grain refinement results in strengthening. The relationship between yield stress and grain size can be described by the Hall-Petch equation [49]:

$$\sigma_y = \sigma_0 + kd^{-n}, \tag{2.2}$$

where k is a material constant, $n \approx 1/2$ is the exponent, d is the average grain diameter, and σ_0 is the frictional stress. The frictional stress can be thought of as the yield stress of a single crystal with $d = 0$ [49]. For pure Al, $\sigma_0 \approx 10$ MPa, and for Al alloys σ_0 generally increases with the alloying element content [35]. From Equation 2.2, the grain boundary strengthening contribution

to the yield stress is given by $\sigma_g \approx k d^{-\frac{1}{2}}$. In general, this relation holds both for grains and subgrains [48], but it does not correctly predict the strength for grains with dimensions $\lesssim 100$ nm [49]. In general, grain size hardening does not give a major strengthening contribution for Al alloys, and k is typically low. However, grain size strengthening has a more prominent effect in some Al alloys, e.g. in underaged and non-heat treatable Al alloys, and in some Al alloys where subgrains have formed during hot working [35].

The alloying elements may be in solid solution or form foreign phase particles that are bulk defects in the Al crystal lattice. A dislocation will pass by an embedded particle either by shearing or looping, depending on which mechanism that requires the lowest stress. *Shearing* occurs when a dislocation cuts directly through a particle, and the stress required for shearing is related to the particle radius by; $\sigma_{ps} \propto \sqrt{r}$ [46]. Therefore, shearing typically dominates for small and coherent precipitates. For a specific precipitate there is a critical radius, r_c, for which a transition occurs between shearing and looping [46]. *Looping* happens for larger or more incoherent particles. The most common looping process is the Orowan process, in which the dislocation curves out around the obstacle, until it meets itself on the other side. The dislocation combines with itself and leaves a circular dislocation segment known as an Orowan loop. In this way, the dislocation can continue to glide without shearing the particle. The yield stress contribution due to looping, is inversely proportional to the mean spacing between particles, Λ, by: $\sigma_{pl} \propto 1/\Lambda$ [46]. Naturally, Λ increases as particles grow larger due to solute expenditure. Other more complex bypassing processes may also take place, but this is not discussed here. The mechanism where impenetrable dispersed phases contribute to strengthening, is also referred to as *dispersion strengthening* [49]. For Al alloys, it is most common to refer to both strengthening by shearing and looping of precipitates as *precipitation strengthening*. Dispersoids may also contribute to strengthening in some cases, and this is especially prominent for some non-heat treatable Al alloys [50].

In total, several strengthening mechanisms contribute collectively. A Pythagorean superposition of contributions has been found adequate based on experiments [51], while a linear summation is a pragmatic and reasonable approximation that has been used in modelling [52, 53]. A linear sum of the strengthening mechanisms covered here reads:

$$\sigma_y = \sigma_0 + \sigma_{ss} + \sigma_d + \sigma_g + \sigma_{ps} + \sigma_{pl}. \tag{2.3}$$

Here σ_0 is the intrinsic strength of pure Al, while the other terms are strengthening contributions by: σ_{ss} solutes, σ_d dislocations, σ_g grain boundaries, σ_{ps} shearing of particles and σ_{pl} looping of particles. It follows that the strength depends strongly on the type, size and number density of foreign phases, the grain sizes and the dislocation density. These parameters can be modified by alloying and thermo-mechanical treatment.

2.2 Iron and steels

Steels have an eminent position as engineering materials. Steels and cast Fe comprise over 80% of all metals in use [37]. The success of steels is a result of the low cost and the endless variation in microstructure and properties that can be achieved by alloying and thermo-mechanical processing [49]. The topic of steels is extremely vast, and this section aims to give only a brief introduction to key concepts. The section begins by giving an overview over the binary Fe-carbon (C) system and important microstructures that result from common heat treatments. Thereafter, strengthening mechanisms important for steels are briefly mentioned, and an overview of common steel types is presented.

2.2.1 The Fe-C system

Fe is the primary constituent of the core of the Earth. In addition, Fe accounts for 4 wt.% of the continental crust of the Earth and is the forth most abundant element after O, Si and Al [11]. In the crust, Fe exists mainly in the form of Fe oxides, except for metallic Fe from meteorites [49]. Production of steel starts by reduction of the Fe oxide with C at high temperature to yield molten Fe [37]. Pure Fe has several allotropes, including three that occur naturally in bulk form [49]. These are the *body centred cubic* (bcc) form *ferrite* (α), the fcc form *austenite* (γ), and the hexagonal close packed form *hexaferrum* (ϵ). At ambient pressures, pure Fe can take the form of ferrite and austenite, while hexaferrum only exists at high pressures. There is also a high temperature bcc variant that is referred to as δ, although δ and α signify the same crystal structure. Untreated pure Fe is relatively soft and ductile. For instance the yield stress of a polycrystalline sample lies below 50 MPa [49]. To alter specific properties, Fe is typically alloyed, most often with C, and subsequently thermo-mechanically treated.

The Fe-rich part of the Fe-C phase diagram is shown in Figure 2.4. The intermediate phase *cementite*, Fe_3C, can be seen. Note that although the shown phase diagram is applicable in practice for steels, cementite is metastable so that the shown diagram is not an equilibrium phase diagram [45]. A wide range of mechanical properties can be achieved in Fe-C alloys due to the great variation in microstructures that can be created by thermo-mechanical treatment. An example is shown in Figure 2.4 for pearlite formation in a hypoeutectoid alloy. As the alloy is cooled from the γ phase field into the $\gamma + \alpha$ region, proeutectoid α precipitates in γ. Below the eutectoid, the remaining γ is transformed into $\alpha + Fe_3C$. Since the composition of γ is different from any of the product phases, the phase transformation $\gamma \rightarrow \alpha + Fe_3C$ requires redistribution of C by diffusion. The smallest diffusion lengths give a thin lamellar structure with alternating α and Fe_3C layers, which is termed *pearlite*. Relatively thick layers, referred to as coarse pearlite, form at high temperatures right below the eutectoid where diffusion is fast, while fine pearlite forms at lower temperatures. Pearlite has intermediate mechanical properties between the soft and ductile ferrite and the hard and brittle cementite.

Martensite is a metastable structure that results from a diffusion-less transformation happening upon rapid cooling or quenching of austenite to relatively low temperature. When cooling happens so quickly that C diffusion is hindered, all the C exists in a SSSS in austenite. This causes the austenite crystal lattice to elongate along one direction so that it transforms into a body centred tetragonal structure that is termed martensite. Martensite is extremely hard and brittle and has negligible ductility [45]. It is common to temper martensite, that is heat treatment at a temperature below the eutectoid, so that the martensite turns into ferrite and cementite.

Bainite is a microstructure that consists of an array of needles or plates of ferrite arranged within smaller regions called sheaves, together with fine particles of cementite. Upon quenching to relatively high temperatures, $\sim 400 - 550°C$, ferrite grows as laths and rejects the C into the untransformed austenite, so that cementite forms between the ferrite laths. The resulting microstructure is known as *upper bainite*. Upon quenching to lower temperatures, $\sim 200 - 400°C$, where C diffusion is less rapid, *lower bainite* forms. Here, the ferrite is supersaturated with C, so that fine carbide needles form both between ferrite laths and in their interiors. Bainitic steels have a wide range of mechanical properties and are largely intermediate between pearlite and martensite in that regard.

The microstructure transformations occurring during heat treatment of a steel can be visual-

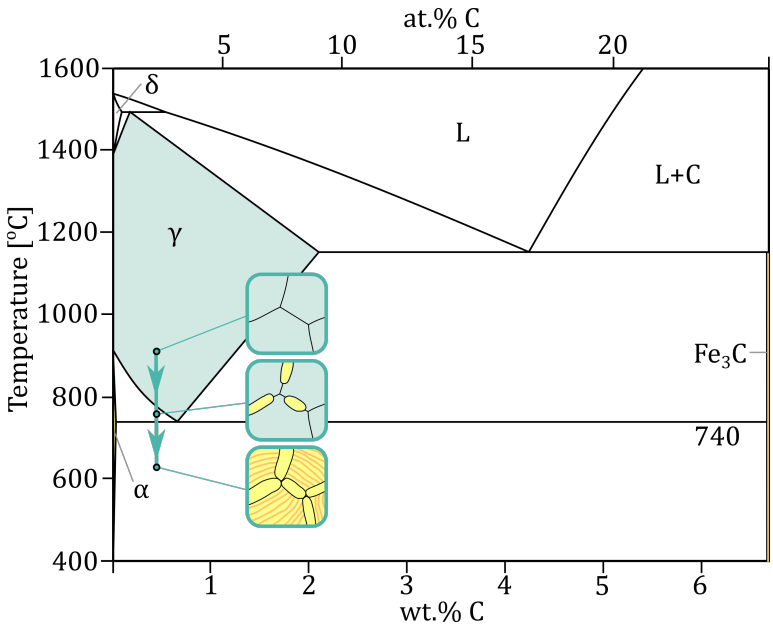

Figure 2.4: The Fe-rich part of the Fe-C phase diagram including the metastable phase cementite Fe_3C. The diagram is adapted from [54]. The insets show an example microstructure evolution for a hypoeutectoid Fe-C alloy that is is cooled from the γ phase field (top inset). As the alloy enters the $\gamma + \alpha$ region, proeutectoid α precipitates in γ (middle inset). Below the eutectoid, the remaining γ is transformed into pearlite consisting of alternating layers of α and Fe_3C (bottom inset). The insets were drawn based on [45].

ised by the aid of an isothermal transformation diagram, commonly known as a time-temperature-transformation diagram. Such a diagram for a hypoeutectoid Fe-C alloy is shown in Figure 2.5. It can be seen that pearlite, bainite and martensite form within specific temperature regimes. The treatment time determines the pearlite and bainite fractions, while the quenching temperature determines the martensite fraction. These microstructures can also be formed by continuous cooling. In general, pearlite forms for relatively slow continuous cooling rates, bainite for moderate and martensite for high.

2.2.2 Overview of steels

Ferrous alloys are alloys where Fe is the main constituent, and these are usually divided into the three following main groups based on their C content: commercially pure Fe, steel, and cast Fe ($2.14 - 6.70$ wt.% C) [45]. Alloys based on Fe that contain one or more alloying element(s), with ≤ 2.14 wt.% C, are defined as steels [37]. Thousands of steel types are available commercially, and the simplest way of classifying them is by their chemical compositions [56], as shown in Figure 2.6. The two main categories are low alloy and high alloy steels. *Low alloy* steels comprise those that have a total content of alloying elements below 8 wt.% [56]. These are further divided into low, medium and high C steels. In general, the strength and hardness increase as the C content increases, while the ductility and toughness decrease [37]. Low C steels typically have good weldability, while high C steels typically have higher risk of brittle

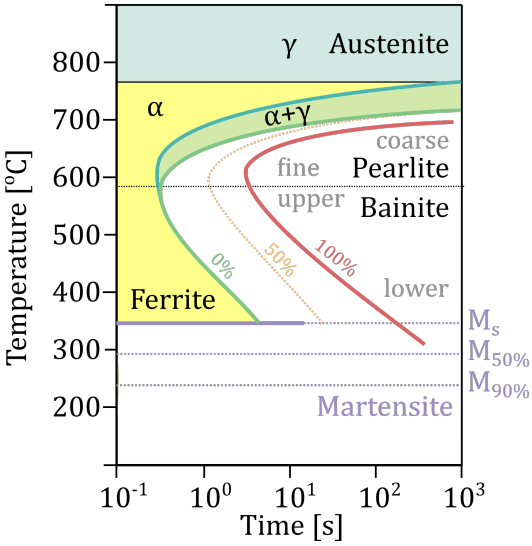

Figure 2.5: Schematic isothermal transformation diagram for a hypoeutectoid Fe-C alloy. Adapted from [55]. The diagram illustrates the microstructures that will form upon quenching from the γ or the $\gamma + \alpha$ region, to the α region, followed by isothermal heat treatment. For isothermal heat treatment at high temperatures, coarse or fine pearlite forms, while upper or lower bainite forms at intermediate temperatures. The green, orange and red lines indicate 0%, 50% and 100% transformation of austenite to pearlite or bainite, respectively. Martensite forms after quenching to temperatures below the martensite start temperature, M_S. A fraction of 50% martensite results for quenching to temperature $M_{50\%}$ and a fraction of 90% for $M_{90\%}$.

martensite formation upon cooling after welding. A subcategory of each of the low alloy steels is *plain C steels*, which can be defined as steels that primarily contain C and low amounts of alloying elements. Another common term is *structural steel*, which is C steel used for construction applications. Although specific types of both low, medium and high C steels can be considered structural steels, the most used are low C steels. Low C structural steels are commonly referred to as *mild steels*. Such a steel was used in **Papers II, IV, B** and **F**, while a low C steel designed for cold forming was used in **Paper V**. Another type of low C steel is *interstitial free* (IF) steel, which contains ≤ 0.002 wt.% C and generally has excellent ductility and formability [4]. Characteristic for IF steels is that they contain no interstitial solutes. Instead, all the C and nitrogen (N) that can be incorporated as interstitial solutes in Fe, are tied up in carbides and nitrides [37]. An IF steel was utilised in **Paper A**.

Low alloy steels are susceptible to corrosion, which limits their applications. In environments containing water and O, Fe oxidises continuously without forming any protective oxide layer, which can severely degrade the properties of the steel. For rustproofing, steel can be coated with Zn or Al, referred to as *galvanising* or *aluminising*, respectively [57]. Common methods include hot-dip galvanising and hot-dip aluminising, where a steel product is immersed into a bath of molten Zn and molten Al, respectively. However, to obtain corrosion protection beyond the surface layer, steels must be heavily alloyed. High alloy steels that are highly resistant to rusting are known as *stainless steels*, and these must contain ≥ 12 wt.% Cr to be passive in aqueous solutions [37]. In general, a thin layer of Cr_2O_3 forms on the surface of a Fe-Cr alloy, which prevents corrosion. Stainless steels often contain other alloying elements in addition to Cr, such as nickel (Ni), molybdenum (Mo) and Mn. Stainless steels have a wide range of properties, and are divided into subcategories based on the predominant phase in their microstructure. These include austenitic, ferritic, duplex, martensitic and precipitation strengthening stainless steels [37]. Duplex stainless steels contain both ferrite and austenite. Austenitic stainless steels constitute the largest and most utilised group. If an austenitic stainless steel is heated above a specific temperature usually in the range of $450 - 870$°C, C reacts with Cr to form Cr carbides that precipitate on the austenite grain boundaries. This causes the regions near the carbides to be depleted of Cr, so that intergranular corrosion can take place.

This phenomenon is known as *sensitisation*. An effective way of reducing the sensitisation susceptibility is to add Ti and/or Nb that form carbides [58]. Another way of limiting the susceptibility to sensitisation is to limit the C content. This is done in L-grades of stainless steel, and such a steel was used in **Paper IV**.

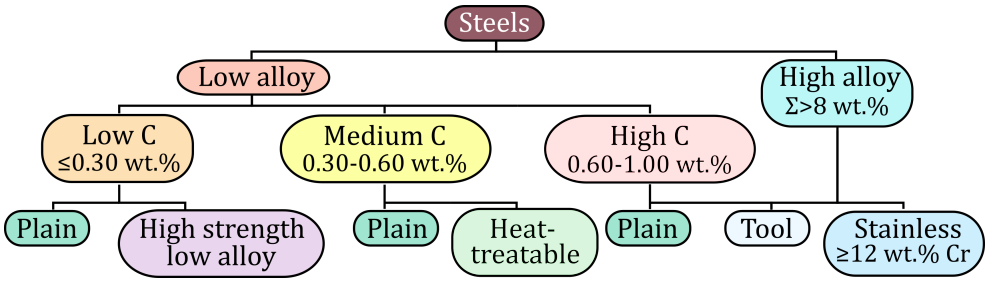

Figure 2.6: Illustration showing the top level classification of steels by chemical composition. Adapted from [37].

New types of steels are continuously being researched and developed. For automotive applications, the aim is often to create higher strength steels so that less material can be used and the total vehicle weight can be reduced [4]. Strengthening of steels arises from several mechanisms that generally contribute collectively [49]. Firstly, the microstructure has a major influence on the properties, as mentioned previously. Further, work hardening is crucial, and e.g. plain C steel may reach UTS values exceeding 1500 MPa by work hardening [49]. Solid solution strengthening is also important, both by C and N giving interstitial solute strengthening, and by substitutional solute strengthening by e.g. Mn, Cr, Mo and Ni. In addition, grain size refinement can give a substantial increase in strength, following the Hall-Petch relationship given in Equation 2.2. Some alloying elements, such as vanadium (V), forms fine and strong carbides that hinder grain growth during austenitisation. Another strengthening mechanism that is important in steels is dispersion strengthening, since other phases often are dispersed within the matrix in steels, such as carbides, nitrides and IMPs. These embedded phases typically give strengthening according to the Orowan mechanism as in Al alloys, which is explained in Section 2.1.3. For overviews of the alloying elements typically found in steels and their functions, the reader is referred to [37, 56, 57][3].

An overview over the strength versus ductility for commonly used steels is presented in Figure 2.7. Such a plot is often called the "ductility ladder" or "banana chart", since the conventional *high strength steels* (HSSs) follow a banana-shaped curve. Conventional HSSs include IF, bake hardened, C-Mn and high strength low alloy steels, while martensitic steels are regarded as ultra high strength steels. Relatively new types of HSSs have been developed that are referred to as *advanced HSSs* (AHSSs). They include a wide range of steels that are characterised by multi-phase microstructures [4]. The first generation of AHSSs include for instance *dual phase* (DP) steels, which are amongst the most used AHSS in automotive applications. Unlike duplex steels, DP steels contain martensite islands dispersed in a ferrite matrix. This microstructure is typically created by *intercritical annealing*, where a cold deformed ferrite-pearlite or ferrite-bainite microstructure is heated into the $\gamma + \alpha$ phase region, called the intercritical region, to form a fraction of austenite, before the alloy is quenched to form martensite [55]. A DP steel

[3] In particular, Table 4 on page 395 in [57] and Table 20.1 on page 372 in [37].

was used in **Paper III**. A second generation of AHSSs has been developed [4], and ongoing research and development is devoted to create a third generation of AHSSs that is intended to fill the gap between the first and second generations [12]. For more information on AHSSs, the reader is referred to [4, 12, 37].

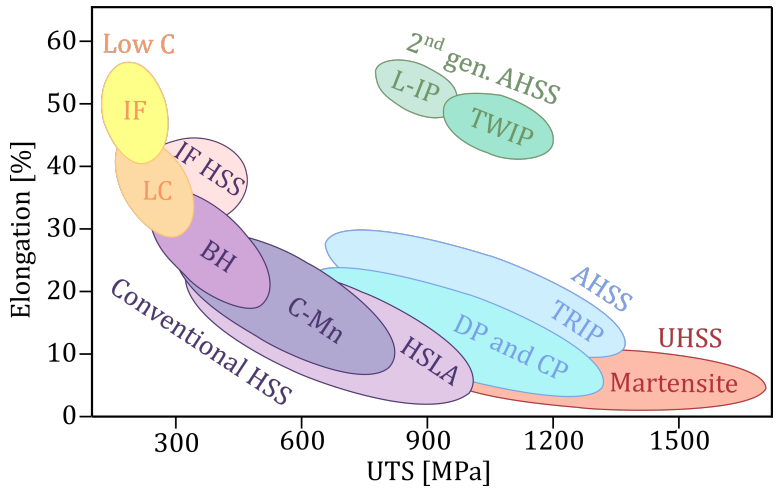

Figure 2.7: Chart showing typical elongation versus UTS values for commonly used steels: interstitial free (IF) and low carbon (LC) steels; conventional high strength steel (HSS) including bake hardened (BH), carbon-manganese (C-Mn) and high strength low alloy (HSLA) steels; first generation advanced HSS (AHSS) including dual phase (DP), complex phase (CP), and transformation induced plasticity (TRIP) steels; ultra HSS (UHSS) including martensite steel; second generation AHSS including twinning induced plasticity (TWIP) steels and lightweight steels with induced plasticity (L-IP). Adapted from [4].

2.3 Joining

After the introduction into Al alloys and steels, the next topic that will be explored is joining of these materials. This chapter begins by giving a brief overview of the types of joining methods, before diving deeper into the joining methods used in this work, with the main focus placed on HYB.

2.3.1 Overview of joining methods

Joining is the process of bringing individual components together to form a common unit. *Dissimilar joining* is joining to create hybrid joints or multi-material joints composed of two or more dissimilar materials. The joints themselves are often classified by their geometries, including for instance butt joints, where the *base materials* (BMs) are joined edge-on, and lap joints, where the BMs are joined in an overlapped configuration. The materials to be joined are often prepared to create single or double grooves, for instance with V- or Y-shapes. Illustration of a lap and two butt weld configurations are shown in Figures 2.8(a), (b) and (c), respectively. Joint efficiency is a simple measure often used to compare the tensile properties of the joint with that of the unaffected BM, and in some cases to compare the joint performance between different joints. *Joint efficiency* is given by the ratio between the UTS of the joint and the UTS of the softest BM [25].

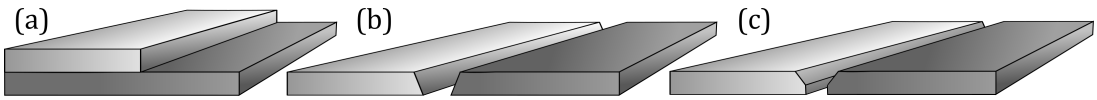

Figure 2.8: Schematic joint configurations. **(a)** Lap joint. Butt joints with double **(b)** V- and **(c)** Y-shaped grooves.

A plethora of various joining methods exists, and there are several commonly used strategies for classifying them. Broadly speaking, they can be classified into three groups; i) mechanical joining, ii) adhesive bonding and iii) metallurgical bonding (welding), depending on whether they rely primarily on i) mechanical interlocking, ii) chemical reactions or iii) applied heat and/or pressure [1, 59]. This largely describes the top level categorisation, although several joining techniques in principle could be classified as hybrid processes that utilise a combination of these.

Mechanical joining methods rely on creating a mechanical interlock that locks the materials into a common unit. Such joining methods include mechanical fastening methods and integral mechanical attachment methods [59]. In mechanical fastening, an additional part, i.e. a fastener, is utilised to achieve interlocking. Examples include nails, screws, bolts and rivets [1, 59]. In self-pierce riveting for instance, a rivet is pushed into stacked sheets to lock them together. Fasteners are often removable, which can be advantageous, but they also add extra weight, and often result in low joint efficiencies [25]. In integral mechanical attachment methods, a mechanical interlock is created without integrating a fastener into the joint. For instance, in clinching of Al and steel sheets, the sheets are joined by using a press machine to drive a punch into the sheets and pushing them downwards into a die to create an interlock [60]. Mechanical joining is usually thought of as working on the macroscopic scale. However, mechanical interlocking may also happen at the microscale [59]. When two surfaces are brought into close contact during joining, surface asperities, i.e. bulges and bumps on the material surfaces, may lead to material getting stuck in or flowing into protrusions on the opposing surface, so that microscale hook- or lock-like features are created, which may contribute to bonding. This is important also in other joining methods, as will be mentioned later.

Adhesive bonding is the process in which two material surfaces are being held together through an adhesive, typically a resin, that acts as a bonding agent and sticks to both of the opposing surfaces [61]. Adhesion is a complex surface physico-chemical phenomena affected by numerous factors. On the molecular scale, the bond strength depends mainly on the chemical bonding, while on the microscale, surface roughness may reduce or enhance the bond strength. Several adhesion mechanism models have been proposed that each explain certain phenomena related to adhesion, such as mechanical interlocking, adsorption, interdiffusion and chemical bonding [62]. Adhesive bonding has several advantages, including uniform stress distribution, as opposed to fasteners and spot-welds, and the possibility to join otherwise incompatible materials [62]. On the other hand, adhesive bonding often requires surface preparation and time consuming curing, and the adhesive can be susceptible to environmental degradation. Thus, if adhesive bonding is used in load-bearing structures, it is most often used in combination with mechanical joining.

Metallurgical bonding or *welding* is uniting parts, in most cases metal parts, by applying heat and/or pressure to bring them into close enough contact so that they form bonds to each other

at the atomic level [59]. Thus, the fundamental principle behind welding is atomic bonding, which requires that the opposing metal surfaces are borough into close enough contact for inter-atomic forces to come into play. Metal surfaces usually have surface irregularities and asperities, surface oxide layers and adsorbed contaminants, which hinder close contact. These must be removed or broken up for metallurgical bonding to occur, and there are largely two ways of achieving this goal. Therefore, welding is divided into two broad categories: fusion and solid state welding, which rely primarily on heat and pressure, respectively.

Fusion welding

Fusion welding methods either join materials by autogenous welding where the meeting edges of the work-pieces are melted, or by the use of a *filler material* (FM) that is melted. The heating enhances interdiffusion and helps to break up or dissolve contaminants and oxide layers, before the liquified materials are allowed to fuse together upon cooling. Fusion welds typically contain a fusion zone, surrounded by a HAZ, that is again surrounded by unaffected BM.

There exist many fusion welding methods, and there are several ways of classifying them. One subclass is *gas welding* methods that use combustion of a fuel gas as heat source [59]. Another subclass is *high energy beam welding* methods, where the high kinetic energy of fast particles in an intense beam acts as heat source. Examples include laser beam and electron beam welding. *Resistance welding* methods on the other hand, rely on resistance heating. *Arc welding* methods are commonly used in industry [61] and utilise an electric arc created between an electrode and a work-piece to provide intense heat [59]. These methods typically use an inert shielding gas to stabilise the arc and prevent oxidation of the metal [61]. The electrode is either consumable and acts both as a FM and a conductor, or is non-consumable and acts only as a conductor. In the latter case, a FM can be supplied separately if needed [61]. For example, gas tungsten arc welding, commonly referred to as tungsten inert gas welding, uses a non-consumable tungsten (W) electrode. On the other hand, *gas metal arc welding* (GMAW) uses a consumable metal electrode that acts as a FM. A subclass is *metal inert gas* (MIG) welding, and CMT is a recently developed modified MIG method [63] that has been used to create sound Al-steel joints with the use of an Al FM. In that case, welding is said to occur between the Al BM and the Al FM, while brazing occurs between the steel BM and the Al FM. This method was used in **Paper V** and is described further in Section 2.3.5. *Brazing* and *soldering* are both subclasses of fusion welding. In these methods, a FM is melted in contact with the BMs to be joined, before it wets and spreads over the BMs by capillary action. In brazing and soldering, the liquidus temperature of the FM is above and below 450°C, respectively [59, 61].

In general, it is challenging to weld dissimilar materials with conventional fusion welding methods, since there often are large differences in their thermo-physical properties and since unwanted phases may form at the interfaces between them. Solid state welding are often more suitable for dissimilar joining.

Solid state welding

Solid state welding comprise welding methods that operate below the melting temperatures and do not rely on melting and subsequent solidification of the materials to be joined. Subclasses include diffusion bonding, cold pressure welding and friction welding. *Diffusion bonding* uses interdiffusion as the primary mechanism for bond formation. A load is usually applied to achieve close contact by plastically deforming surface asperities and by decreasing interfacial voids. The temperature is usually above 50% of the melting temperature, to enhance diffusion [61]. *Cold pressure welding* (CPW) methods, often called cold welding methods, use

high pressure to obtain a high degree of plastic deformation, so that intimate surface contact is achieved and clean metal surfaces form metallurgical bonds. One such method is RB, which is explained in Section 2.3.2 and that was used in **Papers IV, A** and **B**. *Friction welding* methods rely on the frictional forces between materials moving relative to each other to produce local frictional heating and plastic deformation that lead to coalescence of the materials [25]. Examples include ultrasonic welding and FSW. Although FSW was not used in the present work, this method is described further in Section 2.3.3 due to its similarities to HYB. HYB was used in **Papers II, III** and **F** and is explained in Section 2.3.4. For further details on solid-state welding methods, the reader is referred to recent review articles [1, 20, 25, 64].

2.3.2 Roll bonding

RB is a CPW method where metal sheets are placed on top of each other and pushed through a rolling mill. Figure 2.9(a) shows a simple illustration of a typical setup for RB. The sheets experience large thickness reduction and large surface expansion in the rolling direction, while their widths remain constant. The thickness reduction is given by; $x = (t_f - t_i)/t_i$, where t_f and t_i are the final and initial thicknesses, respectively. The surface expansion is given by; $Y = (A_f - A_i)/A_i$, where A_i is the initial surface area, and A_f the final area after rolling. The metal sheets are often rolled at room temperature, referred to as cold RB, but they may also be pre-heated to facilitate bonding [65].

The *film theory* offers an explanation to the bond formation mechanism in CPW methods [66–68]. The metal surfaces to be bonded are presumably covered by a brittle surface layer containing oxide films and adsorbed contaminants that inhibit bonding, referred to as a *contaminant film*. Surface preparation by scratch brushing gives a work-hardened surface layer that covers a fraction of the initial surface, referred to as a *cover layer*, which has been reported to be beneficial [66, 69]. To obtain bonding, a threshold surface expansion has to be reached, which leads to fragmentation of the surface layer, i.e. the contaminant film and the cover layer, by plastic deformation. This allows clean metal surfaces to be extruded through the cracks in the surface layer. If and only if, fresh metal from the opposing surfaces meet and are brought into close enough contact to allow inter-atomic forces to have an effect, it is assumed that they will bond. Several other theories have also been proposed to rationalise the bond formation mechanism in CPW methods, such as the recrystallisation theory, the energy barrier theory and the diffusion bonding theory [65].

Based on the film theory, Bay proposed a model that describes the bond strength in CPW methods in the presence of a work hardened cover layer [68–71]. As mentioned earlier, it is assumed that bonding is achieved if a threshold surface expansion is reached that cracks the surface layer, i.e. the contaminant film and the cover layer. In the model, it was assumed that the contaminant film is thin enough so that the metal surfaces immediately get into contact upon film fracture. However, for a thick cover layer, a critical extrusion pressure has to be reached for metal to be extruded down the cracks in the cover layer [71]. Since the work-hardened cover layer was found to be several magnitudes thicker than the contaminant film, Bay proposed that the normal pressure, i.e. the vertical component of the rolling pressure, had an effect. In the model, if the normal pressure exceeds a threshold pressure for extrusion, p_e, the cover layer fractures and fresh metal is extruded through the cracks. The pressure needed for extrusion depends on the surface expansion, since a low and a large surface expansion would give thick and thin cover layers that would require high and low threshold extrusion pressures, respectively. The bond strength thus escalates with increasing surface expansion until it approaches the strength of the weakest starting material. Figures 2.9(b)-(e) show illustrations of the steps

of bond formation according to Bay's proposition. In Figure 2.9(c), the original cover layer and contaminant film are shown. Figure 2.9(d) shows extrusion of material down the cover layer cracks, together with thinning of the contaminant film. Figure 2.9(e) shows the resulting bonded regions and remnants of cover layers and contaminant films. Bay's model has later been modified, and for instance a more elaborate model for Al-Al bonding has been developed [72].

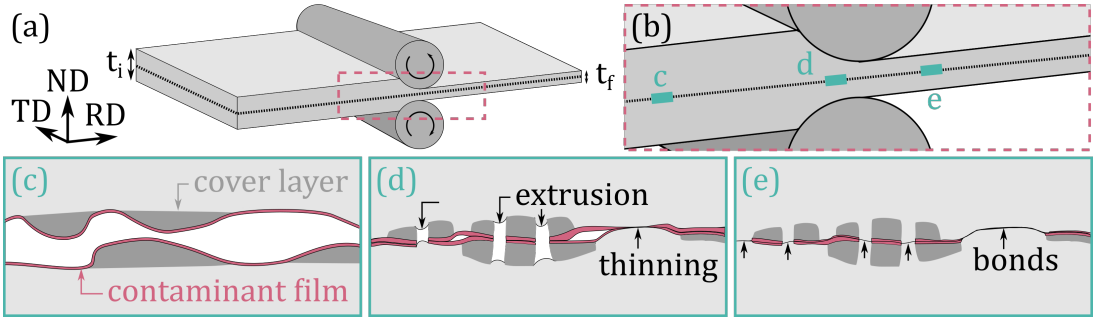

Figure 2.9: Illustrations of RB. **(a)** Schematic setup showing two plates that are being sent through a rolling mill. This causes significant reduction in the thickness of the plates, from initial thickness t_i to final thickness t_f. **(b)** Enlarged view of the illustration in (a) showing the material that is being sent through the rolling mill. Bond formation according to the film theory is shown schematically in (c)-(e), which are adapted from [69]. **(c)** Original material surfaces covered by a work hardened cover layer and a thin contaminant film. **(d)** Extrusion of material through cracks in the cover layer and thinning of the contaminant film. **(e)** Bonded areas between cover layer fragments and residual contaminant film areas.

Since breaking the surface layer is a pre-requisite for bond formation, surface preparation has an immense effect on the bond strength. Different preparation methods have been tested, and several researchers have found that degreasing and scratch-brushing using a rotating steel brush lead to the most successful results [65, 66]. Scratch-brushing increases the surface roughness, which may facilitate local shear forces that may destroy the contaminant film [67]. Also, mechanical interlocking between the bonded sheets likely contributes to the bond strength, at least in shear [69]. Further, post-rolling heat treatment can be done to develop a stronger metallurgical bond through interdiffusion, reduction of residual stresses and increasing the joint toughness [73]. For more information on RB, the reader is referred to [65, 74].

2.3.3 Friction stir welding

FSW is a solid-state friction welding method that was invented and patented by The Welding Institute in 1991 [27]. At the time, it was described as a radically new and revolutionary joining process. FSW can be thought of as a constrained extrusion process that happens under the action of a rotating tool [75]. After its emergence, the FSW technique gained momentum rapidly. Numerous patents were filed, much research activity was initiated, and the method was implemented in industry [75]. Several process and tool variants have been developed, and several joint configurations have been demonstrated. The main focus was initially placed on welding of Al alloys, but also other metal combinations have been welded successfully by FSW [76], including Al-steel joints [77, 78].

A typical setup for FSW butt welding of a steel and an Al BM plate is shown in Figure 2.10(a). The BM plates are securely clamped onto the work table. Central in the process is the FSW tool that is a non-consumable rotating tool made of a harder material than the BMs to be joined.

This tool has a shoulder out from which a threaded pin, also referred to as probe, protrudes [79]. At the start of the welding process, the pin rotates and is pushed downwards into the seam between the BMs, until the shoulder is brought into contact with the upper edges of the BMs. In its submerged position, the tool starts to move forward and traverses the weld seam. The side where the local rotation direction of the tool is the same as its transverse movement direction is referred to as the *advancing side* (AS), while the other side is referred to as the *retreating side* (RS) [80]. For similar metal welding, the tool can be placed symmetrically in the middle of the seam. For dissimilar metals on the other hand, it is custom to place the hardest material on the AS and to place the pin with only a minimal offset into the hardest material, so that the pin plunges mainly into the softest material [25, 78]. This is illustrated in Figure 2.10(b).

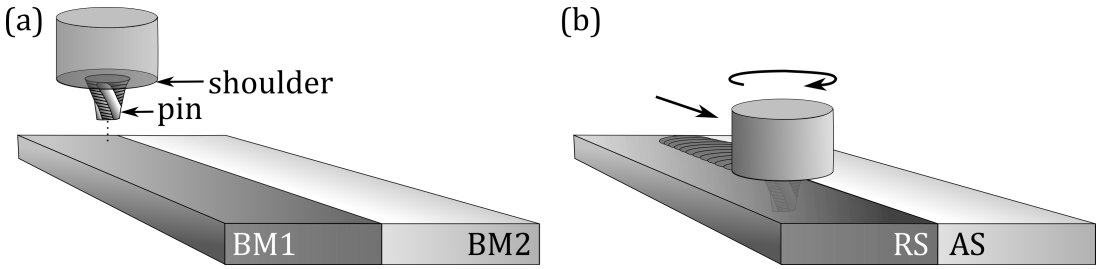

Figure 2.10: Illustrations of a typical setup used for FSW of Al and steel. **(a)** Schematic setup before FSW, which shows the tool with its threaded pin and shoulder and the two BM plates. **(b)** Setup during FSW, which shows the tool traversing the weld seam while it rotates and plastically deforms the materials. Inspired by [81].

The pin continues to rotate as the tool moves forward, which generates high strains. This facilitates breaking of surface oxide layers and forces material to be swept around the pin and subsequently deposited behind the tool, where it is allowed to coalesce. Also, the tool is subjected to a high normal pressure so that the shoulder presses down onto the upper BM edges and ensures that material cannot escape from the weld region [79]. In addition, the shoulder provides additional frictional heating which facilitates the plastic deformation produced by the rotating tool. The combined frictional heating from the shoulder and the pin creates a thermally softened and plasticised region around the tool. The process is asymmetrical, and most of the material is extruded past the RS [75]. Therefore, the pin tends to move away from the RS towards the AS and must be securely fixed to prevent sideways movement [81]. In total, the BM edges are subjected to high plastic deformation and frictional heating, which enables joining in the solid state.

A FSW butt weld is illustrated in Figure 2.11(a). The weld is typically divided into three main microstructural sections. The stir zone, also referred to as the nugget zone, covers the material that has been plasticised and displaced under the action of the pin. For FSW of age-hardenable Al alloys, the microstructure in the stir zone typically consists of fine equiaxed recrystallised grains [75, 82, 83]. Onion ring features can be seen in some cases, and these are circular or elliptical features resulting from the material flow following the stirring of the pin. Often in FSW welds of dissimilar materials, special features can be seen in the stir zone near the bonded interfaces. These are mechanically intermixed regions where the two materials have flowed into each other due to the pin stirring, leading to intercalated layered structures and/or vortex- or

swirl-like structures [84]. In the zone surrounding the stir zone, the material has been subjected to extensive heating and plastic deformation, despite not being directly stirred by the pin. This region is thus referred to as the *thermo-mechanically affected zone* (TMAZ). The TMAZ in FSW welds of age-hardenable Al alloys mainly shows recovered grains that have bendt due to the large deformation [75, 82]. Outside of the TMAZ there is a HAZ where the material has only been subjected to heating, while unaffected BM surrounds the HAZ.

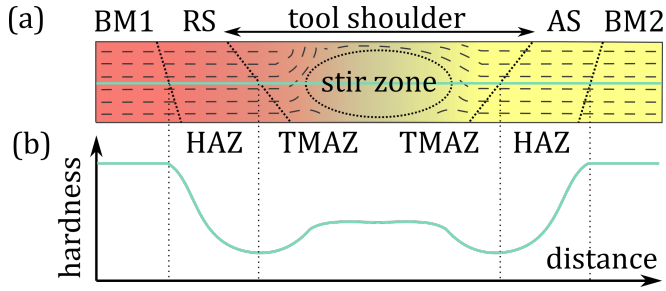

Figure 2.11: **(a)** Illustration of the cross-section of an Al-Al FSW joint of an age-hardenable Al alloy, where the main microstructural zones are indicated; the stir zone, the TMAZ and the HAZ. Adapted from [75]. **(b)** Corresponding schematic hardness profile. Adapted from [85].

The microstructural evolution greatly affects the hardness profiles from FSW welds, and a schematic profile for an age-hardenable Al alloy is included in Figure 2.11(b). There is a hardness drop in the HAZ since an overaged state is reached due to coarsening and dissolution of hardening precipitates, possibly accompanied by re-precipitation of non-hardening precipitates [82, 83, 86, 87]. From the minimum hardness value towards the TMAZ, there is an increase in hardness which is coupled to increasing dissolution of non-hardening precipitates. This leaves increasing amounts of solutes in solid solution, which gives strengthening during natural ageing after consolidation of the weld [85, 86, 88]. Also, the large deformation that occurs in the tool shoulder region, from the TMAZ towards the stir zone, contributes to work hardening and opposes grain growth following frictional heating. Work hardening gives a significant strengthening contribution, as explained in Section 2.1.3, and this contributes to the hardness increase seen from the TMAZ towards the stir zone. The stir zone has experienced the highest amount of plastic deformation and work hardening, so that the hardness typically reaches a plateau in this zone. For more information on FSW of Al alloys the reader is referred to [75, 76, 89–91]. In the context of the research presented in this thesis, the FSW process is interesting in particular due to its similarities to the HYB method that is explained in the following section.

2.3.4 Hybrid metal extrusion & bonding

HYB is a hybrid solid-state welding method that combines addition of a FM and large plastic deformation to achieve bonding between metals. The method is patented [29, 30] and was developed by Ø. Grong [29], together with co-inventors T. Austigard and U.R Aakenes. The main objective of the developments was to create a method that enabled Al welding with lower heat input and that was more flexible than other available methods, such as conventional fusion welding methods and FSW. The HYB method combines favourable aspects of FSW, GMAW and CPW [92], and is therefore closely related to FSW. The main difference between FSW and HYB is that addition of FM is a mandatory requirement in HYB, while not a possibility in conven-

tional FSW [29]. Further, since the groove is filled by FM in HYB, the plates to be joined do not need to fit each other closely, and HYB is therefore less dependent on geometric constraints. The HYB method utilises continuous addition of FM as in GMAW, but while GMAW is a fusion welding method, the FM addition in HYB happens exclusively in the solid state. This makes it possible to perform welding at low temperature whilst exploiting FM addition and is a unique feature of the HYB method. Originally, the idea was to use HYB for joining of Al plates and profiles [92–94].

The standard HYB setup consists of a HYB work bench onto which the BMs are fastened. For butt joining of two BMs, the BMs are fastened on top of a steel backing, so that a groove forms between them that is slightly narrower than the pin diameter, to ensure contact between the pin and the BM sidewalls. For similar metal welding, the pin typically plunges into both BM plates symmetrically, while for dissimilar metal joining, the pin is placed asymmetrically so that it deforms only the softest metal. A possible setup for dissimilar BMs is illustrated in Figure 2.12(a). The sidewalls of the BMs may be pre-machined so that they form for instance V- or Y-grooves. One of the BMs is placed on the AS, where the pin rotation direction is parallel to the extruder tool travel direction. The other is placed on the RS, using FSW nomenclature. The extruder tool is clamped against the BMs in a submerged position so that it overlaps with the groove and at least one BM. During HYB, the extruder tool travels along the weld groove at a constant speed, while the FM is continuously extruded. This allows filling of the weld groove, at the same time as the pin with its dies acts as a stirring tool that plastically deforms at least one of the BMs. The process is sketched in Figure 2.12(b). The process parameters, in particular the wire feed rate, pin rotation rate and extruder travel speed, have to be adjusted with respect to each other to achieve adequate filling of the groove. The pilot HYB machine currently installed at NTNU allows tuning and documentation of the relevant process parameters [95].

During HYB, the FM typically flows down along the sidewall of the BM on the AS, while the edge of the BM on the RS is forced to flow and is dragged along with the pin towards the middle of the weld groove [96]. However, there are variations in the material flow depending on the material combination and joint configuration. As the extruder moves forward, the deformed material is deposited behind the pin. The interfacial shear deformation at the groove walls is presumably sufficient to disperse the surface oxide layers so they become mixed into the Al [92], and so that clean metal can meet and metallurgical bonds form. A finished HYB joint is typically divided into specific microstructure zones. The *extrusion zone* (EZ) lies in the middle of the weld groove and comprise the zone where FM has been deposited and where the materials have experienced extensive plastic deformation. Outside of the EZ, there is a HAZ that has only been affected by heating but not by plastic deformation. This is illustrated in Figure 2.12(c). The EZ typically consists of a mixture of FM and Al BM. The heating of the Al FM during extrusion and the frictional heating resulting from the plastic deformation in the groove are the origins of the soft HAZ in Al. The temperature of the Al in the groove has not been measured. Recently, finite element modelling of the FM wire feeding in the extruder tool showed that the FM becomes heated as soon as it enters the chamber and reaches a peak temperature of $\sim$400°C close to the abutment [95].

In HYB, the principle behind the addition of FM is continuous extrusion [97], often referred to as conform, short for continuous extrusion forming [98]. In this process, an extrusion tool is used that consists of a wheel that has a continuous groove with rectangular cross-section. The wheel is fastened on a shaft so that it can rotate. A shoe is fastened to one end of the wheel, so that a passageway forms between the wheel and the shoe. During continuous extrusion, the

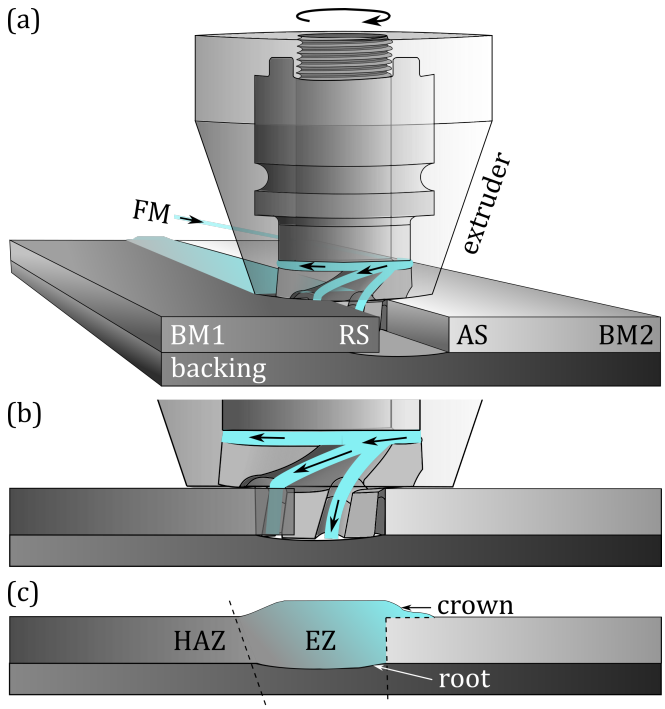

Figure 2.12: Illustration of a HYB setup for butt joining of two dissimilar metals; a soft BM1 and a hard BM2. Schematic of the setup during HYB, seen **(a)** from the side and **(b)** from the front. The BM1 and BM2 plates are placed on top of a steel backing and on the RS and AS, respectively. The FM is fed into the extruder tool that traverses the weld groove at the same time as it rotates. This causes FM to be continuously extruded through the extruder tool and into the weld groove. Simultaneously, the extruder tool stirs the material in the weld groove. The frictional heating and plastic deformation results in bonding. **(c)** Illustration of a finished HYB joint, where the crown and root regions, and the HAZ and EZ, are indicated.

wheel rotates, and the material is fed into the passageway and is moved by frictional drag. An abutment is integrated into the end of the shoe that forms a narrow die opening. When the material meets the abutment, it becomes extruded through the die, and continuous extrusion occurs [97]. The process is illustrated in Figure 2.13(a).

The FM is continuously extruded through a specially designed extruder tool in HYB, which is the core of the HYB invention. This tool mainly consists of a steel pin surrounded by a steel housing. The pin is integrated with an extrusion head with extrusion dies in the bottom. It is connected to a drive spindle that enables rapid pin rotation, while the housing remains stationary. In the lower end of the pin, there is a narrow passageway in between the stationary steel housing and the rotating pin. This opening serves as an extrusion chamber and is slightly thinner than the wire used as FM. During HYB, the FM is fed into the extrusion chamber that has three moving pin walls and one stationary housing wall. As it enters the chamber, the FM becomes dragged around due to the imposed friction grip [92]. Near the end of the extrusion chamber, there is an abutment that blocks further entry into the chamber. When the FM hits this abutment, pressure builds up, and the FM is forced to flow out of the die openings in the

bottom of the rotating pin. In this way, continuous extrusion of FM is enabled.

The extruder tool and pin shape can be adapted to fit a specific joint geometry and material configuration. With time, various prototypes have been developed [93]. One of the first successful extruder tools was the HYB Spindle extruder [29, 92, 93] that had one stationary die right in front of the stationary abutment. This tool is illustrated in Figure 2.13(b). The HYB Spindle extruder enabled continuous extrusion of FM, but it was not customised to plastically deform the BM. Later, the more advanced HYB PinPoint extruder tool was developed. Here, the rotating steel pin was integrated with three or more moving extrusion dies in its lower end, which in addition to extrusion of FM enabled stirring of the BM [96, 99, 100]. Figure 2.13(c) shows an illustration of the PinPoint tool from top view, while Figure 2.14 shows the individual components of the tool seen from the front. The pin is shown in 2.14(a), the spindle tip in (b) and the assembled tool in (c). The PinPoint tool may optionally have a stationary outlet die fixed in the rear end of the stationary housing, which allows FM to flow outwards in the radial direction [96]. By adjusting the geometry of this die, the geometry of the weld reinforcement can be adjusted, ranging from flat to fully reinforced weld faces [96]. The HYB PinPoint extruder tool was used in the joining processes presented in **Papers II-III** and **F**.

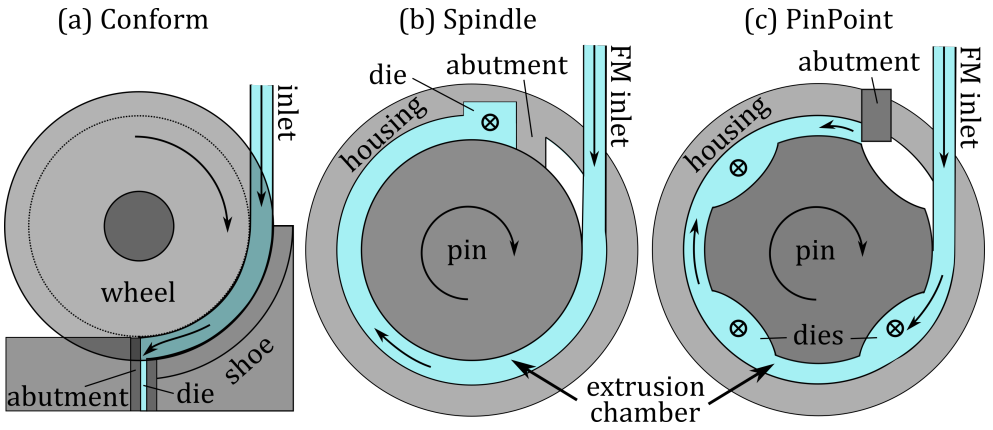

Figure 2.13: Illustration of extruder tools used for continuous extrusion of FM. **(a)** Tool used in the original Conform process. Inspired by [97]. The FM is fed into a passageway between a rotating wheel and a stationary shoe, and rotates with the wheel due to frictional drag, until it hits an abutment. In the abutment there is a narrow die, so that the FM becomes continuously extruded through the die. **(b)** HYB Spindle extruder tool seen from the top. Adapted from [92]. The FM is fed into a narrow space in between a rotating pin and a stationary steel housing, and follows the pin movement due to the imposed frictional grip. The FM moves around with the pin until it hits an abutment integrated into the stationary housing, and is forced to flow out of a die placed right in front of the abutment. The cross indicates that the FM moves into the paper direction as it moves out of the die. **(c)** HYB PinPoint extruder tool seen from the top. Adapted from [101]. This tool is somewhat similar to that in (b), with one major exception being that instead of having one stationary die in front of the abutment, the pin is integrated with four moving extrusion dies.

In principle, various ductile materials with sufficient extrudability may be utilised as FM in HYB. At the time the HYB method was developed, no Al alloy had been designed to fit the task as solid state FM, although several Al alloys previously had been developed to serve as FMs in fusion welding methods. These FMs typically have other specifications than what is

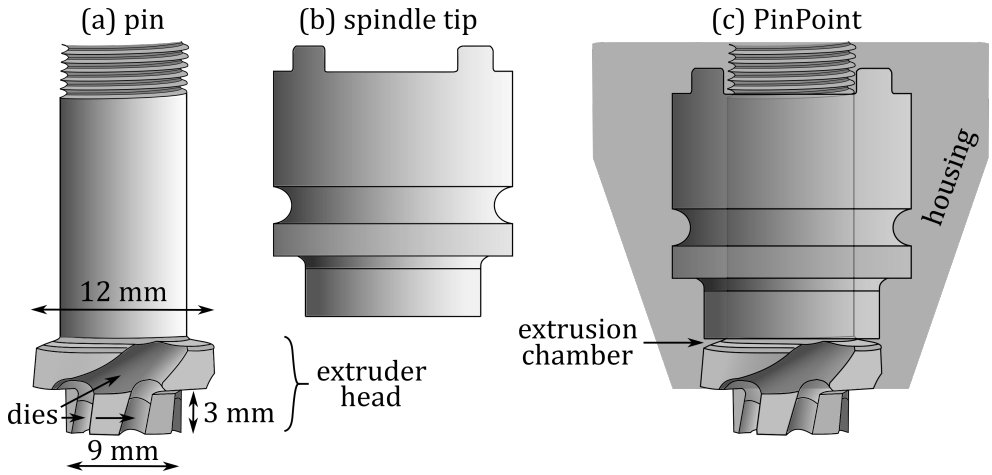

Figure 2.14: Illustration of the HYB PinPoint extruder tool. Adapted from [95]. **(a)** The rotating pin that is integrated with extrusion dies in its bottom end. **(b)** The spindle tip that is fastened onto the pin. **(c)** The assembled tool where the pin constitutes the two rotating sidewalls of the extrusion chamber, the spindle tip acts as the rotating ceiling wall and the housing functions as the stationary sidewall.

sought after in a solid state FM, e.g. they are alloyed to reduce the risk of solidification cracking [102]. Therefore, an Al alloy FM template was specifically designed to fit the task, and this was patented [102]. The goal was to achieve an Al alloy with high work hardening potential that could undergo work-hardening during HYB, so that it did not soften extensively and limited the strength of the finished joint. Since fine dispersoids may prevent recrystallisation during subsequent processing, the alloy should contain considerable amounts of dispersoid-forming elements such as Mn, Cr and zirconium (Zr), in addition to other elements, depending on which Al alloy series it was based on [102]. In principle it is possible to develop a FM specifically to fit the Al BM to be joined. One 6082 Al alloy was specifically tailored to be HYB FM for welding of Al alloy 6082-T6, and this alloy has been used in the HYB joining presented in recent publications. For this 6082 Al FM, the manufacturing route started with direct chill cast billets (⌀ 95 mm) that were homogenised at 540°C for 2h 15 min, before they were cooled at 300°C/h. Afterwards, the billets were pre-heated to 500°C before they were extruded and water quenched (⌀ 2.7 mm). Next, individual as-extruded wires were joined by CPW, before the wire was shaved to remove surface impurities and contaminants. The wire was subsequently cold drawn (⌀ 1.6 mm), and optionally shaved down to become even thinner (⌀ 1.2 mm). In this work, 6082 Al alloy FM wires with thicknesses of ⌀ 1.2 mm and ⌀ 1.6 mm were used as FM in **Paper II** and in **Papers III** and **F**, respectively.

The HYB method has been used to produce Al-steel joints. The first generation of HYB Al-steel joints unfortunately suffered from lack of bonding along a large portion of the weld line [103, 104]. Tensile specimens only reached UTS values in the range of $104 - 140$ MPa [103, 104], which corresponded to joint efficiencies in the range of $34 - 46\%$. Improvements of the setup, together with further developments of the pin geometry, enabled fabrication of a second generation of HYB Al-steel joints that showed significantly improved mechanical properties. Characterisation of a second generation joint is the topic of **Paper II**. Later, further developments of the setup and pin geometry led to a third generation Al-steel HYB joints

that showed even better properties, which is the topic of **Paper F**.

A great advantage of HYB is that minor modifications of the pin and housing geometries enable various configurations, which makes the method flexible [99]. HYB is in continuous development, and there is an increasing research activity related to HYB. Sound Al-Al welds have been fabricated that show adequate mechanical properties comparable to or exceeding those of joints made with competing methods, such as laser beam welding and FSW, in terms of e.g. fatigue properties [105], impact toughness and yield strengths [106]. Further, the flexibility in the geometries of the pin and housing have allowed creation of sound joints with various configurations, including butt, slot and fillet joints [99, 100]. The HYB method has also been used in additive manufacturing to create layered structures of Al [107, 108]. Last but not least, the prospect of multi-material welding was recently explored, and it was found that HYB can be used to join Al to Ti, Cu and steel [99, 100]. A unique demonstration Al-Cu-steel-Ti joint fabricated in one pass is the topic of **Paper III**.

2.3.5 Cold metal transfer

CMT is a modified MIG method that was developed by the company Fronius in 2004 [26, 63, 109, 110]. The method was designed to be automated and performed using a robot. Early reports demonstrated sound Al-steel joints [26, 63, 111], and since, several metal combination have been welded successfully with CMT [110]. An illustration of a typical setup for CMT lap joining of one Al BM and one steel BM is shown in Figure 2.15(a). The welding gun is integrated with a wire feeder which continuously supplies a filler wire that acts as an electrode. The electrode and the BMs are connected to a power supply, and an electrical arc is created between them that melts the filler wire. The welding gun also has a gas nozzle through which an inert gas is supplied that shields the arc and the molten weld pool [61].

During CMT, the welding gun is moved step-wise along the BM plate seams while depositing molten FM droplets, as illustrated in Figure 2.15(b). For each droplet deposition, the electrical signal follows a cycle that can be divided into three stages [112, 113]. The first stage is the peak current stage where the arc is ignited by a high pulse of current. This heats the filler wire so that it melts and a droplet is formed. The second stage is the background current stage where the current is kept constant at a low level to avoid globular transfer, i.e. that the droplet falls down after it has grown large enough, while the wire is moved towards the weld pool. In the third and last stage, the liquid droplet is brought into contact with the weld pool. This extinguishes the arc due to short-circuiting. The power supply is temporarily stopped, and a return signal is sent to the wire feeder, so that the filler wire is drawn backwards. This aids droplet detachment while the power supply is interrupted. The automated control of the process and the integration of the wire motion into the welding process are the main innovations in the CMT method compared to conventional GMAW methods that use short-circuiting transfer [63]. In this way, minimal current can be used, and the heat input and the spatter can be reduced significantly [109, 112, 114]. The method is denoted "cold" since the heat input is lower than in conventional welding, although it is not a cold welding method. For CMT of Al-steel specimens, the peak temperature lies above the melting point of the Al alloy and lower than that of steel. For instance, the temperature has been measured to $\sim$800°C [115] and calculated to $\sim$1300°C in another study [116].

The molten deposited Al FM wets the steel BM before the Al FM solidifies. Welding occurs between the Al plate and the FM, while brazing happens between the steel and the FM. Eventually a consolidated weld is created, as illustrated in Figure 2.15(c). The weld contains a fu-

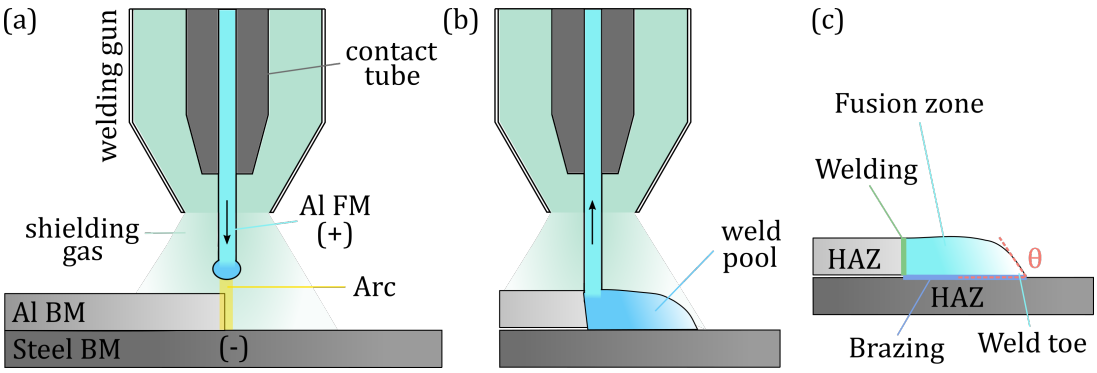

Figure 2.15: Illustrations of the setup used for CMT welding of an Al and a steel BM in lap configuration. **(a)** Illustration of the setup before droplet detachment. A power supply is connected to the BMs and to the Al FM, and the Al FM acts as an electrode. An arc is created between them and the lower end of the FM is melted and forms a droplet. Shielding gas is supplied through a nozzle in the welding gun. The FM is moved towards the weld pool. **(b)** Illustration of the situation when the molten droplet meets the weld pool. The power supply is interrupted and the FM is drawn backwards so that the molten FM droplet is detached. **(c)** Illustration of a CMT joint where the detached molten FM wets the steel BM, so that brazing occurs between the steel and the Al FM, while welding occurs between the Al FM and Al BM. In the finished joint there are HAZs both in the Al BM and the steel BM, while the Al FM constitutes the fusion zone.

sion zone and a HAZ, as is common for fusion welding methods. To increase the wetting of the molten Al FM on the steel, the steel is often coated by Zn [117]. During welding, Zn typically evaporates partly which can lead to presence of notable pores in the fusion zone [118], and Zn-rich zones in the weld toe [119, 120]. Another important factor is the Al FM composition, which influences the IMPs formed and the strength of the joint [111, 117, 121], as will be elaborated on in the next Section, in particular Sections 2.4.5 and 2.4.4.

2.4 Intermetallic phases

The previous section concerned joining methods and in particular a few selected solid state welding methods. During welding, Al and steel have to be brought into close enough contact for bonding to occur. To achieve this, large plastic deformation and/or heat must be applied. This typically enhances diffusion, so that Al and Fe atoms mix into each other across the interface, which is a phenomenon known as interdiffusion. Fe has low solid solubility in Al, and therefore, a layer of IMPs typically forms in welds at the Al-steel interface. This is a major challenge in Al-steel joining, since excessive growth of IMPs is detrimental to the properties of the joints. Therefore, it is crucial to have a fundamental understanding of IMP formation and growth and of how this affects the joint properties. Both the chemical composition of the parent alloys and their thermo-mechanical treatment history govern IMP formation and growth. Numerous Al-Fe(-Si) phases have been described in literature, and several IMPs have been identified at the Al-steel interface in joints.

This section gives an introduction into IMPs, starting with an overview of relevant Al-Fe(-Si) phases. Thereafter, basic aspects of interdiffusion in general are explained. Next, typical characteristics of interfacial IMP layers formed in Al-Fe joints are summarised and exemplified.

Some alloying elements play a major role in the IMP formation and growth, and this topic is also covered. Lastly, mechanical properties of individual IMPs are discussed, before their influence on the joint properties are presented briefly. For completion, other factors influencing the strength of finished Al-steel joints are also mentioned.

2.4.1 Al-Fe(-Si) phases

The binary Al-Fe phase diagram is presented in Figure 2.16, which is adapted from [122] and [21]. It can be seen that the solid solubility of Al in Fe exceeds that of Fe in Al, which is minuscule [21]. Several stable Al-Fe phases can be seen in the phase diagram, and crystallographic information for the Al-rich Al-Fe phases is given in Table 2.3.

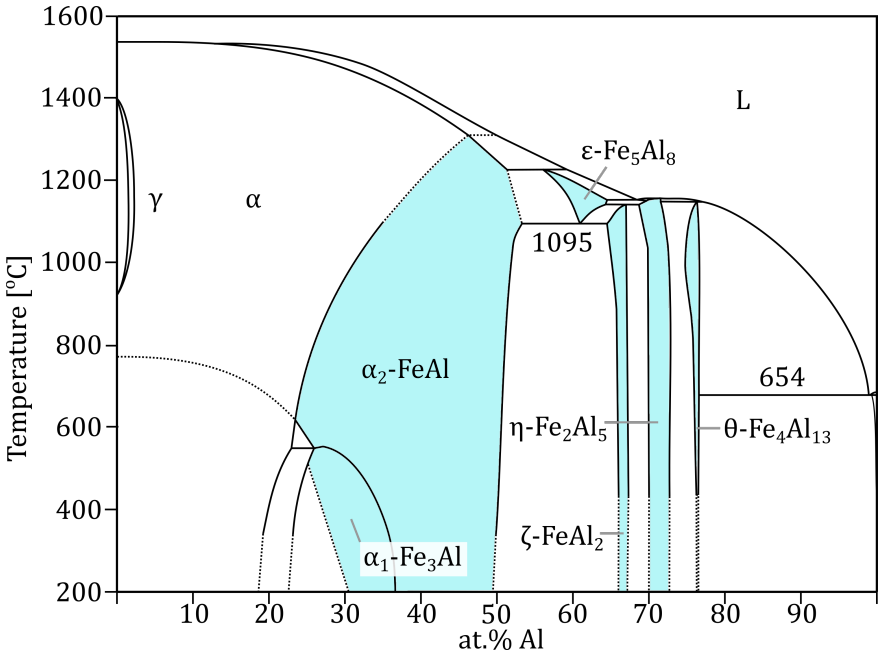

Figure 2.16: Al-Fe binary phase diagram. The Fe-rich region is adapted from [122] and the Al-rich from [21].

The most Al-rich phase in the Al-Fe phase diagram is the θ-Fe_4Al_{13} phase. It has a monoclinic unit cell, as shown in Figure 2.20(a), and is often faulted and twinned [130–132]. The Si content in the θ phase has been measured to $\leq$5.5 at.% at 550°C [133], and the θ phase is in some cases referred to as $Fe_4(Al,Si)_{13}$ or $FeAl_3$. The next phase richest in Al is the η-Fe_2Al_5 phase, and its crystal structure is illustrated in Figure 2.17(b). It has an orthorhombic structure that has a framework of fully occupied sites, together with a partially disordered distribution of Al atoms in channels along the $\vec{c}$-direction [124]. The Si content in the η phase has been measured to $\leq$2.5 at.% at 800°C [134]. Four low-temperature modifications of η have been identified recently, which are located below ca. 350°C in the Al-Fe phase diagram [135]. These are η'-Fe_3Al_8 [125, 136], η'' that is the Al-poorest [135], and η''' that is the Al-richest [135]. A forth ordered structure, η^m, has also been identified, but not yet described [135]. The structure of the η'-Fe_3Al_8 phase can be described as a superlattice based on the η phase, in which Al atoms

Table 2.3: Crystallographic information for Al-rich Al-Fe phases. The bottom three are metastable phases.

Phase	Lattice parameters *a; b; c* [Å] ($\alpha;\beta;\gamma$ [°])	Crystal System	Space Group (#)	Ref.
ζ-$FeAl_2$	$a=4.87; b=6.45; c=8.74$ $\alpha=87.9; \beta=74.4; \gamma=83.1$	Triclinic	$P1$ (1)	[123]
η-Fe_2Al_5	$a=7.66; b=6.42; c=4.22$	Orthorhombic	$Cmcm$ (63)	[124]
η'-Fe_3Al_8	$a=11.32; b=6.37; c=8.64$ $\beta=104.4;$	Monoclinic	$C2/c$ (15)	[125]
θ-Fe_4Al_{13}, $FeAl_3$	$a=15.49; b=8.08; c=12.47$ $\beta=107.7$	Monoclinic	$C2/m$ (12)	[126]
Fe_2Al_9	$a=6.24; b=6.30; c=8.60$ $\beta=95.1$	Monoclinic	$P2_1/c$ (14)	[127]
$FeAl_m$	$a=b=8.84; c=21.60$	Tetragonal	$I\bar{4}2m$ (121)	[128]
$FeAl_6$	$a=6.46; b=7.44; c=8.78;$	Orthorhombic	$Cmc2_1$ (36)	[129]

fully occupy 2/9 of the channel sites [125]. This phase is included in Table 2.3. Both η'' and η''' can be described by incommensurate subsystems. These are not included in the table and the interested reader is referred to [135].

There are also several metastable Al-Fe phases. Those for which the crystal structures have been determined are listed in Table 2.3. Fe_2Al_9 has a monoclinic crystal structure [127, 137] and is isomorphous with Ni_2Al_9 ($a=6.28, b=6.34, c=8.50, \beta=92.4°$ [138]). The structure is illustrated in Figure 2.17(c). Ni and Fe atoms may interchange in the crystal, and therefore this phase is in some cases referred to as $(Fe,Ni)_2Al_9$. Although Ni_2Al_9 and Fe_2Al_9 both are metastable phases in the binary Al-Ni and Al-Fe systems, respectively, the τ_1-$FeNiAl_9$ phase is stable in the ternary Al-Fe-Ni system [114, 127] and in the quaternary Al-Fe-Ni-Si system [139]. The content of Si in $FeNiAl_9$ has been measured to 4 at.% at 500°C [139]. The next metastable phase listed in Table 2.3 is the $FeAl_m$ phase, which is common in rapidly solidified Al alloys [128]. It is Al-rich with $m\sim4$, is often faulted [131] and has been measured to incorporate ≤2.1 at.% Si [140]. Another metastable phase is the $FeAl_6$ phase, which is isomorphous with $MnAl_6$ [129] ($a=6.50; b=7.55; c=8.87$; Å [141]) and is in some cases referred to as $(Fe,Mn)Al_6$ [142]. The solubility of Si in $FeAl_6$ is low, and it has been measured to contain ≤1.9 at.% Si [140].

Further, metastable Al-Fe phases have been identified for which the crystal structures have not been fully determined. Such structures are listed in Table 2.4. Al_xFe was identified in Al-Fe alloys that were cooled at $\sim1-4$ K/s, and its composition was estimated to $x\sim5$ [146] with ≤1.9 at.% Si [140]. A monoclinic unit cell was proposed, although the structure has been reported to be incommensurate and defective. The proposed unit cell corresponded well to recorded electron diffraction data but not with X-ray diffraction data [147]. The Al_pFe phase is body centred cubic with $p\sim4$, and was first observed in cast Al-Fe-Si alloys solidified at cooling rates of ~10 K/s [148].

Numerous IMPs have been described in the ternary Al-Fe-Si system [133, 134, 149–152]. Figure 2.18 shows the liquidus projection of the ternary Al-Fe-Si phase diagram. The isothermal projection at 550°C is shown in Figure 2.19. Crystallographic information for stable Al-Fe-Si phases is presented in Table 2.5. The phase listed first is the α_h (τ_5) $Al_{7.1}Fe_2Si$ phase that has a hexagonal crystal lattice [153]. In some cases, the α_c-$Al_{15}(Fe,M)_3Si_2$ phase forms instead of α_h. The α_c phase has a body centred cubic crystal structure in which certain transition ele-

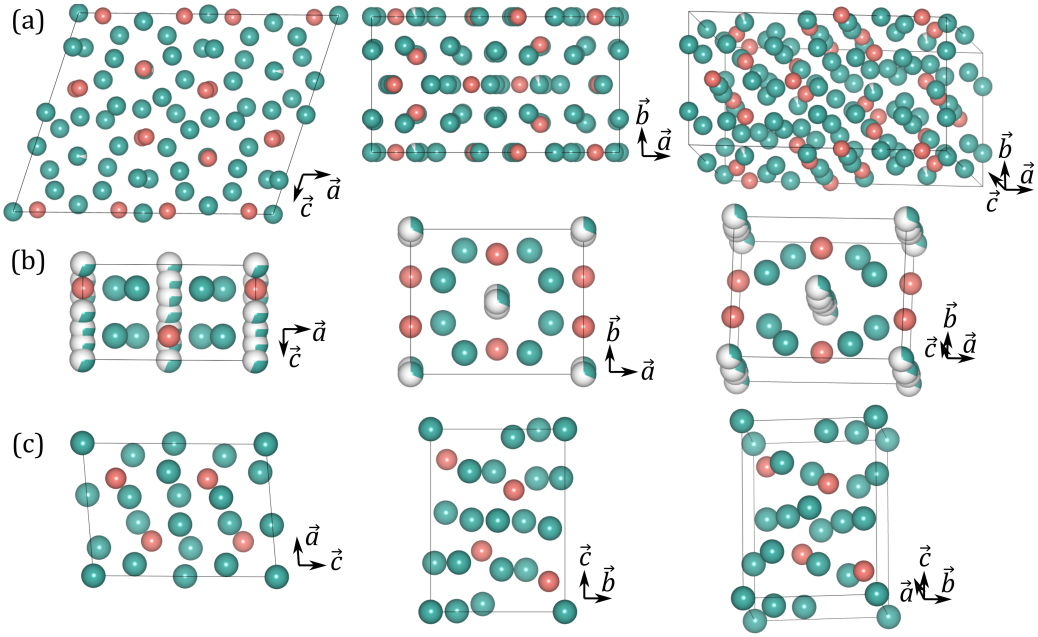

Figure 2.17: Crystal structures of three Al-Fe(-Ni) phases; **(a)** θ-Fe_4Al_{13} based on the crystal structure reported in [126, 143], **(b)** η-Fe_2Al_5 based on [124, 143], and **(c)** τ_1-$FeNiAl_9$ based on [127, 144]. Al atoms are shown in teal while Fe/M atoms are shown in red, and partly filled circles indicate partial occupancy. The figures were produced using the visualisation software VESTA [145].

Table 2.4: Crystallographic information for metastable Al-Fe phases for which the crystal structure has not been fully determined.

Phase	Lattice parameters *a; b; c* [Å] ($\alpha;\beta;\gamma$ [°])	Crystal System	Space Group (#)	Ref.
Al_xFe	$a = 21.6; b = 9.3; c = 9.05; \beta = 94.0$	Monoclinic	-	[146]
Al_pFe	$a = b = c = 10.3$	Cubic	-	[148]

ments, M, may substitute for Fe [154–158]. In general, α_c is regarded as a metastable phase in the Al-Fe-Si system, but it is a stable phase in several quaternary systems, in particular in both the Al-Fe-Si-Mn [152, 159] and the Al-Cr-Fe-Si [160] system. It has been found that <0.3 wt.% M and/or $\gtrsim 4$ wt.% Cu is sufficient to cause formation of the α_c phase in Al-Fe-Si alloys, where M is Mn, Cr, Mo, W or V [154, 155]. The α_c phase has also been identified in rapidly solidified Al-Fe-Si alloys without presence of stabilising transition elements [161]. However, it has been reported that α_c is not present in Al-Fe-Si alloys containing 0.5 wt.% of either Ti, Zr, Co, Ni or Zn [154] or $2-3$ wt.% Mg [155]. In the Al-Mn-Si system, the phase α_{sc}-$Al_{15}(Fe,M)_3Si_2$ is a stable phase, and this phase is highly similar to α_c in terms of both composition and crystal structure. The α_{sc} phase has a simple cubic structure with space group $Pm\bar{3}$ and lattice parameter $a = 12.68$ Å [154]. Formation of α_c versus α_{sc} is governed by the composition, in particular the Fe/M-ratio. The α_c phase has a higher Fe/M-ratio, which has been measured to e.g. $\sim 1-5$ [157, 162], while that of the α_{sc} phase has been measured to e.g. $\lesssim 1$ [157, 162] and $\lesssim 0.1$ [163]. In Al alloys, the α_c phase may form upon solidification as primary particles

with various compositions measured to be in the range of $8-12$ at.% Si and $16-20$ at.% Fe+M [160]. In addition, the α_c phase is also a common dispersoid in Al alloys [164].

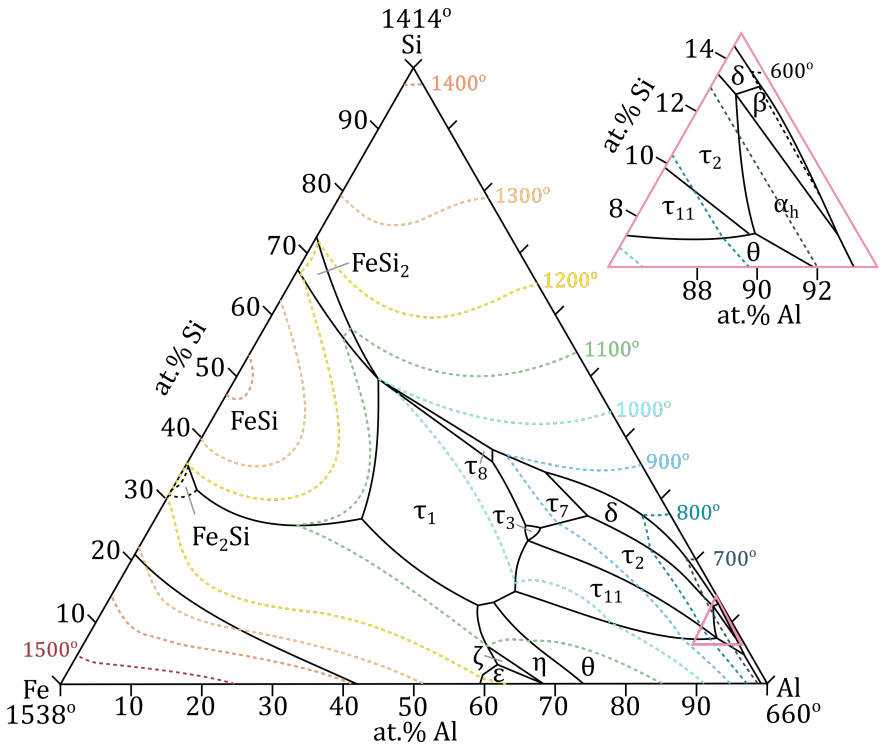

Figure 2.18: Al-Fe-Si liquidus projection. Adapted from [151].

After the α_h phase, the τ_{11}-Al_5Fe_2Si phase has lowest Si content out of the stable Al-Fe-Si phases. Its Si content has been measured to be in the range of $9.2-11.8$ at.% at 800°C [134]. German et al. determined the crystal structure of the τ_{11} phase from an $Al_{60}Fe_{25}Si_{15}$ alloy homogenised at 600°C for 700 h and referred to the phase as $Al_4Fe_{1.7}Si$ [166]. This crystal structure is shown in Figure 2.20(b). Later, Bosselet et al. reported the existence of a similar phase close to τ_{11} in composition that had higher Si content and a different crystal structure, and named it τ_{10} [149, 173]. Note that until then, these two phases were often not differentiated, and the name τ_{10} was often used for either of them in literature [149]. Further, Krendelsberger et al. identified the τ_{10} phase, that contained 15.5 at.% Si, in an $Al_{60}Fe_{25}Si_{15}$ alloy equilibrated at 550°C [133]. They only found the τ_{11} phase in as-cast alloys and assumed that the τ_{11} phase precipitated upon cooling from the liquid state but decomposed at a temperature in the range of $727-600$°C. Thus, τ_{11} can be seen in the liquidus projection shown in Figure 2.18, while τ_{10} can be seen in the isothermal section at 550°C shown in Figure 2.19. The crystal structure of τ_{10} has not yet been determined to the knowledge of the author.

The β-$Al_{4.5}FeSi$ (τ_6) phase has a monoclinic crystal structure [167] that is similar to that of the δ-Al_3FeSi_2 (τ_4) phase [171]. They often appear in Al-Fe-Si alloys as plate-shaped particles. In **Paper C**, it was shown that a few layers of δ is a typical defect in the β phase, and that β and δ often intergrow severely within single Al-Fe-Si particles formed under non-equilibrium

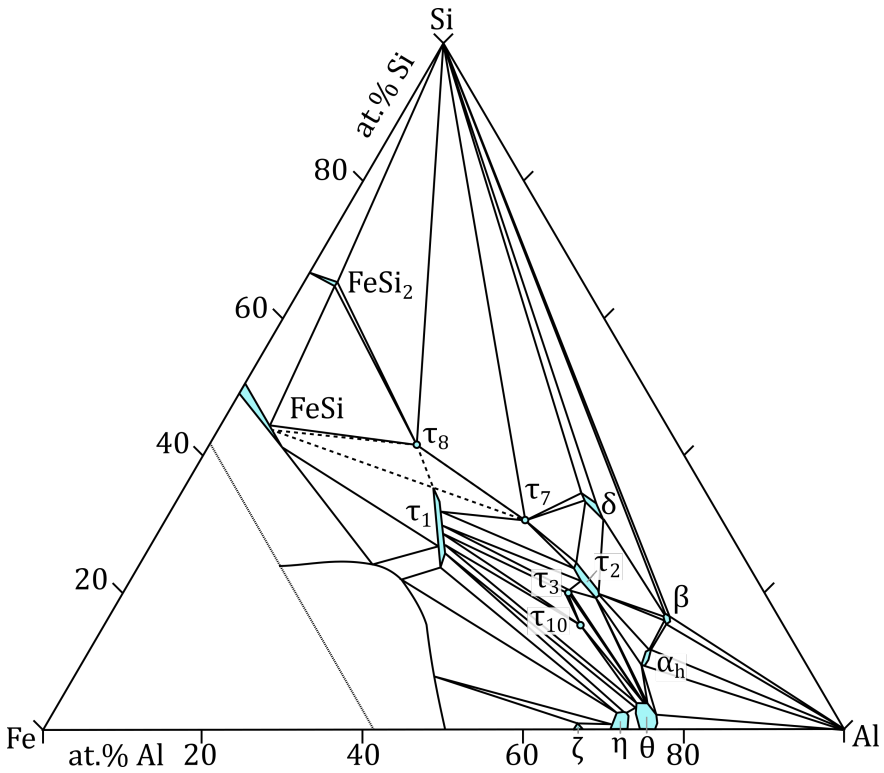

Figure 2.19: Isothermal section of the ternary Al-Fe-Si system at 550°C. Adapted from [150].

conditions. Also, the β phase has several polytypes that were described in the paper.

The next phase listed in Table 2.5 is the γ-Al_3FeSi phase, which Si content has been measured to be in the range of $14.9 - 26.1$ at.% [175, 176]. The crystal structure of the γ phase was first described by Munson to be C-face-centred monoclinic [154], as given in Table 2.5. Much later, Sugiyama et. al determined the structure of a a rhombohedral phase with a composition close to that of γ, which they referred to as λ-AlFeSi [168]. Crystallographic information for this phase is given in Table 2.5. Afterwards, Roger et al. determined the structures of two γ-Al_3FeSi phase crystals as trigonal with space group $R\bar{3}$ (#148), and with lattice parameters $a = b = 10.2223(2), c = 19.6781(4)$ [Å] for an Si-poor crystal and $a = b = 10.1987(2), c = 19.5320(3)$ [Å] for an Si-rich crystal [175]. Subsequently, Yu et al. determined the lattice parameters of presumably the same phase and described it as a trigonal crystal with $a = b = 10.34(5); c = 19.83(8)$ [Å] [177]. These crystal structure descriptions are highly similar, and only the structure reported by Sugiyama et al. is given in Table 2.5. However, the structure proposed by Munson has been confirmed recently [133], and so this one is also included in the table for completion.

Several metastable Al-Fe-Si phases have also been discovered. Crystallographic information for some of these are given in Table 2.6. Note that the crystal structures have not been fully determined. In homogenised commercially pure Al, Dons identified a phase similar to the Fe_2Al_9 phase and named it α_v [178]. The α_v phase had higher Si content, measured to be in the range of $4.5 - 10.5$ at.%, and shorter $\vec{a}$- and $\vec{c}$-axis. Westengen reported a monoclinic β' phase in rap-

Table 2.5: Crystallographic information for Al-Fe-Si phases.

Phase	Lattice parameters *a; b; c* [Å] ($\alpha;\beta;\gamma$ [°])	Crystal System	Space Group (#)	Ref.
α_h, τ_5, $Al_{7.1}Fe_2Si$	$a=b=12.40; c=26.23$	Hexagonal	$P6_3/mmc$ (194)	[153]
α_c, α-AlFeSi, $Al_{15}(Fe,M)_3Si_2$	$a=b=c=12.56$	Cubic	$Im\bar{3}$ (204)	[165]
τ_{11}, Al_5Fe_2Si, $Al_4Fe_{1.7}Si$	$a=b=7.51; c=7.59$	Hexagonal	$P6_3/mmc$ (194)	[166]
τ_{10}, $Al_4Fe_{1.7}Si$	$a=b=15.518; c=7.297$	Hexagonal		[133]
β, τ_6, $Al_{4.5}FeSi$	$a=6.17; b=6.17;$ $c=20.81; \beta=91.00$	Monoclinic	$A12/a1$ (15)	[167]
γ, τ_2, Al_3FeSi	$a=17.78; b=10.25;$ $c=8.90; \beta=132.17°$	Monoclinic	C-centred	[154]
λ, γ, τ_2, Al_3FeSi	$a=b=10.22; c=19.67;$ alt.: $a=8.82; \alpha=70.8;$	Trigonal	$R\bar{3}$ (148)	[168]
τ_{12}, Al_3Fe_2Si	$a=b=c=10.81$	Cubic	$Fd\bar{3}m$ (227)	[134]
τ_3 Al_2FeSi	$a=8.00; b=15.16;$ $c=15.22;$	Orthorhombic	Cmma (67)	[169]
τ_1, τ_9, $Al_2Fe_3Si_3$	$a=4.65; b=6.33$ $c=7.50; \alpha=101.4$ $\beta=105.9; \gamma=101.2$	Triclinic	$P\bar{1}$ (2)	[170]
δ, τ_4, Al_3FeSi_2	$a=b=6.06; c=9.53$	Tetragonal	$I4/mcm$ (140)	[171]
τ_7, $Al_3Fe_2Si_3$	$a=7.18; b=8.35;$ $c=14.46; \beta=93.8$	Monoclinic	$P2_1/c$ (14)	[172]
τ_8, $Al_2Fe_3Si_4$	$a=3.67; b=12.39$ $c=10.15$	Orthorhombic	$Cmcm$ (63)	[170]

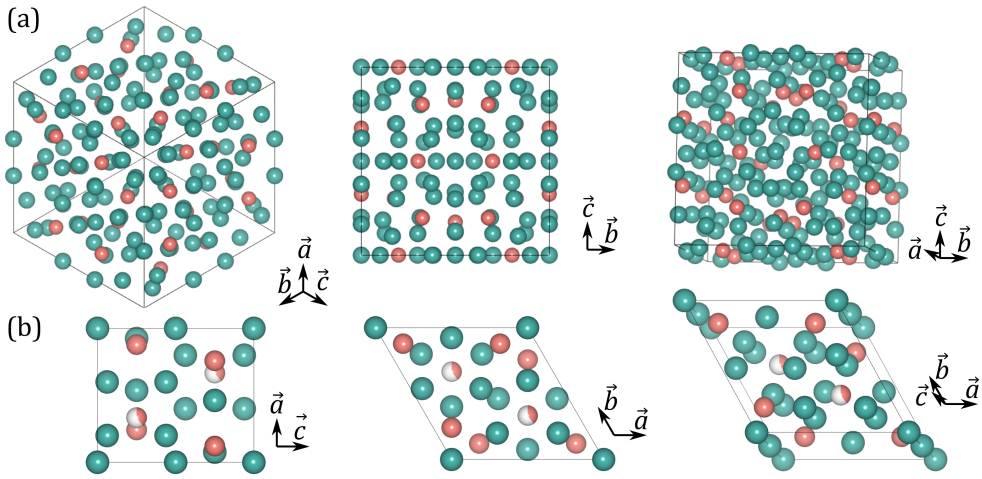

Figure 2.20: Crystal structures of two Al-Fe-Si(-M) phases; **(a)** α_c-$Al_{15}(Fe,M)_3Si_2$ based on the crystal structure reported in [165], and **(b)** τ_{11}-Al_5Fe_2Si based on [166, 174]. Al/Si atoms are shown in teal while Fe/M atoms are shown in red, and partly filled circles indicate partial occupancy. The figures were produced using the visualisation software VESTA [145].

idly solidified Al [156]. Two other phases were also discovered in rapidly solidified Al alloys, q_1 and q_2, that contained ca. 15 at.% Fe and 4 at.% Si [131, 148, 156, 179]. The q_1 phase transformed into the q_2 phase after annealing [148, 179]. Furthermore, several superstructures of the α_c phase have been identified, and these are also listed in Table 2.6. Bendersky et al. found that an amorphous phase formed initially in rapidly solidified Al-Fe-Si alloys, and that it transformed to the α_c phase at $\sim$380°C [180, 181]. Further, it was found that at $\sim$430°C, the α_c phase transformed by ordering into the modified superstructures α' and α" [181–183]. In addition, an α_c superstructure that contained $5.9 - 8.6$ at.% Si was found and termed α_T [157]. The α_T superstructure primarily formed after heat treatments of Al at temperatures in the range of $400 - 450$°C [157]. As remarked in [147], it is unclear whether α_T and α' (α_R) should be considered the same structure. These α_c superstructures and metastable Al-Fe-Si phases are not discussed further here, and the reader is referred to [150, 184] for well presented overviews.

Table 2.6: Crystallographic information for metastable Al-Fe-Si phases and superstructures of α_c.

Phase	Lattice parameters *a; b; c* [Å] ($\alpha; \beta; \gamma$ [°])	Crystal System	Space Group (#)	Ref.
α_v	$a = 8.47; b = 6.35; c = 6.10$ $\beta = 93.4;$	Monoclinic	-	[178]
β'	$a = 8.9; b = 4.9; c = 41.6$ $\beta = 92$	Monoclinic	-	[156]
q_1, α'' [131, 156]	$a = 12.7; b = 36.2; c = 12.7$	Orthorhombic	$Cmmm$ (65)	[179]
q_2	$a = 12.5; b = 12.3; c = 19.3$ $\beta = 109;$	Monoclinic	Pm (6)	[179]
α', α_R [147]	$a = b = c = 20.82; \alpha = 95.2$ alt: $a = b = 30.76; c = 32.6$	Trigonal Hexagonal	$R\bar{3}$ (148)	[181–183]
α''	$a = b = 17.76; c = 10.88$	Trigonal	$P\bar{3}$ (147)	[181, 182]
α_T	$a = 27.950; b = 30.619; c = 20.729$ $\beta = 97.79;$	Monoclinic	C-centred	[157]

2.4.2 Interdiffusion

In solid state welding of Al and steel, IMPs typically form at the Al-steel interface following interdiffusion. *Interdiffusion* is the process in which dissimilar species diffuse into each other across an interface. The phenomenon of *diffusion* is central in several fields, and in general diffusion means spreading or transport of a specific property. In materials science, diffusion is used to describe transport of matter that happens as a result of stochastic motion at the atomic scale activated by thermal energy [185]. At finite temperature, atoms in crystalline solids oscillate around their equilibrium lattice positions, and collective lattice vibrations are referred to as phonons. If an atom gains sufficient energy, it may jump to an adjacent available position. Diffusion results from many individual jumps of the diffusing specie. In crystals, diffusion is enabled by crystal defects, and there are two main diffusion mechanisms. *Interstitial diffusion* describes atoms jumping from an interstitial site to another, and is important for C and N interstitials in steels. *Substitutional diffusion* describes atoms jumping to adjacent vacant lattice sites and is also known as the *vacancy mechanism*. The latter mechanism is dominant for matrix atoms and substitutional solutes, and is the predominant mechanism in Al alloys.

In the absence of any driving forces, the probabilities of forward and backward jumps are equal, and there will be no net transfer of matter. However, if there is a driving force, F, the successful jump rate will be higher in specific directions, and there will be a net diffusive flux.

The flux of specie j is the amount of j passing through a unit area per unit time, and is given by $J_j = c_j v_j$, where c_j is the concentration and v_j is the flow velocity. Flow may arise from a force, $F_j = \zeta_j v_j$, where ζ_j is a friction coefficient, of which the inverse is often referred to as the mobility $1/\zeta_j = B_j$. In general, systems tend towards their state of minimum free energy and thus experience a driving force to decrease the free energy of the system. A force can be described by the gradient of a potential energy surface. The partial free energy of a system, either per mole or per number of molecules of specie j, is referred to as the chemical potential, μ_j [186]. In a system at constant temperature and pressure and where the number of other species is constant, the chemical potential is the partial molar Gibb's free energy. That is the free energy change occurring when a specific number of atoms or molecules of type j are entering or exiting the system. The chemical potential thus describes the tendency for free energy exchange via specie exchange, or the escaping tendency, since particles tend to escape regions with high to regions with low chemical potential. This means that particles move to maximise their entropy, but also towards species for which they have chemical affinity. The chemical potential gradient acts as a driving force for diffusion.

Consider a binary diffusion couple composed of metal A and metal B. The diffusive flux of A in one dimension is given by:

$$J_A = -c_A B_A \frac{\partial \mu_A}{\partial x}. \tag{2.4}$$

The chemical potential is often expressed as $\mu_A = \mu_A^o + RT\ln(\gamma_A c_A/c)$, where μ_A^o is the standard chemical potential, c_A is the molar concentration, and c is the total molar concentration. γ_A is the activity coefficient, which takes into account the interactions between the atoms. For an ideal solution, the species are considered non-interacting so that $\gamma_A = 1$. In this case, the diffusive flux is proportional to the concentration gradient by $J_A = -B_A RT \frac{\partial c_A}{\partial x}$. By introducing the intrinsic *diffusivity* of specie A, which is given by $D_A = B_A RT$, the well-known Fick's first law in one dimension appears:

$$J_A = -D_A \frac{\partial c_A}{\partial x}. \tag{2.5}$$

This means that only for an ideal or dilute solution, the chemical potential gradient is proportional to the concentration gradient [185]. Under such conditions, components tend to diffuse down the concentration gradient.

The *diffusivity* or *diffusion coefficient*, D, describes the rate of diffusion and has SI units $\mathrm{m}^2\,\mathrm{s}^{-1}$. In a solid, the diffusivity generally has an Arrhenius-type dependency on temperature, and is given by:

$$D = D_0 e^{-\frac{E_A}{RT}}. \tag{2.6}$$

D_0 is a temperature-independent pre-exponential factor, T temperature and R the gas constant. E_A is the activation energy of diffusion, which is in some cases switched with the activation entalphy, $\triangle H$. This means that from a plot of $\ln(D)$ versus $1/T$, the slope is given by $-E_A/R$, and the activation energy can be estimated. The activation energy is associated with the breaking of bonds and the elastic deformation that the jumping atom must impose on its neighbours [187]. It follows that near defects such as interfaces, surfaces, dislocations and grain boundaries, the activation energy is typically lower, so that such defects may act as high diffusivity paths. In general, diffusion is fastest on free surfaces, followed by grain boundaries, and the slowest is lattice, also called volume, diffusion [37]. Furthermore, for a given crystal structure and bond type, the activation energy for self-diffusion is in general proportional to

the melting temperature [188]. This implies that a solid with lower melting temperature often has a higher diffusivity.

The original interface between two components in a diffusion couple can be marked by inert markers. The marked plane is referred to as the *Kirkendall marker plane*. In general, the intrinsic diffusivities of A and B are not equal. This means that the flux cannot be explained solely based on any of the intrinsic diffusivities. Rather, an interdiffusion coefficient, $\tilde{D}$, must be defined that depends on each of the intrinsic diffusivities. This topic will not be covered here, and the interested reader is referred to [185, 187]. During interdiffusion, the marker plane will move, as a result of $D_A \neq D_B$, and this phenomenon is known as the *Kirkendall effect* [187]. For example, if $D_B > D_A$ at the Kirkendall marker plane, this plane will move towards higher concentration of B. This causes a net flux of atoms in one direction that must be balanced by an equal flux of vacancies in the opposite direction. This may result in formation of *Kirkendall voids* by coalescence of vacancies at the side of the fastest diffusing specie. The Kirkendall effect is illustrated in Figure 2.21, where (a) shows the original interface with inert markers. Figure 2.21(b) shows that the Kirkendall marker plane moves towards higher concentration of the fastest diffusing specie during interdiffusion, and that Kirkendall porosity eventually forms. The Kirkendall effect was observed in particular in **Paper B**.

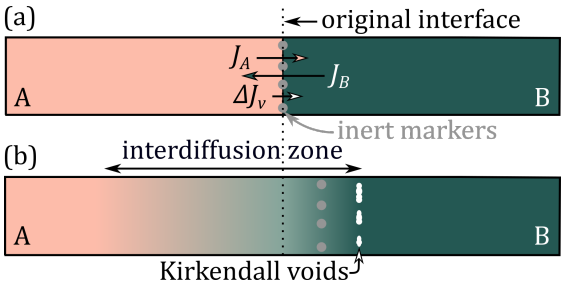

Figure 2.21: Simple illustration of the Kirkendall effect in a binary diffusion couple. **(a)** The couple before interdiffusion. The original interface is marked by inert markers. The flux of A, J_A, is smaller than that of B, J_B, and the difference must be balanced by a net vacancy flux, $\triangle J_v$. **(b)** During interdiffusion, the Kirkendall marker plane moves towards higher concentration of B, and the net vacancy flux eventually leads to formation of Kirkendall porosity.

During interdiffusion mixing occurs, and if the A-B phase diagram contains IMPs, an IMP may form and grow. For predicting the phase sequence evolution in binary diffusion couples, Pretorius et al. [189–192] proposed the effective heat of formation rule. They assumed that the driving force is the change in Gibb's free energy. Since the entropy change mostly is small during solid state formation of ordered phases, they neglected the entropy term and approximated Gibb's free energy as the entalphy change, which is also known as the heat of formation. This quantity is given by: $\triangle H' = \triangle H^o c_e / c_p$, where $\triangle H^o$ is the heat of formation, c_e is the effective concentration of the limiting element, i.e. that for which $c_p > c_e$, and c_p is its concentration in the phase to be formed [190]. By assuming absence of any activation or nucleation barriers, the effective heat of formation could be used for prediction purposes. The highest mobility was expected at a composition equal to the lowest eutectic or liquidus, and so this was chosen as the effective concentration. This leads to the general rule that [191, 192] "Phases will react with each other to form a phase, with a composition lying between that of the interacting phases, whose effective heat of formation, calculated at the concentration closest to that of the liquidus minimum within this composition range, is the most negative."

If a local equilibrium is reached during interdiffusion, all the relevant phases in the binary phase diagram should eventually be present. However, the various phases often grow at different rates, so that some phase layers may dominate. For a phase layer growing during iso-

thermal interdiffusion, the growth rate can be written as:

$$\triangle x = kt^n, \tag{2.7}$$

where $\triangle x$ is the increase in layer thickness, k is the rate constant, n the rate exponent and t is the isothermal annealing time. If a chemical reaction occurring at the interface is the rate controlling mechanism, the layer grows linearly with time: $n = 1$ [191]. If the rate controlling mechanism is lattice diffusion: $n = 1/2$. Therefore, for a diffusion-controlled process, a plot of $\triangle x$ versus $\sqrt{t}$ should follow a straight line. If several phases grow simultaneously in the layer, and each of these grow with a parabolic time dependency, the total layer growth will also follow a parabolic dependency. The parabolic growth rate constant depends on the temperature and can be expressed by an Arrhenius relation, given by

$$k = k_0 e^{-\frac{Q}{RT}}. \tag{2.8}$$

k_0 is the pre-exponential factor, and Q is the activation energy for layer growth. Thus, the slope in a plot of $\ln(k)$ versus $1/T$ can be used as an estimate for the activation energy. In general, the activation energy for growth depends on the composition of the end members. The interdiffusion process becomes more complicated for multicomponent systems. This will not be considered here, and the interested reader is referred to [187, 193, 194].

2.4.3 Al-Fe phases in joints

It is generally agreed upon that in joints of low-alloyed Al and Fe, the θ-Fe_4Al_{13} and subsequently the η-Fe_2Al_5 phase form along the bonded Al-Fe interface [195–197]. With time at elevated temperatures, the η phase dominates the IMP layer growth. The interface between Fe and η typically develops an irregular appearance described as tooth- or tongue-like, serrated, jagged and spiked, while the η-Al interface is much flatter [195–201]. With increasing temperature or time at elevated temperatures, the irregularity of the Fe-η interface typically becomes more pronounced [200, 202]. It has been observed that the η phase grains first nucleate as fine equiaxed grains with random texture [203]. As the layer grow, the grains start to develop a texture, before they grow into preferentially oriented columnar grains. The η grains are typically preferentially oriented along the $\vec{c}$-direction, so that the $\vec{c}$-direction lies normal to the Al-Fe interface [200, 201, 203–205]. This is thought to be a result of the open crystal structure of η, shown in Figure 2.20(b), that has several partly occupied sites which may facilitate fast diffusion along the $\vec{c}$-direction [204].

A typical IMP layer formed at an Al-Fe interface is illustrated in Figure 2.22(a). The displayed schematic is drawn based on the results presented by Bouché et al. [197], where Fe was dipped in molten commercially pure Al at 800°C and allowed to react for 15 min. The Fe-η interface appeared highly irregular with columnar η grains sticking into Fe, as is typical. A much thinner θ-Fe_4Al_{13} layer formed towards Al. With time at elevated temperatures, the θ-Al interface also became more irregular, with thin platelets and needles sticking into or being uniformly dispersed within the Al matrix [197, 201]. This was believed to happen during solidification of the Al melt containing some dissolved Fe [197, 201].

During interdiffusion, thickening of the Al-Fe IMP layer generally shows a parabolic time dependence [197, 199], which is characteristic for diffusion-controlled growth, as introduced in Section 2.4.2. Most often, diffusion of Fe into the IMP layer limits the IMP layer growth rate [202]. Some researchers have noted that the layer growth becomes diffusion-controlled first after an initial transient growth period, which most likely signifies that a chemical interface

reaction dictates the growth to start with [197, 199]. Several authors have attempted to use the parabolic rate law for the growth kinetics, Equation 2.7, to calculate the apparent activation energy, Equation 2.8. The results are scattered, and for growth of the η phase in couples of essentially pure Al and Fe, activation energies of e.g. 74 kJ/mol [206] and 281 kJ/mol [207] have been reported. By combining experimental data with a modelling approach, Xu et al. found that both lattice and grain boundary diffusion are significant in Al-Fe IMP layer growth [208]. A transition from grain boundary to lattice dominated diffusion occurred for increasing temperature, which could explain the scatter in the reported activation energies [208].

Most studies have reported only the presence of the η and the θ phase, although the Al-Fe phase diagram contains several other Al-Fe phases, as shown in Figure 2.16. It has been suggested that the Fe-richer phases, FeAl and ζ-$FeAl_2$, have a much slower growth rate compared to the Al-rich IMPs η and θ, and that they therefore cannot be observed [197]. In fact, a $\lesssim 1\ \mu\mathrm{m}$ thick layer of FeAl has been observed around the rim of columnar η phase grains [22]. It has also been pointed out that equilibrium conditions usually are not reached, at least not in hot-dipping of Fe into molten Al, where the dipping times typically are short [195]. Several studies have found that Fe-richer Al-Fe IMPs form after longer times at elevated temperatures. For instance, in hot-dip aluminising of C steel, FeAl and Fe_3Al were identified after interdiffusion at temperatures exceeding $\sim 1000°\mathrm{C}$ [202]. Metastable phases have also been reported. For instance, $FeAl_m$ formed after hot-dip aluminising of steel at 700°C [209].

2.4.4 Influence of alloying elements

Addition of alloying elements may significantly alter the formation and growth of IMPs at Al-steel interfaces. Numerous studies have looked at the effect of Si additions to Al, and various ternary Al-Fe-Si phases have been identified in Al-steel joints. The hexagonal α_h-$Al_{7.1}Fe_2Si$ (τ_5) phase has been reported to form first and grow on the Al side of the Al-steel interface in several studies. Examples include joints where the Al alloy was melted and contained 5 wt.% Si [22, 210–212], 7 wt.% Si [213], 10 wt.% Si [214–216] and 12 wt.% Si [211–213, 217]. However, in some cases β (τ_6) formed closest to Al. Formation of β was often accompanied by a layer of α_h towards the steel side. The β phase has been identified in several Al-steel joints, e.g. for molten Al with 7 wt.% Si [218] and 10 wt.% Si [215], and for Al with 5 wt.% Si heated to temperatures in the range of $450 - 600°\mathrm{C}$ [22, 24]. Other Al-Fe-Si phases have also been identified at Al-steel interfaces, including τ_2 [22], τ_3 [22], δ (τ_4) [215], τ_{10} [22, 218] and τ_{11} [219]. For prolonged IMP layer growth, the growth of the first formed ternary Al-Fe-Si phase(s) is generally followed by growth of the θ phase and later the η phase at the interface towards steel. The θ and η phases then typically contain minor amounts of Si. Si enrichment at grain boundaries in the η phase layer has been reported [220]. Also, the τ_1 phase may form as precipitates in the η phase layer and/or along the η-θ phase boundary [22, 213, 214, 216].

Example IMP layers are illustrated in Figure 2.22. Figure 2.22(b) was drawn based on the results presented by Springer et al. [22] who performed interdiffusion between C steel and Al containing 5 wt.% Si. After 2 hours at 600°C, the IMP layer contained the β phase closest to Al, followed by an intermediate layer containing a mixture of the phases θ, τ_3 and α_h. A layer of η containing some τ_1 precipitates had formed closest to steel. The phase mixture in the intermediate layer changed to a mixture of θ, τ_3, α_h and τ_2 after 4h, and to a mixture of τ_3, τ_2 and τ_{10} after 8h. Figure 2.22(c) was drawn based on the results presented by Cheng et al. [214] who performed hot dipping of mild steel in molten Al containing 10 wt.% Si at 700°C, followed by heat treatment at 750°C. After annealing for 5 min, the IMP layer contained the phases β, α_h and η. However, after annealing for 15 min, the phase sequence was Al-α_h-θ-η-Fe, where

η contained some τ_1 precipitates, and this situation is illustrated in Figure 2.22(c). These examples demonstrate that the first formed ternary Al-Fe-Si phases can be replaced by other phases after prolonged heat treatment.

There is consensus that addition of Si generally leads to a significant reduction in the IMP layer growth rate. This has been reported frequently both for processes where the Al alloy is melted [22, 196, 198, 211–213, 219, 221–223], and for processes relying on solid-state interdiffusion [224, 225]. Several mechanisms explaining why Si decelerate the growth have been proposed. Nicholls observed that the strong directional growth of the η phase was reduced with Si additions and suggested that Si might occupy the structural vacancies in the η phase and thereby reduce its growth rate [226]. Later studies confirmed that Si affected the diffusion rate of the η phase [223], and also that with Si additions, the η-steel interface became flatter as a result of retarded diffusion [213]. However, no findings were presented to support that Si occupied vacant sites, and it was observed that the Si content in the η phase did not increase as the IMP layer growth rate was reduced [22, 216], which cast doubt on the vacancy-based explanation. Kurakin proposed that the first formed ternary Al-Fe-Si phase acted as a diffusion barrier to Fe, which altered the entire subsequent interdiffusion process and lowered the growth rate [225]. Lemmens et al. found Si enrichment at grain and phase boundaries of the η phase [220], which could possibly act as a barrier to diffusion [216], perhaps together with the observed Al-Fe-Si phases. Akdeniz et al. proposed that Si increases the chemical potential of Al in Fe, and that this reduces the diffusivity of Al, so that the growth rate decreased [227]. Despite that there are numerous publications on the topic, the IMP formation and growth in the presence of Si, and the mechanism of Si in reducing the growth rate of the IMP layer, are still not fully understood.

Furthermore, several studies have focused on the IMP layer formation and growth at Al-steel interfaces when Si has been added to Al in conjunction with other elements. In particular, some transition elements such as Mn and Cr may influence the IMP layer growth together with Si. For example, Mn additions to Al did not notably alter the IMP layer [121, 213]. However, with either Al containing 3 wt.% Si and 1 wt.% Mn or Al containing 5 wt.% Si, 0.15 wt.% Mn and 0.3 wt.% Cu, the IMP layer was thinner and contained the α_c phase in addition to the θ and η phases [121]. Figure 2.22(d) shows an illustration of the IMP layer presented by Jacome et al. for this case [121]. Large polyhedral α_c phase grains grew into Al, followed by smaller elongated θ grains and thereafter a thin layer of η closest to steel. As explained in Section 2.4.1, the presence of transition elements that substitute for Fe in α_c, typically leads to formation of α_c instead of α_h. A similar result was reported by Kurakin [225] who performed CRB and subsequent annealing of Armco iron and commercially pure Al with 1.2 wt.% Si added. After annealing at temperatures $\geq$350°C, a phase referred to as Fe_3SiAl_{12} (cubic, $a = 12.548$ Å) started to form [225], which is highly similar to the α_c phase. The composition of the steel was not given in the referenced paper, but in a previous work by Layner and Kurakin [224], the Armco iron was reported to contain amongst other elements 0.24 wt.% Mn and 0.15 wt.% Cu. This may explain why α_c formed despite that the Al alloy was not reported to contain transition elements. At higher temperatures ($\geq$450°C), they also found the θ and η phases towards Fe, and the η phase was reported to grow in a columnar fashion. These examples underline that the formation and growth of the Al-Fe-Si IMPs may be influenced by elements only present in minor amounts.

Alloying elements typically found in steel may also influence the IMP layer formation and growth notably. For steels containing Cr, Al-Cr IMPs have been found together with the η and θ phases [228, 229]. Furthermore, the α_c phase has also been observed in Al-steel joints where

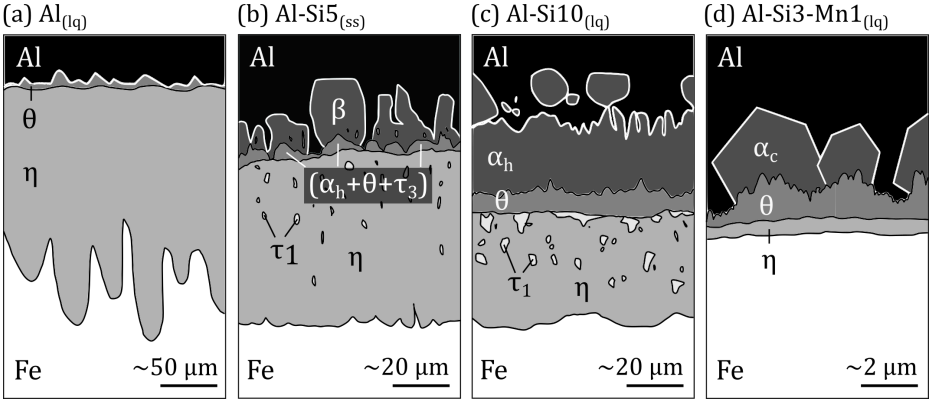

Figure 2.22: Illustrations of typical IMP layers. **(a)** A θ layer and a thicker irregular η layer sticking into Fe, formed after immersion of Fe in molten Al at 800°C for 15 min. Drawn based on results presented by Bouché et al. [197]. **(b)** IMP layer consisting of the β phase, a mixture of the phases θ, τ_3 and α_h, and a layer of η with τ_1 precipitates, formed after 2 hours of interdiffusion between C steel and Al with 5 wt.% Si at 600°C. Drawn based on the results by Springer et al. [22]. **(c)** IMP layer consisting of α_h, θ and η with τ_1 precipitates, formed after hot dipping of mild steel in molten Al containing 10 wt.% Si at 700°C, followed by heat treatment at 750°C for 15 min. Drawn based on the results by Cheng et al. [214]. **(d)** IMP layer of polyhedral α_c grains, elongated θ grains and a thin layer of η, formed following CMT of steel and an Al FM containing 3 wt.% Si and 1 wt.% Mn. Drawn based on the results by Jacome et al. [121].

the steel contained Cr [215], and it has been suggested that Cr might form precipitates in the η phase layer [229]. In joints containing Ni, Al-Ni(-Fe) phases have been identified, such as $FeNiAl_9$ [230, 231]. Also, Ni-rich precipitates have been found in the η phase layer [232]. Cr and/or Ni typically reduce the IMP growth rate and lead to a flatter η-steel interface [199, 215, 233], with Ni being the most effective [199]. Both Ni and Cr have been found incorporated into the θ and η phases [199, 217, 234]. Moreover, as for additions to Al, Si additions to steel reduce the IMP layer growth rate [232]. Lastly, for steels containing C, a thin layer of κ-$AlCFe_3$ has been observed at the interface to Al [22]. These findings underline the importance of studying the combined effect of alloying elements contained within the Al alloy and the steel. This is the main focus of **Paper IV**.

2.4.5 Mechanical properties

Al-rich IMPs are hard and brittle, and fracture has often been reported to propagate through Al-rich IMP layers in various Al-steel joints. Several have reported that the fracture ran mainly through the η phase layer [24, 211], while some reported that it passed mainly through the θ [211, 217] or the α_h phase layer [210, 211]. The properties of the IMP layers may deviate slightly depending on their chemical compositions and grain sizes. Irrespectively, the η phase has often been reported to be amongst the hardest of the Al-Fe phases. For instance, its hardness has been measured to $\lesssim$1400 $HV_{0.01}$ [203], 1100 $HV_{0.05}$ [235] and 1000 $HV_{0.025}$ [202], where x in HV_x indicates the load in kg. With increasing η phase layer thickness, the hardness increased while the fracture toughness decreased [203]. For the θ phase, hardness values have been measured ranging from 835 HV for θ containing 7 wt.% Si [217] and to 645 HV when θ contained ca. 4 wt.% Cu [217]. The hardness of the α_h phase has been measured to 1025 HV [217] and to ca. 950 HV [210]. Fe-richer IMPs are typically less hard and brittle than Al-rich

IMPs. For instance, the hardnesses of FeAl and Fe_3Al have been measured to $660\ HV_{0.025}$ and $320\ HV_{0.025}$, respectively, and they were both reported to be more fracture resistant than the η phase [202]. Modelling approaches have also been used to calculate the mechanical properties of Al-Fe phases. In descending order of brittleness the phases can be arranged as $\eta > \theta > \zeta$ > FeAl > Fe_3Al [236]. In **Paper IV**, nanoindentation and DFT is used to assess the mechanical properties of the individual IMP layers formed in annealed Al-steel cold RB specimens.

Due to the brittleness of the IMPs, they have a major influence on the mechanical properties of the joints. Mainly, it is the thickness of the IMP layers that govern the joint strength [23, 24, 237, 238]. Typically during tensile testing of Al-steel joints, there is a competition between the softest zone in the Al and the brittle IMP layer. If the IMP layer is more fracture resistant than the Al, final fracture typically propagates through the Al, which is the preferred fracture mode in the view of structural integrity. This typically happens if the IMP layer thickness is under a critical value. Thick IMP layers have detrimental effects and typically lead to fracture running through the IMP layer and a substantial decrease in tensile strength and ductility. For this reason, several researchers have examined the relation between IMP layer thickness and joint strength. The trend for all joining methods is that the joint strength decreases as the IMP layer thickness increases [23, 24, 203, 237, 238]. Tanaka et al. found that the joint strength decreased exponentially with increasing IMP layer thickness [23]. Many have reported a critical thickness under which fracture through the IMP layer does not occur during tensile or shear testing, which implies that a sufficiently thin IMP layer does not have a detrimental influence on the joint strength. Naturally, values for critical thicknesses depend on the specific joining process, the process parameters and the chemical compositions of the joined alloys. For example, in one study it was concluded that IMP layers $< 2\ \mu m$ thick did not negatively affect the the joint quality [239]. In another study, the tensile strength was measured to $\gtrsim 250$ MPa and $\lesssim 100$ MPa for IMP layer thicknesses of $\lesssim 0.5\ \mu m$ and $\gtrsim 2\ \mu m$, respectively [238]. In a third study, the joint strength decreased from 327 MPa to 205 MPa when the IMP layer thickness increased from 0.11 μm to 0.34 μm [23].

The morphology of the IMP layer grains may also have a notable effect on the mechanical properties. As the IMP layer grows, grain growth typically happens concurrently, which often is detrimental. Furuya et al. observed that the bond strength decreased as the width of η grains increased, where the width was measured parallel to the Al-steel interface [240]. They found that Ni, Cr, Ti and Mn additions to Al all gave grain refinement of η and consequently higher joint strength [240]. Further, more pronounced steel regions between the columnar η grains have been found to be beneficial, since these regions act as crack-interception points that may hinder cracks from propagating along the interface [24, 203].

There are also other factors that may have an influence on the mechanical properties. Naturally, presence of unbonded interface areas decreases the bond strength and may lead to interfacial fracture along the Al-steel interface [241]. Also, Kirkendall porosity has been observed at the Al side of the interface after extensive Al-Fe IMP layer growth, and such porosity is detrimental irrespective of the IMP layer thickness [24]. Further, for FSW joints in particular, steel fragments detached from the steel BM may be stirred into Al during joining, and cracks may propagate along such steel particles during tensile testing [242]. Another feature often observed in FSW joints is mechanically intermixed layered or swirl-like areas, which originate from the stirring of the steel pin [84]. These areas may contribute to the bond strength by microscale mechanical interlocking, but they may also promote brittle interfacial fracture, depending primarily on their thicknesses and whether they comprise IMP layers [243]. Further,

for RB of Al and steel, it has been reported that cracks readily formed between the hard surface layer and the rest of the steel after scratch brushing, which led to detached steel fragments that reduced the bond strength [244].

To summarise, factors that may lead to brittle interfacial fracture through the IMP layer and a decrease in strength include a thick IMP layer, wide IMP layer grains, Kirkendall porosity and an IMP morphology with no ductile pockets in between IMP layer grains. These factors are illustrated schematically in Figure 2.23(a). Another extreme is shown in Figure 2.23(b). Presence of unbonded areas, cracks in a hard steel surface layer and steel fragments in Al also lead to a reduction in strength and possibly result in brittle interfacial fracture running along the Al-steel interface. Since bond formation in Al and steel welding generally rely on IMP formation, high bond strength and fracture in the soft zone in Al can be achieved for a situation intermediate between Figure 2.23(a) and (b). A thin IMP layer consisting of fine grains creating a wavy interface with interlocks contribute to higher strength, and these factors are illustrated in Figure 2.23(c). Naturally, if significant softening occurs in Al through a decrease in the number density of hardening precipitates, a reduction of dislocation density or notable grain growth, fracture may happen in Al during tensile testing at the same time as the joint strength is reduced. Thus, several factors must in general be assessed to fully understand the performance of Al-steel joints. In **Paper II, III, IV** and **F**, the tensile strengths of various Al-steel joints are discussed in light of findings from microstructural characterisation of the interfaces, and in particular from characterisation of the formed IMP layers.

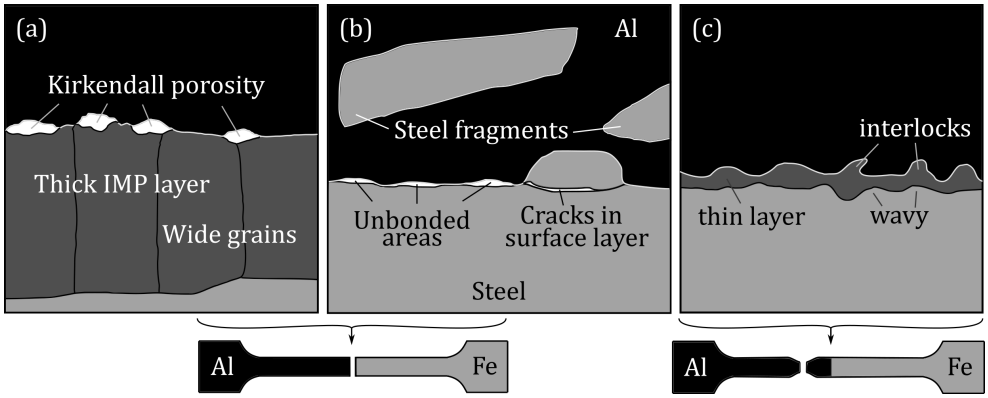

Figure 2.23: Illustrations of Al-steel interface characteristics that typically influence the bond strength. Factors contributing to low bond strength and possibly brittle fracture running near the Al-steel interface during tensile testing include; **(a)** a thick IMP layer, wide IMP layer grains and Kirkendall porosity, and **(b)** unbonded areas, cracks in hard surface layers and steel fragments in Al. **(c)** A thin IMP layer and a wavy interface with interlocking features typically contribute to high bond strength and possibly lead to ductile fracture in the soft zone in Al during tensile testing.

Chapter 3

Methods — Electron microscopy

In this chapter, basic underlying principles of EM are introduced, with the main focus placed on TEM. The chapter begins by giving a brief overview of EM, before explaining key concepts of diffraction theory and selected electron diffraction techniques. Introductions into analysis of scanning electron diffraction data, spectroscopy in EM and specimen preparation by FIB, are also included. In total, this chapter gives an overview of the characterisation methods used in this work, from specimen preparation to data analysis.

3.1 Overview of electron microscopy

The working principle in EM is to direct a beam of fast electrons towards a specimen, and to record and analyse selected signals resulting from the electron-matter interactions. The electron is a subatomic particle that has a charge equal to the negative of one elemental charge, $e \approx 1.602 \cdot 10^{-19}$ C, and that has an extremely small mass; $m_0 = 9.11 \cdot 10^{-31}$ kg [33]. An electron can be accelerated to high speed by an electrostatic potential, V_a, whereby it obtains a kinetic energy equal to: $-eV_a$ [245]. In EM, acceleration voltages in the range of 1 kV to 1 MV are typically used, and for high voltages, relativistic effects must be considered. This can be done by incorporating the relativistic mass: $m = m_0/\sqrt{(1 - v^2/c^2)}$, where m_0 is the rest mass, c is the speed of light and v is the speed of the electron. Furthermore, following the principle of particle-wave duality, an electron has a wave character and a de Brogile wavelength, λ, that is given by: $\lambda = h/p$, where h is Planck's constant and $p = mv$ is the momentum [246]. For example, an electron accelerated through a 200 kV potential obtains a wavelength of 2.51 pm and a speed of $2.086 \cdot 10^8$ m/s ($0.7c$). Correcting for relativistic effects, the electron wavelength is given by [247]:

$$\lambda = \frac{hc}{\sqrt{eV_a(2m_0c^2 + eV_a)}}. \tag{3.1}$$

Several events may occur as a beam of fast electrons meets a specimen, leading to generation of various signals. Some of these signals are listed in Figure 3.1, for an electron transparent specimen $\lesssim$100 nm thick. The part of the beam that remains parallel to the incoming beam after passing through the specimen is termed the *direct beam* or the central beam. Incoming electrons may interact with an atom in the specimen through electrostatic Couloumb forces arising from both the nucleus and the electron cloud[1], resulting in scattering. *Scattering* is a broad term used for processes in which an incoming particle becomes deflected after interacting with an obstacle [33]. In the field of EM, the terms *inelastic* and *elastic* scattering are used depending on whether there is or is not a measurable loss of energy, respectively. Incoming electrons may be inelastically scattered due to single electron excitations, leading to e.g. emission of characteristic X-rays and bremssthralung X-rays, visible light, *secondary electrons*

[1] An incoming electron may also interact with a magnetic specimen through the Lorentz force, but this is not included here.

(SEs) or Auger electrons, as illustrated in Figure 3.1. They may also be inelastically scattered following creation of plasmons or phonons [33, 248].

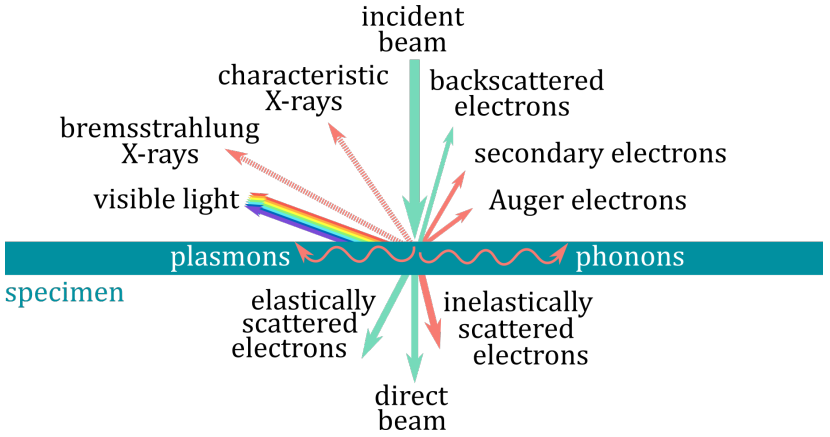

Figure 3.1: Simple illustration listing some of the signals that may be generated as an incident beam of fast electrons meets a thin specimen $\lesssim$100 nm thick. Signals in red result from inelastic scattering, while signals in green predominantly result from elastic scattering. Inspired by Figure 1.3 in [33].

Electron scattering can be described as a wave phenomenon. *Coherent* and *incoherent* scattering are used if there is or is not a phase relationship between the incoming wave and the scattered wave. Inelastic scattering is most often incoherent, while elastic scattering typically becomes more incoherent at higher scattering angles [33]. Waves may be deviated as they interact with an object that has features with dimension(s) on the same order of magnitude as the wavelength, resulting in diffraction. *Diffraction* is the interaction in which an incoming wave becomes deviated by a specimen so that secondary waves are created and interference effects come into play. It is one of several sub-classes of scattering, and concerns primarily waves that are coherently and elastically scattered.

Further, scattering is typically divided into sub-classes depending on the resulting scattering angle, 2θ, i.e. the angle between the incoming and scattered beam. Forward scattering is used when $2\theta<90°$, while back-scattering is used when $2\theta>90°$ [33]. Low angle elastic scattering typically results from electrons interacting with the electron cloud in the atoms in the specimen. High angle elastic scattering happens if an incoming electron travels close to and becomes strongly attracted to the positively charged nucleus, which is referred to as *Rutherford scattering*. Complete back-scattering; $2\theta\approx180°$, may occur in some cases, which is often referred to as reflection [32].

In total, several complimentary signals are generated that can be recorded and analysed. For this reason, a broad range of characterisation techniques can be employed within a single EM instrument. In spectroscopy techniques, the energy distribution of scattered electrons or generated radiation is measured, while imaging techniques concern the spatial distribution of these. Diffraction techniques focuses on the angular distribution of scattered electrons. A combination of conventional imaging, X-ray spectroscopy and diffraction techniques has been the backbone of the EM characterisation done in this work.

3.1.1 Transmission electron microscopy

In a transmission electron microscope, electrons are emitted from an electron gun and accelerated to high speeds through an anode. The electrons travel down the column, and their paths are controlled via several electromagnetic lenses, deflection coils and apertures. These can be divided into three groups: the illumination system which controls the incoming beam, the objective stage where an image of the specimen is created, and the imaging system that magnifies the created image and projects it onto the detector [33]. In the illumination system, a set of condenser lenses is used to control the size and brightness of the incoming beam, and a condenser aperture is used to limit its angular extent. A converged or a largely parallel incoming beam can be formed, and the latter is used in conventional TEM imaging.

The incoming beam meets and interacts with the specimen which sits in the objective stage. Here, an objective lens is used to control the resulting image of the specimen. Either a real space image or a diffraction pattern can be viewed, depending on whether the image plane or the back focal plane of the objective lens is set to coincide with the next lens that is the intermediate lens [33]. Also, the objective stage contains an objective aperture that sits in the back focal plane of the objective lens. This aperture can be used to block selected electrons depending on their scattering vectors. Conventional *bright field* (BF) or *dark field* (DF) TEM images can be formed if the incoming beam is largely parallel and the objective aperture is positioned so that it only allows collection of electrons in the direct beam or in a diffracted beam, respectively. Further, another aperture, the selected area aperture, sits in a conjugate image plane of the objective lens. This aperture is used to select the specimen area from which a diffraction pattern is formed in *selected area electron diffraction* (SAED). Lastly, the transmitted electrons pass through the imaging system. This system includes the intermediate lens and the projector lens, and it magnifies and projects the image or the diffraction pattern onto the detector.

In conventional BF- and DF-TEM images, the image contrast is dominated by *amplitude contrast*, which involves mass-thickness and diffraction contrast [33]. A thicker and/or denser region appear darker in BF-TEM images, since the probability of scattering increases with the atomic number, Z, and with the thickness of the specimen. Moreover, local variations in diffraction conditions give *diffraction contrast*, so that regions that diffract more strongly also appear darker in BF-TEM images. Conversely, in conventional DF-TEM images, only the diffracted beam selected with the objective aperture is allowed to contribute to the image, which means that regions diffracting more strongly into the selected condition appear brighter. Further, the interference between several coherently scattered beams can contribute to the image intensity and give rise to *phase contrast*. This results in for instance *lattice fringes* in *high resolution* (HR)-TEM images. In general, HRTEM images show complicated intensity variations and cannot be interpreted directly in terms of the specimen structure [249]. Conventional HR-TEM images are formed under coherent imaging conditions, with no or a large objective aperture inserted, so that many beams contribute to the image intensity. In *coherent imaging*, the intensity recorded is given by a convolution between the exit wave and a contrast transfer function that explains the imaging characteristics of the microscope [250]. In short, the wave that exits the specimen is blurred by the imaging system, especially by the spherical aberrations [249]. The spatial resolution can be improved by integrating the image forming optics with a spherical aberration corrector. For more information on conventional TEM and HRTEM imaging, the reader is referred to [33, 250].

3.1.2 Scanning transmission electron microscopy

In *scanning transmission electron microscopy* (STEM), the beam is focused to form a fine probe that is scanned in a raster pattern over a specimen *region of interest* (ROI). Designated microscopes exist for STEM, but most transmission electron microscopes are integrated with scanning coils so that TEM and STEM can be performed with the same instrument. At each probe position, the intensity of the scattered electrons is integrated over detectors situated in the back focal plane. A BF detector covers the area including and surrounding the central beam, corresponding to scattering angles in the range of $0 - \lesssim 10$ mrad [33]. *Annular DF* (ADF) detectors, on the other hand, cover areas surrounding, but not including, the direct beam. ADF signals are divided into subcategories that are loosely defined based on the inner scattering angle of the detector, including for instance *annular bright field* (ABF) and *high angle ADF* (HAADF). In HAADF-STEM, the inner scattering angle of the detector is $\gtrsim 50$ mrad [33]. In some microscopes, the BF- and (HA)ADF-STEM signals can be acquired simultaneously, and STEM can be combined with spectroscopy so that an energy spectrum can be recorded at each probe position.

HAADF-STEM images are often interpreted as *Z-contrast* images, where Z refers to the atomic number. High-angle scattering is dominated by Rutherford scattering and *thermal diffuse scattering*, and the cross-section for Rutherford scattering is proportional to $\sim Z^2$ [251], which will be further discussed in Section 3.2.1. At smaller scattering angles, the charge of the nucleus is screened by the electron cloud, so that the Z-dependency is reduced. Further, at high scattering angles the atoms can be considered as independent incoherent scattering sources [252]. In *incoherent imaging*, the image intensity is blurred by the size of the probe, and the spatial resolution is mainly controlled by the probe size [249]. If a small illumination aperture is used, the probe size is broadened by diffraction through the aperture, while the probe is broadened mainly due to aberrations if a larger illumination aperture is used. In that case, a smaller and brighter probe can be formed if the probe forming optics are integrated with a spherical aberration corrector. A probe with dimensions similar to those of an atom can be obtained so that atomic resolution STEM imaging can be performed.

3.1.3 Scanning electron microscopy

In *scanning EM* (SEM), an incoming electron beam with a kinetic energy in the range of $0.1-30$ keV, is focused to a fine probe and scanned in a raster pattern to form an image [253]. The microscope in short consists of an electron gun, a set of condenser lenses, a condenser aperture, a set of scan coils and and an objective lens [254]. The instrumentation enables the incident beam to be focused to a small probe and to be shifted laterally. The working principle is similar to that in STEM, except that reflected electrons are detected instead of transmitted electrons. Consequently, the electron detectors are placed above the specimen instead of below, and SEM specimens are not limited in terms of thickness, so that bulk specimens can be studied.

There are two main types of scattered electrons that are detected in SEM; *backscattered electrons* (BSEs) and SEs. BSEs are scattered to high angles with no or low detectable energy loss, while SEs are low energy electrons that escape after being ejected from the specimen. Accordingly, two main types of electron detectors are used in SEM: Everhart-Thornley detectors that are sensitive to both SEs and BSEs, and dedicated BSE detectors that are largely insensitive to SEs [253]. The Everhart-Thornley detector is placed to the side and is typically operated with a positive bias to attract the low energy SEs that mainly give *topographical contrast*. In addition,

the Everhart-Thornley detector collects BSEs directly emitted into the solid angle of the detector, and the BSEs mainly give Z-contrast. In addition, weak crystallographic contrast can be seen in some cases in BSE images, since the incoming beam undergoes *channeling* that increases the beam penetration for certain orientations [253]. Further, BSEs that exit the specimen undergo diffraction, referred to as *electron backscatter diffraction* (EBSD). Some microscopes are equipped with a dedicated detector that can be inserted to record EBSD patterns, which is typically done with the specimen tilted to a high angle. Moreover, the X-ray spectrum can be recorded with a dedicated EDS detector, in order to measure the chemical composition.

The lateral spatial resolution in SEM is limited by the probe size and the interaction volume. The probe size can be reduced by increasing the incoming beam energy. The incoming electrons undergo multiple scattering events in the specimen and loose energy due to inelastic events, and the electron *interaction volume* is defined as the volume in which the incident electrons have sufficient energy to interact with the specimen [32]. The interaction volume increases with beam energy, and it decreases as the atomic number of the atoms in the specimen increases [254]. For instance, the depth of the interaction volume for incident beam energies of 10 keV and 20 keV have been estimated to 1.3 μm and 4.2 μm for Al, and to 0.5 μm and 1.6 μm for Fe [253]. However, SEs suffer rapid energy loss with travelled distance, so that only SEs generated close to the surface escape and can be detected. Thus, the maximum *escape depth* of the BSEs is much larger than that of the SEs.

3.2 Electron diffraction theory

Electron diffraction techniques concerns the recording of diffraction patterns that show the angular intensity distribution of scattered electrons. Such patterns are most often used to obtain information on the arrangement of atoms in the specimen. In a diffraction experiment, it is often complicated to explain the diffracted intensities, since a diffracted beam typically becomes diffracted again and undergoes repeated diffraction, referred to as *dynamical diffraction*. In most cases however, the position of most of the intensity maxima in the patterns can be explained by *kinematical diffraction* theory, where only single scattering events are considered. This section gives a brief introduction into kinematical electron diffraction theory, which focuses on waves that are coherently and elastically scattered only once. It gives a basic introduction to electron diffraction based mainly on [32, 248, 252]. For more elaborate descriptions the reader is referred to [32, 33, 247, 248, 252, 255].

3.2.1 Kinematical electron diffraction theory

To describe an electron diffraction pattern, it is useful to start by describing the wave characteristics of an electron. In quantum mechanics, the state of the electron can be described by a wave function $\Psi(\vec{r},t)$ that depends on spatial position, $\vec{r}$, and time, t. In a diffraction experiment, the distribution of the scattered electrons is the measured quantity, which can be described by a probability density. The probability density of finding a particle at a given time and position is given by: $I = |\Psi|^2 = \Psi^* \cdot \Psi$, where Ψ^* is the complex conjugate of Ψ [32].

The wave function of the incoming electron is assumed to be a sinusoidal wave expressed by: $\Psi_0(\vec{r},t) = A_0 e^{2\pi i \vec{k}\cdot\vec{r} - i\omega t}$, where A_0 is the complex amplitude, $\vec{k}$ is the wave vector with length $|\vec{k}| = 1/\lambda$, λ is the wavelength, and ω is the angular frequency. For such a sinusoidal wave the phase only changes in the direction in which the wave propagates, $\hat{k}$, while it is constant in the plane normal, and it is therefore referred to as a plane wave [32]. The wave function can

be separated into two factors: $\Psi(\vec{r},t) = \Psi(\vec{r})A_0e^{-i\omega t}$, where the first factor is position dependent and the second time dependent. The incoming plane wave encounters a potential field, $V(\vec{r})$, in the specimen. This *scattering potential* can be assumed to be time independent, since the electron wave oscillates at a time period several orders of magnitudes shorter than the time period of atomic vibrations, and since the measurements occur over a much longer time period [32]. Thus it is sufficient here to only consider the position dependent term, and the wave function can then by expressed by the time independent Schrödinger equation [246]:

$$-\frac{h^2}{8\pi^2 m}\nabla^2\Psi(\vec{r}) - eV(\vec{r})\Psi(\vec{r}) = E\Psi(\vec{r}). \tag{3.2}$$

In this equation, E is the total energy, while $-eV(\vec{r})$ is the potential energy and $-\frac{h^2}{8\pi^2 m}\nabla^2$ represents the kinetic energy. The equation can be rewritten by introducing $k^2 = 2mE/h$ and $U(\vec{r}) = 2meV(\vec{r})/h^2$ [32], which give:

$$(k^2 + \frac{1}{4\pi^2}\nabla^2)\Psi(\vec{r}) = -U(\vec{r})\Psi(\vec{r}). \tag{3.3}$$

In the search of a solution, a Green's function, $G(\vec{r},\vec{r_0})$, is applied, so that: $(k^2+\frac{1}{4\pi^2}\nabla^2)G(\vec{r},\vec{r_0}) = \delta(\vec{r_0})$. In general, the Green's function for a linear differential equation describes the response of the wave function to a point scatterer represented by the Dirac delta function located at $\vec{r_0}$ [246]. The point scatterer produces a spherical wave at location $\vec{r_0}$, which at the location of the detector, $\vec{r}$, is given by: $G(\vec{r},\vec{r_0}) = -\pi e^{2\pi ik|\vec{r}-\vec{r_0}|}|\vec{r}-\vec{r_0}|^{-1}$. This situation is illustrated in Figure 3.2. Since the wave equation is linear, a sum of solutions is also a solution, following the principle of superposition [32]. Therefore, the total scattered wave can be expressed as a sum of spherical wavelet amplitudes originating from point sources located all over the scattering potential. This implies that here, the total scattered wave can be expressed as an integration over the Green's function: $\Psi_s(\vec{r}) = -\int U(\vec{r})\Psi(\vec{r})G(\vec{r},\vec{r_0})\mathrm{d}^3\vec{r_0}$ [252].

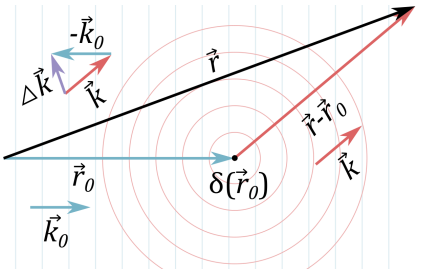

Figure 3.2: Simple illustration of scattering of an incoming plane wave with wave vector $\vec{k_0}$ by a point scatterer represented by the Dirac delta function: $\delta(\vec{r_0})$, located at position $\vec{r_0}$. The point scatterer produces a spherical wave with wave vector $\vec{k}$. The detector is located at $\vec{r}$, and the difference between the wave vectors of the scattered and incident waves is the scattering vector $\triangle\vec{k} = \vec{k} - \vec{k_0}$. Inspired by Figure 4.7 in [252].

The total wave function is the sum of the incident and the scattered wave: $\Psi(\vec{r}) = \Psi_0(\vec{r}) + \Psi_s(\vec{r})$. This allows writing the time-independent Schrödinger equation in integral form:

$$\Psi(\vec{r}) = \Psi_0(\vec{r}) + \pi\int\frac{e^{i2\pi k|\vec{r}-\vec{r_0}|}}{|\vec{r}-\vec{r_0}|}U(\vec{r_0})\Psi(\vec{r_0})\mathrm{d}^3\vec{r_0}. \tag{3.4}$$

To find a solution, it is supposed that the potential is located around $\vec{r_0}$ and that it falls off to zero outside this region. It is also assumed that the wave function is calculated far from the scattering centre, so that: $|\vec{r}|\gg|\vec{r_0}|$, which allows the approximation [246]:

$$\frac{e^{2\pi ik|\vec{r}-\vec{r_0}|}}{|\vec{r}-\vec{r_0}|}\cong\frac{e^{2\pi ikr}}{r}e^{-2\pi i\vec{k}\vec{r_0}}. \tag{3.5}$$

Further, the first Born approximation is invoked, which implies kinematical scattering. Within this approximation it is assumed that the incoming plane wave is not substantially altered by the scattering potential, so that: $\Psi(\vec{r_0}) = e^{2\pi i\vec{k_0}\cdot\vec{r}}$. With these assumptions and approximations, the integral form of Equation 3.4 becomes [32]:

$$\Psi(\vec{r})\approx\Psi_0(\vec{r}) + \frac{e^{2\pi ikr}}{r}\left\{\pi\int e^{2\pi i(\vec{k}-\vec{k_0})\cdot\vec{r_0}}U(\vec{r_0})\mathrm{d}^3\vec{r_0}\right\} = Ae^{i\vec{k_0}\cdot\vec{r}} + \frac{e^{i2\pi kr}}{r}f(\triangle\vec{k}), \tag{3.6}$$

where

$$f(\triangle\vec{k}) = \pi\int e^{2\pi i\triangle\vec{k}\cdot\vec{r_0}}U(\vec{r_0})\mathrm{d}^3\vec{r_0}, \tag{3.7}$$

and $\triangle\vec{k} = \vec{k} - \vec{k_0}$ is the *scattering vector* given by difference in the wave vectors of the incoming and scattered waves. To summarise, the incoming electron beam experiences a scattering potential, which causes generation of new spherical wavelets [248]. These interfere with each other constructively or destructively depending by the path difference between the incident and scattered waves: $\triangle\vec{k}\cdot\vec{r_0}$, to give the total scattered wave with amplitude: $f(\triangle\vec{k})/r$ [248]. The expression for $f(\triangle\vec{k})$ is a *Fourier transform*, $\mathcal{F}$, of the potential $U(\vec{r_0})$. Thus, within the kinematical approximation, the scattering amplitude is given by the Fourier transform of the scattering potential [32]. This is a general principle that unifies kinematical electron, optical and X-ray diffraction theory. The same result can be found by using the weak phase object approximation, and for an explanation of that approach, the reader is referred to [32].

Atomic scattering factor

Consider scattering of an incoming electron by an individual atom with atomic number Z. There are two contributions to the scattering potential seen by the incoming electrons, one from the positive nucleus and one from the surrounding negative electron cloud. There is a relation between the atomic potential and the charge density that is given by: [248]; $\nabla^2V(\vec{r_0}) = -e(\rho_n(\vec{r_0}) - \rho_e(\vec{r_0}))/\epsilon_0$, where $\rho_n(\vec{r_0})$ is the charge density of the nucleus, and $\rho_e(\vec{r_0})$ that of the electron cloud [32]. The nucleus charge density can be approximated as a point with charge Z, so that: $\rho_n(\vec{r_0}) = Z\delta(\vec{r_0})$. Further, $\nabla^2\int V(\vec{r_0})e^{-2\pi i\triangle\vec{k}\cdot\vec{r_0}} = 0$, which yields: $\int\nabla^2V(\vec{r_0})e^{-2\pi i\triangle\vec{k}\cdot\vec{r_0}} + \int V(\vec{r_0})\nabla^2e^{-2\pi i\triangle\vec{k}\cdot\vec{r_0}} = 0$ [32], where the last right-hand term is equal to $4\pi^2|\triangle\vec{k}|^2\int V(\vec{r_0})e^{-2\pi i\triangle\vec{k}\cdot\vec{r_0}}$. Inserting into Equation 3.7 yields the *atomic scattering factor* [248]:

$$f^a(\triangle\vec{k}) = -\frac{me^2}{2\pi h^2\epsilon_0|\triangle\vec{k}|^2}\int e^{2\pi i\triangle\vec{k}\cdot\vec{r_0}}(Z\delta(\vec{r_0})-\rho_e(\vec{r_0}))\mathrm{d}^3\vec{r_0} = \frac{me^2}{2\pi h^2\epsilon_0|\triangle\vec{k}|^2}(Z-f^X(\triangle\vec{k})), \tag{3.8}$$

where $f^X(\triangle\vec{k}) = \int e^{2\pi i\triangle\vec{k}\cdot\vec{r_0}}\rho_e(\vec{r_0})\mathrm{d}^3\vec{r_0} = \mathcal{F}(\rho_e(\vec{r_0}))$ is the *form factor* for X-ray scattering, i.e. the Fourier transform of the electron charge density. Note that the magnitude of $f^a(\triangle\vec{k})$ is typically $1-10$ Å, which is much larger than $f^X(\triangle\vec{k})\sim10^{-4}$ Å [248]. $f^X(\triangle\vec{k})$ is sharply forward peaked, and at large scattering angles, $f^X(\triangle\vec{k})$ tends to zero, so that [248]:

$$f^a(\triangle\vec{k})_{\theta\to90^o} = \frac{2me^2}{h^2\epsilon_0\triangle\vec{k}^2}Z. \tag{3.9}$$

This implies that the intensity is proportional to the atomic number squared: $I_s(\triangle\vec{k})_{\theta\to90^o}\propto Z^2$ for large scattering angles. Scattering by the nucleus is referred to as *Rutherford scattering*, as mentioned earlier. The atomic scattering factor describes the scattering amplitude from only a single atom, and to describe the diffraction from a thin specimen, the arrangement of the atoms in the specimen must be considered.

3.2.2 Kinematical electron diffraction by a perfect crystal

A perfect crystal consists of a periodic arrangement of atoms and can be described as a convolution between a unit cell and a periodic arrangement of lattice points [32]. The convolution theorem states that the Fourier transform of two convoluted functions is equal to the product of the Fourier transforms of the individual functions; $\mathcal{F}(f(\vec{r}) * g(\vec{r})) = F(\vec{k})G(\vec{k})$ [245]. This allows calculating independently the Fourier transform of the unit cell, $F(\triangle\vec{k})^u$, and the Fourier transform of the lattice, $F(\triangle\vec{k})^l$. Thereafter, they can be multiplied to find the total scattering amplitude from a perfect crystal: $F(\triangle\vec{k}) = F(\triangle\vec{k})^l F(\triangle\vec{k})^u$.

Reciprocal lattice

Consider first the lattice, which is a periodic array of lattice points, each described by: $\vec{r_n} = n_a\vec{a} + n_b\vec{b} + n_c\vec{c}$, where $\vec{a}$, $\vec{b}$ and $\vec{c}$ are the lattice vectors and n_a, n_b and n_c are integers. Consider a specimen with the shape of a rectangular prism with dimensions N_a, N_b and N_c along the x- y- and z-direction. The whole lattice can be described as an array of delta points each placed at $\vec{r_n}$, so that the lattice is given by [32]:

$$V^l(\vec{r}) = \sum_{n_a=0}^{N_a-1} \sum_{n_b=0}^{N_b-1} \sum_{n_c=0}^{N_c-1} \delta(\vec{r} - \vec{r_n}). \tag{3.10}$$

The Fourier transform of the lattice is known as the *reciprocal lattice* and is given by [32, 252]:

$$F^l(\triangle\vec{k}) = \sum_{n_a=0}^{N_a-1} e^{-2\pi i \triangle\vec{k}\cdot\vec{a}n_a} \sum_{n_b=0}^{N_b-1} e^{-2\pi i \triangle\vec{k}\cdot\vec{b}n_b} \sum_{n_c=0}^{N_c-1} e^{-2\pi i \triangle\vec{k}\cdot\vec{c}n_c}. \tag{3.11}$$

The sums converge, so that the reciprocal lattice becomes [252]:

$$F^l(\triangle\vec{k}) = e^{-i\phi} \frac{\sin(\pi N_a \triangle\vec{k}\cdot\vec{a})}{\sin(\pi\triangle\vec{k}\cdot\vec{a})} \frac{\sin(\pi N_b \triangle\vec{k}\cdot\vec{b})}{\sin(\pi\triangle\vec{k}\cdot\vec{b})} \frac{\sin(\pi N_c \triangle\vec{k}\cdot\vec{c})}{\sin(\pi\triangle\vec{k}\cdot\vec{c})}, \tag{3.12}$$

where $e^{-i\phi}$ is a phase factor: $\phi = \pi((N_a-1)\triangle\vec{k}\cdot\vec{a}) + ((N_b-1)\triangle\vec{k}\cdot\vec{b}) + ((N_c-1)\triangle\vec{k}\cdot\vec{c}))$[2]. The function in Equation 3.12 is built up of three $\sin(N_i x)/\sin(x)$-type functions that each will approach maxima of value N_i when the nominator and the denominator approach zero. The conditions for maxima can be written: $\triangle\vec{k}\vec{a} = h$, $\triangle\vec{k}\vec{b} = k$, and $\triangle\vec{k}\vec{c} = l$, where h, k and l are integers. The maxima are periodically arranged in wave vector space, and reciprocal vectors can be defined to describe their locations. The principal reciprocal lattice vectors can be defined by $\vec{a}^* = \frac{\vec{b}\times\vec{c}}{V_c}$, $\vec{b}^* = \frac{\vec{c}\times\vec{a}}{V_c}$ and $\vec{c}^* = \frac{\vec{a}\times\vec{b}}{V_c}$, where V_c is the volume of the unit cell, so that $\vec{a}\cdot\vec{a}^* = \vec{b}\cdot\vec{b}^* = \vec{c}\cdot\vec{c}^* = 1$. Then any reciprocal lattice vector can be written as: $g_{\vec{hkl}} = h\vec{a}^* + k\vec{b}^* + l\vec{c}^*$ [33]. For a finite crystal, the maxima sharpens as the crystal dimensions increase. This is illustrated in one dimension in Figure 3.3, where (a) shows the plot of the function $\sin(\pi N x)/\sin(\pi x)$ for $N = 4, 7$ and 10, and (b) shows the plot of the square of this function, which corresponds to the intensity.

If the crystal is large in all directions: $N_a, N_b, N_c \to \infty$, the reciprocal lattice can be described

[2] This phase factor arises due to the choice of limits on the sums and is not included for a choice of $-(N-1)/2$ to $(N-1)/2$ for instance. Compare page 43 in [255] with page 52 in [256].

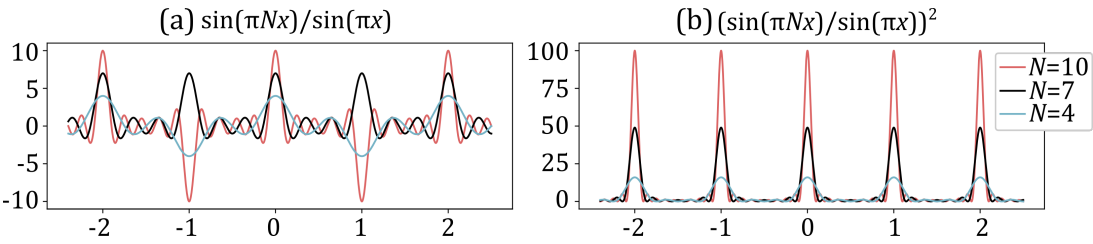

Figure 3.3: **(a)** Plot of the function $\sin(\pi Nx)/\sin(\pi x)$ for $N = 4, 7$ and 10. **(b)** Plot of the square of the function in (a), which corresponds to the intensity. The maxima with values N^2 sharpen as N increases.

by delta functions located at the reciprocal lattice points [255]:

$$F^l(\triangle\vec{k}) \approx \frac{1}{V_c}\sum_{hkl}\delta(\triangle\vec{k} - g_{\vec{hkl}}). \tag{3.13}$$

In this case, an intensity maximum can be found in the diffraction pattern where the scattering vector equals a reciprocal lattice vector: $\triangle\vec{k} = g_{\vec{hkl}}$. This condition is known as the *Laue condition*. The Laue condition can be visualised by drawing a sphere with radius $|\vec{k_0}| = 1/\lambda$, which is located so that the periphery of the sphere cuts through the origin of the reciprocal lattice and the vector from the origin to the centre of the sphere equals the incident wave vector, $\vec{k_0}$. This sphere is known as the *Ewald sphere* and represents the possible scattering vectors allowed by elastic scattering. The reciprocal lattice points that the surface of the Ewald sphere intersects fulfil the Laue condition and give rise to Bragg spots in the diffraction pattern. Figure 3.4(a) shows an illustration of an Ewald sphere, where the Laue condition is fulfilled for a specific $g_{\vec{hkl}}$. For elastic scattering, the scattering vector, $\triangle\vec{k}$, is related to the scattering angle by: $\triangle\vec{k} = 2\sin(\theta)/\lambda$ [33]. The reciprocal lattice vector, $\vec{g}_{hkl}$, is perpendicular to the plane (hkl) and has length: $|\vec{G}_{hkl}| = 1/d_{hkl}$. From this the similarity between the Laue condition in reciprocal space and the well-known Bragg's law in real space can be realised. Bragg's law is given by [33]:

$$2d_{hkl}\sin\theta_B = \lambda, \tag{3.14}$$

where θ_B is the Bragg angle. This equation was first formulated for scattering at a glacing angle where the beam exits the specimen at the same side as it enters, i.e. reflection of an incoming beam by mirror-like atomic planes [33]. Figure 3.4(b) illustrates Bragg diffraction from lattice planes with interplanar spacing d_{hkl}.

Structure factor

Consider a unit cell in which the atom positions are described by fractional coordinates: $\vec{r_j} = x_j\vec{a} + y_j\vec{b} + z_j\vec{c}$. The unit cell potential can be expressed as the sum of the atomic potentials of the N atoms it comprises: $V^u(\vec{r}) = \sum_{j=1}^{N} V_j^a(\triangle\vec{k}) * \delta(\vec{r} - \vec{r_j})$ [32]. The Fourier transform of the unit cell potential, $F^u(\triangle\vec{k})$, is known as the *structure factor*. Since the Fourier transform of the crystal potential is given by a multiplication of the reciprocal lattice and the structure factor, it is sufficient to evaluate the structure factor at the reciprocal lattice points only. The structure

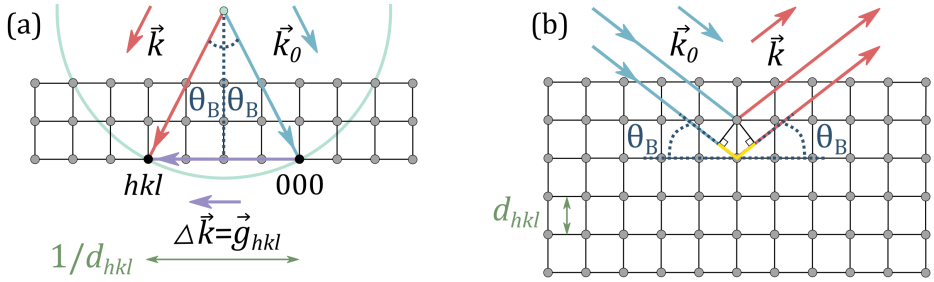

Figure 3.4: Illustration of diffraction by an incoming wave with wave vector $\vec{k_0}$ from lattice planes with interplanar spacing d_{hkl}. The scattered wave has wave vector $\vec{k}$, and θ_B is the Bragg angle. **(a)** Ewald sphere (turquoise semi-circle) intersects a reciprocal lattice point, (hkl) (black dot), and the scattering vector, $\triangle\vec{k} = \vec{k} - \vec{k}_0 = g_{\vec{hkl}}$, fulfils the Laue condition. **(b)** Bragg diffraction, where the path difference (yellow line) between the incoming and the scattered wave is: $2d_{hkl}\sin\theta_B$. In (a) the grey circles connected by black lines illustrate reciprocal lattice points, while in (b) they illustrate real space lattice points.

factor then becomes:

$$F^u(\triangle\vec{k}) = \sum_{j=1}^{N} f_j^a(\triangle\vec{k})e^{-2\pi i\triangle\vec{k}\cdot\vec{r_j}} = \sum_{j=1}^{N} f_j^a(\triangle\vec{k})e^{-2\pi i(hx_j+ky_j+lz_j)}. \tag{3.15}$$

For non-primitive unit cells, the structure factor is zero for certain scattering vectors $\triangle\vec{k} = \vec{G_{hkl}}$, which implies that the scattered intensity is zero for these scattering vectors. Where this happens, the corresponding reciprocal lattice vectors, $\vec{G_{hkl}}$, are said to be extinct, and so-called *extinction rules*, also referred to as selection rules, can be formulated to describe these $\vec{G_{hkl}}$. For instance, for fcc crystals such as Al and γ-Fe (austenite), reflections for which h, k and l are all either even or odd correspond to non-zero structure factors, while reflections with mixed indices are extinct.

Shape factor

The reciprocal lattice was derived above for a large three dimensional crystal, for which the reciprocal lattice approaches a periodic arrangement of delta functions. For a finite crystal however, the shape must also be taken into account to adequately describe the distribution of scattered intensity. A finite crystal can be described as the convolution of a unit cell with an infinite lattice multiplied by a shape function that is unity within the crystal and zero outside it. The multiplication theorem: $\mathcal{F}(f(\vec{r})g(\vec{r})) = F(\vec{k}) * G(\vec{k})$ [245], states that a multiplication in real space equals a convolution in reciprocal space. The Fourier transform of the potential of a finite crystal can therefore be written as: $F(\triangle\vec{k}) = F(\triangle\vec{k})^s * F(\triangle\vec{k})^l F(\triangle\vec{k})^u$, where $F(\triangle\vec{k})^l$ is the reciprocal lattice of an infinite crystal given by Equation 3.13, and $F(\triangle\vec{k})^s$ is the *shape factor*, i.e. the Fourier transform of the shape function. This means that each reciprocal lattice point is convoluted with a shape factor that allows scattered intensity outside the exact Laue condition. A small reciprocal vector can be defined that describes the deviation from the exact Laue condition, and this vector is known as the *deviation vector*, given by $\vec{s} = s_a\vec{a}^* + s_b\vec{b}^* + s_c\vec{c}^*$. The deviation vector is defined as positive when the nearest reciprocal lattice point is inside the Ewald sphere and negative if it is outside [248]. Then the relaxed Laue condition can be written:

$$\triangle\vec{k} = \vec{g} + \vec{s}. \tag{3.16}$$

Consider again the reciprocal lattice of a crystal with the shape of a rectangular prism, as in Equation 3.11. Inserting the relaxed Laue condition, Equation 3.16, into Equation 3.11 results in exponential terms of type: $-2\pi i \triangle\vec{k} \cdot \vec{r_n} = -2\pi i(\vec{g} + \vec{s_g}) \cdot \vec{r_n}$. This gives for the $\vec{a}$-term: $-2\pi i(h\vec{a^*} \cdot n_a\vec{a} + s_a\vec{a^*} \cdot n_a\vec{a}) = -2\pi i(hn_a + s_a n_a)$, and similar for the two other directions. Since $e^{-2\pi i h n_a} = 1$, the hn_a-type terms can be omitted, and the result only depends on the deviation parameter, $\vec{s}$. Further, the sums in Equation 3.11 can be approximated to an integral, which gives [33]:

$$F^l(\triangle\vec{k}) = \int_0^A \int_0^B \int_0^t \frac{e^{-2\pi i(s_a x + s_b y + s_c z)}}{V_c} \mathrm{d}x\mathrm{d}y\mathrm{d}z = \frac{e^{-i\phi_2}}{V_c} \frac{\sin(\pi s_a A)}{\pi s_a} \frac{\sin(\pi s_b B)}{\pi s_b} \frac{\sin(\pi C s_c)}{\pi s_c}, \tag{3.17}$$

where $e^{-i\phi_2} = e^{-\pi i(s_a A + s_b B + s_c C)}$ is a phase factor. The intensity is proportional to $F^l(\triangle\vec{k})^2$, and thus contains three terms of type $(\frac{\sin(\pi s_a A)}{\pi s_a})^2 = \mathrm{sinc}^2(\pi s_a A)$. The specimen has to be thin, $C \lesssim 100$ nm, to admit transmission of electrons, while the lateral dimensions, A and B, can be larger. For large A and B, the sinc-type terms in A and B can be approximated to delta functions, using $(\frac{\sin(\pi s_a A)}{\pi s_a})^2 \approx A\delta(s_a)$ for large A. The expression for the scattered intensity then becomes, with the thickness inserted as $C = t$ [248]:

$$I_s = |\Psi_s(\vec{r})|^2 = \left(\frac{ABF_g^u}{rV_c}\right)^2 \mathrm{sinc}^2(\pi s_c t)\delta(s_a)\delta(s_b). \tag{3.18}$$

Thus, the intensity of the diffracted beam varies strongly with thickness, and this equation is analogous to the Fraunhofer intensity diffracted by a single slit of width t [248]. The full width at half maximum is close to $1/t$, which means that the shape factor can be represented by convolution of the reciprocal lattice with a line of length $1/t$ that lies along the z-direction. In this case, reciprocal lattice points are known as reciprocal lattice rods, in short *rel-rods*. Using the Ewald sphere construction, the Laue condition is fulfilled if the surface of the Ewald sphere intersects a rel-rod.

Consider the case where Bragg planes lie normal to the crystal surface, so that the rel-rods bisect the angle $2\theta_B$ between the incident and diffracted beams. The diffracted beam flux, i.e. the intensity of the scattered beam per unit area, can be obtained by integration of Equation 3.18, which is in this case becomes [248]:

$$I_g(t) = \left(\frac{\pi}{\zeta_g}\right)^2 \frac{\sin^2(\pi t s_c)}{(\pi t s_c)^2}. \tag{3.19}$$

In this equation, the *extinction distance* has been defined to $\zeta_g = \pi k V_c \cos(\theta)/F_g^u(2\theta_B)$, which has unit length [m] [248]. For instance, for Al and Fe at 100 kV, the excitation distances for reflection (200) are 69 nm and 41 nm, respectively [33]. At thicknesses $t = n\zeta_g$, where n is an integer, the intensity of the diffracted beam is zero. The total intensity is the sum of the intensities of the diffracted and the direct beam: $I_g + I_0 = 1$. At the exact Bragg condition, $s = 0$ and Equation 3.19 becomes $I_g(t) = \left(\frac{\pi t}{\zeta_g}\right)^2$. Since there is an upper limit for the diffracted beam intensity; $I_g \leq 1$, there is an upper limit for the thickness; $t \leq \zeta_g\sqrt{I_g}/\pi$, for which kinematical diffraction theory can be used to describe the diffracted beam intensity. It was earlier assumed that the diffracted beam is much weaker than the direct beam, and taking for instance $I_g \leq 0.1$ as in [248], kinematical theory breaks down for $t \geq 7$ nm and $t \geq 4$ nm for the (200) reflection for Al and Fe, respectively. Thus, in almost all practical cases, dynamical diffraction must be considered to explain the diffracted beam intensities.

One well-known way of formulating dynamical electron diffraction theory relays on starting with the Schrödinger equation as given in Equation 3.2 and expressing the wavefunction within the specimen as a linear superposition of waves, referred to as Bloch waves, and expanding the crystal potential as a Fourier series. In this treatment, the crystal acts as an interferometer which divides the incident wave into Bloch waves that propagate through the crystal and that obtain phase differences which lead to interference [248]. It turns out that within the two-beam approximation, the dynamical theory yields an expression similar to Equation 3.19, but where s_c is substituted by the *effective excitation error* given by: $s_e = \sqrt{s_c^2 + \zeta_g^{-2}}$. In this case, the direct and diffracted beams act similar to a coupled harmonic oscillator with intensity continuously being transferred between them [33]. Only if s_c is large so that the diffracted beam is very weak: $s_c \approx s_e$, and otherwise dynamical theory must be used [248]. Dynamical theory is not explained here, and the interested reader is referred to [32, 247, 248].

Other factors

There are other important factors that was not considered above in the description of kinematical diffraction from a crystal. Firstly, for a complete description, inelastic scattering should also be considered. This is often done by adding an imaginary term to the potential, which describes the *absorption*, i.e. the depletion, of the elastic wave, so that: $V(\vec{r})' = V(\vec{r}) + iV^i(\vec{r})$ [248]. Inelastic scattering is a prerequisite for spectroscopy techniques including EDS that is the topic of Section 3.5.

Further, *diffuse scattering* was not considered, which is a broad term for scattering responsible for intensity outside of Bragg peaks. The crystal was here assumed to be static, which allowed diffraction to be treated independent of time. However, the atoms in crystals experience thermally activated lattice vibrations called phonons, in addition to zero-point fluctuations due to the uncertainty principle [256]. Therefore, a displacement term must be added to the lattice positions at any time, t: $\vec{r_n}' = \vec{r_n} + \vec{u_n}(t)$, where $\vec{u_n}(t)$ is the time dependent displacement vector away from the lattice site [32]. This causes a decrease in the intensity of the Bragg peaks, and the intensity is redistributed to appear as *thermal diffuse scattering* between Bragg peaks. The smearing out of intensity can be accounted for by replacing the atomic scattering factor, $f^a(\triangle\vec{k})$, in Equation 3.15 by: $f^a(\triangle\vec{k})e^{-M}$, where the exponential is known as the *Debye-Waller factor* [256]. To account for the redistribution of intensity, a term describing the correlation between the vibrating atoms must also be included. Moreover, for imperfect crystals, a similar but time independent displacement term must be included, which causes redistribution of intensity away from the Laue condition to *elastic diffuse scattering* [248]. Neither inelastic scattering nor deviations from ideal lattice positions are treated further here, and the interested reader is referred to [32, 248, 256].

3.3 Electron diffraction techniques

Several electron diffraction techniques can be performed within a transmission electron microscope. They can be divided into main categories based on the character of the incident beam, depending on whether it is primarily parallel or convergent and whether the beam is static or is being rocked and/or scanned. This section gives an overview of some conventional diffraction techniques within TEM, with the focus on the character of the incident beam and the implications on the diffraction patterns. Thereafter, key aspects of *precession electron diffraction* (PED) and *scanning (precession) electron diffraction* (S(P)ED) are introduced.

3.3.1 Conventional techniques

Selected area electron diffraction

In SAED, the incident beam is spread over a large specimen area, and an aperture is inserted into a virtual image plane that is conjugate to the specimen plane, to block beams originating from outside of the selected region [32]. The incoming beam is largely parallel and has a neglectable convergence angle. A SAED pattern from a crystalline specimen typically shows sharp maxima, referred to as spots or reflections. These spots correspond to reciprocal lattice points described by indices hkl and to real space lattice planes with the same Miller indices hkl. From the previous section it is known that the intersection between the relrods and the Ewald sphere surface determines the spots seen.

The reciprocal lattice plane that the Ewald sphere cuts through and that contains the origin is referred to as the *zero order Laue zone* (ZOLZ). The intersection of the Ewald sphere with this plane defines the *Laue circle*. The curvature of the Ewald sphere causes it to also cut through higher order planes parallel to the ZOLZ that are referred to as the *first order*, the *second order* and *higher order Laue zones* (FOLZ, SOLZ and HOLZs), as shown schematically in Figure 3.5. These Laue zones contain reciprocal lattice points that correspond to real lattice planes that are not parallel to the incoming beam. The spots in the n-th Laue zone must lie in the plane normal to the zone axis $[uvw]$, so that: $hu+kv+lw = n$ [33]. The *zone axis* is the direction of the incoming beam with respect to the crystal. The projected radius of the n-th Laue circle, R_n, depends on the spacing between the reciprocal lattice planes parallel to the incoming beam, $|[uvw]|= 1/d_{uvw}$, and is given by: $R_n^2 = 2n|\vec{k}|/d_{uvw} + (n/d_{uvw})^2 \approx 2n|\vec{k}|/d_{uvw}$.

The position of high intensity features seen in SAED patterns can in most cases be explained based on kinematical electron diffraction theory as described previously, with important exceptions being double diffraction spots and Kikuchi lines. Parts of one Bragg diffracted beam may be Bragg diffracted again, since the sum of scattering vectors that fulfil the Laue condition also fulfil this condition. Therefore, if two spots, $h_1k_1l_1$ and $h_2k_2l_2$, are excited, the sum: $(h_1 + h_2, k_1 + k_2, l_1 + l_2)$, is a possible *double diffraction* spot [248]. This means that spots that are forbidden due to the structure factor (Equation 3.15) may be visible due to double diffraction. Double diffraction is a consequence of dynamical diffraction and causes variations in the intensities of the Bragg spots that cannot be explained by kinematical theory, although the spot positions remain the same.

The incoming beam can be diffusively scattered in all directions, and parts of the diffusively scattered beams can be Bragg diffracted if they travel towards a lattice plane at the Bragg angle, θ_B. To visualise the beams that may be Bragg diffracted from a specific plane, a *Kossel cone* can be constructed so that all lines from the vertices of this cone subtend the Bragg angle to the diffracting plane [252]. Neglecting energy loss, the Kossel cone has a tip to bottom edge distance of $1/\lambda$ [32]. All the possible pairs of incident and scattered beams satisfying the Bragg condition reside on the Kossel cone [32]. The projection of the Kossel cone onto the detector plane, which is largely parallel to the ZOLZ, gives rise to a line in the SAED pattern [32]. This line is referred to as a *Kikuchi line* and is perpendicular to the reciprocal lattice vector $\vec{g}_{hkl}$. Bragg diffraction also happens from the other side of the same plane, so that two Kossel cones can be constructed, which results in a hkl and a -h-k-l Kikuchi line pair that is referred to as a *Kikuchi band*. The distance between the two Kikuchi lines is equal to $|\vec{g}_{hkl}|$. The Kikuchi line that resulted from diffusively scattered beams that were originally more forward peaked is bright, since diffusive scattering is forward peaked, while the other is dark. These two are

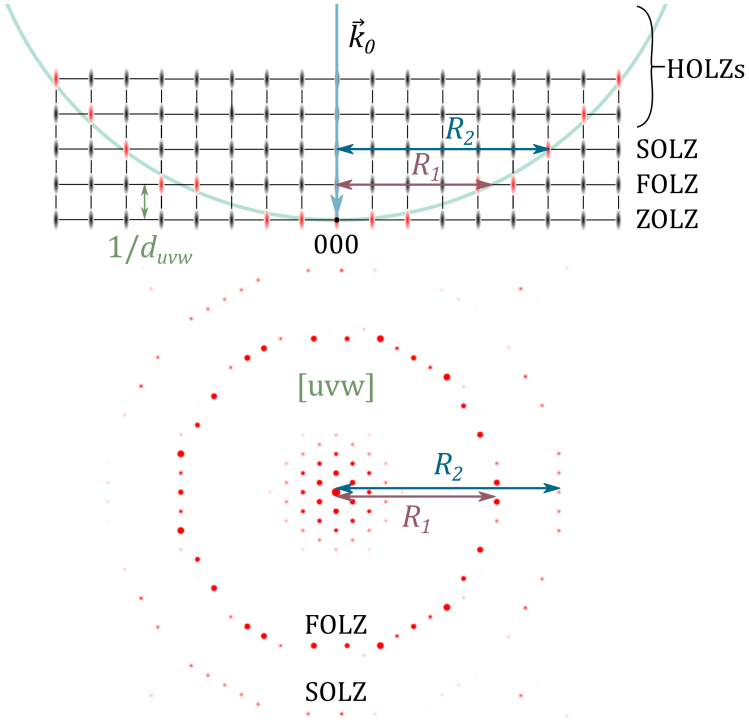

Figure 3.5: Illustration showing the Ewald sphere construction for SAED (top), as seen in cross-section, and a simulated diffraction pattern from zone axis $[uvw]$ (bottom). The relrods (black ovals) that are cut by the Ewald sphere (turquoise semi-circle) fulfil the relaxed Laue condition (red ovals) and give rise to spots in the diffraction pattern. The plane perpendicular to the incident beam that contains the origin is referred to as the ZOLZ, while the planes parallel to the ZOLZ that lie above the origin are referred to as the FOLZ, SOLZ and HOLZs. The intersection of the Ewald sphere with these planes give rise to spots forming Laue circles in the pattern. The radius of the FOLZ, R_1, and the radius of the SOLZ, R_2, are indicated. The pattern was simulated using Recipro [257].

therefore referred to as the *excess* and the *deficient* Kikuchi line, respectively.

A small tilt does not change the spot positions in the SAED pattern. The Kossel cones however, are fixed at subtending the Bragg angle to the lattice planes, which means that the Kikuchi lines move with the lattice planes and are sensitive to small tilts [33]. This makes them useful for determining the value of the excitation error, $\vec{s}$, and for orienting the crystal. If a spot fulfils the Bragg condition so that $\vec{s} = 0$, the Kikuchi line cuts through the spot, while for a crystal oriented to a zone axis, the Kikuchi line bisects the vector $\vec{g}_{hkl}$. An example is shown in Figure 3.6, where (a) and (b) show zone axis SAED patterns from a thinner and a thicker part of the same crystal, respectively. It can be seen that the Kikuchi lines are stronger for thicker specimens in SAED, which happens since the diffuse background increases with specimen thickness as long as electron transparency is not lost [252].

Convergent beam electron diffraction

In *convergent beam electron diffraction* (CBED), the incoming beam is focused to form a spot on the specimen and has a relatively large convergence angle, 2α, typically on the order of

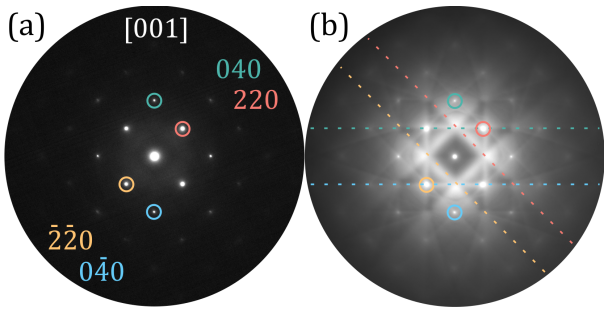

Figure 3.6: SAED patterns from a Si crystal oriented to zone axis $[001]$. **(a)** and **(b)** show patterns from a thin and a thick part of the crystal. In (a), high intensity spots can be seen, while relatively strong Kikuchi lines can be seen in addition to the spots in (b). The 040, $0\bar{4}0$, 220 and $\bar{2}\bar{2}0$ spots are marked by green, blue, red and orange circles, and in (b) their corresponding Kikuchi lines are marked by dashed lines.

$\sim 5-50$ mrad. A range of incoming wave vectors therefore meet the specimen, and a range of Ewald spheres can be constructed, so that the total Ewald sphere effectively has a thickness, as illustrated in Figure 3.7. The cone of incoming beams gives a CBED pattern that consists of Bragg disks instead of spots as seen in SAED. The disk diameter is given by: $2\alpha|\vec{k}|$, and Bragg disks can be well separated ($\alpha<\theta_B$), referred to as Kossel-Möllenstedt condition, slightly overlapping ($\alpha>\theta_B$) or strongly overlapping ($\alpha>>\theta_B$), referred to as Kossel condition.

Each point within a CBED disk corresponds to a beam direction that sees a slightly differently oriented specimen, which means that the excitation error varies across each disk. There is an elastic contribution to the Kikuchi lines where they pass through Bragg disks. In general, the Kikuchi lines are sharper in CBED than SAED also since the diffusively scattered beams will be forward peaked in a larger angular range, and since the illuminated area is much smaller and often more homogeneous [33]. In Kossel conditions, where the disks are completely overlapping, there is a continuous elastic contribution to the Kikuchi lines, which causes them to appear much more prevalent. Such Kikuchi patterns can be used to determine the crystal symmetry and provide navigation maps of reciprocal space [32]. Also, the elastic part of the HOLZ Kikuchi lines, referred to simply as HOLZ lines, appear as lines within Bragg disks [33]. If a HOLZ reflection is excited, intensity is redistributed from the 000 disk to the HOLZ line, which gives an excess hkl line at $\vec{g}_{hkl}$ and a deficient hkl line in the 000 disk [33]. At a zone axis, the HOLZ line segments form a HOLZ ring, as opposed to the weak HOLZ ring formed by spots in SAED. An example can be seen in Figure 3.8, where (a) and (b) show a SAED and a CBED pattern, respectively, from the same zone axis.

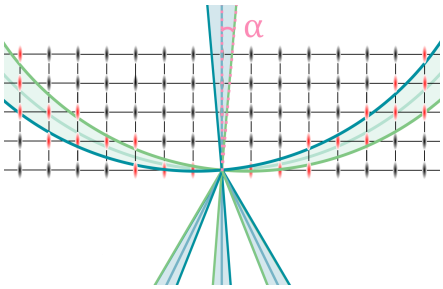

Figure 3.7: Illustration showing the Ewald sphere construction for CBED. The incoming beam has a convergence semi-angle α, and due to the beam convergence, a range of Ewald spheres can be drawn so that the Ewald sphere in practice has a thickness. The relrods (black ovals) that are cut by the Ewald sphere (turquoise semicircle) fulfil the relaxed Laue condition (red ovals) and give rise to disks in the diffraction pattern.

In total, a CBED pattern typically contains a wealth of information about e.g. the three dimensional geometry of the crystal lattice, the specimen thickness and the acceleration voltage, and can be used e.g. to determine the lattice parameters and the space group. However, if the specimen is extremely thin so that dynamical diffraction is highly unlikely, each CBED disk

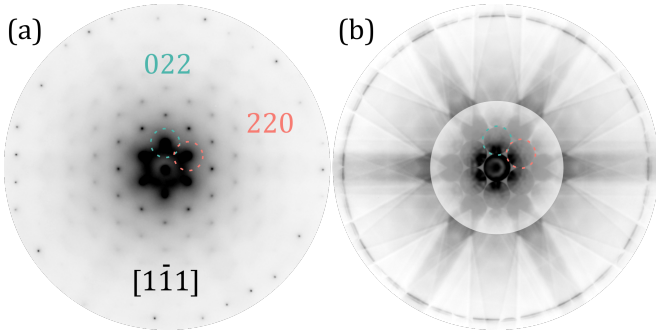

Figure 3.8: **(a)** SAED and **(b)** CBED pattern from a Si crystal oriented to zone axis [1$\bar{1}$1]. The contrast has been inverted, and in (b) the contrast has been enhanced in the outer region compared to the inner region, to make weak intensities more visible.

will contain an even distribution of intensity and not provide more information than a corresponding SAED pattern from the same small area [33]. Various CBED techniques exist, such as large angle CBED (LACBED) and position-averaged CBED (PACBED) [251]. Finally, it should be noted that STEM is typically performed with overlapping CBED disks, and that EBSD patterns are analogous to Kossel patterns.

Nanobeam electron diffraction

Nanobeam electron diffraction (NBD) is used when the combination of a largely parallel incident beam and a small probe is needed. In NBD, a nanometre-sized probe is focused on the specimen, and the convergence angle is typically much smaller than in CBED but larger than in SAED, so that small and most often non-overlapping disks form in the NBD pattern of a crystalline specimen. A small circular condenser aperture is typically used to yield a convergence angle of $\sim$1 mrad, in which case the minimum size of the focused probe is diffraction limited. Under incoherent imaging conditions, the probe intensity distribution, I_P, then takes the form of the square modulus of the Fourier transform of the circular aperture function, which yields an *Airy disk* consisting of concentric circles of decreasing intensity. It is proportional to the first order Bessel function, $J_1(x)$, by: $I_P \propto ((J_1(2\pi r\sin(\alpha)/\lambda))/(\pi r\sin(\alpha)/\lambda)^2$ [32], and $(J_1(x)/x)^2$ is plotted in Figure 3.9(a). Following the *Rayleigh criterion* typically used in optics, the resolution is the distance between the global maximum (at $x = 0$), and the first minimum of the Airy disk (at $x \approx 3.832$) [32]. By using $x = 3.832 = 2\pi r\sin(\alpha)/\lambda$, the Rayleigh criterion for resolution becomes:

$$r_0 = 0.61\lambda/\sin(\alpha). \tag{3.20}$$

Equation 3.20 states that the diffraction limited probe size, r_0, decreases as the convergence semi-angle, α, increases, so that improvements in angular resolution can only be done at the expense of reduced spatial resolution, and vice versa. Figure 3.9(b) shows a plot of convergence semi-angle versus diffraction-limited probe size, as given by Equation 3.20. For comparison, the Airy disk can also be approximated to a Gaussian with full width at half maximum of $0.52\lambda/\alpha$ [32]. It should be noted that the Rayleigh criterion holds for two incoherent point sources. For coherent imaging, the scattering amplitude resulting from the two point sources must be added before the sum is squared to get the intensity, so that the peaks broaden and the resolution increases [251]. Thus in general, better resolution can be obtained for incoherent imaging than for coherent imaging. Diffraction was performed in NBD mode with a convergence semi-angle of $\alpha = 1.0$ mrad in **Papers I, IV** and **F** and with $\alpha \lesssim 0.5$ mrad in **Paper II**.

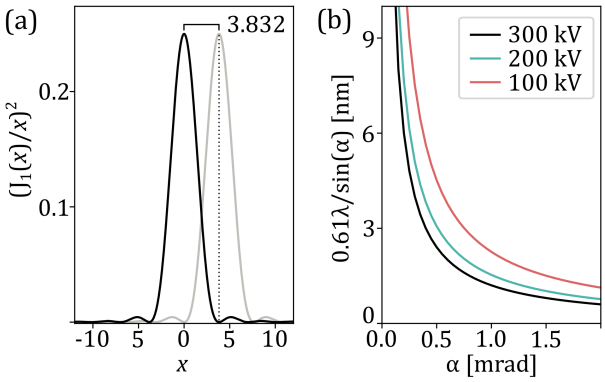

Figure 3.9: The Airy disk and the Rayleigh criterion. **(a)** Plot illustrating the intensity distribution for an Airy disk in one dimension given by: $(J_1(x)/x)^2$, where J_1 is the first order Bessel function. The grey curve has an offsets of $x = 3.832$, which corresponds to the first minimum of the black curve. **(b)** Plot of convergence semi-angle versus diffraction limited probe size, as given by the Rayleigh criterion, for acceleration voltages of 100 kV, 200 kV and 300 kV.

3.3.2 Precession electron diffraction

In PED, the incoming beam is rocked at a constant precession angle, ϕ, around the optical axis during acquisition of the diffraction pattern [258]. The beam rocking produces a range of incoming wave vectors. Integrated over one full rotation cycle, the incoming beam forms a cone with inner angle $\phi - \alpha$ and outer angle $\phi + \alpha$. The cone is thus hollow if $\phi > \alpha$, and in this case precession is similar to hollow cone illumination with an annular illumination aperture. This means that the diffraction pattern from a crystalline specimen acquired with precession shows one annuli per spot seen in a corresponding SAED pattern. To recover the conventional diffraction pattern geometry, the beam is *de-rocked* under the specimen in PED. The PED technique is therefore in some cases referred to as the *double-conical beam rocking method*. An example is shown in Figure 3.10, where (a) shows a PED pattern formed with a small convergence angle of ca. 1 mrad, and (b) shows the resulting pattern without de-rocking.

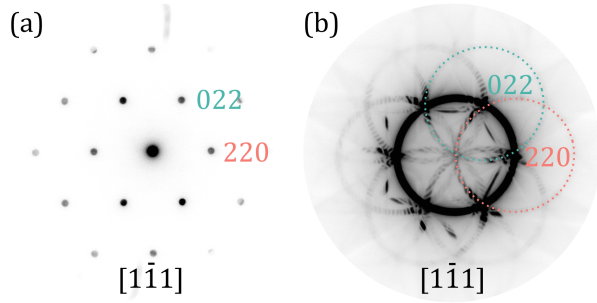

Figure 3.10: Diffraction patterns from Al oriented to zone axis $[1\bar{1}1]$ acquired in NBD mode with a convergence semi-angle of 1 mrad. **(a)** PED pattern acquired with a precession angle of 17 mrad (1°). **(b)** Pattern corresponding to that in (a) acquired with beam rocking but without de-rocking. The contrast has been inverted.

PED is typically performed in NBD mode with a precession angle of $\phi \lesssim 3°$ ($\lesssim 50$ mrad) and a convergence semi-angle of $\phi \sim 1$ mrad. Figure 3.11 shows a simplified sketch of a typical setup. A set of pre-specimen deflector coils are used to tilt the beam off the optical axis by the precession angle, ϕ, while a set of post-specimen deflection coils counteracts the beam tilting [259]. During alignment, the beam pivot point is set to coincide with the specimen plane, and the beam pivot point and the de-rocking, often referred to as *descan*, are iteratively adjusted in diffraction mode to obtain stationary disks [260].

During precession, the Ewald sphere rotates around the optical axis at the precession angle, so that its centre traces a circle with a radius given by ϕ. Consequently, the Ewald sphere sweeps

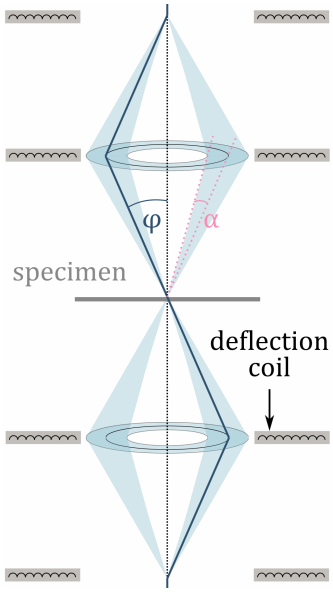

Figure 3.11: Simplified schematic of a typical PED setup. Inspired by [258]. The incoming beam has a convergence semi-angle α. A set of beam deflector coils situated above the specimen is used to tilt the beam an angle ϕ off the optical axis, while a set of deflector coils below the specimen counteracts the tilting. As a PED pattern is acquired, the beam is rotated around the optical axis so that it traces a circle with a radius given by ϕ.

through and excites Bragg reflections temporarily, so that the Laue circles rotate around the zone axis. Naturally, the rotating Ewald sphere gives a much larger total intersection volume than a static Ewald sphere. A PED pattern therefore shows more reflections than a corresponding SAED pattern. Figure 3.12 illustrates the Ewald sphere construction corresponding to a zone axis PED pattern. In total, the intersection of the Ewald sphere with the ZOLZ plane is expanded from a single circle to a circular area with outer radius given by: $R_{0,+} = 2|\vec{k}|\sin\phi$, while the HOLZ rings are expanded to annuli with widths given by: $|\vec{k}|\sin\phi$. The outer and the inner radius, $R_{n,+}$ and $R_{n,-}$, of a n-th order HOLZ annulus are given by $R_{n,\pm} = \sqrt{R_n^2 + R_{0,+}^2} \pm R_{0,+}$ [258]. For large precession angles, a challenge is that HOLZ reflections can start to overlap with the ZOLZ, which is referred to as "HOLZ creep" [259].

A PED pattern is recorded while the incoming beam is scanned over a range of incoming directions. Therefore, a PED pattern is equivalent to the sum of a series of individual patterns each recorded with a tilted but static incoming beam, where the incoming beams together trace the precession cone. Interestingly, a zone axis PED pattern is thus formed from a range of off-axis incoming beams. This implies that at any time, less beams fulfil the Bragg condition and less dynamical diffraction paths are available [261]. Precession can therefore give "kinematic-like" intensities approaching those predicted by kinematical theory [262]. However, this does not necessarily happen in all cases, and for instance if the Laue annuli are wide enough, several reflections can be excited simultaneously along a systematic row so that double diffraction paths are allowed [259]. Further, since the incoming beam sees a slightly differently oriented specimen at any time during the precession cycle, the positions of the orientation sensitive Kikuchi lines will vary so that they become less pronounced in the final PED pattern.

The intensity recorded at a point in a PED pattern corresponds to an integration over the precession angle. For a specific reflection, this integration can be rewritten to an integration over the excitation error. As a result, the disks seen in PED patterns typically show uniform intensities. For the ZOLZ, reflections for which: $|\vec{g}_{hkl}|<2(\phi - \alpha)|\vec{k}|$, pass through Bragg condition

twice and are completely integrated during one precession cycle, while reflections at higher scattering angles are incompletely integrated [258]. The integration can also be limited for low order reflections due to the proximity to the rotation axis centre. This means that in order to adequately compare the intensities of reflections measured in a PED pattern, they must be corrected by a geometric factor taking into account the integration path [259]. For reflections in the ZOLZ, a relation between the measured and the corrected intensity has been derived: $I_g \propto [1 - \{|\vec{g}_{hkl}|/(2R_{0,+})\}^2] I_g^p$ [263].

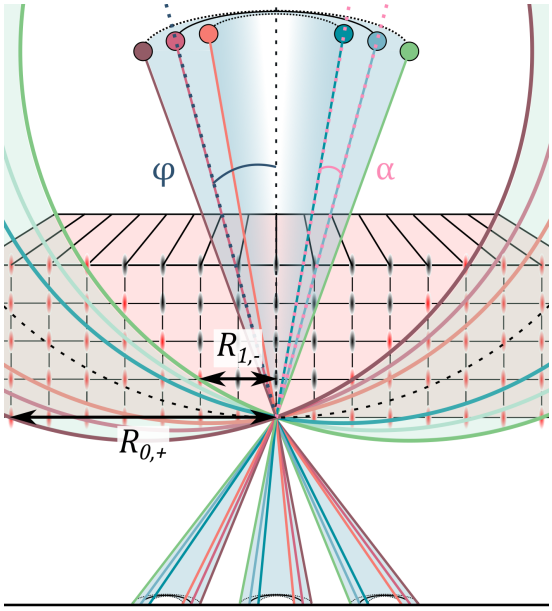

Figure 3.12: Illustration of the Ewald sphere construction for PED. A cross-section through the reciprocal lattice is shown. The incoming beam has a convergence semi-angle α, and a precession angle ϕ. For clarity, the radius of the Ewald sphere has been undersized, while the precession and convergence angles have been oversized. During precession, the incoming beam rotates about the optical axis so that the Ewald sphere sweeps through reciprocal space. Over a full precession cycle, the Ewald sphere centres (filled coloured circles) trace a hollow illumination cone (light blue), the ZOLZ circle is expanded to a circular area and HOLZ circles are expanded to annuli. The radius of the ZOLZ, $R_{0,+}$, and the inner radius of the FOLZ, $R_{1,-}$, are marked. Without de-rocking of the beam, the diffracted beams appear as annuli in the PED pattern.

To summarise, precession leads to more reflections being excited, integration of intensities, and possibly more kinematic intensities [259, 264]. Precession is beneficial for several applications, especially for structure refinement [265]. Further, the uniform disk intensity makes disk identification and indexing easier, which can be exploited in e.g. orientation and strain mapping. Several of the advantages of precession are evident in Figure 3.13, which shows a comparison between patterns obtained by (a) SAED, (b) NBD, (c) PED and (d) kinematic simulation. PED patterns like the one shown in (c) were acquired for **Papers IV** and **F**.

3.3.3 Scanning (precession) electron diffraction

Several electron diffraction techniques can be combined with scanning of the beam over a ROI, so that a single diffraction pattern can be recorded at each scan position. This yields a *four dimensional* (4D) dataset with two scan, i.e. real space, dimensions and two pattern, i.e. reciprocal space, dimensions. The umbrella term for such techniques is *4D STEM* [266], but the term 4D STEM is most often used where a larger convergence angle is employed. SED is by convention used for the case where a nanometre-sized probe with relatively small convergence angle is used, and this technique is also referred to as *scanning electron nanodiffraction* [32]. Further, PED can be combined with scanning to give SPED [267]. S(P)ED combined with (semi-)automatic data analysis strategies have several applications, the main being phase and orientation [268, 269] and strain [270, 271] mapping.

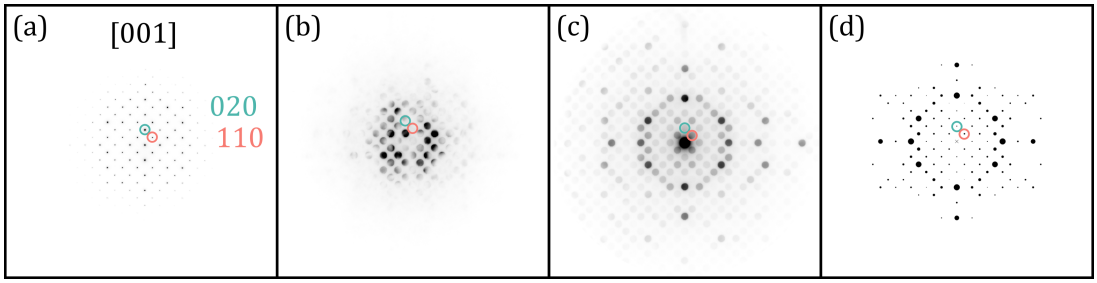

Figure 3.13: Patterns from an α_c-Al-(Fe,Mn)-Si crystal oriented to zone axis [001] obtained by **(a)** SAED, **(b)** NBD, **(c)** PED and **(d)** kinematical diffraction simulation using the software *Recipro* [257]. The contrast has been inverted.

In SPED, a precession angle of $\phi \lesssim 1°$ is typically employed. For higher precession angles it becomes increasingly challenging to maintain a focused probe due to aberrations. The probe size approaches $d = 4C_s\phi^2\alpha$ for high ϕ, where C_s is the spherical aberration coefficient of the probe forming lens [258, 260]. Experiments have shown that for low precession angles, $\phi \lesssim 1°$, noise in the scan system may limit the spatial resolution [260]. In addition, the inclination of the beam contributes to a conical blur depending on the specimen thickness. The acquisition time at each probe position should be synchronised with the precession frequency, so that each PED pattern is recorded over an integer number, n, of full precession cycles. The precession frequency is in practice often a set number, e.g. 100 Hz, so that a set exposure time should be employed, e.g. $10n$ ms.

The first commercial solution for a SPED setup included an externally mounted *charge coupled device* (CCD) camera that imaged the fluorescent phosphor viewing screen of the microscope [267, 269]. This setup comes with inherent challenges. Since the camera views the screen at an inclination, geometric distortions must be corrected. Also, the fluorescence emitted does not decay instantaneously, which gives *afterglow*, that is residual intensity in each subsequent pattern originating from the previous pattern. Recently, advances have been made in electron detection [272]. *Direct electron detectors* have become available that eliminate the challenges mentioned and that offer significant improvements of the dynamical range, acquisition speed and sensitivity. In this work, SPED was performed in **Paper I** using a setup with a externally mounted CCD camera, while in **Paper II**, SED data were acquired over a range of specimen tilt conditions on a direct electron detector.

3.4 Scanning (precession) electron diffraction data analysis

S(P)ED datasets are in general large 4D datasets with two scan dimensions, x and y, and two pattern dimensions, k_x and k_y. A typical dataset can contain for instance 512×512 scan pixels that each are associated with a single diffraction pattern with size 256×256 pixels. Due to the large dataset size, development of (semi-)automatic analysis routines is key to enable assessment of local crystallography by for instance phase, orientation and strain mapping. In S(P)ED data acquired from a nanocrystalline specimen, the data frequently include some patterns that contain scattering from multiple crystals sampled along the beam trajectory. Both the high number of patterns and the overlap of crystals pose challenges to several analysis routines aiming at phase and orientation mapping, which can be mediated by *nanocrystal*

segmentation. The aim of nanocrystal segmentation is to isolate the signal from individual crystals. Several strategies can be employed for nanocrystal segmentation in S(P)ED data, including strategies based on decomposition and virtual imaging, which both can be performed without any prior knowledge on the crystal structures contained within the specimen. In general, virtual imaging is an intuitive and simple method for visualisation of a S(P)ED dataset, where diffraction contrast images of the scanned area are produced. Further, decomposition can be advantageous in many cases, both to inspect the underlying patterns in the data and to reduce the dimensionality or noise. These two methods were used in **Papers I** and **II**.

This section gives an introduction to visualisation and decomposition methods that were used in this work, and the methods discussed are illustrated with the MgO SPED dataset used in **Paper I**. The analysis and visualisation were mainly done using *pyxem* [273], an open-source Python library for crystallographic electron microscopy, that builds on *hyperspy* [274], which again builds on scientific Python packages, particularly *scikit-image* [275] and *scikit-learn* [276].

3.4.1 Virtual imaging

Virtual imaging is performed using a 4D S(P)ED dataset by integrating the intensity within a window, referred to as a *virtual aperture*, with respect to probe position, to form diffraction contrast images of the scanned area. Virtual imaging offers a quick and intuitive way of visualising a S(P)ED dataset, that is similar to conventional BF and DF imaging. However, in SPED data, precession leads to averaging of thickness variations, small mistilts and bending, as opposed to in conventional imaging and virtual imaging in SED data. Since the virtual imaging can be done after acquisition, full flexibility is retained. In principle, an integration window of any size, shape and position can be used. Most often, virtual imaging is performed with a circular or an annular virtual aperture covering the central beam or diffracted beams to form *virtual (A)BF* (V(A)BF) or *virtual* (A)DF (V(A)DF) images, respectively.

Figure 3.14 shows a VBF image, a VADF image and two VDF images created from the SPED dataset of partly overlapping MgO nanoparticles. Note that the direct beam is saturated in the dataset, so that the contrast in the VBF image in (a) appears nearly inverted compared to a standard VBF image. For comparison, a VADF image is shown in (b). In Figure 3.14(e), the circular integration windows used are plotted on top of a pattern showing the maximum intensity from the whole scan area with respect to detector position. The pattern in (e) provides a simple way of visualising all the strong intensity spots. Figures 3.14(c) and (d) display two VDF images formed from two Bragg peaks corresponding to two individual MgO nanoparticles. Note that afterglow is prominent in the fast scan direction that is from left to right in the images.

Before performing virtual imaging, it is crucial to ensure that the central beam is stationary across all the recorded patterns, and applying a central beam alignment routine is most often a mandatory pre-processing step. As an optional pre-processing step, background subtraction can be done. After background subtraction, the diffraction spots are more prominent, and sharper VDF images can be obtained. Moreover, VDF imaging can be used for nanocrystal segmentation in S(P)ED data. This strategy was reported by Meng and Zuo in [277], and involves creation of VDF images for each of the Bragg spots contained within the dataset. All the VDF images are compared to each other in order to identify images showing the same crystal. The VDF images corresponding to the same crystal are then added to form a single merged VDF image from that crystal, and a corresponding diffraction pattern is made from the corresponding Bragg spots used to create the VDF image. This strategy was adapted and tested on

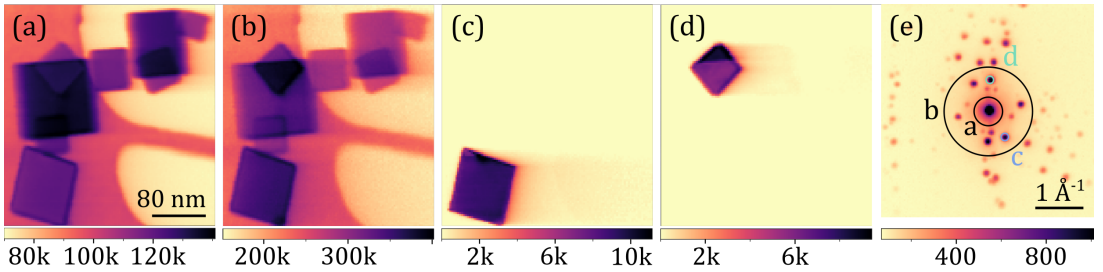

Figure 3.14: SPED of partly overlapping MgO nanoparticles. **(a)** VBF image, **(b)** VADF image, **(c)** and **(d)** VDF images. **(e)** Maximum intensity from the whole dataset per detector position, where the inner black circle illustrates the virtual aperture used in (a), the annulus between the inner and outer black circles illustrates that used in (b), and the blue and turquoise circles those used in (c) and (d), respectively. Note that each image has its designated colour bar.

the MgO dataset in **Paper I**.

3.4.2 Decomposition

S(P)ED datasets are most often big datasets containing $\lesssim$500k individual patterns. However, one dataset from a nanocrystalline specimen typically samples $10-1$k crystals and thus contains a much lower number of unique patterns. Decomposition of the dataset into its unique patterns can provide substantial dimensionality reduction, and it can also be used to unmix signals and to perform denoising. There are several *data matrix decomposition* methods, also called *factorisation* methods, and this section focuses on a few central linear decomposition methods applied in this work. The methods mentioned here can each be considered to be a type of *unsupervised machine learning*, since they learn the underlying patterns in the data without any prior knowledge.

Singular value decomposition

The first step in decomposition is to represent the 4D S(P)ED dataset as a $n \times m$ data matrix that takes the form: $\boldsymbol{X} = [\vec{x}_1 \vec{x}_2 ... \vec{x}_m]$, where each of the m individual patterns are stored as a $n \times 1$ column vector, $\vec{x}_i$.

Singular value decomposition (SVD) is a unique matrix decomposition given by: $\boldsymbol{X} = \boldsymbol{U}\boldsymbol{\Sigma}\boldsymbol{V}^T$ [278], where $\boldsymbol{U}$ and $\boldsymbol{V}$ are unitary matrices with dimensions $n \times n$ and $m \times m$, respectively, while $\boldsymbol{\Sigma}$ is a $n \times m$ diagonal matrix. The columns of $\boldsymbol{U}$ and $\boldsymbol{V}$ are the eigenvectors of $\boldsymbol{X}\boldsymbol{X}^T$ and $\boldsymbol{X}^T\boldsymbol{X}$, respectively [278], and they thus provide an orthonormal basis for the column and the row space of $\boldsymbol{X}$. They are known as the left and right *singular vectors* of $\boldsymbol{X}$, respectively. The diagonal elements in $\boldsymbol{\Sigma}$ are referred to as the *singular values*, and these are ordered from largest to smallest. The singular values are the positive square roots of the eigenvalues of $\boldsymbol{X}^T\boldsymbol{X}$, which are correlated to the amount of variance in the data that is accounted for by the corresponding eigenvectors. The number of non-zero singular values gives the *rank*, r, of $\boldsymbol{X}$.

The SVD can be truncated after a chosen number of singular values to reduce the rank. This is known as a *truncated SVD* and is given by: $\tilde{\boldsymbol{X}} = \tilde{\boldsymbol{U}}\tilde{\boldsymbol{\Sigma}}\tilde{\boldsymbol{V}}^T$ [278]. The matrices $\tilde{\boldsymbol{U}}$ and $\tilde{\boldsymbol{V}}$ contain the first r columns of $\boldsymbol{U}$ and $\boldsymbol{V}$, respectively. If the rank r is larger than or equal to the number of non-zero singular values, the truncated SVD is exact, so that: $\tilde{\boldsymbol{X}} = \boldsymbol{X}$. On the other hand, if the

rank is less than the number of non-zero singular values, the truncated SVD gives an optimal compressed approximation to the data matrix: $\tilde{\boldsymbol{X}} \approx \boldsymbol{X}$. The truncated SVD can be written as a minimisation of $||\boldsymbol{X} - \tilde{\boldsymbol{X}}||_F$, where $||\boldsymbol{Z}||_F$ is the Frobenius norm: $\sqrt{\sum_{i=1}^{m}\sum_{j=1}^{n}|z_{ij}|^2}$ [278]. The truncated SVD is an approximate factorisation of the data matrix and can also be written: $\tilde{\boldsymbol{X}} = \boldsymbol{W}\boldsymbol{H}$. In the Python repository *hyperspy* [274], $\boldsymbol{W} = \tilde{\boldsymbol{U}}\tilde{\boldsymbol{\Sigma}}$ is referred to as the *factor*, and $\boldsymbol{H} = \tilde{\boldsymbol{V}}^T$ is referred to as the *loading* matrix.

Determination of the rank to employ is a major concern in the use of the truncated SVD. In making this decision, it is common to investigate a plot known as the *scree plot*, which shows the fraction of total variance in the dataset that each component accounts for. One strategy for determining the rank is to use the number which leads to capture of a pre-determined amount of the variance, e.g. 90% [278]. Another strategy is to identify the point where the variance captured is relatively low and starts to decay slowly, so that the plot takes the form of an elbow or knee. Assuming that signals amount for the highest variance in the data while noise accounts for low variance, the "elbow point" then defines the transition between the values that are interpreted as signal and as noise. Often a clear transition can be found in for instance spectroscopy datasets, where typically a rank of $\sim$10 is sufficient according to this strategy [279]. However, many factors typically contribute to the intensity in the recorded patterns in S(P)ED data, which means that a high number of values often must be used. If the data is not aligned, the data redundancy cannot be exploited in the same way and a much higher rank must be used to appropriately express the data [278]. For S(P)ED data, alignment is done by centring the direct beam, which is a much used pre-processing step.

In electron microscopy and spectroscopy, counting type detectors are used in general, and for these the noise is dominated by counting statistics which is Poissonian in nature [279]. This means that the uncertainty increases with the number of counts, and the noise is non-uniform. It has been reported that for such data, the decomposition results can be improved by weighting the data to normalise Poisson noise prior to decomposition [279]. For noise normalised spectroscopy data, the decomposition results were reported to be more robust and easier to interpret, and the selection of rank was more obvious [279]. In the implementation in *hyperspy* it is possible to do this step before decomposition, and that was done in this work for application of either of the decomposition methods.

SVD of the SPED dataset of MgO nanoparticles is presented in Figure 3.15. This particular dataset is relatively small and contains 109×114 scan pixels, each having a pattern of size 142×142 pixels, in total $\sim$250M pixels. The scree plot is shown in (a), and the elbow point was identified to be at index number 10, as marked in the figure. Figures 3.15(a) and (b) display the first five resulting factors and loadings, respectively. A circular area surrounding and including the central beam was masked out prior to SVD, and this area appears white in Figure 3.15(b). The masking excluded the intensity variations occurring within this area from influencing the SVD results, and this was done since the direct beam was saturated and not of interest here. The zero index factor and loading strongly resemble the average of the dataset calculated over the signal (pattern) and navigation (scan) axes, respectively. They represent the single singular vector pair that best describes the data. Further, it can be seen that the SVD factors and loadings contain both positive and negative values. This is especially prominent for the factor with index 1 and the loading with index 4. Thus, individual SVD factors and loadings cannot be directly physically interpreted.

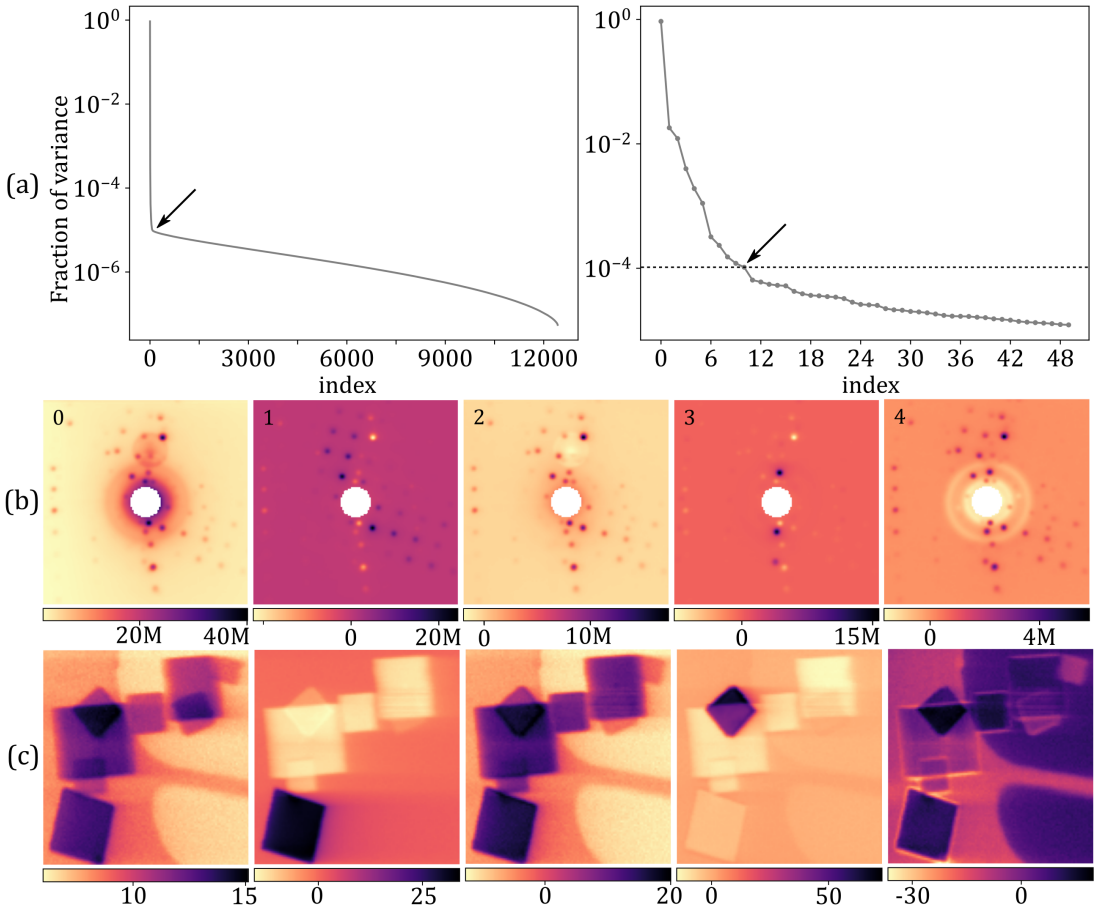

Figure 3.15: SVD of the SPED dataset of partly overlapping MgO nanoparticles. **(a)** Scree plot showing the fraction of total variance accounted for versus singular value index. The plot to the right shows the scree plot over a smaller index interval, and the horizontal dashed line corresponds to index number 10 that was identified to represent the transition between signal and noise. This point is marked by arrows in (a) and (b). The first five **(b)** factors and **(c)** their corresponding loadings.

Principal component analysis

Principal component analysis (PCA) uses the statistical distribution in the large data matrix to find a low dimensional coordinate system in which the data can be re-expressed [278]. The dataset is interpreted statistically by assuming that the important features in the data are contained in the directions with the largest variance. The goal in PCA is to find the basis which re-expresses the data along the axes of highest variance and which is a linear combination of the original basis [280]. These directions are known as the *principal directions* or principal axes, and they are constrained to be orthogonal to each other. The data matrix projected onto a principal direction is a *principal component*. By finding these, the dominant patterns that best describe the data can be found, and noise can be filtered out.

PCA works by finding a normalised direction in m-dimensional space where the variance in the data is maximised, and this direction becomes the first principal component [280]. Next, a direction that is orthogonal to the first and that maximises the remaining variance is sought, which becomes the second principal component, and so on. In practice, the principal components can be found by calculating the eigen-decomposition of the covariance matrix, $(\boldsymbol{X} - \bar{\boldsymbol{X}})(\boldsymbol{X} - \bar{\boldsymbol{X}})^T/(n-1)$, where $\bar{\boldsymbol{X}}$ is the row-wise mean of $\boldsymbol{X}$. Then the principal directions are the eigenvectors. Subtraction of the mean is often referred to as *mean-centring* of the data. For S(P)ED data the mean corresponds to the average diffraction pattern. From the previous section it is known that calculation of the SVD results in the eigenvectors and eigenvalues of $\boldsymbol{X}\boldsymbol{X}^T$. Thus, the principal components can be found by calculating the SVD of a mean subtracted dataset, and PCA is one of the central uses of SVD [278].

Results from PCA of the SPED dataset of partly overlapping MgO nanoparticles are shown in Figure 3.16. The scree plot is shown in Figure 3.16(a), which is highly similar to the scree plot in the SVD case, except that the elbow point occurs at index 9 instead of index 10 and that the last component accounts for zero of the variance. The PCA factors and loadings are displayed in Figures 3.16(a) and (b), respectively. The factor with index zero no longer resemble the average pattern but resemble the maximum pattern in Figure 3.14(e). As in the case of SVD, the factors and loadings resulting from PCA take both positive and negative values and cannot be directly physically interpreted.

Non-negative matrix factorisation

Non-negative matrix factorisation (NMF) is the approximation of a non-negative data matrix, $\boldsymbol{X}$, as a product of two non-negative factors, $\boldsymbol{W}$ and $\boldsymbol{H}$, for a selected rank r, so that $\boldsymbol{X} \approx \boldsymbol{W}\boldsymbol{H}$ [281, 282]. Here $\boldsymbol{W}$ and $\boldsymbol{H}$ are matrices with dimensions $n \times r$ and $r \times m$, respectively. The method is similar to truncated SVD and PCA in that all three methods construct lower dimension approximations to the original data matrix. The important difference is that NMF imposes non-negativity constraints, in contrast to the orthogonality constraints in PCA. In PCA the data can in general be reconstructed by a linear superposition of both positive and negative components, while NMF only allows additive combinations. The constraint in NMF is in line with the intuitive understanding that a whole is constructed by the addition of parts, and NMF in general gives individual components that are more physically meaningful [281].

In practice, NMF is implemented as an iteration over the minimisation of the error made in the approximation, where the error is typically calculated by the Frobenius norm. The constraints imposed by NMF are not sufficient to result in a unique solution for the matrices $\boldsymbol{W}$ and $\boldsymbol{H}$, and the iterative scheme used can in some cases converge slowly and end at a local minimum. Due to the iterative nature, the initialisation is important [282]. *Hyperspy* uses the implementation in *scikit-learn*, which relays on a non-negative double SVD initialisation. This initialisation method has been shown to provide a rapid reduction of the approximation error and does not depend on any randomisation [282]. Simply put, the method is based on computing the SVD and extracting the positive values. In practice, SVD is often also used to generate a scree plot that serves as a guide in the determination of the rank to use for NMF. The rank, i.e. the number of components, that is chosen plays a huge role on the resulting individual NMF components.

NMF of the SPED dataset of MgO nanoparticles is shown in Figure 3.17. Since only additive combinations are allowed in NMF, the zero index loading and factor here resemble an average background, in contrast to SVD where the first loading and factor resembled an average of the

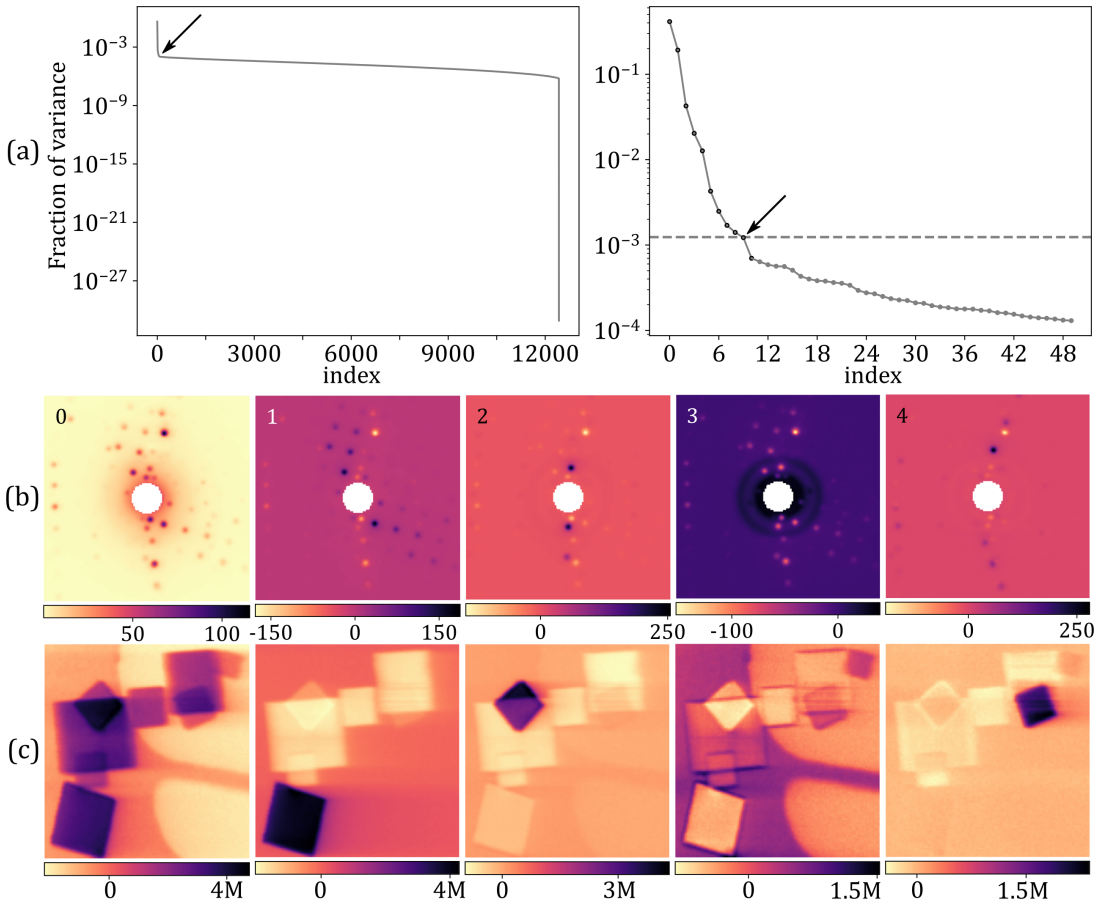

Figure 3.16: PCA of the SPED dataset of partly overlapping MgO cubes. **(a)** Scree plot showing the fraction of total variance accounted for versus singular value index. The plot to the right shows the scree plot over a smaller index interval, and the horizontal dashed line corresponds to index number 9 that was identified to represent the elbow point. The first five **(b)** factors and **(c)** corresponding loadings.

whole dataset. "Pseudo-subtractive" intensities can though be seen, which are intensities that are apparently missing. The factor and loadings with index 1 and 3 resemble the diffraction patterns and VDF images of the two nanoparticles imaged in Figures 3.14(c) and (d). This demonstrates that NMF components are easier to interpret than SVD and PCA components, and that NMF can be used to segment the signals from individual crystals. NMF has previously been used for nanocrystal segmentation [283, 284], and it is applied and further discussed in **Papers I** and **II**.

3.5 Spectroscopy in transmission electron microscopes

Spectroscopy techniques within EM concerns the measurement of intensity versus energy of transmitted electrons or photons emitted following inelastic scattering of the incoming electrons by the specimen. There are three main spectroscopy techniques that can be performed

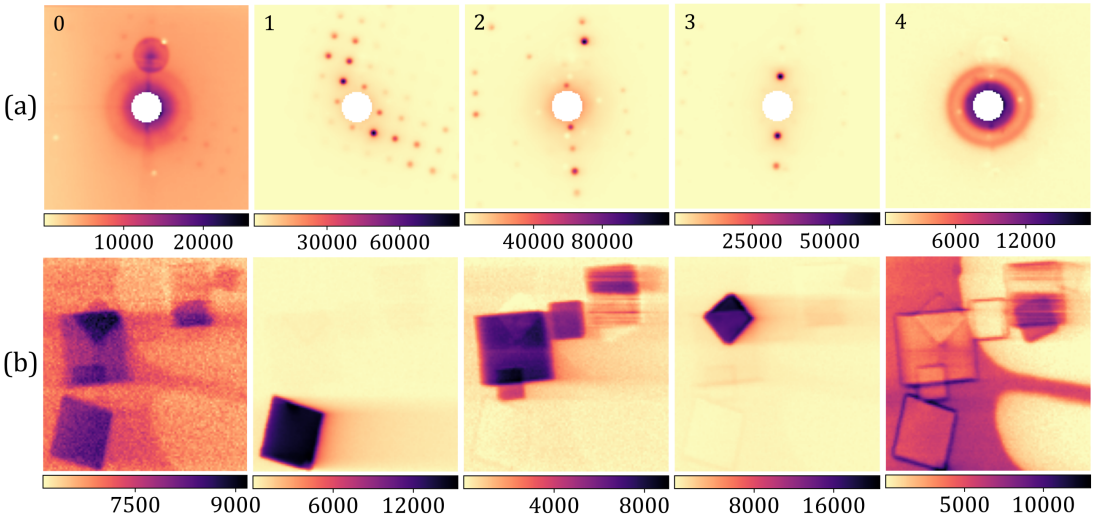

Figure 3.17: NMF of the SPED dataset of MgO with 11 components. The first five **(b)** factors and **(c)** loadings.

in EM: *electron energy loss spectroscopy* (EELS) which concerns measuring the intensity versus energy of the transmitted electrons, *X-ray energy dispersive spectroscopy* (EDS) which involves measuring the emitted X-rays, and cathodoluminescence which measures emitted light [33]. Such techniques can provide information on the chemical composition, electronic structure and thickness of the specimen. The energy spectrum can be acquired from one spatial position, or energy spectra can be recorded at each probe position as the beam is scanned over a ROI, as is routinely done in STEM mode, which enables acquisition of maps with high spatial resolution. For EELS, the energy spectrum can alternatively be recorded as a function of scattering vector, which is commonly referred to as momentum-transfer or angle-resolved EELS [33]. In many cases, spectroscopy techniques offer complimentary information to that provided by imaging and diffraction techniques, and together they enable a complete characterisation of the specimen at the nanometre scale. Primarily EDS was used in this work to assess the chemical composition of the specimens. The following section introduces this technique as used within a transmission electron microscope and describes the data analysis used in this work.

3.5.1 X-ray energy dispersive spectroscopy

In EM, two kinds of X-rays are produced as the incident beam hits the specimen: characteristic X-rays and bremssthrahlung X-rays. An incident electron can decelerate if it enters the charge field of the nucleus, so that it suffers energy loss and produces *bremsstrahlung X-rays*, i.e. braking radiation [33]. In the X-ray spectrum, the bremsstrahlung X-rays can be seen as a continuous background up to the incident energy. If an incident beam electron transfers more than a critical amount of energy, referred to as the ionisation energy, to an inner shell electron, the electron is ejected and the atom is left in an excited state. The atom tends to revert to its ground state by filling the hole with an outer shell electron. In doing so, it emits either a *characteristic X-ray* or an Auger electron with an energy given by the energy differ-

ence between the excited and the ground state. There is a competition between emission of characteristic X-rays and Auger electrons, and the probability ratio between them is referred to as the *fluorescence yield*. The fluorescence yield decreases fast as the atomic number decreases, which means that low Z atoms favour the Auger process [33]. Characteristic X-rays are labelled according to the electron shell of the hole being filled, for which K, L, M, ... are used in ascending order from the innermost shell. Also, the difference in electron shell levels between the hole and the electron that fills the hole is indicated by a Greek letter, α, β, γ... in ascending order. For instance, a Kα X-ray line results from a K shell hole being filled by an electron from the L shell. Optionally, both K, L, M, ... and α, β, γ, ... can be given subscripts denoting their subshells. Each characteristic X-ray has an energy specific to the element and the electron transition. The various X-ray lines from one element have different relative intensities, referred to as weights, according to how probable the corresponding electron transition is. The α lines are generally the most intense.

An EDS spectrum presents X-ray counts versus energy, and it can be acquired either in TEM or STEM mode. In STEM, EDS is routinely collected pixel-by-pixel together with STEM images, and EELS can also be acquired simultaneously in some microscopes, which has several advantages. The X-rays are collected by a designated detector, usually made of Si, placed above the specimen. The energy resolution of Si detectors generally increases, i.e. becomes poorer, as the energy increases, and it is typically 140 eV measured for the Mn Kα line [33]. Since the X-rays are emitted in all directions, the collection angle of the detector is an important parameter that determines the amount of generated X-rays that can be detected. In some cases, parts of the specimen or the holder can limit the effective collection angle by shadowing, and in that case the count rate can be increased by tilting the specimen towards the detector. Further, *spurious X-rays*, often referred to as *stray radiation*, from the specimen grid or microscope instrumentation can be visible in the spectrum. For instance, in this work the specimens were most often fastened to half grids made from Cu, which resulted in Cu X-ray lines in the recorded spectra. Moreover, if a Si detector is used, an incoming X-ray can loose energy by generating a Si Kα X-ray, with an energy of 1.74 keV, in the detector. Consequently, Si *escape peaks* can be found at $E - 1.74$ keV, where E is the energy of a major X-ray line in the spectrum. Also, incoming photons may produce an *internal fluorescence peak* by generating Si Kα X-rays within the detector. Another possible artefact is *sum peaks*, which result from two photons hitting the detector at the same time, so that they are recorded as one count with an energy equal to the sum of their energies. Sum peaks are not particularly common, and they are seen only for the major peaks in a spectrum, if the detector dead time and the count rate are high.

The main use of an X-ray spectrum is to quantify the chemical composition of a specific region in the specimen. By quantifying an EDS map spectrum-by-spectrum, maps of the scanned area can be produced that show the relative composition with respect to probe position. In the field of TEM, the well-known *Cliff-Lorimer method* has been used routinely for several decades. The Cliff-Lorimer equation states [33, 285]:

$$\frac{C_A}{C_B} = k_{AB}\frac{I_A}{I_B}, \tag{3.21}$$

where C_A and C_B are the weight percents of elements A and B, and I_A and I_B are the integrated intensities of their characteristic lines above the background, respectively. k_{AB} is a sensitivity factor that depends on the specific microscope setup and analysis conditions, and it is not a constant even though it in practice often is used as that. The k-factors can be determined either by experiments or by theoretical calculations. Experimental determination is generally

tedious and often requires several thin film standards with known compositions. Theoretical calculation, on the other hand, is quick and simple, but can give significant systematic errors ($\sim$20 at.%) [285]. Further, the Cliff-Lorimer method assumes that the specimen is thin enough so that absorption and fluorescence can be neglected. If significant, absorption lowers the X-ray counts of specific lines, which can compromise the quantification. Low energy X-rays are much more likely to be absorbed than the higher energy ones. To limit absorption, the specimen can be made thinner at the expense of lower count rate. Alternatively, absorption correction can be done by incorporating an additional absorption term into the Cliff-Lorimer equation, but that requires known specimen thickness and density [285]. The *ζ-factor method* offers a more sophisticated alternative to the Cliff-Lorimer method, as it incorporates additional parameters such as the probe current and dose [285]. This method has several advantages, including built-in absorption correction, determination of the thickness, and that pure standards can be used for calibration. Still, the Cliff-Lorimer method has remained the standard method, mainly due to its simplicity and availability in commercial software.

Data analysis

To perform quantification based on an X-ray spectrum it is necessary to extract the integrated intensities of the individual X-ray lines above the background. Several approaches can be used for this purpose, including the use of integration windows and model fitting [33]. In this work, EDS maps were mainly acquired in STEM mode, and the data analysis performed was largely the same for all maps. The analysis and visualisation was done in *hyperspy* [274], an open-source Python repository mentioned also in Section 3.4. The data analysis routine employed is explained in the following by using a dataset from **Paper II** as example. First, the sum spectrum was inspected to determine the X-ray lines present, as shown in Figure 3.18.

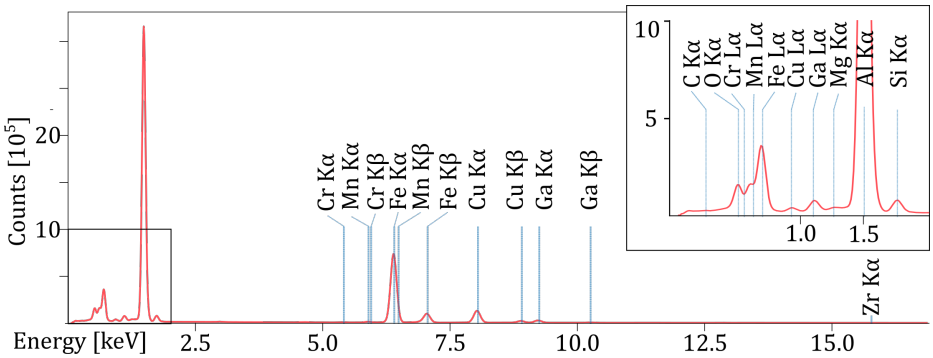

Figure 3.18: A sum spectrum from an EDS map acquired in STEM mode from an Al-steel interface region in **Paper II**. The X-ray lines identified are marked.

The dataset was binned in the spatial axes to achieve at least $\sim 1-2$k total counts per individual spectrum. A model was created that comprised one Gaussian per X-ray line identified, and a polynomial of order six to model the X-ray background. Then, the dataset was model fitted spectrum-by-spectrum with the amplitude of each Gaussian as a free parameter. Examples of individual spectra and their model fits are shown in Figure 3.19(a). The intensities of the Kα-lines were extracted from the model fitted Gaussians and used for relative quantification by the Cliff-Lorimer method, for which calculated k-factors were used. From the quantification results, element maps showing the relative composition in at.% were created.

To quantify single phase regions, masks were created by thresholding selected maps, optionally followed by hole filling and removal of small disconnected segments. Figure 3.19(b) shows one Al, Fe and Si map, and a mask created by thresholding of the Si map. The raw spectra inside the mask were summed, and the sum spectrum was model fitted and quantified, using the same approach as explained above. It must be noted that in this work, phase overlap, use of un-calibrated k-factors and lack of absorption correction, made it impossible to obtain an accurate composition by the method used. Therefore, the resulting compositions should only be regarded as semi-quantitative estimates.

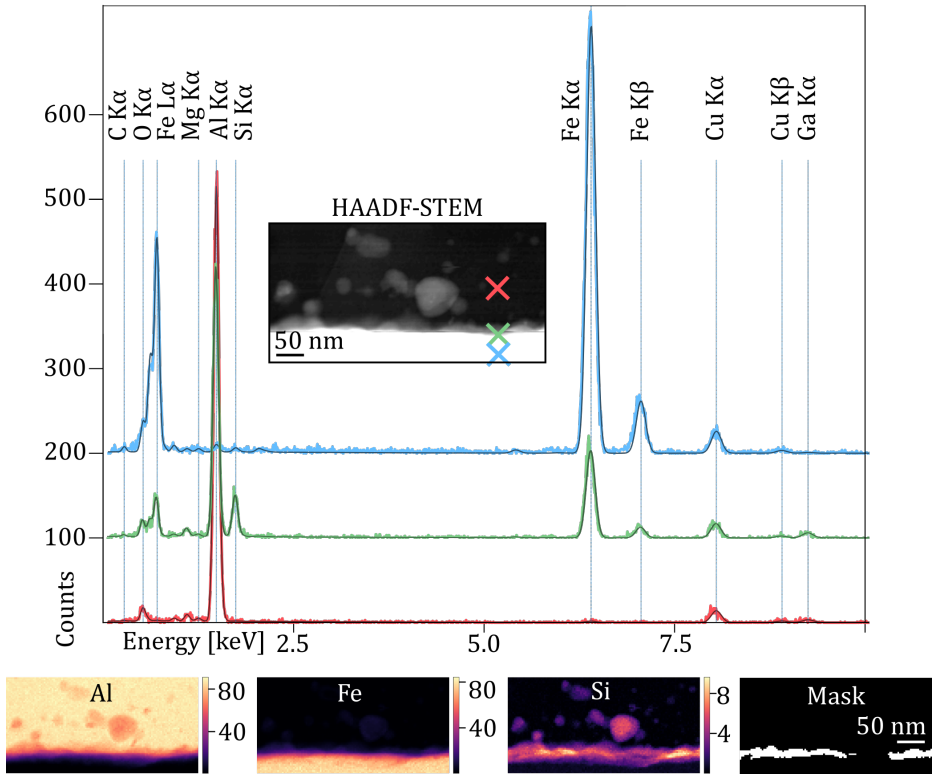

Figure 3.19: Model fitting and element maps based on an EDS map acquired in STEM mode from an Al-steel interface region in **Paper II**. **(a)** Three individual spectra with their model fit (darker colour), and a HAADF-STEM image of the mapped area where the locations of the individual spectra are marked. For clarity, the green and blue spectra were shifted upwards along the y-axis relative to the red curve. **(b)** Al, Fe and Si element maps showing the relative composition in at.%, and a mask created by thresholding of the Si map. The maps were made based on spectrum-by-spectrum model fitting.

3.6 Focused ion beam

A *focused ion beam* (FIB) is a finely focused beam of ions, usually Ga^+. The FIB is produced from an ion source within a FIB instrument, which is equipped with a set of electrostatic lenses, apertures and coils to control the beam [286]. Several events can occur when energetic ions hit a specimen, including: production of *ion-induced secondary electrons* that can be used for

imaging, *sputtering* or *milling* which is removal of atoms from the specimen, *ion implantation* which is ions being incorporated into the specimen, and changes in the specimen surface structure such as amorphisation [253]. Further, material can be deposited in the area illuminated by the FIB if a reactive precursor gas is injected locally. Parts of the precursor gas becomes fixed onto the specimen where it is struck by the FIB, which is commonly used to deposit material such as platinum (Pt) and C. Consequently, the FIB itself has four main basic functions: milling, deposition, implantation and imaging [286]. A FIB column is often combined with a SEM column to yield a *dual-beam FIB-SEM* instrument, so that the FIB can be used for nanostructuring at the same time as the electron beam can be used for damage-free imaging. In addition, electron beam deposition can also be done with injection of a precursor gas. FIB-SEM systems are versatile and have several applications such as destructive tomography by "slice and view", and lamellae preparation. Standard FIB lift-out techniques have been developed for preparation of electron transparent lamellae for TEM. To enable straightforward lamella preparation, the FIB-SEM system is integrated with a lift-out needle that can be moved in three dimensions with a precision on the nanoscale. In this work, dual-beam FIB-SEM instruments were used for preparation of site-specific cross-sections from interface regions. The following lists the main steps in the lamella preparation routine used here, which was mainly developed by P.E. Vullum.

3.6.1 Fabrication of electron transparent lamellae

The first step in preparation of a lamella was deposition of a protection layer ($\sim 12 \times 2 \times 1\ \mu m$) by electron beam and then by ion beam deposition. For most of the specimens prepared in this work, C was deposited, but Pt can also be used. Subsequently, large trenches ($\sim 22 \times 15 \times 12$) were milled out on both of the long sides of the deposited protection layer, and a smaller trench was created on one of the short sides, as shown in Figure 3.20(a). The next step was undercutting of the cross-section so that it became free from the rest of the specimen, except that it remained attached along one of the short sides. Afterwards, it was time to insert the lift-out needle and to move it so that it almost touched the free short side of the cross-section. The needle was fastened to the cross-section by depositing C with the ion beam. The bridge that secured the cross-section to the rest of the specimen could then be removed by milling. This situation is shown in Figure 3.20(b). Subsequently, the specimen could be lifted out and fastened to a half grid for TEM specimens, as shown in Figures 3.20(c) and (d). The lift-out needle was afterwards cut off by milling. The final step consisted of thinning of the lamella, so that it reached electron transparency. Coarse thinning was done first at 30 kV, before final fine polishing was performed at 5 kV and optionally at 2 kV. The final polishing was done to limit the depth of ion beam surface damage, which typically results in an amorphous surface layer with notable ion implantation. Lastly, the lift-out needle was cut off by milling.

For the Al-steel specimens fabricated in this work, the best quality lamellae were achieved when thinning was performed with the ion beam directed normal to the Al-steel interface. In this way, thickness variations arising from the difference in milling rates in Al and steel could be limited. This could be done if the lift-out needle was fastened to the very edge of the lamella and then rotated $180°$, before fastening it to the specimen grid and depositing new protection layers on the side facing the ion beam. Figure 3.20(e) shows a lamella directly after standard lift-out, while (f) shows the same lamella after rotating the lift-out needle $180°$. For comparison, two lamellae from **Paper II** that were thinned with the ion beam directed nearly parallel to the interface and normal to the interface are shown in Figure 3.21.

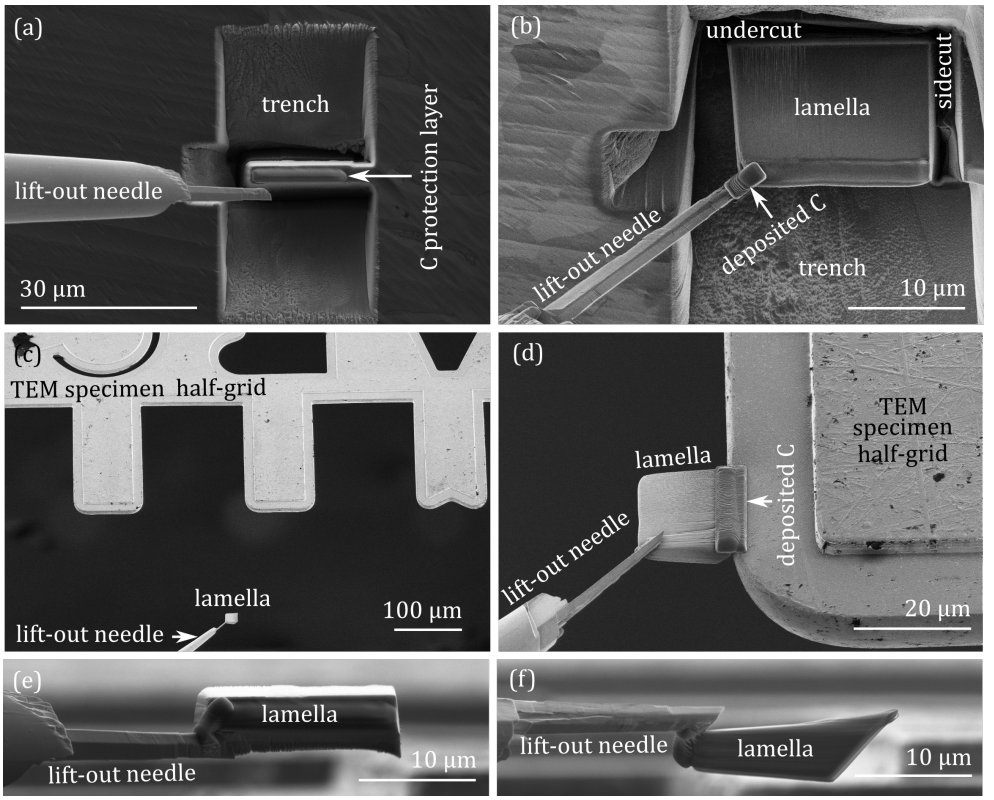

Figure 3.20: SE SEM images taken during FIB lift-out of a lamella from **Paper V**. **(a)** A rectangular C protection layer was deposited, trenches were milled out and the lift-out needle was inserted. **(b)** The lift-out needle was fastened to the lamella by C deposition, and the lamella was cut free from the specimen via an undercut and a sidecut. The image was taken at 7° tilt relative to (a). **(c)** The lift-out needle was used to transfer the lamella to a TEM specimen half-grid. **(d)** The lamella was fastened to the grid by C deposition. The lamella **(e)** directly after standard lift-out and **(f)** after rotating the lift-out needle 180°.

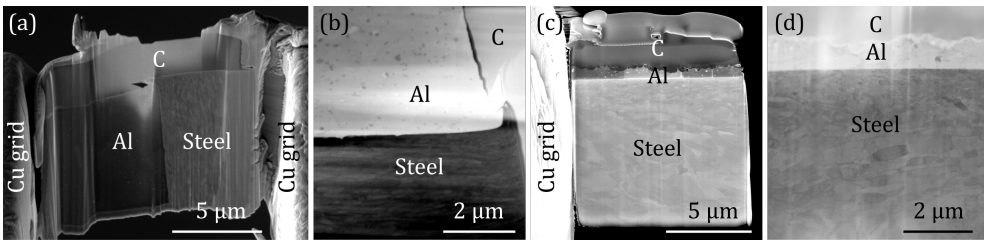

Figure 3.21: Images of two TEM lamellae from **Paper II**: **(a)** and **(c)** SE SEM images and **(b)** and **(d)** BF-STEM images. The lamella shown in **(a)** and **(b)** was thinned with the ion beam directed nearly parallel to the Al-steel interface, while that in **(c)** and **(b)** was thinned normal to the interface.

Part II

Research

Chapter 4

Experimental

This chapter gives a brief overview over the Al alloys, steels and electron microscopes used in this thesis. The first section lists the chemical compositions of the various Al alloys and steels, while the second lists the electron microscopes used.

Material selection in this thesis

Five different 6082 Al alloys were used in **Papers II, IV, A** and **F**, and a 5754 Al alloy was used as BM and a 4020 Al alloy as FM in **Paper V**. The nominal compositions of the Al alloys used are given in Table 4.1. In addition, commercially pure Al 1080 (99.8 wt.% Al) was used in **Papers IV** and **B**. In **Paper II**, a structural steel S355 was used as BM, and a second structural steel S355 was used as BM in **Paper F**. A galvanised dual-phase steel HCT590 was used in **Paper III**, but the galvanised surface layer on the steel BM was removed by machining to prevent any influence of the Zn-layer. Stainless steel 316L was used in **Paper IV**. In **Paper V**, a hot dip galvanised steel DX51D Z275 was used, and the composition of the steel plate was determined by optical emission spectroscopy. An IF steel was used in **Paper A**. The nominal compositions of the steels used are given in Table 4.2.

Microscopes used in this thesis

In this work, TEM was mainly performed using microscopes within the TEM Gemini Centre at NTNU in Trondheim. Two microscopes, a JEOL JEM-2100F and a JEOL ARM200CF, were used for TEM characterisation in most of the papers. The JEOL ARM200CF has a cold field emission electron gun and is fitted with CEOS spherical aberration correctors in both the probe and image forming optics. EDS maps were collected in STEM mode using the ARM200CF, which is equipped with a $100\,\mathrm{mm}^2$ Centurio EDS detector. The JEM-2100F has a field emission electron gun and is equipped with a Nanomegas ASTAR system that enables SPED. This microscope was used for acquiring SAED patterns in various papers, the PED patterns in **Papers IV** and **F**, and the SPED dataset in **Paper I**. Using the JEM-2100F, the zone-axis SAED and PED patterns were acquired on an Ultrascan CCD camera fitted to the microscope, while the SPED data were collected using an externally mounted Stingray camera. In addition, for **Paper II**, SED data were acquired using a JEOL ARM300F (Diamond Light Source, UK) fitted with JEOL spherical aberration correctors in both the probe and image forming optics. The microscope was equipped with a Merlin Medipix direct electron detector which was used to collect the SED data. For fabrication of the TEM lamellae characterised in **Papers II-V**, **A-B**, and **E-F**, the FIB-SEM instruments within NTNU NanoLab were used, including a FEI Helios G2 and a FEI Helios G4. The Helios G4 is integrated with an EasyLift lift-out needle system. These instruments were also used to collect SEM images. In addition, several SE and BSE SEM images were captured using a Zeiss Gemini Ultra 55 and a Hitachi SU6600 microscope. The Hitachi SU6600 was employed in **Paper V** to collect EBSD data using a NORDIF UF-1100 EBSD detector. These scanning electron microscopes have field emission electron guns.

Table 4.1: Nominal compositions in wt.% of the Al alloys used in this thesis. The papers in which the alloys were used, and the welding methods employed, are also listed.

Paper	Method	BM/FM	Alloy	Si	Mg	Mn	Fe	Cr	Zr	Ti	Cu	Zn	B	Other
II,F	HYB	FM	6082	1.11	0.61	0.51	0.2	0.14	0.13	0.043	0.002	-	0.006	0.029
II	HYB	BM	6082	0.9	0.8	0.42	0.45	0.02	-	0.02	0.06	0.05	-	0.02
F	HYB	BM	6082	1.21	0.71	0.59	0.24	0.04	-	0.020	0.060	0.04	-	0.150
IV	RB	BM	6082	0.9	1.00	0.58	0.29	-	-	0.04	0.01	-	-	-
A	RB	BM	6082	1.04	0.67	0.54	0.2	-	-	-	0.003	-	-	-
V	CMT	BM	5754	0.091	2.82	0.182	0.312	0.119	-	0.015	0.017	0.005	-	-
V	CMT	FM	4020	2.5-3.5	$\leq$0.01	0.8-1.2	$\leq$0.20	$\leq$0.01	-	$\lesssim$0.0005	$\lesssim$0.03	$\lesssim$0.01	-	

Table 4.2: Nominal compositions in wt.% of the steels used in this thesis. The papers in which the alloys were used, and the welding methods employed, are also listed. For DX51D, the composition was determined by optical emission spectroscopy. For HCT590, the specification states that the sum of Cr and Mo is $\leq$1.40* and the sum of Nb and Ti is $\leq$0.15**.

Paper	Method	Alloy	Cr	Ni	Mn	Mo	Al	Si	C	V	Ti	S	Co	Cu	B	P
II	HYB	S355	0.05	0.05	0.69	0.009	0.040	0.02	0.067	0.008	0.001	0.005	-	0.028	0.0001	0.010
F	HYB	S355	0.02	0.04	0.46	-	0.041	0.01	0.056	-	-	0.003	-	0.01	0.0001	0.009
IV,B	RB	S355	0.03	0.03	0.62	-	0.05	0.01	0.07	-	-	-	-	-	-	-
IV	RB	316L	16.65	10.06	1.3	2.025	-	0.34	0.022	-	-	-	-	-	-	-
III	HYB	HCT590	$\leq$1.40*	-	$\leq$2.50	$\leq$1.40*	0.015-1.50	$\leq$0.75	$\leq$0.15	-	$\leq$0.15**	$\leq$0.015	-	-	-	$\leq$0.04
V	CMT	DX51D	0.016	0.036	0.22	0.003	0.04	0.005	0.045	-	-	0.004	0.012	0.008	-	0.004
A	RB	IF	-	-	0.15	-	0.04	0.01	0.002	-	-	-	-	-	-	-

Chapter 5

Results

This chapter gives a short summary of the results presented in each manuscript included in this thesis. The idea behind the studies and the relation between them are also discussed. For each manuscript the results are illustrated with $1-2$ figures that convey the main findings seen from the perspective of the objectives of this work. The full papers are included in Part III.

Paper I

Nanocrystal segmentation in scanning precession electron diffraction data

Paper I is related to challenges in the assessment of the crystal structures of overlapping nanocrystals. It relates back to the main aim of characterising the IMP layers formed at Al-steel interfaces during welding, since the IMP layers in sound joints often have thicknesses on the nanoscale. In particular, the IMP layer characterised in **Paper II** posed extra challenges since it was only a few tens of nanometres thick. Due to the small size of the individual crystals and since there are no orientation relationships between the small IMP crystals in the formed layer with either steel or Al, it is near impossible to acquire conventional NBD patterns by tilting the specimen manually to reach a zone axis. With S(P)ED it is possible to scan a nanometre-sized probe across the interface region to collect numerous patterns from the IMP layer crystals in various orientations, and then to index (some of) the patterns using more or less automatic indexation routines. An issue that must be overcome with such an approach is that S(P)ED data from nanocrystalline materials often contain some patterns where diffraction from multiple crystals is prominent. To solve this issue, nanocrystal segmentation can be performed so that the location of each individual crystal within the scan region, and its diffraction signal, can be isolated from the rest. This also reduces data dimensionality significantly.

Paper I presents two approaches to nanocrystal segmentation, the first based on VDF imaging [277] (Section 3.4.1) and the second on NMF [281] (Section 3.4.2). The two methods were applied to a SPED dataset of partly overlapping MgO nanoparticles, which was also used for demonstration purposes in Section 3.4. Figure 5.1 shows a VADF image and average patterns from each of the nine crystals sampled. It can be seen that the crystals named P3, P4, P6 and P8, excited the same diffraction conditions, and this dataset therefore emphasised situations where neither of the two methods could distinguish all crystals. To overcome this issue, a watershed segmentation routine was included in both methods, which allowed segmentation of crystals that had highly similar diffraction patterns but were sufficiently distinguishable in diffraction contrast images.

The results from both methods are presented in Figure 5.2. Note that the NMF-based method also gave a result for the small particle P2 and additional segments corresponding to particle P8. These were however neglected in the figure shown here, to allow for a more straightforward comparison between the results from the two methods. From Figure 5.2, it can be seen that

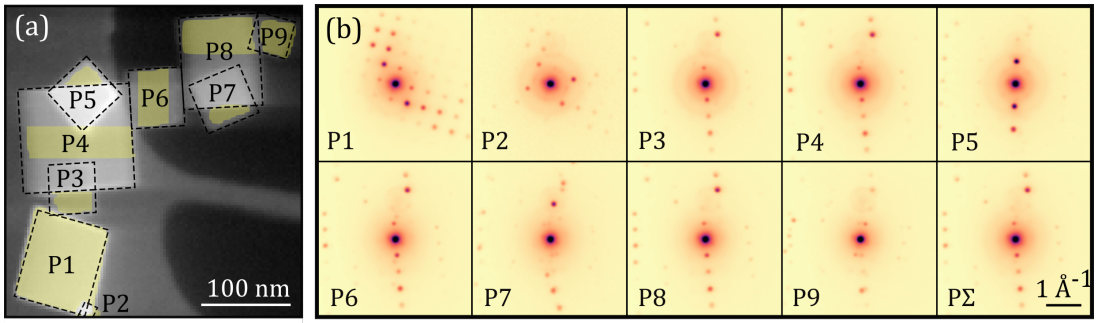

Figure 5.1: The demonstration SPED dataset of MgO nanoparticles. **(a)** VADF image showing nine MgO particles (grey), labelled P1–P9, lying on top of a holey amorphous carbon film (dark grey) or over vacuum (black). The outlines of the MgO particles are indicated by dashed rectangles. **(b)** Sum of PED patterns within the yellow areas in (a). PΣ is the sum of P3, P4, P6 and P8.

it was possible using either of the two methods to segment most of the crystals and to create representative diffraction patterns from each. However, it can be seen that particles P3 and P4 in Figure 5.1 were not separated from each other in Figure 5.2. This highlights a special case for which the segmentation was incomplete, since these two crystals shared the same orientation and also overlapped significantly in real space.

In **Paper I** the two methods were compared, and each method demonstrated advantages and disadvantages. The VDF imaging-based segmentation neglected weak peaks and crystals yielding a relatively small number of peaks, since the segmentation required that each crystal to be segmented exhibited several detectable diffraction peaks. Moreover, incorrect segmentation happened for some VDF images due to the watershed image segmentation approach used, so that some diffraction vectors were lacking in the patterns from the VDF imaging-based method. The NMF-based approach yielded patterns that included information regarding the intensity distribution associated with individual diffraction vectors, which is information not included in the patterns from the other method. Also, the NMF-based segmentation approach required minimal pre-processing and was more sensitive in the sense that no major intensity contribution was neglected and in that subtle intensity variations could be identified. Lastly, the patterns from both methods (Figure 5.2) were compared to the sum patterns (Figure 5.1). Notable intensity differences near diffraction peaks were seen for both of the explored methods, which indicated that neither could necessarily be used quantitatively.

The main conclusion of **Paper I** was that even though they have limitations, both VDF imaging- and NMF-based segmentation can be valuable tools for nanocrystal segmentation in SPED data, as long as they are used with care and artefacts are considered critically. The workflows associated with **Paper I** are available open-source, so that they can be used as a starting point for further developments, and they were applied also in **Paper II**.

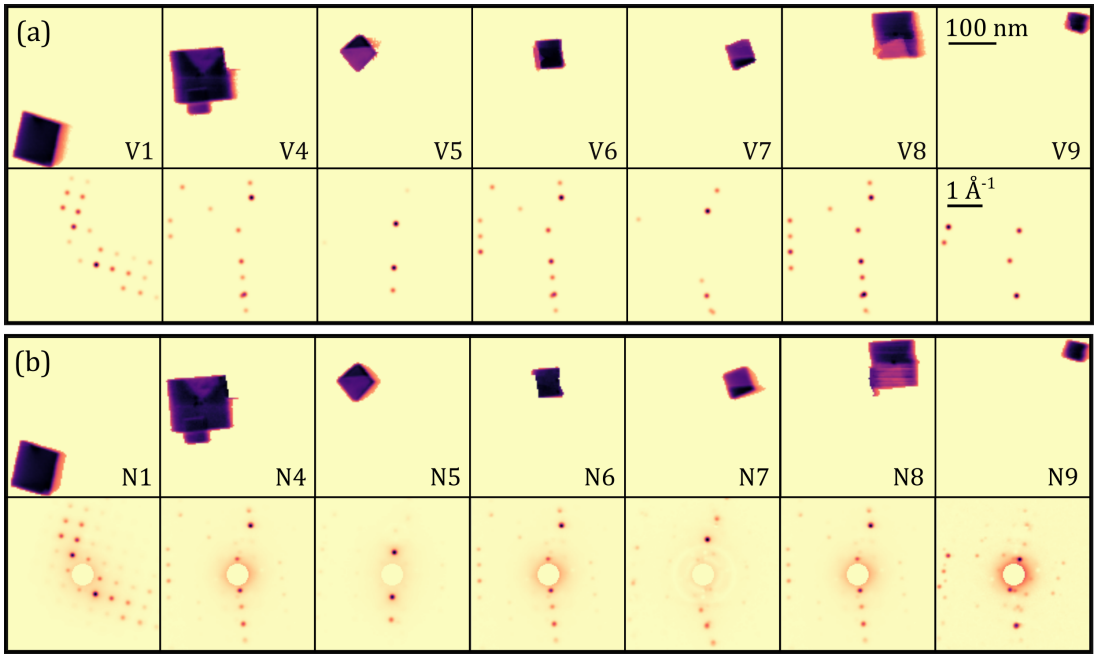

Figure 5.2: Results from nanocrystal segmentation using a **(a)** VDF imaging-based and **(b)** NMF-based approach. In both (a) and (b) the top rows show real space images of the individual crystals after segmentation, and the bottom rows show their corresponding representative diffraction patterns. Note that to allow a clear comparison, some of the results from the NMF-based approach were excluded.

Paper II

Microstructural and mechanical characterisation of a second generation hybrid metal extrusion & bonding aluminium-steel butt joint

The underlying motivation for **Paper II** was to assess the prospect of performing Al-steel joining by the HYB method (Section 2.3.4). HYB had previously been used to produce Al-steel joints, but the first generation joints suffered from lack of bonding and showed relatively low UTS values ($104 - 140$ MPa) [103, 104]. Effort was made to improve the HYB joints, and after improvements of the setup and development of the pin geometry, a second generation of HYB Al-steel joints could be produced that showed significantly improved mechanical properties.

Paper II presents mechanical and microstructural characterisation of a second generation HYB butt joint of Al alloy 6082 and structural steel S355 as BMs and Al alloy 6082 as FM. A schematic drawing of the joint is shown in Figure 5.3(a). The mechanical characterisation showed that a HAZ extended 13.5 mm into Al, while steel was unaffected. Tensile testing was performed, and the UTS was measured to be in the range of $184 - 220$ MPa, which corresponded to $60 - 72$% joint efficiency. The strain development during tensile testing was analysed using digital image correlation, which revealed that the fracture propagated from root cracks and ran close to the Al-steel interface. The fracture surfaces were imaged by SEM, which re-

vealed that the steel fracture surface was covered by a significant amount of residual Al. This was seen especially in regions that experienced higher pressure during joining, i.e. near the middle and around the bottom half of the Al-steel interface as seen in cross-section. SEM of polished cross-sections revealed signs of microscale mechanical interlocking and showed that the Al-steel interface was rough, again especially on the bottom half. Lamellae were made by FIB from selected regions along the Al-steel interface, as shown in Figure 5.3(b). The lamellae were characterised by TEM, and mainly three different interface appearances were seen; straight, rough with some deformed and intermixed Al-steel regions, and slightly wavy, as shown in Figure 5.3(c).

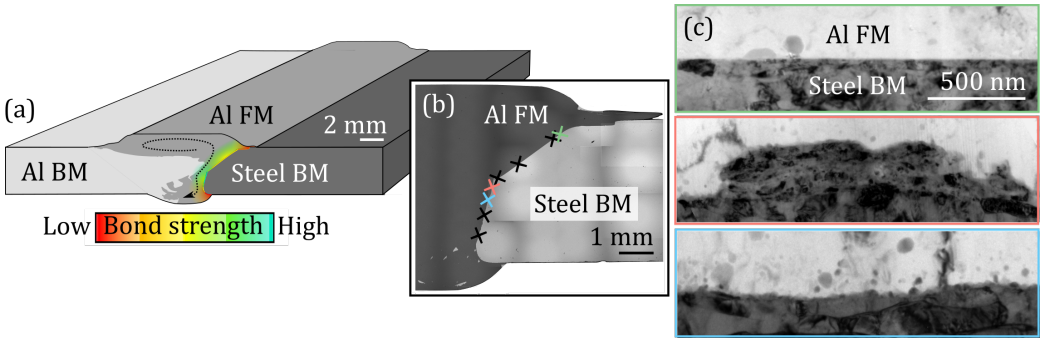

Figure 5.3: **(a)** Simplified illustration of the investigated Al-steel joint. The flow of FM during joining is illustrated by a black curved arrow, and the Al-steel interface is coloured according to low (red) to high (turquoise) relative bond strength. **(b)** BSE SEM image showing the locations from where TEM lamellae were lifted out by FIB. **(c)** BF-TEM images of three lamellae showing a straight, rough, and slightly wavy interface appearance, from top to bottom.

The TEM characterisation further revealed an interfacial discontinuous $10-50$ nm thick IMP layer. Quantification by EDS indicated that the layer was mainly composed of Al, Fe and Si with a relative Si content of $\gtrsim 9$ at.%. Example Al, Fe and Si maps from an interface region are shown in Figure 5.4(a). In addition, some regions showed ~ 5 nm thick interfacial oxide layers mainly composed of Al, O and Mg with minor amounts of Si. At some locations an IMP layer was seen to grow preferentially through gaps in the oxide layer. To assess the crystal structures of the Al-Fe-Si crystals, SED data were recorded in a tilt series to increase the probability of recording data from some crystals oriented close to zone axes. This was done since it was not possible to acquire conventional zone-axis patterns, as explained previously under **Paper I**. The dataset acquired at zero tilt was subjected to VDF imaging-based segmentation, and Figure 5.4(b) shows a VBF image onto which the resulting individual crystal images have been superimposed with various colours. Further, individual patterns were selected manually from the SED data based on that they seemed to be close to zone axes, and these were subjected to NMF-based segmentation to reduce intensity associated with background or overlap. Indexing of the selected patterns indicated that the IMP layer was polycrystalline with nanocrystals of the cubic α_c phase. An example pattern is shown in Figure 5.4(c). However, several patterns were recorded that did not fit α_c, and further investigations are needed to fully understand the formed Al-Fe-Si layer. In total, the considerable bond strength of the investigated Al-steel HYB joint was attributed to a combination of microscale mechanical interlocking and a nanoscale interfacial Al-Fe-Si layer.

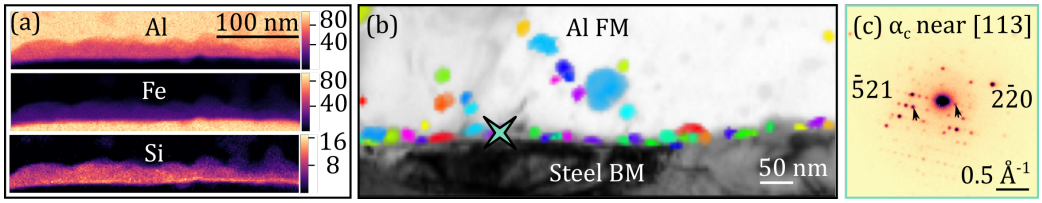

Figure 5.4: TEM characterisation of the lamella lifted out from the region marked by blue in Figure 5.3(b). **(a)** Element maps, showing at.%, based on STEM-EDS from an interface region. **(b)** VBF image with overlayed coloured VDF image segments from some individual crystals in the IMP layer and some dispersoids in the Al FM. **(c)** A pattern indexed with respect to the α_c phase close to [113], from the location marked by a four-armed star in (b).

Paper III

Microstructure and tensile properties of a multi-material aluminium-copper-steel-titanium butt joint made in one pass by hybrid metal extrusion & bonding

After the fabrication of the second generation of Al-steel HYB joints characterised in **Paper II**, additional improvements were done concerning the geometry of the pin, which enabled fabrication of a third generation. These showed tensile strengths surpassing the second generation, and one such joint was characterised in **Paper F**. The rising success of the Al-steel joints sparked the ambition to fabricate multi-metal HYB joints, and as hoped, it was possible to fabricate also four-metal joints in one pass using HYB.

Paper III presents an Al-Cu-steel-Ti HYB butt joint that was made in one pass. The goal was to explore the prospect of multi-material HYB joining through mechanical and microstructural characterisation of the four-metal joint. In this joint, Cu was placed on the RS and Ti on the AS, while steel was placed below. All the three BMs were bonded to the Al FM, but not to each other. An optical micrograph of the joint cross-section is shown in Figure 5.5(a). Each of the three dissimilar metal interface regions were characterised individually by SEM and TEM, and by tensile testing of miniature specimens (⌀1 mm). For the Al-Cu interface, TEM showed a ~ 0.5 µm thick IMP layer, and EDS and SAED showed that the layer consisted mainly of the phases θ-Al_2Cu and γ_1-Al_4Cu_9, as shown in Figure 5.5(b). Although Al and Cu were bonded in some areas, several regions suffered from lack of bonding and porosity, which caused the Al-Cu specimens to fracture during machining of tensile specimens. When it comes to the Al-Ti interface, TEM revealed a ~ 50 nm thick Al-Ti-Si IMP layer, together with some intermixed swirl-like regions a few microns thick, as shown in Figure 5.5(c). During miniature tensile testing, ductile fracture ran through Al, and the UTS was 306 ± 2 MPa. The good quality achieved for the Al-Ti bond was believed to mainly result from the low process temperature and the favourable placement of Ti on the AS. At the Al-steel interface, an IMP layer was seen that showed local thickness variations, together with several microscale intermixed Al-steel regions. TEM characterisation of the IMP layer in the middle of the joint showed a $\sim 0.1 - 1$ µm thick Al-Fe-Si(-Cu) layer, as shown in Figure 5.6. During miniature tensile testing, brittle fracture ran near the interface, and the average UTS was 257 ± 35 MPa. Altogether, this work established, through examination of an Al-Cu-steel-Ti demonstration joint, that the HYB method shows great potential for dissimilar metal joining involving bonding of Al to Cu, steel and Ti.

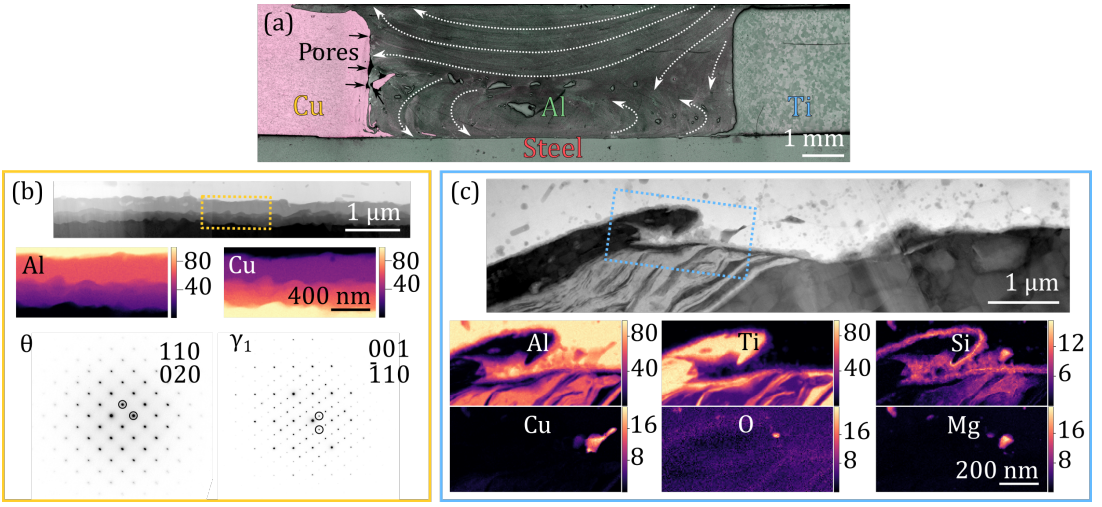

Figure 5.5: **(a)** Optical micrograph of a leached cross-section, where the Al FM flow pattern is indicated by white lines. BF-STEM overview images and element maps, showing at.%, based on STEM-EDS from an interface region from the **(b)** Al-Cu and **(c)** Al-Ti interface regions. In addition, (b) shows SAED patterns indexed with respect to the phase θ-Al_2Cu oriented to zone axis [001], and the phase γ_1-Al_4Cu_9 oriented to zone axis [110]. Note that for clarity, only the element maps of the major elements constituting the IMP layers are shown.

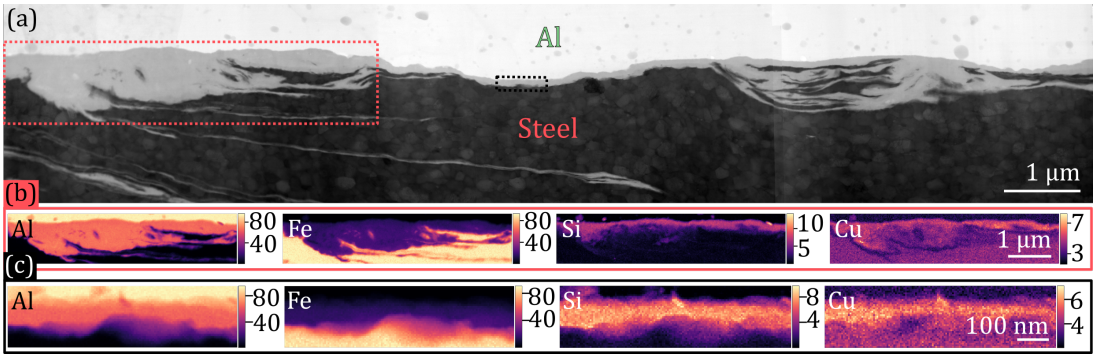

Figure 5.6: **(a)** BF-STEM overview image of an Al-steel interface region in a lamella lifted out from the middle of the weld. **(b)** and **(c)** element maps, showing at.%, based on STEM-EDS from the interface region outlined in red and black in (a), respectively. Note that for clarity, only the element maps of the major elements constituting the IMP layers are shown.

Paper IV

On intermetallic phases formed during interdiffusion between aluminium alloys and stainless steel

Paper IV is more oriented towards fundamental research than the previous two papers on HYB joints, and it adresses specifically the formation and growth of IMPs at Al-steel interfaces. The growth of brittle IMP layers is one of the biggest challenges in Al-steel joinining, as has been repeated throughout this thesis, and it depends on both the thermo-mechanical processing history and the presence of alloying elements. Although much literature exists on the influence of alloying elements, especially Si, see Section 2.4.4, better understanding of the combined effect of alloying elements found in widely used Al alloys and stainless steels is still needed. **Paper IV** focuses on the IMP layers formed in roll bonded composites of Al alloy 6082 and stainless steel 316L after interdiffusion at temperatures in the range of $450 - 550$°C.

By SEM it was found that notable growth of the IMP layers happened first at temperatures $\gtrsim$500°C, and four distinct IMP layers (Layers $1 - 4$) were identified. For heat treatments conducted at 550°C, one layer (Layer 1) could be seen after 2 min, two layers after 10 min and four layers after 60 min. Layer 1 formed first, was continuous and created an irregular interface to Al (Figure 5.7(a)), before the discontinous Layer 2 formed at the Al-Layer 1 interface (Figure 5.7(b)). Subsequently, Layer 3 that consisted of elongated grains, and Layer 4 that consisted of numerous small grains, formed along the steel-Layer 1 interface (Figure 5.7(c)).

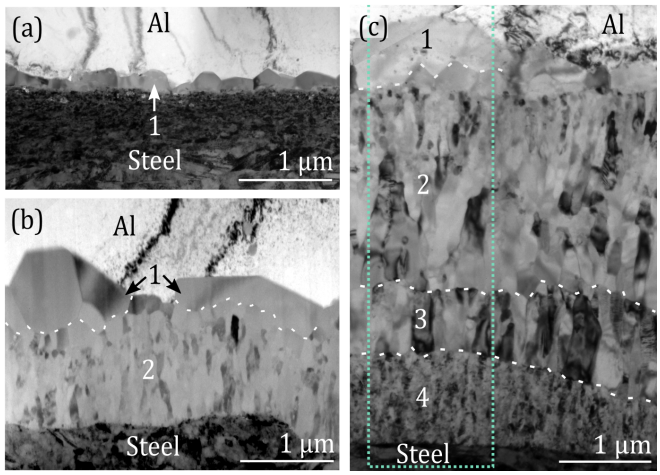

Figure 5.7: BF-TEM images of 6082-316L composites heat treated at **(a)** 500°C for 3 h, 550°C for **(b)** 10 min and **(c)** 60 min. Four IMP layers (Layers $1-4$) were identified, and some of the boundaries between them are indicated with dashed white lines.

To identify the predominant phases that constituted the four IMP layers, their chemical compositions were assessed by EDS and their crystal structures by NBD with precession, as shown in Figure 5.8. Figures 5.8(a) and (b) show a HAADF-STEM image and element maps, respectively, of the 550°C 60 min specimen, while Figure 5.8(c) shows a diffraction pattern from each of the phases identified. Based on this it was reasoned that Layer 1 consisted mainly of α_c-$Al_{15}(Fe,Cr,Mn)_3Si_2$, Layer 2 of τ_1-$FeNiAl_9$, Layer 3 of θ-Fe_4Al_{13} and τ_{11}-Al_5Fe_2Si, and Layer 4 of η-Fe_2Al_5. Both Layers 3 and 4 contained notable amounts or Cr, Ni and Si, and Layer 4 contained nanoscale precipitates rich in Cr and Si or Ni.

Based on nanoindentation, the layers could be arranged after ascending hardness as: Layer 2

< Layer 3 < Layer 1 < Layer 4. According to *density functional theory* (DFT) calculations, the identified IMPs could be arranged after increasing brittleness as: $\tau_{11} < \eta < \alpha_c$-Al-(Fe,Cr)-Si < $\theta < \tau_1$. Miniature tensile testing confirmed that heat treatments leading to thicker IMP layers containing brittle phases reduced the bond strength and caused brittle interfacial fracture. The highest tensile strengths were obtained for the specimens containing only a thin α_c layer (Layer 1).

When it comes to the growth of the total IMP layer, the growth rate was drastically reduced for the 6082-316L composites compared to a low alloyed 1080-S355 reference combination. The reduction demonstrated the strong influence of alloying elements in both Al and steel, and it was mainly believed to result from slower Fe diffusion through the first formed α_c phase relative to the diffusion through the θ and η phases in the 1080-S355 joints.

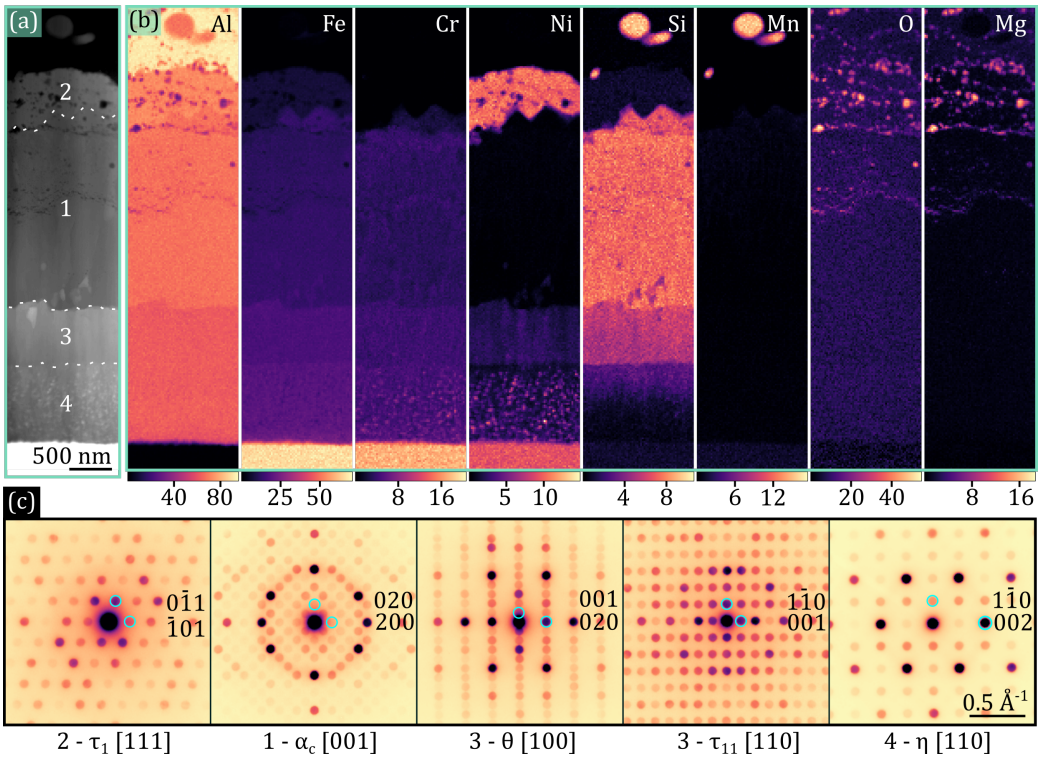

Figure 5.8: TEM characterisation of heat treated 6082-316L composites. STEM-EDS results from the region highlighted in Figure 5.7(c): **(a)** HAADF-STEM image and **(b)** element maps showing at.%. **(c)** One diffraction pattern from each of the phases identified within the IMP layer: τ_1-$FeNiAl_9$ (Layer 2), α_c-$Al_{15}(Fe,Cr,Mn)_3Si_2$ (Layer 1), θ-Fe_4Al_{13} (Layer 3), τ_{11}-Al_5Fe_2Si (Layer 3) and η-Fe_2Al_5 (Layer 4).

Paper V

On interfacial intermetallic phase layers in cold metal transfer aluminium-steel joints made with an Al-Si-Mn alloy as filler material

The three previous papers, **Papers II-IV**, all focused on the formation and growth of IMP layers in Al-steel joints made with solid state welding techniques. **Paper V** however, focused on the IMP layers formed in Al-steel joints made with the welding method CMT, which is a fusion welding method, see Section 2.3.5. Note that **Paper V** contains unpublished work and focuses on reporting the methods used and the results obtained rather than giving an extensive discussion. The joints were made with a 4020 Al alloy containing notable amounts of Si and Mn as FM. These alloying elements were also contained within the Al FM used in **Papers II** and **III**, so that the main differences between the joints are the welding method and the amounts of alloying elements. TEM showed that the formed ~ 2.5 µm thick IMP layer consisted of coarse polyhedral α_c-Al-(Fe,Mn)-Si, elongated θ-Fe_4Al_{13} and equiaxed η-Fe_2Al_5 grains, arranged from the Al to the steel side. The morphologies can be seen in Figure 5.9(a), while (b) and (c) show element maps based on STEM-EDS and SAED patterns that were used in the identification of the IMPs. By EBSD it was observed that the η phase grains showed a tendency to be preferentially oriented with the [001]-direction normal to the Al-steel interface. The results reported agree with findings reported in literature [121].

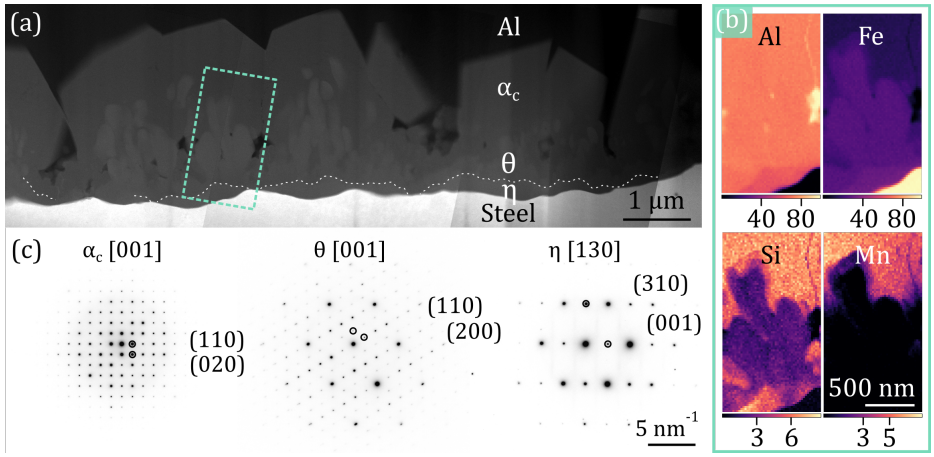

Figure 5.9: TEM of the interfacial IMP layer in a CMT joint. **(a)** HAADF-STEM image of the interface region. Parts of the phase boundaries between the η and the θ phase layers are highlighted with dashed white lines. **(b)** Element maps based on STEM EDS that show the relative compositions in at.% of the major constituents Al, Fe, Si and Mn. **(c)** SAED patterns of the three IMPs identified; α_c-Al-(Fe,Mn)-Si, θ-Fe_4Al_{13}, and η-Fe_2Al_5.

Chapter 6

Discussion and outlook

This chapter gives an overall discussion of the interrelated findings reported in the individual papers included in this thesis. Three main topics are discussed that are recurrent in several of the papers. First, the main topic is a comparison of the HYB Al-steel joints that have been characterised in this work, which concerns **Papers II, III** and **F**. Second, the IMP phase sequence identified in the various Al-steel joints that have been characterised, is reviewed and examined in a more general sense by looking at the findings reported in **Papers II, III, IV, V, A** and **F** as a whole. Third, the characterisation of nanoscale IMP layers with TEM techniques will be discussed, in particular by considering future possibilities for characterisation by employing S(P)ED and *in-situ* heating, which relates primarily to **Papers I** and **II**. This section also includes unpublished results from various *in-situ* heating studies conducted as a part of this thesis.

6.1 Hybrid metal extrusion & bonding aluminium-steel joints

HYB was one of the main welding techniques employed for Al-steel joining in this work. Thus, it is natural to compare the various Al-steel HYB joints that have been characterised in terms of the underlying bonding mechanisms and bond strengths, which is the aim of this section. Primarily this discussion concerns **Papers II** and **III**. To allow a complete discussion, the characterisation of the first generation joints, which is reported by Abbatinali et al. in [103] and Berto et al. in [104], and the characterisation of the third generation joints reported in **Paper F**, are also included in the discussions.

The HYB method was originally developed for Al-Al welding, and it is therefore beneficial to review the principles of Al-Al welding before Al-steel HYB welding is discussed (see also Section 2.3.4). Typically during HYB Al-Al welding, the FM flows down along the BM on the AS, while the BM on the RS is pushed towards the AS [96]. The sidewalls on the BMs are believed to be deformed sufficiently so that their native surface oxide layers break up and metallurgical bonds form [92]. The flow of FM during an Al-Al HYB welding trial is drawn schematically in Figure 6.1(a), based on the findings reported by Sandnes et al. in [96]. Naturally, there are variations in the material flow depending on the material combination and joint configuration.

The first generation

The first generation of HYB Al-steel joints showed that HYB held potential for Al-steel joining. The first generation joints were characterised in a proof-of-concept study [103, 104]. The joint was examined by SEM, but no IMP layer was identified, and the specimen was not studied further by TEM. An illustration of the joint and flow of the FM is shown in Figure 6.1(b), which was drawn based on optical micrographs presented in [103, 104]. During tensile testing, fracture ran along the approximate Al BM-FM interface in the bottom part and along the Al-steel interface in the top part. This demonstrated the potential for Al-steel welding by HYB, but the lack of bonding along the top part was detrimental. Consequently, the joint showed relatively

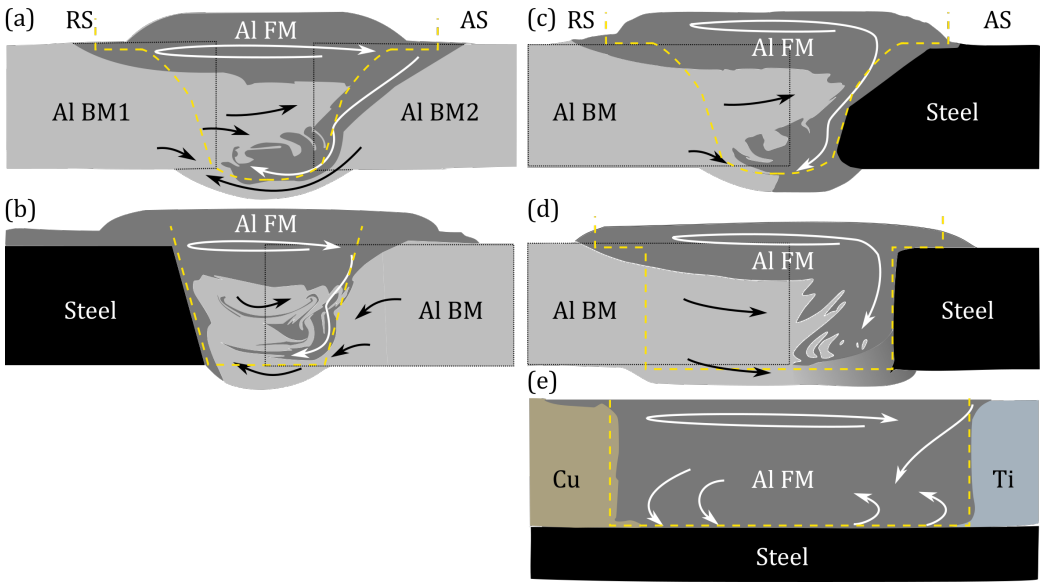

Figure 6.1: Schematic drawings of various HYB joints. **(a)** Al-Al joint drawn based on micrographs presented in [96]. **(b)** First generation Al-steel joint drawn based on the micrographs in [103, 104]. **(c)** Second generation Al-steel joint drawn based on the micrographs in **Paper II**. **(d)** Third generation Al-steel joint drawn based on the micrographs in **Paper F**. **(d)** Multi-material Al-Cu-steel-Ti joint drawn based on the micrographs in **Paper III**. Al BMs are shown in light grey, Al FM in dark grey and steel BMs in black. In (d), the Cu BM and Ti BM are shown in yellow and blue, respectively. The flow of Al FM and Al BM are indicated schematically by arrows, and the outline of the steel pin is indicated with dashed yellow lines.

low UTS values ($104 - 140$ MPa) [103, 104]. Referring back to the material flow typical in Al-Al welding, the BM on the RS is supposed to be deformed by the pin and forced to flow towards the centre of the weld groove. Hence, the most ductile material should be placed on the RS to allow material flow, as is also common practice in FSW [25, 78]. Further, the BM placed on the AS first comes into contact with freshly extruded Al FM and experiences higher pressure than the BM on the RS, which was expected to give better Al-steel bonding.

The second generation — Paper II

After the lessons learned with the first generation, the setup and pin geometry were improved and a second generation of Al-steel HYB joints was created that showed improved mechanical properties. In the second generation, the steel BM was placed on the AS and the steel sidewall was machined to obtain a bevelled edge with half Y-form that fitted the geometry of the improved pin. These changes led to a significant increase in UTS, and the second generation had an UTS measured to 197 ± 15 MPa, as reported in **Paper II**. A schematic of the joint cross-section is shown in Figure 6.1(c), where the flow of the FM is highlighted. It can be seen that there was larger downflow of Al FM along the steel BM in the second than in the first generation joint.

By SEM and TEM characterisation it was concluded that bonding was achieved by a combin-

ation of microscale mechanical interlocking and formation of a discontinuous Al-Fe-Si layer. SEM studies showed that a portion of the interface was rough with small hook-like features. The increase in surface area achieved for a rough interface is typically beneficial for bond strength. Also, features where one material has flowed into protrusions on the opposing material surface, indicate microscale mechanical interlocking, that may contribute to the bond strength [287]. TEM showed a discontinuous Al-Fe-Si IMP layer with thickness in the range of $10 - 50$ nm, which in the context of Al-steel welding is thin and can be expected to not deteriorate the bond strength significantly, as a thicker IMP layer would [23, 24, 237, 238]. TEM lamellae extracted from the top region showed predominantly no or only limited signs of interlocking and IMP layers, and less residual Al was found on the steel fracture surface in this region. On the other hand, the bottom half showed a large amount of residual Al on the steel fracture surface, and lamellae lifted out from this region showed more signs of interlocking and nanoscale IMP layers. The characterisation indicated that stronger Al-steel bonding was achieved for interface regions that displayed both a nanoscale IMP layer and more interlocking features. It was believed that the low HYB process temperature and the favourable Al FM composition, made it possible to avoid excessive IMP growth and to achieve substantial bond strength.

During tensile testing, root cracks formed which caused fracture close to the interface. Poor bonding in the root region was connected to the shape of the steel groove, which created a pit filled with FM underneath the steel plate, as can be seen in Figure 6.1(c). The shear forces acting in this region were modest, resulting in poor bonding and formation of root cracks. The fracture surfaces resulting from tensile testing showed a smaller portion of residual Al in the top half, which indicated that the fracture ran close to the Al-steel interface in this region. In the bottom half, a significant amount of residual Al was seen on the steel fracture surface, and the residual Al showed a wavy pattern that resembled an impression of the extrusion dies in the pin. This suggested that the weakest part in the bottom region was not the Al-steel interface, but rather the bonding between new and previously deposited Al as the pin traversed the weld groove. This indicated that sufficient Al-steel bonding was achieved in regions that experienced high pressure. It was believed that higher strength and fracture in the soft zone in Al could be achieved if the issue with the limited bonding in the root region could be solved.

The third generation — Paper F

In the third generation of Al-steel HYB joints, the setup and pin geometries were subjected to additional improvements. Both the groove and the pin were given an I-form, and they closely fitted each other. A schematic drawing of the cross-section of a third generation joint is shown in Figure 6.1(d), which indicates that the downflow of Al FM was even more vigorous in the third generation joint than in the second generation joint. A couple of root flaws were seen, as reported in **Paper F**, but these were not located near the Al-steel interface, and they were not expected to be detrimental to the tensile properties, since they were internal and oriented parallel to the tensile force. Consequently, no root cracks formed during tensile testing, ductile fracture always occurred in the soft part of Al, and the UTS was higher: $238 - 266$ MPa.

When it comes to the bonding mechanisms, SEM and TEM revealed more prominent signs of both mechanical interlocking and IMP layers relative to the second generation joint. The IMP layer reached thicknesses of up to ~ 1 µm, and could therefore be observed by SEM at several locations, in contrast to the thin IMP layer in the second generation joint. TEM results are shown in Figure 6.2, and it was found that the 0.2 µm thick Al-Fe-Si layer seen here contained the α_c phase, similar to the second generation joint. The increase in IMP layer thickness was

mainly believed to result from an increase in temperature owing to the change in geometry and the pin machining the steel BM to a higher degree. Based on the thickness of the IMP layers alone, it would be expected that that the second generation joint would reach higher UTS values than the third, since higher bond strengths are expected for thinner IMP layers [23, 24, 237, 238]. However, there were other factors that determined the bond strengths in this case. The root flaws in the second generation joint were critical, and the thin IMP layer was discontinuous and did not cover the interface to the same extent as the IMP layer in the third generation. The elimination of the detrimental root flaws and the larger pressure achieved by the improved geometry, which presumably led to an increase in bonded interface area, were therefore believed to be the main reasons for the increase in strength seen for the third generation joint.

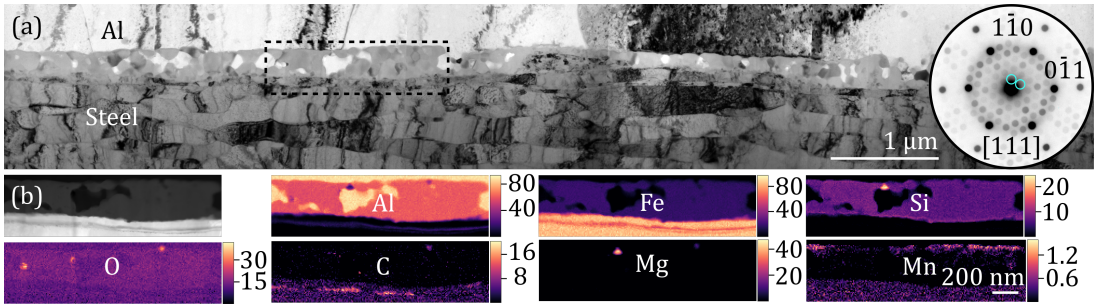

Figure 6.2: TEM characterisation of an interface region in a third generation Al-steel HYB joint from **Paper F**. **(a)** BF-TEM overview image and a NBD pattern acquired with precession that was indexed with respect to the α_c phase oriented to zone axis [111]. **(b)** HAADF-STEM image and element maps based on STEM-EDS of the interface region outlined in (a).

The multi-material Al-Cu-steel-Ti joint — Paper III

The results achieved following the improvements done for the third generation Al-steel joints encouraged multi-material joining using a setup similar to the third generation. The geometry of the multi-material joint characterised in **Paper III** is shown schematically in Figure 6.1(e). The steel BM was placed below the pin, so that it experienced a range of conditions from the AS near the Ti BM to the RS near the Cu BM. SEM of one cross-section indicated that both IMP layers and intermixed regions were more widespread on the AS than the RS. Although such features typically lead to brittle fracture and lower bond strength, they clearly demonstrate bond formation. Since Al-steel specimens from the AS reached slightly higher UTS values than specimens from the RS, the SEM observations hinted to the possibility that there were some unbonded areas and/or defects on the RS, despite that no signs of such were observed by SEM. From the fracture surfaces it was seen that the fracture ran close to the interface, most likely predominantly through IMP layer regions. Still, the HYB method again showed promising results for Al-steel joining.

6.2 Intermetallic phase layers in joints

The main topic of this thesis is the IMP layers formed in Al-steel joints, in particular the phase sequence that forms, and the morphologies, crystal structures and chemical compositions of the IMPs. This section discusses the IMP layers characterised in the various papers in a more general sense and focuses on the interrelated results reported in **Papers II, III, IV** and **V**. Since the findings in **Papers A** and **F** also are highly relevant to this discussion, they are also included here. First, the focus lies on the phases that form at the bond line between different Al alloys and steels subjected to various thermo-mechanical treatments. After that, the formation of the IMP layers at the nanoscale is elaborated on in the light of possible future studies.

6.2.1 Phase formation sequence and influence of alloying elements

The α_c phase

Papers II, IV, V, A and **F** all have in common that the α_c phase was identified as the first phase to grow at the Al-steel interfaces. Electron diffraction techniques were used for phase identification by assessing the crystal structure of the formed IMP crystals. In all cases, the patterns could be indexed with respect to the crystal structure reported by Cooper [165], with space group $Im\bar{3}$ and lattice parameter $a = 12.56$ Å. It is well known that certain transition elements, M, such as Mn, Cr and Cu, may substitute for Fe in α_c-$Al_{15}(Fe,M)_3Si_2$ [154–158] (see Section 2.4.4). Space group $Im\bar{3}$ (204) is expected for high Fe/M-ratio, while $Pm\bar{3}$ (200) is expected for low Fe/M-ratio ($\lesssim 1$ [157, 162, 163]). An overview of the estimated compositions based on STEM EDS of the α_c phase layers in the various Al-steel specimens characterised in this work is shown in Table 6.1. The values should only be considered as semi-quantitative values, since they were subjected to considerable systematic errors stemming from the use of calculated k-factors and from absorption of low energy X-rays. This, together with the variations in specimen geometry, can explain some of the large variations in the estimated compositions. Further, these factors explain partly why the estimated Al contents were below the expected values of $70 - 73$ at.% Al [165, 288]. Similarly, the estimated Si contents lay on the Si-lean side of previously reported values of $5.9 - 11.1$ at.% [157] and $7.7 - 14.1$ at.%[165, 288].

The Fe/M-ratio was > 3 for all specimens, which agrees with the space group identified to be $Im\bar{3}$. The amount of transition elements M varied greatly, as can be seen from Table 6.1, and it naturally depended on the content and availability of elements M in the alloys used. In all specimens, the total M content was relatively low, except for the 6082-316L specimens where α_c contained 4 at.% Cr, which is explained by the stainless steel 316L containing 16.65 wt.% Cr (see Section 4). Further, thin α_c layers in the 6082-316L specimens also showed a higher Mn-content than the other specimens, presumably due to the total Mn content in the steel 316L and the 6082 Al alloy being higher than in the other material combinations. However, as the α_c phase layer grew, the Mn content decreased from 2 to <1 at.% (Table 6.1), due to limited supply of Mn, and reached similar values as measured for the other specimens. Another abnormality is the high Mn content in the α_c phase layer in the 4020-DX51D CMT specimen, where a 4020 Al alloy was used that had a higher Mn content than in the 6082 Al alloys.

Common for all the studied joints in which the α_c phase was identified, is that the Al alloys that were in contact with the steel BM contained a notable amount of Si ($0.9 - \leq 3.5$ wt.%, see Section 4). As has been the focus of numerous studies, Si additions to the Al alloy significantly influence the formation and growth of IMPs at Al-steel interfaces and typically lead to formation of Al-Fe-Si IMPs (see Section 2.4.4). Various Al-Fe-Si phases have been identified in joints,

Table 6.1: Estimated compositions of the α_c phase layer based on STEM EDS from various Al-steel joints characterised in this work. The relative compositions of the major constituting elements, Al, Fe, Cr, Ni, Si and Mn, are given in at.%. The primary phase identified in the layer, the paper the specimen is related to, the alloy combination, the welding method, and the thicknesses of the phase layers, are also listed. The joints made by RB were subjected to post-rolling heat treatments, and for these specimens, the temperature and times are also given. *Specimen 6082-IF was after heat treatment at 540°C also aged at 185°C for 180 min.

Paper	Al-steel	Method	Temp. °C	Time [min]	Thickness [µm]	Al	Fe	Cr	Ni	Si	Mn
						at.%					
II	6082-S355	HYB 2.	-	-	$0.01-0.05$	64	35	-	-	9	$<\frac{1}{2}$
F	6082-S355	HYB 3.	-	-	0.22	67	23	-	-	9	0.5
[289]	6082-S355	RB	500	60	0.2	77	18	-	-	5	0.3
A	6082-IF	RB	540*	2*	0.2	67	28	-	-	5	-
IV	6082-316L	RB	500	180	$0.1-1$	71	15	2	0.2	9	3
IV	6082-316L	RB	550	2	0.13	63	21	4	0.9	9	2
IV	6082-316L	RB	550	10	0.8	70	16	4	0.5	9	0.3
IV	6082-316L	RB	550	60	1.7	74	14	4	0.4	8	0.5
V	4020-DX51D	CMT	-	-	$\lesssim 2$	73	15	-	-	7	5

and the α_h-$Al_{7.1}Fe_2Si$ (τ_5) phase [22, 211, 214] or the β-$Al_{4.5}FeSi$ (τ_6) phase [22, 24, 214] has been reported to form first in several studies. However, these studies did not report that the Al alloy contained notable amounts of other alloying elements than Si. As mentioned earlier, transition elements M, such as Mn, Cr and Cu, may substitute for Fe in α_c [154–158], and this has been shown to lead to the formation of cubic α_c-$Al_{15}(Fe,M)_3Si_2$ instead of the hexagonal α_h-$Al_{7.1}Fe_2Si$ phase that would be expected to form otherwise. In fact, the α_c phase has been reported to form in Al alloys with as little as 0.1 wt.% Mn [155], and all the Al alloys reported in Table 6.1 contained at least 0.51 wt.% Mn. Moreover, the α_c phase is the most Al-rich stable phase reported in the Al-Fe-Si-Mn system that allows $\gtrsim 9$ at.% Si [152], and it is therefore natural that the α_c phase was found here. The α_c phase has also been identified at other Al-steel interfaces in the presence of Mn and/or Cr [121, 215, 290]. Further, a phase highly similar to α_c, referred to as Fe_3SiAl_{12} (cubic, $a = 12.548$ Å), was reported to form after solid-state interdiffusion of roll bonded Al-steel specimens where the Al alloy only contained 1.2 wt.% Si and the steel presumably contained low amounts of Mn and Cu [225] (see Section 2.4.4).

The thicknesses of the α_c phase layers and the morphologies of the α_c grains varied between the characterised joints. In joints fabricated by RB or HYB that had a nanoscale α_c phase layer, the α_c grains had a rounded, near equiaxed morphology, as can be seen in particular for the second generation HYB joint in Figure 5.4 and the 6082-316L composite heat treated at 500°C in Figure 5.7(a). In the 6082-316L specimens, as the α_c phase layer grew to $\gtrsim 1$ µm in thickness, the α_c phase grains developed into elongated grains oriented normal to the interface, as can be seen in Figures 5.7(b) and (c). However, this extended growth and morphology development of the α_c layer did not happen in heat treated RB joints of the same 6082 Al alloy where a low-alloyed steel was used instead of the stainless steel 316L, in particular IF steel or S355. A 6082-IF composite was characterised in **Paper A**. This specimen was fabricated by RB, and it was solution heat treated at 540°C for 2 min and subsequently aged at 185°C for 180 min, after rolling. The RB and heat treatments were conducted by S.M. Arbo [289]. Some TEM results from this specimen are shown in Figure 6.3. It can be seen that a ~ 0.8 µm thick θ phase layer and a ~ 0.3 µm thick η phase layer had already formed even though the α_c layer was only ~ 0.2

µm thick. Similar results were obtained from a 6082-S355 composite heat treated at 500°C for 60 min, for which some TEM results are shown in Figure 6.4. This specimen was roll bonded and heat treated by S.M. Arbo, and further details on this specimen can be found in the PhD thesis of S.M. Arbo [289]. Both the second and the third generation HYB Al-steel joints were also produced with a 6082 Al alloy and a S355 steel, so that results similar to these could be expected if longer interdiffusion times or higher temperatures had occurred during HYB. The α_c phase layer in the CMT joint showed a different appearance with coarse polyhedral and up to ~2 µm thick α_c phase grains within the IMP layer and complex dendritic α_c phase grains within the Al FM, as can be seen in Figure 5.9. This joint was the only joint produced by a fusion welding method, which is the main reason for the differences in morphologies between the CMT joint and the remaining joints. Morphologies similar to those seen in this work have been found previously for α_c phase grains in Al alloys, and it has been explained that the polyhedral crystals grow as primary particles, while the morphology changes to an eutectic structure once the Al dendrites start to form [291]. Polyhedral morphology developed near the Al surface also in **Paper D**, while script morphology developed in the Al bulk.

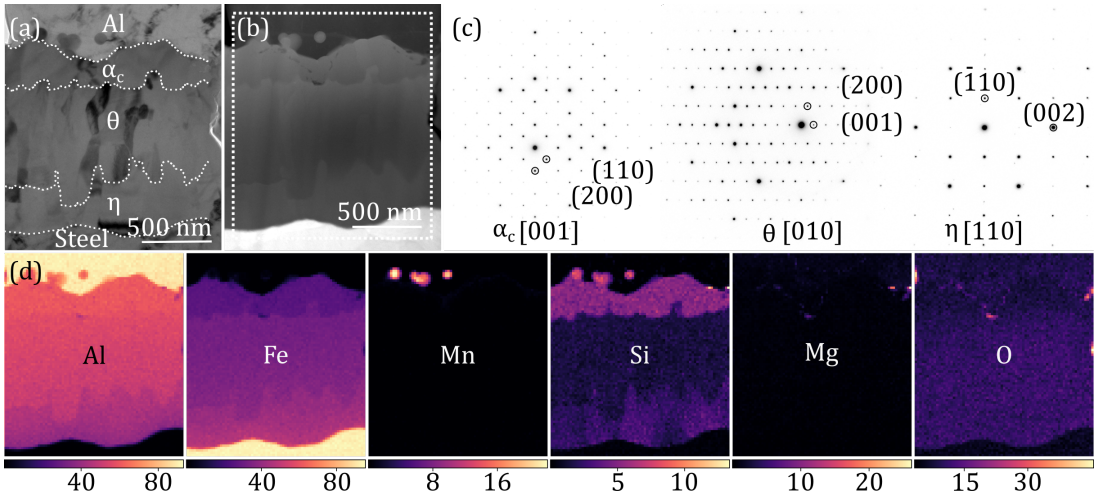

Figure 6.3: TEM characterisation of a roll bonded 6082-IF composite that was after rolling solutionised at 540°C for 2 min and aged at 185°C for 180 min. The results are from **Paper A**. **(a)** BF-TEM and **(b)** HAADF-STEM overview images of an Al-steel region. In **(a)**, phase boundaries are highlighted by white dashed lines. **(c)** Three zone-axis SAED patterns, one from each of the IMPs identified; α_c, θ and η. **(d)** Element maps, showing at.%, based on STEM-EDS from the region marked in **(b)**.

Other intermetallic phases

In joints where the total IMP layer grew larger than a few hundred nanometres, other phase layers started to form after the α_c phase layer. Table 6.2 gives an overview of the estimated compositions based on STEM EDS of the phase layers identified in the various Al-steel specimens. These values should only be regarded as semi-quantitative estimates, for reasons explained earlier. In most joints where a second IMP layer formed, this consisted of the θ phase. However, in the 6082-316L specimens, the second phase to form was the τ_1-FeNiAl$_9$ phase, which formed at the α_c-Al interface. The Ni in the τ_1 phase must have diffused from the steel and through the first formed α_c phase, to reach the Al side, presumably driven by the enthalpy

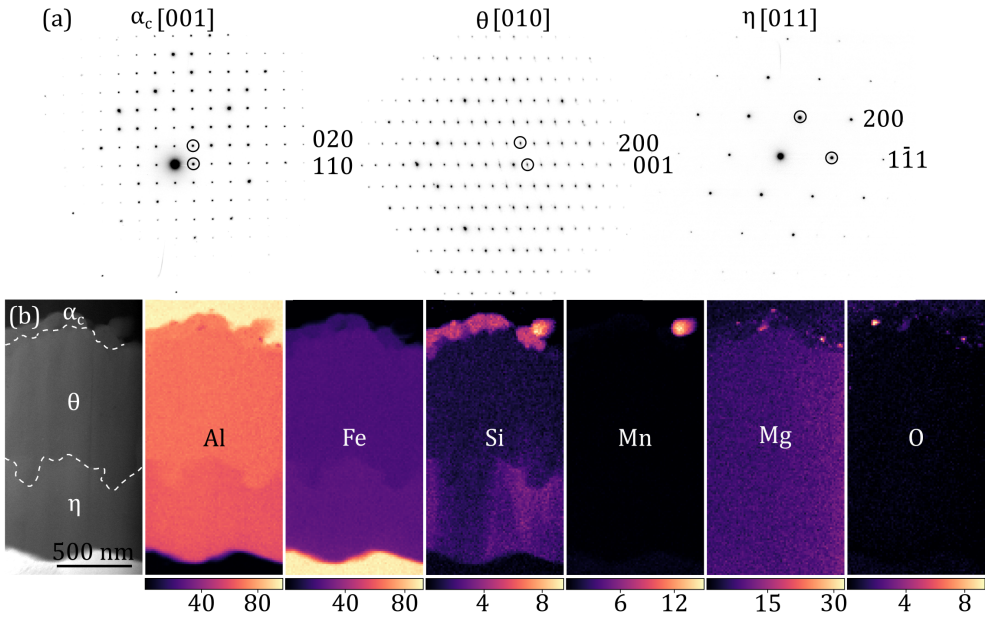

Figure 6.4: TEM characterisation of a roll bonded 6082-S355 composite that was after rolling heat treated at 500°C for 60 min. Results from this specimen are also shown in [289]. **(a)** Three zone-axis SAED patterns, one from each of the IMPs identified: α_c, θ and η. **(b)** HAADF-STEM image and element maps based on STEM-EDS, showing at.%, of an Al-steel region. In the HAADF-STEM image, some phase boundaries are highlighted by white dashed lines.

of mixing being more negative for Al-Ni than Fe-Ni [292]. Further, the τ_1 phase is the most Al-rich phase reported in the Al-Fe-Ni-Si system [293], and the Al content in τ_1 was higher than that in α_c, so that the Al content was sufficiently high to promote growth of the τ_1 phase first at the Al-α_c interface. The τ_1-FeNiAl$_9$ phase has only been reported to form at Al-Fe interfaces in a few studies [230, 231]. However, the metastable η-Ni$_2$Al$_9$ [138] and Fe$_2$Al$_9$ [137] phases have been reported at Al-Ni [294–296] and at Al-Fe interfaces [297], respectively. In this work, the τ_1 grains were frequently faceted towards Al, as can be seen in Figure 5.7(b). The morphology may suggest a possible crystallographic relationship, as has been found for Ni$_2$Al$_9$ in Al [298], and this could be investigated further.

A layer of the θ phase formed at the α_c-steel interface after prolonged IMP layer growth, which was seen in all the RB specimens. Formation of a θ phase layer at Al-steel interfaces has been reported previously numerous times [195, 197], and it has been reported that the θ phase layer may incorporate several alloying elements, for instance Si [214], Cu [217], Ni and Cr [199, 234]. From Table 6.2, it can be seen that the θ phase layers all contained minor amounts of Si. In addition, the θ phase layer contained notable amounts of Ni and Cr in the 6082-316L specimens. In one of the 6082-316L specimens, another phase, τ_{11}-Al$_5$Fe$_2$Si, was identified in the same layer as θ. The τ_{11} phase has only been reported in a few studies of Al-steel joints, either as inclusions in the η phase layer [219], or in co-existence with the α_h and η phases [299]. It must be stressed that the τ_{11} phase is similar to the phase τ_{10} in both composition and lattice parameters (see Section 2.4.1), and the τ_{10} phase has also been reported to form at Al-steel

interfaces in relation to the θ phase layer [22, 173, 218]. In this work, the τ_{11} phase was identified in a specimen heat treated at 550°C, although only τ_{10} and not τ_{11} can be found in the Al-Fe-Si phase diagram at 550°C [133, 151] (see Section 2.4.1). Local temperature variations and the presence of alloying elements could have promoted the formation of τ_{11}. Still, it must be emphasised that τ_{11} was observed together with θ in one TEM lamella only, while solely θ was found in another lamella. Further electron diffraction studies must be done to confirm that only τ_{11} and not τ_{10} or both formed, and to clarify the interplay between θ and τ_{11} (and τ_{10}) at Al-steel interfaces when several alloying elements participate.

With prolonged interdiffusion, a layer of the η phase formed in the RB specimens following growth of the θ phase. In all specimens, the η phase layer contained minor amounts of Si, as can be seen in Table 6.2, consistent with other studies [134, 300]. In the 6082-316L specimens, the η phase layer also contained Cr and Ni, which agrees with previous studies of aluminised stainless steels [199, 234]. Since the estimated amounts of 3 at.% Ni and 5 at.% Cr exceeded reported solubility limits of 1 at.% Ni at 850°C [127] and 3 at.% Cr at 700°C [301], Cr- and Ni-rich phases were expected to form within the η phase layer, which has been reported previously [229, 232]. In fact, the η phase layer characterised in this study contained numerous nanoscale precipitates rich in Cr and Si or Ni, both possibly also containing Al and/or Fe, and further characterisation is needed to determine the type of precipitates formed.

Lastly, the estimated compositions of two IMP layers (Figure 5.6) that formed at the Al-steel interface in the multi-material HYB joint from **Paper III** are also listed in Table 6.2, although the phases constituting these layers have not yet been determined. The results stand out due to the high Cu contents measured. It is important to note that most specimens were attached to Cu TEM specimen grids, which meant that the Cu contents could not be determined to a satisfactory degree, and Cu was therefore not included in the compositions reported for the other specimens. However, from the element maps of the IMP layer in the multi-material HYB joint (Figures 5.6(b) and (c)), it could be seen that this layer contained Cu. Thus, the Cu content was included as measured, even though stray radiation caused overestimation of these values. Since the steel BM and Al FM used in this joint did not contain notable amounts of Cu, detached Cu BM fragments stirred into the Al FM were believed to be the major source of Cu. It is interesting to note that Cu-rich fragments could be seen even on the opposite side of the weld groove close to the Al-Ti interface (Figure 5.5(c)). Based on the compositions in Table 6.2 and the previous results discussed here, it can be hypothesised that the IMP layer may have contained the α_c phase and the θ phase. However, future electron diffraction studies are required to allow phase identification, and larger areas should preferably be studied since local fluctuations in both the compositions and the thicknesses of the IMP layers are expected.

6.2.2 Formation of nanoscale phase layers

The first phase identified to form at the Al-steel interfaces was the α_c phase, and the Si contained within this phase was believed to primarily originate from the Al alloy and to diffuse relatively fast to the Al-steel interface during heat treatment. This is plausible since the diffusivity of Si in Al at 550°C is higher than that of the other main alloying elements present [302], and since the enthalpy of mixing is more negative for Fe-Si than Al-Si [292], which presumably provided a driving force for Si segregation to the Al-steel interface. A similar argument has also been presented for an Al-Ti interface where Si was believed to diffuse rapidly from the Al alloy towards Ti during joining [303]. Further, in Al alloys containing Si, an amount of Si typically segregates to the surface and becomes incorporated in the surface oxide layer [304]. Initially, the α_c grains had a rounded equiaxed shape with the curved side sticking into Al, which suggested

Table 6.2: Estimated compositions of various IMP phase layers based on STEM EDS from various Al-steel joints characterised in this work. The relative compositions of the major constituting elements, Al, Fe, Cr, Ni, Si, Mn and Cu, are given in at.%. The primary phase identified in the layer, the paper the specimen is related to, the alloy combination, the welding method, and the thicknesses of the phase layers, are also listed. The joints made by RB were subjected to post-rolling heat treatments, and for these specimens, the temperatures and times, are also given. *Specimen 6082-IF was after heat treatment at 540°C also aged at 185°C for 180 min. **In Paper III, the IMPs were not determined.

Phase	Paper	Al-steel	Temp. °C	Time [min]	Thickness [µm]	Al	Fe	Cr	Ni	Si	Mn	Cu
									at.%			
τ_1	IV	6082-316L	550	10	$\lesssim 0.5$	77	11	<0.1	10	2	<0.1	-
τ_1	IV	6082-316L	550	60	$\lesssim 0.7$	80	8	<0.1	11	1	<0.1	-
θ	A	6082-IF	540*	2*	~ 0.8	62	36	-	-	2	-	-
θ	[289]	6082-S355	500	60	$1-2$	74	24	-	-	1	-	-
θ/τ_{11}	IV	6082-316L	550	60	0.8	69	18	5	2	6	0.3	-
θ	V	4020-DX51D	-	-	$\lesssim 1$	71	26	-	-	3	≤ 0.1	-
η	A	6082-IF	540*	2*	~ 0.3	53	42	-	-	5	-	-
η	[289]	6082-S355	500	60	0.5	69	29	-	-	2	0.3	-
η	IV	6082-316L	550	60	0.3-1.5	69	21	5	3	2	0.3	-
η	V	4020-DX51D	-	-	$\lesssim 1$	63	32	-	-	5	0	-
1**	III	6082-HCT590	-	-	0.1	70	17	0.2	-	7	0.6	5
2**	III	6082-HCT590	-	-	0.1	69	22	0.1	-	3	0.6	4

that α_c initially grew predominantly into the Al side, consistent with the solid solubility of Al in Fe exceeding that of Fe in Al [21]. However, this understanding does not seem to explain the full picture, as is discussed in the following.

In the 6082-316L CRB specimens, a ~ 10 nm thick Si-rich layer was found at the α_c-steel interface at an early stage, and it is unclear whether this Si-rich layer was composed of other phases richer in Si than α_c. Moreover, in the second generation Al-steel HYB joint characterised in **Paper II**, SED data from an interface region were acquired, and selected patterns were indexed considering all the Al-Fe(-Si) phases listed in Section 2.4.1. It was found that α_c could explain several patterns (Figure 5.4), but no single phase could explain all the patterns recorded. This indicated that α_c likely co-existed with one or more Al-Fe(-Si) phases that could not be identified. However, several of the Al-Fe(-Si) phases have superstructures and are often faulted (see Section 2.4.1), which complicates such analyses. In general, electron diffraction studies of interfacial nanoscale Al-Fe(-Si) layers in Al-steel joints are lacking. There are some reports on HRTEM imaging of amorphous nanoscale IMP layers in Al-steel joints. Some studies have reported that under specific Al-steel welding conditions where high shear strain rates are sustained, nanoscale amorphous layers can form instead of IMP layers [305, 306]. Such amorphous layers have been associated with high bond strengths, and they form by a mechanical alloying process occurring during severe plastic deformation [307, 308]. It was suggested that the amorphous phase likely was an intermediate stage before formation of IMPs [307]. Further, it has been reported that a glassy phase, termed q-glass, which is related to the α_c phase, forms in rapidly solidified Al-Fe-Si alloys [309, 310], and it has been reported that this amorphous phase transforms to the the α_c phase upon heat treatment [181]. More research is needed to understand the initial nanoscale phase formation, especially for joints formed under severe plastic deformation.

Another interesting observation is that the number of small dispersoids seemed to be higher close to the Al-steel interface in some HYB joints. This has also been reported in another study on Al-steel joints [311]. In the second generation HYB Al-steel joint, some of the small Al-(Fe, Mn, Cr)-Si dispersoids located close to the Al-steel interface (see Figure 5.4), from which SED data were acquired, were also identified as α_c phases. Further, some dispersoids contained increasing amounts of Fe towards their edges, consistent with previous work explaining this based on Fe diffusing more slowly into the dispersoids during prolonged growth [164]. Here it was possible that Fe diffusion across the Al-steel interface during HYB promoted formation of small dispersoids in parallel to growth of already formed dispersoids. An increase in the number density of small Ti-rich dispersoids was also seen in some areas near the Al-Ti interface in the multi-material HYB joint (Figure 5.5(c)). To reach conclusions regarding this, future studies could focus on comparing the dispersoid number density close to the interface with the density in the Al alloy before welding.

At some Al-steel interfaces, nanoscale oxide layers were seen. Several oxide particles were seen at and near the Al-steel interface in the 6082-316L specimens in **Paper IV**. Further, in the second generation HYB Al-steel joint (**Paper II**), some interface regions were found that were covered by a $\sim$5 nm thick Al-O-Mg-Si layer, and it was observed that the Al-Fe-Si layer may grow thicker into Al where there were gaps in the oxide layer. This observation was consistent with the general belief that an interfacial oxide film acts as an interdiffusion barrier for growth of Al-Fe phases [312, 313]. Note that the oxide layer itself may undergo changes in the crystal structure above certain temperatures, which may affect the diffusivities [312]. SPED of the oxide layer in the HYB specimen from **Paper II** was done (not shown), and no indications were seen that the oxide layer was crystalline, implying that it most likely was an amorphous layer. Similar findings have been made in studies of Al-Au [314], Al-Cu [315] and Al-Ti [303] joints. In the latter study, inversely distributed Si-rich and O-Mg-rich nanoscale interfacial layers were reported, and the O-Mg-rich layer was believed to act as an interdiffusion barrier that originated from a broken native alumina surface layer [303]. The oxide layer observed in this study bore a close resemblance to the native Al_2O_3 layer, that may also contain Mg and Si, typically found on Al surfaces exposed to air [304, 316, 317]. It was believed that the original oxide layer on the Al surfaces disintegrated due to the high deformation during HYB, similar to that in FSW [318, 319], and that the nanoscale Al-O-Mg-Si layer formed as a result of air access during the process. Oxide films have also been in focus in other studies of Al-steel joints, and interfacial nanoscale oxide films have also been identified in FSW joints [320–322]. Such films have been coupled to interfacial fracture [321], since they may represent poorly bonded areas. At the same time, the combination of thin interfacial IMP and oxide layers has been reported to give high bond strengths [313, 322], and it has been reported that oxide films on the steel and on the Al surfaces may mix to form other oxide layers [313, 321]. In this work, interfacial Al-O-Mg-Si layers were also seen in regions where Al stuck to steel after tensile testing, which suggested that limited interface regions covered by interfacial oxides formed during joining not necessarily have detrimental effects on the overall bond strength. Further, there might also be a connection between the Al-Fe-Si IMPs and the oxide layers, since the α_c phase has been reported to nucleate preferentially on Al_2O_3 oxide films [323, 324]. It is evident that further studies are needed to fully understand the role of nanoscale interfacial oxide layers in solid state Al-steel bonding.

6.3 Characterisation methods

Advanced TEM techniques are crucial to be able to study IMP layer formation and growth at the nanoscale. For Al-steel joints, there are several candidate IMPs with similar compositions that may form, and therefore it is important to assess the crystal structures of the formed IMPs to reach conclusive phase identification. Conventional electron diffraction techniques where zone axis patterns are acquired after manual tilting of the crystal are highly impractical in this case, since the IMP crystals are only a few nanometre wide and grow at highly disordered interfaces, as mentioned earlier. S(P)ED techniques offer the possibility to assess the crystal structures of such phases and can in addition provide better statistics, at the expense of more challenging data handling and analysis. Further, *in-situ* heating offers a great opportunity to better understand the kinetics and the evolution of the IMP layers by studying the formation and growth directly as they happen. S(P)ED and *in-situ* heating have not yet been exploited to their full potential, and they are expected to be particularly powerful if exploited jointly. There is still a great potential for improvement, and this section discusses some aspects that can be considered in future S(P)ED studies of nanocrystalline specimens. Thereafter, this section presents and discusses unpublished *in-situ* heating results from proof-of-concept studies that were conducted as a part of this work. Specimen preparation routines, various *in-situ* heating challenges that arose in this work, and possible future studies are mentioned.

6.3.1 Scanning (precession) electron diffraction

S(P)ED is a powerful technique that together with (semi-)automatic data analysis routines enables assessment of local crystallography on the nanometre scale (see Section 3.3.3). Nanocrystal segmentation of SPED data is the topic of **Paper I**, and this was utilised in **Paper II**. However, several analysis steps typically remain to be done after nanocrystal segmentation, most importantly to index the patterns. In **Paper II**, selected patterns were analysed both manually and semi-automatically using a code written for the purpose of indexing zone axis patterns. In general, an algorithm that offers reliable automatic indexing of both zone axis and off-axis patterns is required. A much used approach is *template matching*, where a bank of simulated patterns covering all possible candidate orientations and phases is constructed [269, 325]. Each experimental pattern is compared to the bank of simulated patterns, and a metric, such as normalised cross-correlation, is employed to decide which template that best fits the experimental pattern. There are some challenges with template matching, including that it requires prior knowledge on the candidate crystal structures and determination of the simulation parameters. For S(P)ED data of IMPs this is especially challenging due to the relatively high number of candidate phases and the complexity of their crystal structures, which is one of the reasons why such an approach was not used in this work. Due to the large potential for applications, future improvements that make indexing more straightforward and robust also for more complex problems should be developed. There are other strategies for automatic indexing apart from template matching, including for instance *vector pair matching* [326] and *Groth's triangle algorithm* [327]. The latter has been shown to provide better accuracy for off-axis NBD patterns [327]. Still, a challenge with all of the above is to assess precision and accuracy. A previous study found that template matching of spot patterns can give a precision in the orientation determination of 1.1°, with 95% confidence [328]. Ideally, it should be possible to assess these parameters for the orientation mapping of each crystal. One possibility is to record S(P)ED data over a range of specimen tilt conditions, as was done in **Paper II**, and then to index the same crystals for the range of known specimen tilts and compare the results to assess both precision and accuracy.

New opportunities can emerge by collecting the data in other ways than two dimensional S(P)ED scans. For instance, by recording S(P)ED data over a range of tilt conditions, tomographic reconstructions can be done both in real space and wave vector space, which allow three dimensional crystallographic analysis of nanostructures [277, 283]. Further, *rotation electron diffraction* (RED) combines discrete specimen tilts with small beam tilts to enable collection of continuous RED data from which the diffraction from a crystal can be reconstructed in three dimensions and used for structure refinement [329, 330]. Algorithms have also been developed that enable automatic tracking and collection of diffraction patterns or RED datasets from several single crystals in a specimen, referred to as serial (R)ED [331]. New opportunities also arise currently following the recent revolution in electron detection devices with direct electron detectors becoming commercially available [272]. As mentioned in Section 3.3.3, these detectors have a much improved sensitivity and dynamical range, and they solve problems associated with afterglow, background noise and geometrical distortions due to external mounting of the camera [332]. This allows for analysis of weak spots, for instance from nanocrystals embedded in other phases, and to work under low dose conditions to enable studies of beam sensitive materials, even biological materials. Needless to say, electron diffraction techniques combined with scanning, rotation and/or precession offer a wide range of opportunities and potential applications, and it can be expected that developments in this area give large impacts.

6.3.2 *in-situ* heating

In-situ heating TEM experiments offer the possibility of studying IMP layer formation and growth directly. Publications on such studies are few, but some promising results have been published for *in-situ* interdiffusion experiments of Al-Au [314] and Al-Cu [315] specimens, where formation and growth of IMPs were observed. As a part of this work, three sets of *in-situ* heating experiments were conducted with the aim of obtaining better understanding of the formation and growth of various IMPs. The first set of experiments relates to **Paper B**, the second to **Papers II** and **Paper F**, and the last relates to a study by Sunde et. al [333]. For these experiments, various specimens were prepared by FIB lift-out, and heating chips and a heating holder supplied by DENS solutions were utilised.

Growth of interfacial Al-Ni phases

In **Paper B**, a Ni foil was used as interlayer in roll bonded Al-steel composites of Al alloy 1080 and structural steel S355. The Ni interlayer was introduced in order to avoid formation and growth of the brittle Al-Fe IMPs. The composites were heat treated after RB for various times at temperatures in the range of $400 - 550$°C. In this study, RB, heat treatments and SEM imaging were performed by S.M. Arbo [289]. An overview SEM image of a heat treated composite is shown in Figure 6.5(a). Based on SEM and TEM of specimens heat treated *ex-situ*, it was seen that a layer of Al_3Ni formed first at the Al-Ni interface. With prolonged interdiffusion, a layer containing fine equiaxed grains of Al_3Ni_2 formed at the Al_3Ni–Ni interface, as can be seen in Figure 6.5(b). The Al_3Ni_2 layer grew at the expense of the Al_3Ni layer until it had fully consumed the Al_3Ni layer. As this happened, a duplex morphology developed in the Al_3Ni_2 layer, as shown in Figures 6.5(c) and (d). Eventually, Kirkendall voids formed at the Al side of the Al_3Ni layer. A BF-TEM image showing the duplex morphology and the pores in the Al_3Ni_2 layer is presented in Figure 6.5(e). Due to the characteristic morphology development and the extensive *ex-situ* heating experiments that had been conducted, it was believed that these specimens were good candidates for *in-situ* heating. Previous studies on *in-situ* heating of Al-Ni specimens have been published, but these looked at multi-layer Al-Ni structures using TEM

imaging and SAED techniques [334, 335]. In this work, the plan was to study both the growth of and the morphology development within the Al_3Ni_2 layer in detail by collecting SPED data at various stages during *in-situ* heating.

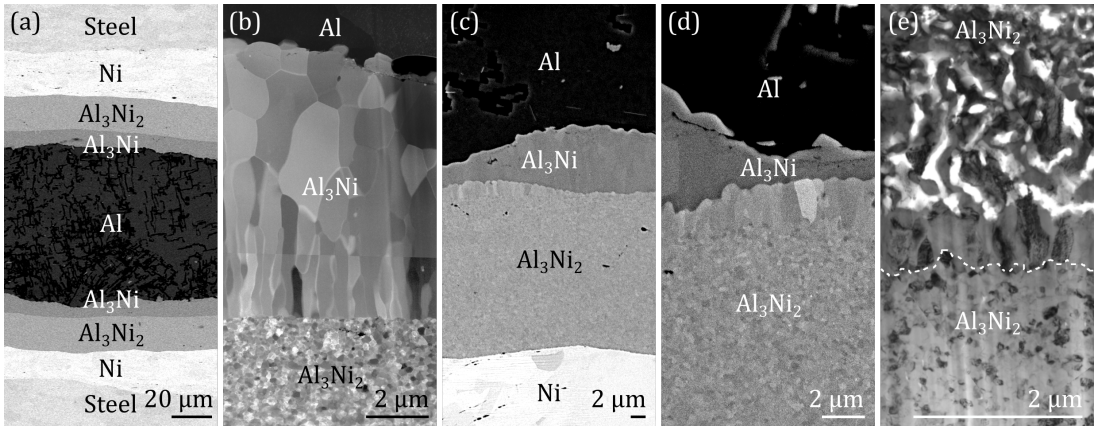

Figure 6.5: SEM and TEM of roll bonded Al-Ni-steel composites subjected to *ex-situ* post-rolling heat treatments. **(a)** An overview BSE SEM image and **(b)** an ADF-STEM image, of a specimen heat treated at 550°C for 1 h. **(c)** and **(d)** SE SEM images, and **(e)** BF-TEM image, of the interface region in specimens heat treated at 550°C for 2 h. The SEM images shown in **(c)** and **(d)** are reprinted from the PhD thesis of S.M. Arbo [289] with permission. In all the images, two IMP layers consisting of Al_3Ni_2 and Al_3Ni can be seen, except in **(e)** where the Al_3Ni_2 layer has fully consumed the Al_3Ni, and a duplex morphology and a porous structure have formed near the Al_3Ni_2-Al interface.

It was decided to start with a specimen where the two Al_3Ni_2 and Al_3Ni layers had already formed, but where development of the duplex morphology had not started. The specimen preparation was performed by FIB, and it posed challenges first and foremost due to the dimensions of the system. Regarding *in-situ* interdiffusion experiments, it is important to note that thin film diffusion couples can act differently than bulk couples. While all equilibrium phases are expected to appear in bulk couples as long as they overcome nucleation barriers, not all equilibrium phases appear in thin film systems [336]. In bulk, a second phase typically starts to grow after the first has exceeded a critical thickness, but in thin film systems, the supply of one component can be restricted so that the second phase forms before the critical thickness is reached [336]. In this study, it was crucial that significant amounts of Al and Ni were connected to Al_3Ni and Al_3Ni_2, respectively, to provide sufficient supply of these elements and avoid thin film effects. This meant that a relatively long specimen had to be lifted out by FIB. The first specimen, Specimen A, was prepared in collaboration with S. Wenner who performed the FIB lift-out and FIB thinning. A long rectangular area was milled out in plan-view geometry, and the lamella was transferred to and attached to a heating chip and subsequently thinned and polished by ion milling. SEM images taken during specimen preparation are shown in Figure 6.6, where (a) shows the interface area from which the lamella was fabricated, (b) and (c) were taken during milling, and (d) shows the lamella attached to the heating chip. During milling it is important to not damage the chip and to not thin the specimen too much, as that could influence the diffusion phenomena. A second specimen, Specimen B, was made in a slightly different way, where the plan-view lamella was first thinned while attached to a standard TEM Cu specimen grid, before it was transferred to a heating chip.

In this specimen, some redeposition was seen near the edge of the specimen, but the ROI did not show extensive damage.

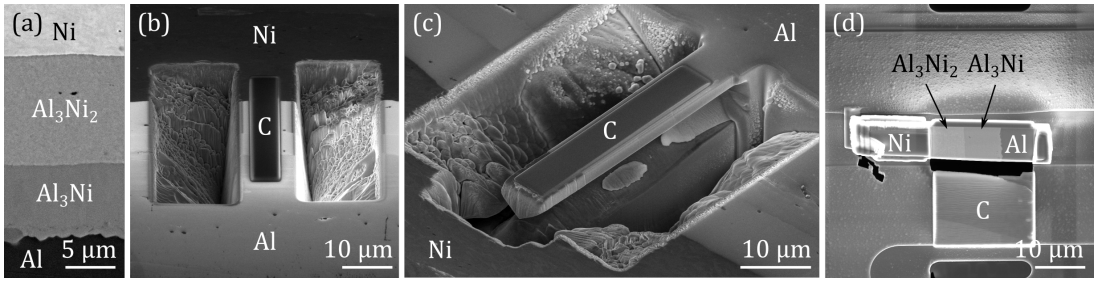

Figure 6.6: FIB preparation of an Al-Ni specimen (Specimen A) for *in-situ* heating. The specimen had been heat treated at 550°C for 1 h *ex-situ*. **(a)** BSE SEM image of the interface area from which the lamella was fabricated. **(b)** SE SEM image taken during milling. **(c)** SE SEM image showing the long plan-view lamella after milling. **(d)** SE SEM image of the lamella after thinning, where the lamella was attached to a heating chip and a C protection layer had been deposited to protect the chip.

ADF-STEM images of the two specimens prior to *in-situ* heating are shown in Figures 6.7(a) and 6.8(a), for Specimen B and Specimen A, respectively. The specimens were subjected to *in-situ* heating at temperatures in the range of $400 - 550$°C, similar to the *ex-situ* heating procedures. First, nuclei started to form and grew inside the Al_3Ni layer, primarily at grain boundaries. This happened in both specimens, as can be seen in Figures 6.7(b) and (c) and Figure 6.8(b). The growth of the Al_3Ni_2 layer progressed much slower than the growth of the particles within the Al_3Ni layer. In Specimen B, large particles eventually formed within the Al_3Ni layer, while the Al_3Ni–Al_3Ni_2 interface only showed a small movement, as can be seen in Figure 6.7(d). This was unexpected based on the *ex-situ* experiments, where Al_3Ni_2 grew into and consumed Al_3Ni. However, Specimen A showed an even more unexpected behaviour than Specimen B. In this specimen, the Al in contact with Al_3Ni became completely consumed, and new phases started to grow from the Al_3Ni layer and into the Al_3Ni_2 layer, which can be seen in Figures 6.8(c) and (d). It was believed that the unexpected behaviour could, at least partly, be explained based on the dimensions of the system with the thickness of the lamella being several magnitudes smaller than the lateral lengths of the layers, which potentially opened up for surface diffusion domination. Whatever the cause, it was believed that some of the issues encountered could be solved by fabricating specimens where the IMP layers had thicknesses much below the lamella thickness.

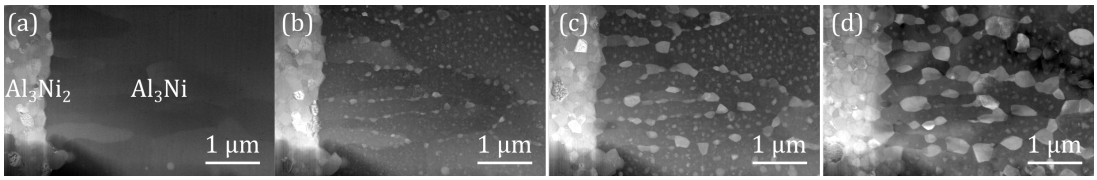

Figure 6.7: *In-situ* heating of an Al-Ni specimen (Specimen B) that had been *ex-situ* heat treated at 550°C for 1 h. **(a)** ADF-STEM image of the specimen before *in-situ* heating. ADF-STEM images after *in-situ* heating at (additive) **(b)** 400°C for 30 min, **(c)** 450°C for 15 min and then 500°C for 15 min, and **(d)** 550°C for 30 min. The shown images were acquired at 20°C.

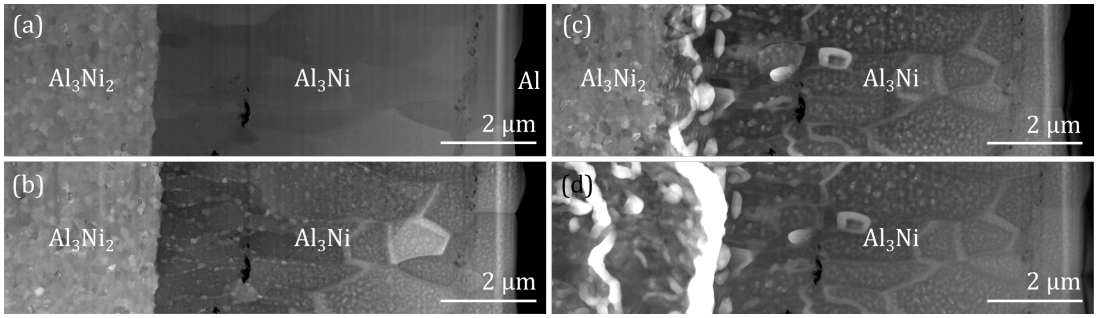

Figure 6.8: *In-situ* heating of an Al-Ni specimen (Specimen A) that had been *ex-situ* heat treated at 550°C for 1 h. **(a)** ADF-STEM image of the specimen before *in-situ* heating. ADF-STEM images after *in-situ* heating at (additive) **(b)** 1 min at 400°C, 1 min at 450°C, 3 min at 500°C and 1 min at 550°C; **(c)** 550°C for 12 min; and **(d)** 550°C for 10 min, 500°C for 1 min, 525°C for 2 min and 535°C for 2 min. Note that during the *in-situ* heating performed between **(b)** and **(c)**, the Al in contact with Al_3Ni became completely consumed. The shown images were acquired at 20°C.

Formation and growth of intermetallic phases in aluminium-steel joints

The second generation HYB Al-steel joint presented in **Paper II** showed a discontinuous $10-50$ nm thick interfacial Al-Fe-Si IMP layer. Due to the much reduced thickness, it was believed that specimens from this joint would fit better for *in-situ* heating TEM studies than the Al-Ni specimens. Specimens were prepared from the second generation HYB joint following the same approach as described above for Al-Ni Specimen B. SEM images taken during specimen preparation are shown in Figures 6.9(a)-(c), where (a) shows the thinned Al-steel lamella attached to the lift-out needle after it had been separated from the Cu grid by milling. Figure 6.9(b) shows the lamella after it had been attached to the heating chip by ion beam deposition of C, and (c) shows the finished lamella after it had been detached from the needle. In some of the specimens, redeposition of Cu appeared as small nanoparticles on the lamellae surfaces, which could have been avoided if the lamellae were thinned while attached to a heating chip instead of a Cu grid.

An Al-steel specimen from a second generation HYB Al-steel joint (**Paper II**) where no IMP layer had formed *ex-situ* was studied first. No signs of Al-Fe interdiffusion or IMP layer formation was seen even after heat treatments at temperatures approaching the melting point of Al. Instead, some dispersoids dissolved, and a substance started growing from one of the edges of the specimen. Figure 6.10(a) shows the lamella before heating, while (b) and (c) show the lamella after growth of new phases, supposedly on the lamella surface, which according to EDS results contained major amounts of Ga, Fe, Al and some Si. In this specimen an interfacial surface oxide layer was present, which presumably hindered interdiffusion. New specimens were fabricated from regions where a nanoscale IMP layer had already formed *ex-situ*, since it was believed that IMP layer growth would occur more readily in such specimens.

Two specimens were made in which IMP layers had formed *ex-situ*, one from a second generation (**Paper II**) and one from a third generation (**Paper F**) HYB Al-steel jont. In both of these specimens, some limited growth of the IMP layers was observed initially during *in-situ* heating, but the growth was halted quickly. BF-STEM images of the specimen from the third generation joint is shown in Figure 6.11, where (a) and (b) show the IMP layer before and after heat-

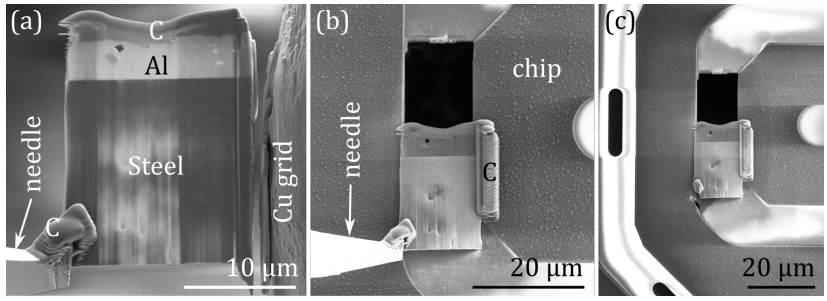

Figure 6.9: Specimen preparation of an Al-steel specimen from a second generation HYB joint for *in-situ* heating TEM experiments. **(a)** SE SEM image showing the Al-steel lamella after it had been thinned while attached to a Cu grid. The lamella had been fastened to the lift-out needle by ion beam deposition of C, and had subsequently been detached from the Cu grid by milling. **(b)** and **(c)** SE SEM images showing the lamella attached to the heating chip. In **(b)**, the lamella is also attached to the lift-out needle, while in **(c)** it has been separated from the needle by milling.

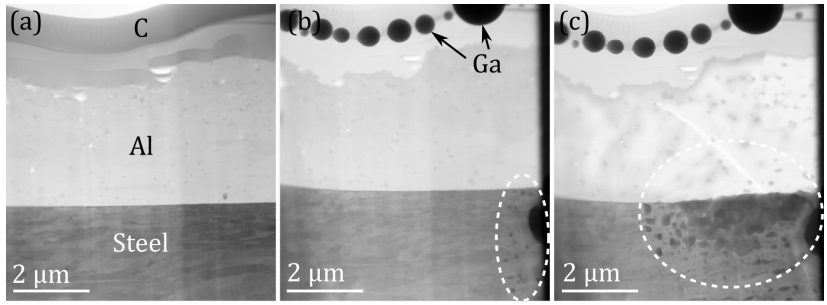

Figure 6.10: *In-situ* heating TEM studies of an Al-steel specimen from a second generation HYB joint where no IMP layer had formed prior to *in-situ* heating. BF-STEM images **(a)** before heating, and **(b)** and **(c)** after *in-situ* heating at temperatures in the range of $300°C-600°C$. Ga droplets formed in the C protection layer at the top, and an unknown phase, highlighted by dashed white ellipses, started growing from the C layer deposited to the right.

ing, respectively. Again, a substance started to grow from the edges of the lamellae where protection layers had been deposited using FIB, as can be seen in Figures 6.11(c) and (d). Clearly, the proof-of-concept studies discussed so far did not show great prospects. One difference between the experiments conducted here and the successful *in-situ* heating TEM experiment reported for an Al-Cu joint [315], is that Si shows an affinity for segregating to the surface oxide layer on Al, while Cu remains within the Al bulk [304]. Preferential (surface) segregation of some elements was possibly detrimental to Al-steel interdiffusion in this work. In any case, better understanding of *in-situ* TEM heating experiments of Al-steel joints is needed.

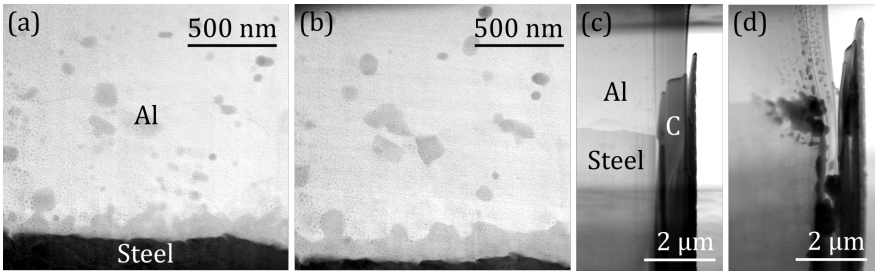

Figure 6.11: *In-situ* heating TEM studies of an Al-steel specimen from a third generation HYB joint where a nanoscale IMP layer had formed prior to *in-situ* heating. BF-STEM images **(a)** and **(c)** before heating and **(b)** and **(d)** after *in-situ* heating at temperatures in the range of $350°C-525°C$. By comparing **(a)** and **(b)**, minor growth of the IMP layer and coarsening of dispersoids can be seen, while **(d)** shows an unknown phase that started growing from the C layer deposited to the right.

Evolution of precipitates in aluminium alloy 6082

When it comes to the properties of Al-steel joints, the response of the used Al alloy to the heating occurring during welding also has a major influence, in addition to the IMP layer characteristics. In most of the Al-steel joints studied in this work, the Al alloys used were of type 6082 [333]. Around the same time as the above experiments were conducted, J.K. Sunde et al. performed a successful *in-situ* heating TEM study of a 6082 Al alloy. The alloy studied was a 6082 Al-Mg-Si alloy that contained a small amount of Cu. The addition of Cu generally alters the precipitation sequence substantially from that expected for Al-Mg-Si alloys as given in Equation 2.1 [337]. In fact, this alloy showed a larger number density of L-type precipitates that have better thermal stability than the β'' phase typically found in age-hardened $6xxx$ alloys. The alloy was aged *in-situ* and the precipitate evolution was analysed from SPED data acquired at various stages during the heat treatment. The results from this experiment was published in [333], and they were compared to results from *ex-situ* heating reported in [338]. The experiment was deemed successful in that the precipitate evolution during *in-situ* heating was similar to the evolution as studied *ex-situ*. There were some discrepancies, however. The region studied by SPED was measured to be ~ 90 nm thick, and this region was still in an underaged state after *in-situ* heat treatments that gave peak hardness *ex-situ*. In the ~ 90 nm thick region, the precipitates were only ~ 30 nm long, while in a ~ 130 nm thick region, they were $\gtrsim 100$ nm long. This was believed to be connected to surface segregation of the main alloying elements Mg and Si, which reduced the amount of available solute. Even though these thickness effects must be studied in more detail, the results were extremely promising.

Due to the promising results and that 6082 Al alloys were used in most of the Al-steel joints studied in this thesis, it was decided to work further on *in-situ* TEM heating of this 6082 Al alloy as a part of this thesis and in collaboration with J.K. Sunde. Specimen preparation was performed using a different approach from that used previously. In the study by Sunde et al. [333], specimens were prepared by mechanical grinding and electropolishing, before EBSD was performed to find a grain oriented close to $[001]$ zone axis. The selected grain was milled out using FIB and transferred to a heating chip where it was thinned by ion beam milling. If ion beam milling is used, the specimen surface becomes damaged and implanted with Ga. To avoid these issues, specimens were prepared in this work without using ion beam milling for thinning. After electropolishing, the specimens were studied by TEM to find correctly oriented

and adequately thick grains. Using FIB, a large region surrounding a selected grain was cut out in a way so that milling was performed at least $\gtrsim 20\ \mu m$ away from the ROI. The large and thin Al flake was transferred to a heating chip to which it was attached by depositing C as far away from the ROI as possible. Figures 6.12(a)-(c) show SEM images taken during FIB -lift-out of one such specimen. Since no FIB thinning was required, it was possible to limit the surface damage and Ga implantation in the ROI. At best, lamellae with little to no visible damage could be produced. *In-situ* heating proof-of-concept studies were performed that showed great promise, and several specimens were prepared from alloys heat treated to various conditions *ex-situ*. Some TEM images acquired during an *in-situ* heating experiment are shown in Figure 6.13, where it can be seen that it was possible to follow precipitate formation, growth and dissolution *in-situ*. Unfortunately, the corona pandemic caused postponement of the planned experiments, which were intended to be performed using a direct electron detector to collect S(P)ED data. The combination of *in-situ* heating and S(P)ED data collection holds great potential for characterisation of nanocrystalline materials, and this potential should absolutely be investigated further in future studies.

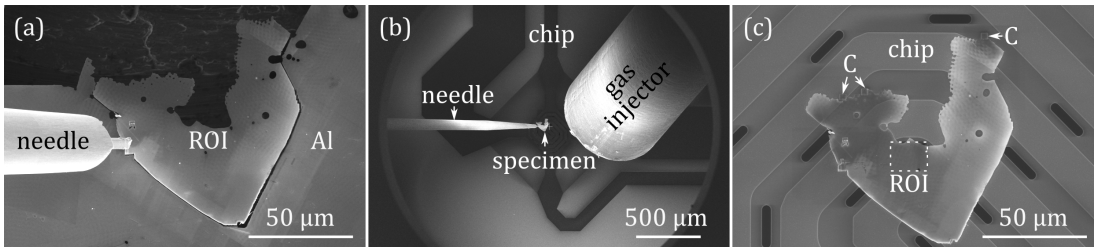

Figure 6.12: FIB preparation of a specimen of Al alloy 6082 to be used for *in-situ* heating. The specimen had prior to FIB preparation been electropolished and examined in TEM to located thin grains oriented close to zone axis [001]. The ROI was identified using SEM, and it was cut out by performing milling at least $\gtrsim 20\ \mu m$ away from the ROI. SE SEM images taken **(a)** after the lift-out needle had been attached to the edge of the Al flake by ion beam deposition of C, **(b)** while the lift-out needle was being used to transfer the specimen to the heating chip, and **(c)** after the Al flake had been attached to the heating chip by ion beam deposition of C, so that the ROI laid over a hole in the chip.

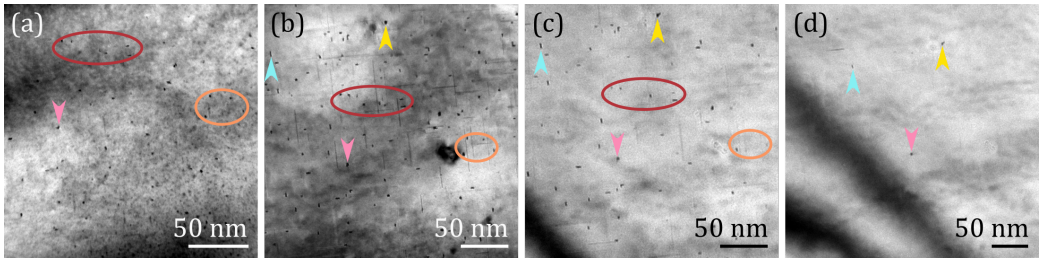

Figure 6.13: BF-TEM images from a proof-of-concept *in-situ* heating experiment. The specimen was a 6082 Al alloy that had been solutionised and heat treated at 170°C for 3 min *ex-situ*. BF-TEM images after *in-situ* heating (additive): **(a)** for 2 h at 180°C and quenching to 20°C, and **(b)** after heating from 240°C to 280°C at a rate of 10°C/s and subsequently quenching to 20°C. BF-TEM images acquired during *in-situ* heating from $280 - 440$°C at a rate of 10°C/s, recorded at a temperature of **(c)** ∼290°C and **(d)** ∼320°C. In the images, the coloured arrow heads and ellipses indicate corresponding specimen locations.

Chapter 7

Conclusions

This work focused on EM characterisation of the interfacial IMP layers that had formed in Al-steel joints. Various Al-steel joints fabricated by the welding methods HYB, RB and CMT, were studied. The HYB method showed great prospects for multi-metal welding, and the underlying bonding mechanisms were identified to be microscale mechanical interlocking and formation of nanoscale interfacial IMP layers.

A second generation HYB Al-steel joint showed an IMP layer that was only $10 - 50$ nm thick, and zone axis patterns could not be collected in a conventional manner from the IMP layer crystals. Instead SED was employed. S(P)ED is a powerful technique that together with (semi-)automatic data analysis enables assessment of the local crystallography on the nanoscale. A typical challenge in S(P)ED data analysis is that diffraction from several crystals can appear in a single diffraction pattern. To overcome this, two nanocrystal segmentation strategies were explored, one based on VDF imaging and the other on NMF. The two approaches were applied to MgO SPED data, and it was found that both could be used for segmentation, as long as artefacts were critically evaluated.

The formation and growth of the interfacial IMP layers strongly depend on the alloying elements in both the Al alloy and the steel, in addition to the thermo-mechanical processing history. The joints studied in this work were made using Al alloys containing Si and Mn, amongst other elements, and the interfacial IMP layers in these joints had in common that they contained the α_c-Al-(Fe,Mn)-Si phase. With prolonged interdiffusion, the θ-Fe_4Al_{13} and η-Fe_2Al_5 phases also formed. Moreover, the alloying elements Si, Mn, Cr and Ni led to a reduction in the growth rate of the total IMP layer. The morphologies, chemical compositions and crystal structures of the IMPs were assessed using EM techniques, mainly by combining EDS with imaging and diffraction techniques.

Lastly, some unpublished proof-of-concept studies were discussed that highlighted challenges with *in-situ* heating TEM experiments where interdiffusion phenomena are investigated. In general, combining *in-situ* heating with spectroscopy and S(P)ED data collection holds great potential, which should be further explored in future work. Especially with the emergence of direct electron detectors, S(P)ED techniques offer a broad range of opportunities, including the possibility of studying weak diffraction signals and beam sensitive materials. Overall, this work demonstrates the importance of TEM diffraction techniques in the characterisation of the interface regions in Al-steel joints, and the methods used can be applied to a wide range of materials.

Bibliography

[1] K. Martinsen, S. J. Hu and B. E. Carlson, "Joining of dissimilar materials," *CIRP Annals - Manufacturing Technology*, vol. 64, pp. 679–699, 2015. DOI: 10.1016/j.cirp.2015.05.006.

[2] H. Wargnier, F. X. Kromm, M. Danis and Y. Brechet, "Proposal for a multi-material design procedure," *Materials and Design*, vol. 56, pp. 44–49, 2014. DOI: 10.1016/j.matdes.2013.11.004.

[3] X. Cui, S. Wang and S. J. Hu, "A method for optimal design of automotive body assembly using multi-material construction," *Materials and Design*, vol. 29, no. 2, pp. 381–387, 2008. DOI: 10.1016/j.matdes.2007.01.024.

[4] C. D. Horvath, "Advanced steels for lightweight automotive structures," in *Materials, Design and Manufacturing for Lightweight Vehicles*, 2010, pp. 35–78. DOI: 10.1533/9781845697822.1.35.

[5] F Ashby, "Overview no. 80 On the engineering properties of materials," *Acta Metallurgica*, vol. 37, no. 5, pp. 1273–1293, 1989.

[6] I. Polmear, D. St John, J. F. Nie and M Qian, *Light alloys: metallurgy of the light metals*, 2017.

[7] J. Hirsch, "Aluminium in Innovative Light-Weight Car Design," *Materials Transactions*, vol. 52, no. 5, pp. 818–824, 2011. DOI: 10.2320/matertrans.L-MZ201132.

[8] ——, "Recent development in aluminium for automotive applications," *Transactions of Nonferrous Metals Society of China (English Edition)*, vol. 24, no. 7, pp. 1995–2002, 2014. DOI: 10.1016/S1003-6326(14)63305-7.

[9] M. H. Kaiser, "The aluminium spaceframe," *Manufacturing Engineer*, pp. 125–129, 1998.

[10] A. Kochan, "Audi moves forward with all-aluminium cars," *Assembly Automation*, vol. 20, no. 2, pp. 132–135, 2000. DOI: 10.1108/01445150010321751.

[11] K. Hans Wedepohl, "The composition of the continental crust," *Geochimica et Cosmochimica Acta*, vol. 59, no. 7, pp. 1217–1232, 1995. DOI: 10.1016/0016-7037(95)00038-2.

[12] T. Nanda, V. Singh, V. Singh, A. Chakraborty and S. Sharma, "Third generation of advanced high-strength steels: Processing routes and properties," *Proceedings of the Institution of Mechanical Engineers, Part L: Journal of Materials: Design and Applications*, vol. 233, no. 2, pp. 209–238, 2019. DOI: 10.1177/1464420716664198.

[13] T. Hottle, C. Caffrey, J. McDonald and R. Dodder, "Critical factors affecting life cycle assessments of material choice for vehicle mass reduction," *Transportation Research Part D: Transport and Environment*, vol. 56, pp. 241–257, 2017. DOI: 10.1016/j.trd.2017.08.010.

[14] I. Polmear, *Light alloys: from traditional alloys to nanocrystals*, 2005.

[15] J. Motavalli, "For lightweight cars, a materials race," *The New York Times*, vol. Oct 11, 2012. [Online]. Available: https://www.nytimes.com/2012/10/12/automobiles/for-lightweight-cars-a-race-among-steel-aluminum-and-carbon-fiber.html{\%}0A.

[16] D Paratore, "Material wars - who's going to win the automotive metals race?" *Industry Week*, vol. Jul 9. 2015. [Online]. Available: https://www.industryweek.com/leadership/companies-executives/article/21965870/material-wars-whos-going-to-win-the-automotive-metals-race.

[17] I. Maw, "The Battle of the Bodies: Steel vs. Aluminum in Automotive Production," *Engineering.com*, vol. Feb 5. 2018. [Online]. Available: https://www.engineering.com/AdvancedManufacturing/ArticleID/16437/The-Battle-of-the-Bodies-Steel-vs-Aluminum-in-Automotive-Production.aspx{\%}0A.

[18] L. Berger, M. Lesemann and C. Sahr, "SuperLIGHT-CAR – the Multi-Material Car Body," *7th European LS-DYNA Conference*, pp. 1–10, 2009. [Online]. Available: https://www.dynamore.de/de/download/papers/forum08/dokumente/F-III-01.pdf.

[19] European Aluminium Association, "EAA Aluminium Automotive Manual – Joining," pp. 1–5, 2015. [Online]. Available: https://www.european-aluminium.eu/resource-hub/aluminium-automotive-manual/.

[20] K. I. Mori, N. Bay, L. Fratini, F. Micari and A. E. Tekkaya, "Joining by plastic deformation," *CIRP Annals - Manufacturing Technology*, vol. 62, no. 2, pp. 673–694, 2013. DOI: 10.1016/j.cirp.2013.05.004.

[21] X. Li, A. Scherf, M. Heilmaier and F. Stein, "The Al-Rich Part of the Fe-Al Phase Diagram," *Journal of Phase Equilibria and Diffusion*, vol. 37, no. 2, pp. 1–12, 2016. DOI: 10.1007/s11669-015-0446-7.

[22] H. Springer, A. Kostka, E. J. Payton, D. Raabe, A. Kaysser-Pyzalla and G. Eggeler, "On the formation and growth of intermetallic phases during interdiffusion between low-carbon steel and aluminum alloys," *Acta Materialia*, vol. 59, no. 4, pp. 1586–1600, 2011. DOI: 10.1016/j.actamat.2010.11.023.

[23] T. Tanaka, T. Morishige and T. Hirata, "Comprehensive analysis of joint strength for dissimilar friction stir welds of mild steel to aluminum alloys," *Scripta Materialia*, vol. 61, no. 7, pp. 756–759, 2009. DOI: 10.1016/j.scriptamat.2009.06.022.

[24] H. Springer, A. Kostka, J. F. dos Santos and D. Raabe, "Influence of intermetallic phases and Kirkendall-porosity on the mechanical properties of joints between steel and aluminium alloys," *Materials Science and Engineering A*, vol. 528, no. 13-14, pp. 4630–4642, 2011. DOI: 10.1016/j.msea.2011.02.057.

[25] W. Cai, G. Daehn, A. Vivek, J. Li, H. Khan, R. S. Mishra and M. Komarasamy, "A state-of-the-art review on solid-state metal joining," *Journal of Manufacturing Science and Engineering, Transactions of the ASME*, vol. 141, no. 3, pp. 1–35, 2019. DOI: 10.1115/1.4041182.

[26] J. Bruckner, "Considering thermal processes for dissimilar metals: joining steel to aluminum in heat-intensive applications," *Fabricator*, 2003.

[27] W. M. Thomas, E. D. Nicholas, J. C. Needham, M. G. Murch, P Temple-Smith and C. J. Dawes, *Friction welding*, 1995.

[28] Honda Motor Co., *Honda Develops New Technology to Weld Together Steel and Aluminum and Achieves World's First Application to the Frame of a Mass-production Vehicle - Hybrid-Structured Front Subframe Achieves Both Weight Reduction and Increased Rigidity* -, 2012. [Online]. Available: https://global.honda/newsroom/news/2012/4120906beng.html.

[29] Ø. Grong, *Method and device for joining of metal components, particularly light metal components*, 2003.

[30] U. R. Aakenes, Ø. Grong and T. Austigard, *Device for Solid State Joining of Light Metals*, 2013.

[31] HyBond AS, *HyBond AS - a bonding revolution.* [Online]. Available: http://www.hybond.no/.

[32] J. M. Zuo and J. C. H. Spence, *Advanced Transmission Electron Microscopy Imaging and Diffraction in Nanoscience*, 2017.

[33] D. B. Williams and C. Barry Carter, *Transmission Electron Microscopy A Textbook for Materials Science.* Springer Science and Business Media, 2009.

[34] *SFI Manufacturing*, 2019. [Online]. Available: https://www.sfimanufacturing.no/sfi-manufacturing.html.

[35] G. E. Totten and D. S MacKenzie, *Handbook of aluminum: vol. 1: physical metallurgy and processes*, 2003.

[36] F. C. Campbell, *Lightweight Materials - Understanding the Basics*, 2012.

[37] ——, *Elements of Metallurgy and Engineering Alloys*, 2008.

[38] M. Humphreys, Frederick John Hatherly, *Recrystallization and related annealing phenomena*, 2012.

[39] S. J. Andersen, C. D. Marioara, J. Friis, S. Wenner and R. Holmestad, "Precipitates in aluminium alloys," *Advances in Physics: X*, vol. 3, no. 1, pp. 790–814, 2018. DOI: 10.1080/23746149.2018.1479984.

[40] T. Saito, E. A. Mørtsell, S. Wenner, C. D. Marioara, S. J. Andersen, J. Friis, K. Matsuda and R. Holmestad, "Atomic Structures of Precipitates in Al–Mg–Si Alloys with Small Additions of Other Elements," *Advanced Engineering Materials*, vol. 20, no. 7, pp. 1–18, 2018. DOI: 10.1002/adem.201800125.

[41] G. A. Edwards, K. Stiller, G. L. Dunlop and M. J. Couper, "The precipitation sequence in Al-Mg-Si alloys," *Acta Materialia*, vol. 46, no. 11, pp. 3893–3904, 1998. DOI: 10.1016/S1359-6454(98)00059-7.

[42] K. Matsuda, Y. Sakaguchi, Y. Miyata, Y. Uetani, T. Sato, A. Kamio and S. Ikeno, "Precipitation sequence of various kinds of metastable phases in Al-1.0mass% Mg2Si-0.4mass% Si alloy," *Journal of Materials Science*, vol. 35, no. 1, pp. 179–189, 2000. DOI: 10.1023/A:1004769305736.

[43] C. D. Marioara, S. J. Andersen, H. W. Zandbergen and R. Holmestad, "The influence of alloy composition on precipitates of the Al-Mg-Si system," *Metallurgical and Materials Transactions A*, vol. 36, no. 13, pp. 691–702, 2005. DOI: 10.1007/s11661-005-1001-7.

[44] O. Reiso, "Extrusion of AlMgSi alloys," *Materials Forum*, vol. 28, pp. 32–46, 2004.

[45] W. D. J. Callister, *Materials Science and Engineering An Introduction*, 7th ed. John Wiley & Sons Inc, 2007.

[46] D. Hull and D. J. Bacon, *Introduction to Dislocations*, 2011. DOI: 10.1016/C2009-0-64358-0.

[47] A Kelly and K. M. Knowles, *Crystallography and crystal defects*, 2012. DOI: 10.1016/0047-7206(70)90050-6.

[48] J. D. Verhoeven, *Fundamentals of physical metallurgy*, 1975.

[49] H. Bhadeshia and R. Honeycombe, *Steels - Microstructure and properties*, 2017.

[50] A. M. F. Muggerud, E. A. Mørtsell, Y. Li and R. Holmestad, "Dispersoid strengthening in AA3xxx alloys with varying Mn and Si content during annealing at low temperatures," *Materials Science and Engineering A*, vol. 567, pp. 21–28, 2013. DOI: 10.1016/j.msea.2013.01.004.

[51] A. J. Ardell, "Precipitation hardening," *Metallurgical Transactions A*, vol. 16A, pp. 2131–2165, 1985. DOI: 10.1063/1.1714842.

[52] O. R. Myhr, Ø Grong and S. J. Andersen, "Modelling of the age hardening behaviour of Al–Mg–Si alloys," *Acta Materialia*, vol. 49, pp. 65–75, 2001.

[53] O. R. Myhr, Ø. Grong and K. O. Pedersen, "A combined precipitation, yield strength, and work hardening model for Al-Mg-Si alloys," *Metallurgical and Materials Transactions A: Physical Metallurgy and Materials Science*, vol. 41, no. 9, pp. 2276–2289, 2010. DOI: 10.1007/s11661-010-0258-7.

[54] H. Okamoto, "The C-Fe (Carbon-Iron) System," *Journal of Phase Equilibria*, vol. 13, no. 5, pp. 543–565, 1992.

[55] C. C. Tasan, M. Diehl, D. Yan, M. Bechtold, F. Roters, L. Schemmann, C. Zheng, N. Peranio, D. Ponge, M. Koyama, K. Tsuzaki and D. Raabe, "An Overview of Dual-Phase Steels: Advances in Microstructure-Oriented Processing and Micromechanically Guided Design," *Annual Review of Materials Research*, vol. 45, pp. 391–431, 2015. DOI: 10.1146/annurev-matsci-070214-021103.

[56] B. L. Bramfitt and A. O. Benscoter, "Introduction to Steels and Cast Irons," in *Metallographer's Guide: Practices and Procedures for Irons and Steels*, ASM International, 2019, pp. 1–21. DOI: 10.31399/asm.tb.mgppis.t60400001.

[57] ASM Handbook Committee, *Properties and Selection: Irons, Steels, and High-Performance Alloys*, 1990. DOI: 10.31399/asm.hb.v01.9781627081610.

[58] A. S. Lima, A. M. Nascimento, H. F. Abreu and P. De Lima-Neto, "Sensitization evaluation of the austenitic stainless steel AISI 304L, 316L, 321 and 347," *Journal of Materials Science*, vol. 40, no. 1, pp. 139–144, 2005. DOI: 10.1007/s10853-005-5699-9.

[59] R. W. Messler, *Joining of materials and structures: from pragmatic process to enabling technology*, 2004.

[60] J. Varis, "Ensuring the integrity in clinching process," *Journal of Materials Processing Technology*, vol. 174, no. 1-3, pp. 277–285, 2006. DOI: 10.1016/j.jmatprotec.2006.02.001.

[61] F. C. Campbell, *Joining: understanding the basics*, 2011.

[62] T. A. Barnes and I. R. Pashby, "Joining techniques for aluminum spaceframes used in automobiles. Part II - adhesive bonding and mechanical fasteners," *Journal of Materials Processing Technology*, vol. 99, no. 1, pp. 72–79, 2000. DOI: 10.1016/S0924-0136(99)00361-1.

[63] J. Bruckner, "Cold metal transfer has a future joining steel to aluminum," *Welding Journal*, vol. 84, no. 6, pp. 38–40, 2005.

[64] P. Groche, S. Wohletz, M. Brenneis, C. Pabst and F. Resch, "Joining by forming - A review on joint mechanisms, applications and future trends," *Journal of Materials Processing Technology*, vol. 214, no. 10, pp. 1972–1994, 2014. DOI: 10.1016/j.jmatprotec.2013.12.022.

[65] L. Li, K. Nagai and F. Yin, "Progress in cold roll bonding of metals," *Science and Technology of Advanced Materials*, vol. 9, no. 023001, 2008. DOI: 10.1088/1468-6996/9/2/023001.

[66] L. R. Vaidyanath and D. R. Milner, "Significance of surface preparation in cold pressure welding," *British Welding Journal*, 1960.

[67] H. Mohamed and J. Washburn, "Mechanism of solid state pressure welding," *Welding journal*, vol. 54, pp. 302–310, 1975.

[68] N Bay, "Cold pressure welding - The mechanisms governing bonding," *Journal of Engineering for Industry*, vol. 101, pp. 121–127, 1979.

[69] N Bay, C Clemensen, O Juelstorp and T Wanheim, "Bond Strength in Cold Roll Bonding," *Annals of the CIRP*, vol. 34, no. 2, pp. 221–224, 1985.

[70] N. Bay, "Mechanisms Producing Metallic Bonds in Cold Welding," *Welding Journal (Miami, Fla)*, vol. 62, no. 5, pp. 137–142, 1983.

[71] Zhang.W and N. Bay, "Cold welding-Experimental Investigation of the Surface Preparation Methods," *Welding Reseach Supplement*, vol. 76, no. 8, pp. 326–330, 1997.

[72] D. R. Cooper and J. M. Allwood, "The influence of deformation conditions in solid-state aluminium welding processes on the resulting weld strength," *Journal of Materials Processing Technology*, vol. 214, no. 11, pp. 2576–2592, 2014. DOI: 10.1016/j.jmatprotec.2014.04.018.

[73] M Movahedi, A. H. Kokabi and S. M. S. Reihani, "Investigation on the bond strength of Al-1100 / St-12 roll bonded sheets , optimization and characterization," *Materials and Design*, vol. 32, no. 6, pp. 3143–3149, 2011. DOI: 10.1016/j.matdes.2011.02.057.

[74] R Jamaati and M. R. Toroghinejad, "Cold roll bonding bond strengths: review," *Materials Science and Technology*, vol. 27, no. 7, pp. 1101–1108, 2011. DOI: 10.1179/026708310X12815992418256.

[75] P. L. Threadgilll, A. J. Leonard, H. R. Shercliff and P. J. Withers, "Friction stir welding of aluminium alloys," *International Materials Reviews*, vol. 54, no. 2, pp. 49–93, 2009. DOI: 10.1179/174328009X411136.

[76] A. Heidarzadeh, S. Mironov, R. Kaibyshev, G. Çam, A. Simar, A. Gerlich, F. Khodabakhshi, A. Mostafaei, D. P. Field, J. D. Robson, A. Deschamps and P. J. Withers, "Friction stir welding/processing of metals and alloys: A comprehensive review on microstructural evolution," *Progress in Materials Science*, no. March 2019, 2020. DOI: 10.1016/j.pmatsci.2020.100752.

[77] W. H. Jiang and R. Kovacevic, "Feasibility study of friction stir welding of 6061-T6 aluminium alloy with AISI 1018 steel," *Proceedings of the Institution of Mechanical Engineers, Part B: Journal of Engineering Manufacture*, vol. 218, no. 10, pp. 1323–1331, 2004. DOI: 10.1243/0954405042323612.

[78] K. Kimapong and T. Watanabe, "Friction stir welding of aluminum alloy to steel," *Welding Journal (Miami, Fla)*, vol. 83, no. 10, pp. 277–282, 2004.

[79] W. M. Thomas and E. D. Nicholas, "Friction stir welding for the transportation industries," *Materials and Design*, vol. 18, no. 4-6, pp. 269–273, 1997. DOI: 10.1016/s0261-3069(97)00062-9.

[80] P. L. Threadgill, "Terminology in friction stir welding," *Science and Technology of Welding and Joining*, vol. 12, no. 4, pp. 357–360, 2007. DOI: 10.1179/174329307X197629.

[81] W. M. Thomas and R. E. Dolby, "Friction stir welding developments," *6th International Conference on Trends in Welding Research*, no. April 2002, 2002. DOI: 10.1201/b10386.

[82] L.-E. Svensson, L. Karlsson, H. Larsson, B. Karlsson, M. Fazzini and J. Karlsson, "Microstructure and Mechanical Properties of Friction Stir Welded 5083 and 7075 Aluminum Alloys," *Science and Technology of Welding and Joining*, vol. 5, pp. 285–296, 2000. DOI: 10.1007/s11665-017-2543-8.

[83] B. Heinz and B. Skrotzki, "Characterization of a friction-stir-welded aluminum alloy 6013," *Metallurgical and Materials Transactions B: Process Metallurgy and Materials Processing Science*, vol. 33, no. 3, pp. 489–498, 2002. DOI: 10.1007/s11663-002-0059-5.

[84] L. E. Murr, Y. Li, R. D. Flores, E. A. Trillo and J. C. McClure, "Intercalation vortices and related microstructural features in the friction-stir welding of dissimilar metals," *Mat Res Innovat*, vol. 2, pp. 150–163, 1998.

[85] A. Steuwer, M. J. Peel and P. J. Withers, "Dissimilar friction stir welds in AA5083-AA6082: The effect of process parameters on residual stress," *Materials Science and Engineering A*, vol. 441, no. 1-2, pp. 187–196, 2006. DOI: 10.1016/j.msea.2006.08.012.

[86] O. R. Myhr and Ø. Grong, "Process modelling applied to 6082-T6 aluminium weldments II. Applications of model," *Acta Metallurgica Et Materialia*, vol. 39, no. 1, pp. 2703–2708, 1991.

[87] Y. S. Sato, H. Kokawa, M. Enomoto and S. Jogan, "Microstructural evolution of 6063 aluminum during friction-stir welding," *Metallurgical and Materials Transactions A*, vol. 30, no. 9, pp. 2429–2437, 1999. DOI: 10.1007/s11661-999-0251-1.

[88] Ø. Frigaard, Ø. Grong and O. T. Midling, "A process model for friction stir welding of age hardening aluminum alloys," *Metallurgical and Materials Transactions A*, vol. 32, no. 5, pp. 1189–1200, 2001. DOI: 10.1007/s11661-001-0128-4.

[89] R. S. Mishra and Z. Y. Ma, "Friction stir welding and processing," *Materials Science and Engineering R: Reports*, vol. 50, no. 1-2, pp. 1–78, 2005. DOI: 10.1016/j.mser.2005.07.001.

[90] A. Simar, Y. Bréchet, B. De Meester, A. Denquin, C. Gallais and T. Pardoen, "Integrated modeling of friction stir welding of 6xxx series Al alloys: Process, microstructure and properties," *Progress in Materials Science*, vol. 57, no. 1, pp. 95–183, 2012. DOI: 10.1016/j.pmatsci.2011.05.003.

[91] D. Jacquin and G. Guillemot, "A review of microstructural changes occurring during FSW in aluminium alloys and their modelling," *Journal of Materials Processing Technology*, vol. 288, 2021. DOI: 10.1016/j.jmatprotec.2020.116706.

[92] Ø Grong, "Recent advances in solid-state joining of aluminum," *Welding Journal*, vol. 91, no. 1, pp. 26–33, 2012.

[93] U. R. Aakenes, "Industrialising of the Hybrid Metal Extru usion & Bonding (HYB) method – from prototype towards commercial process," PhD thesis, Norwegian University of Science and Technology, 2013.

[94] U. R. Aakenes, Ø. Grong and T. Austigard, "Application of the Hybrid Metal Extrusion & Bonding (HYB) method for joining of AA6082-T6 base material," *Materials Science Forum*, vol. 794-796, pp. 339–344, 2014. DOI: 10.4028/www.scientific.net/MSF.794-796.339.

[95] F. Leoni, Ø. Grong, L. Sandnes, T. Welo and F. Berto, "Finite element modelling of the filler wire feeding in the hybrid metal extrusion & bonding (HYB) process," *Journal of Advanced Joining Processes*, vol. 1, no. November 2019, p. 100 006, 2020. DOI: 10.1016/j.jajp.2020.100006.

[96] L. Sandnes, Ø. Grong, J. Torgersen, T. Welo and F. Berto, "Exploring the hybrid metal extrusion and bonding process for butt welding of Al–Mg–Si alloys," *International Journal of Advanced Manufacturing Technology*, vol. 98, no. 5-8, pp. 1059–1065, 2018. DOI: 10.1007/s00170-018-2234-0.

[97] D. Green, *Extrusion*, 1975.

[98] C Etherington, "Conform — A New Concept for the Continuous Extrusion Forming of Metals," *Journal of Engineering for Industry*, pp. 893–900, 1974.

[99] Ø. Grong, L. Sandnes and F. Berto, "A status report on the hybrid metal extrusion & bonding (HYB) process and its applications," *Material Design & Processing Communications*, vol. 1, no. 2, e41, 2019. DOI: 10.1002/mdp2.41.

[100] ——, "Progress in solid state joining of metals and alloys," *Procedia Structural Integrity*, vol. 17, pp. 788–798, 2019. DOI: 10.1016/j.prostr.2019.08.105.

[101] F. Leoni, Ø. Grong, P. Ferro and F. Berto, "Simulating the dependence of the filler wire feeding on the wire size in the hybrid metal extrusion & bonding (HYB) process," *Procedia Structural Integrity*, vol. 26, no. 2019, pp. 321–329, 2020. DOI: 10.1016/j.prostr.2020.06.041.

[102] Ø. Grong, U. R. Aakenes, T. G. Austigard and T. Bjering, *Extrusion material*, 2016.

[103] F. Abbatinali, L. Sandnes, Ø. Grong, J. Torgersen, F. Berto and P. Ferro, "Mechanical Characterization and Crack Growth Path Analysis of a Hybrid Metal Extrusion & Bonding (HYB) Joint of AA6082-T6 Aluminium Alloy and S355 Structural Steel," *6th International Conference on Crack Paths (CP 2018)*, no. September, pp. 1–6, 2018.

[104] F. Berto, L. Sandnes, F. Abbatinali, O. Grong and P. Ferro, "Using the Hybrid Metal Extrusion & Bonding (HYB) Process for Dissimilar Joining of AA6082-T6 and S355," *Procedia Structural Integrity*, vol. 13, pp. 249–254, 2018. DOI: 10.1016/j.prostr.2018.12.042.

[105] L. Sandnes and T. Welo, "Fatigue properties of AA6060-T6 butt welds made by hybrid metal extrusion & bonding," *Fatigue Fract Eng Mater Struct.*, no. July, pp. 2349–2358, 2020. DOI: 10.1111/ffe.13302.

[106] L. Sandnes and F. Berto, "Qualification of the hybrid metal extrusion & bonding (HYB) process for welding of aluminium offshore structures," *Material Design & Processing Communications*, no. June, pp. 1–9, 2020. DOI: 10.1002/mdp2.194.

[107] J. Blindheim, T. Welo and M. Steinert, "First demonstration of a new additive manufacturing process based on metal extrusion and solid-state bonding," *International Journal of Advanced Manufacturing Technology*, vol. 105, no. 5-6, pp. 2523–2530, 2019. DOI: 10.1007/s00170-019-04385-8.

[108] ——, "Rapid prototyping and physical modelling in the development of a new additive manufacturing process for aluminium alloys," *Procedia Manufacturing*, vol. 34, pp. 489–496, 2019. DOI: 10.1016/j.promfg.2019.06.212.

[109] K Furukawa, "New CMT arc welding process - welding of steel to aluminium dissimilar metals and welding of super-thin aluminium sheets," *Welding International*, vol. 20, no. 6, pp. 440–445, 2006. DOI: 10.1533/wint.2006.3598.

[110] S Selvi, A Vishvaksenan and E Rajasekar, "Cold metal transfer (CMT) technology - An overview," *Defence Technology*, vol. 14, no. 1, pp. 1–17, 2017. DOI: 10.1016/j.dt.2017.08.002.

[111] J. Agudo, N Jank, S Weber, C Schmaranzer, E Arenholz, J Bruckner, H Hackl and A Pyzalla, "Investigation of Microstructure and Mechanical Properties of Steel-Aluminium Joints Produced by Metal Arc Joining," *Materials Technology*, vol. 79, no. 7, pp. 2–7, 2008.

[112] J. Feng, H. Zhang and P. He, "The CMT short-circuiting metal transfer process and its use in thin aluminium sheets welding," *Materials and Design*, vol. 30, no. 5, pp. 1850–1852, 2009. DOI: 10.1016/j.matdes.2008.07.015.

[113] H. T. Zhang, J. C. Feng, P. He, B. B. Zhang, J. M. Chen and L. Wang, "The arc characteristics and metal transfer behaviour of cold metal transfer and its use in joining aluminium to zinc-coated steel," *Materials Science and Engineering A*, vol. 499, no. 1-2, pp. 111–113, 2009. DOI: 10.1016/j.msea.2007.11.124.

[114] L. Zhang, Y. Du, H. Xu, C. Tang, H. Chen and W. Zhang, "Phase equilibria of the Al-Fe-Ni system at 850 °C and 627 °C," *Journal of Alloys and Compounds*, vol. 454, no. 1-2, pp. 129–135, 2008. DOI: 10.1016/j.jallcom.2006.12.042.

[115] Z. Silvayeh, B. Götzinger, W. Karner, M. Hartmann and C. Sommitsch, "Calculation of the Intermetallic Layer Thickness in Cold Metal Transfer Welding of Aluminum to Steel," *Materials*, vol. 12, no. 35, pp. 14–16, 2018. DOI: 10.3390/ma12010035.

[116] E. P. Zapico, A. H. Lutey, A. Ascari, C. R. Gómez Pérez, E. Liverani and A. Fortunato, "An improved model for cold metal transfer welding of aluminium alloys," *Journal of Thermal Analysis and Calorimetry*, vol. 131, no. 3, pp. 3003–3009, 2018. DOI: 10.1007/s10973-017-6800-8.

[117] M. Kang and C. Kim, "Joining Al 5052 alloy to aluminized steel sheet using cold metal transfer process," *Materials and Design*, vol. 81, pp. 95–103, 2015. DOI: 10.1016/j.matdes.2015.05.035.

[118] M. R. Ahsan, Y. R. Kim, C. H. Kim, J. W. Kim, R. Ashiri and Y. D. Park, "Porosity formation mechanisms in cold metal transfer (CMT) gas metal arc welding (GMAW) of zinc coated steels," *Science and Technology of Welding and Joining*, vol. 21, no. 3, pp. 209–215, 2016. DOI: 10.1179/1362171815Y.0000000084.

[119] H. Zhang and J. Liu, "Microstructure characteristics and mechanical property of aluminum alloy / stainless steel lap joints fabricated by MIG welding – brazing process," *Materials Science and Engineering A*, vol. 528, pp. 6179–6185, 2011. DOI: 10.1016/j.msea.2011.04.039.

[120] S. Yang, J. Zhang, J. Lian and Y. Lei, "Welding of aluminum alloy to zinc coated steel by cold metal transfer," *Materials and Design*, vol. 49, pp. 602–612, 2013. DOI: 10.1016/j.matdes.2013.01.045.

[121] L. A. Jacome, S. Weber, A. Leitner, E. Arenholz, J. Bruckner, H. Hackl and A. R. Pyzalla, "Influence of Filler Composition on the Microstructure and Mechanical Properties of Steel - Aluminum Joints Produced by Metal Arc Joining," *Advanced Engineering Materials*, vol. 11, no. 5, pp. 350–358, 2009. DOI: 10.1002/adem.200800319.

[122] U. Kattner and B. Burton, "Al-Fe (Aluminum-Iron)," *ASM Metals Handbook*, vol. Volume 3 A, pp. 294–295, 1992.

[123] I. Chumak, K. W. Richter and H. Ehrenberg, "Redetermination of iron dialuminide, FeAl2," *Acta Crystallographica*, vol. 66, no. 9, pp. 87–88, 2010. DOI: 10.1107/S0108270110033202.

[124] U. Burkhardt, Y. Grin, M. Ellner and K. Peters, "Structure refinement of the iron–aluminium phase with the approximate composition Fe2Al5," *Acta Crystallographica*, vol. 50, no. 3, pp. 313–316, 1994. DOI: 10.1107/S0108768193013989.

[125] N. L. Okamoto, J. Okumura, M. Higashi and H. Inui, "Crystal structure of η'-Fe3Al8; low-temperature phase of η-Fe2Al5 accompanied by an ordered arrangement of Al atoms of full occupancy in the c -axis chain sites," *Acta Materialia*, vol. 129, pp. 290–299, 2017. DOI: 10.1016/j.actamat.2017.02.060.

[126] J. Grin, U. Burkhardt, M. Ellner and K. Peters, "Refinement of the Fe4Al13 structure and its relationship to the quasihomological homeotypical structures," *Zeitschrift fur Kristallographie*, vol. 209, no. 6, pp. 479–487, 1994. DOI: 10.1524/zkri.1994.209.6.479.

[127] I. Chumak, K. W. Richter and H. Ipser, "The Fe-Ni-Al phase diagram in the Al-rich (>50 at.% Al) corner," *Intermetallics*, vol. 15, no. 11, pp. 1416–1424, 2007. DOI: 10.1016/j.intermet.2007.04.012.

[128] J. Gjønnes, V. Hansen, B. S. Berg, P. Runde, Y. F. Cheng, K. Gjønnes, D. L. Dorset and C. J. Gilmore, "Structure Model for the Phase AlmFe Derived from Three-Dimensional Electron Diffraction Intensity Data Collected by a Precession Technique. Comparison with Convergent-Beam Diffraction," *Acta Crystallographica*, vol. A54, no. 3, pp. 306–319, 1998. DOI: 10.1107/S0108767397017030.

[129] L. K. Walford, "The structure of the intermetallic phase FeAl6," *Acta Crystallographica*, vol. 18, no. 2, pp. 287–291, 1965. DOI: 10.1107/S0365110X65000610.

[130] P Skjerpe and J Gjønnes, "Solidification structure and primary Al-Fe-Si particles in direct-chilled-cast aluminium alloys," *Ultramicroscopy*, vol. 22, pp. 239–250, 1987.

[131] P. Skjerpe, "Intermetallic phases formed during DC-casting of an Al-0.25 Wt Pct Fe-0.13 Wt Pct Si alloy," *Metallurgical Transactions A*, vol. 18, no. 2, pp. 189–200, 1987. DOI: 10.1007/BF02825700.

[132] P. Skjerpe, "Structure of AlmFe," *Acta Crystallographica Section B*, vol. 44, no. 5, pp. 480–486, 1988. DOI: 10.1107/S0108768188005245.

[133] N. Krendelsberger, F. Weitzer and J. C. Schuster, "On the Reaction Scheme and Liquidus Surface in the Ternary System Al-Fe-Si," *Metallurgical and Materials Transactions A*, vol. 38, no. August, 2007. DOI: 10.1007/s11661-007-9182-x.

[134] M. C. J. Marker, B. Skolyszewska-Kühberger, H. S. Effenberger, C. Schmetterer and K. W. Richter, "Intermetallics Phase equilibria and structural investigations in the system Al-Fe-Si," *Intermetallics*, vol. 19, no. 12, pp. 1919–1929, 2011. DOI: 10.1016/j.intermet.2011.05.003.

[135] H. Becker and A. Leineweber, "Atomic channel occupation in disordered η-Al5Fe2 and in two of its low-temperatures phases, η " and η "'," *Intermetallics*, vol. 93, no. August 2017, pp. 251–262, 2018. DOI: 10.1016/j.intermet.2017.09.021.

[136] H. Becker, L Amirkhanyan, J Kortus and A. Leineweber, "Powder X-ray diffrcation analysis of the crystal structure of the η'-Al8Fe3 (η'-Al2.67Fe) phase," *Journal of Alloys and Compounds*, vol. 721, pp. 691–696, 2017. DOI: 10.1016/j.jallcom.2017.05.336.

[137] C. J. Simensen and R Vellasamy, "Determination of phases present in cast material of an Al-0.5Wt.% Fe-0.2 Wt.% Si alloy," *Zeitschrift für Metallkunde*, pp. 428–431, 1977.

[138] X. Z. Li and K. H. Kuo, "Decagonal quasicrystals with different periodicities along the tenfold axis in rapidly solidified al-ni alloys," *Philosophical Magazine Letters*, vol. 58, no. 3, pp. 167–171, 1988. DOI: 10.1080/09500838808214749.

[139] D. Hao, B. Hu, K. Zhang, L. Zhang and Y. Du, "The quaternary Al-Fe-Ni-Si phase equilibria in Al-rich corner: Experimental measurement and thermodynamic modeling," *Journal of Materials Science*, vol. 49, no. 3, pp. 1157–1169, 2014. DOI: 10.1007/s10853-013-7795-6.

[140] W. Khalifa, F. H. Samuel and J. E. Gruzleski, "Iron intermetallic phases in the Al corner of the Al-Si-Fe system," *Metallurgical and Materials Transactions A*, vol. 34, no. 13, pp. 807–825, 2003. DOI: 10.1007/s11661-003-1009-9.

[141] A. D. I. Nicol, "The structure of MnAl6," *Acta Crystallographica*, vol. 6, no. 3, pp. 285–293, 1953. DOI: 10.1107/S0365110X53000788.

[142] G. Phragmén, "On the phases occurring in alloys of aluminium with copper, magnesium, manganese, iron, and silicon," *Journal of the Institute of Metals*, vol. 77, no. 6, pp. 489–551, 1950.

[143] P. Villars and K. Cenzual, Eds., *Fe2Al5 (FeAl2.8) Crystal Structure*. [Online]. Available: https://materials.springer.com/isp/crystallographic/docs/sd{_}1250468.

[144] P. Villars and K. Cenzual, Eds., *Fe2-xNixAl9 (FeNiAl9) Crystal Structure*. [Online]. Available: https://materials.springer.com/isp/crystallographic/docs/sd{_}1323225.

[145] K. Momma and F. Izumi, "VESTA 3 for three-dimensional visualization of crystal, volumetric and morphology data," *Journal of Applied Crystallography*, vol. 44, no. 6, pp. 1272–1276, 2011. DOI: 10.1107/S0021889811038970.

[146] R. M. K. Young and T. W. Clyne, "An Al-Fe intermetallic phase formed during controlled solidification," *Scripta Metallurgica*, vol. 15, pp. 1211–1216, 1981.

[147] I. Todd, *Solidification Microstructure Selection In Aluminium-Based Alloys*, 1996.

[148] P. Liu, T Thorvaldsson, G. L. Dunlop and G. L. Dunlop, "Formation of intermetallic compounds during solidification of dilute Al-Fe-Si alloys," *Materials Science and Technology*, vol. 2, no. 10, pp. 1009–1018, 1986. DOI: 10.1179/mst.1986.2.10.1009.

[149] F Bosselet, S Pontevichi, M Sacerdote-Peronnet and J. C. Viala, "Affinement experimental de l'isotherme Al-Fe-Si a 1000 K," *J Phys IV France*, vol. 122, pp. 41–46, 2004.

[150] G. Ghosh, "Aluminim-Iron-Silicon (Iron Systems, Part 1)," *SpringerMaterials Landolt-Börnstein - Group IV Physical Chemistry 11D1*, pp. 1–83, 2008. DOI: 10.1007/978-3-540-69761-9_11.

[151] Y. Du, J. Clemens, Z.-k. Liu and R. Hu, "A thermodynamic description of the Al - Fe - Si system over the whole composition and temperature ranges via a hybrid approach of CALPHAD and key experiments," *Intermetallics*, vol. 16, pp. 554–570, 2008. DOI: 10.1016/j.intermet.2008.01.003.

[152] H. L. Chen, Q. Chen, Y. Du, J. Bratberg and A. Engström, "Update of Al-Fe-Si, Al-Mn-Si and Al-Fe-Mn-Si thermodynamic descriptions," *Transactions of Nonferrous Metals Society of China (English Edition)*, vol. 24, no. 7, pp. 2041–2053, 2014. DOI: 10.1016/S1003-6326(14)63310-0.

[153] R. N. Corby and P. J. Black, "The Structure of α-(AlFeSi) by Anomalous-Dispersion Methods," *Acta Crystallographica*, vol. B33, pp. 3468–3475, 1977. DOI: 10.1107/S0567740877011224.

[154] D Munson, "A clarification of the phases occurring in aluminium-rich aluminium-iron-silicon alloys, with particular referance to the ternary α-AlFeSi," *Journal of the institute of metals*, vol. 95, pp. 217–219, 1967.

[155] C. Y. Sun and L. F. Mondolfo, "A clarification of the phases occurring in aluminium-rich aluminium-iron-silicon alloys," *Journal of the institute of metals*, vol. 95, p. 384, 1967.

[156] H Westengen, "Formation of intermetallic compounds during DC casting of a commercial purity Al-Fe-Si alloy," *Zeitschrift für Metallkunde*, vol. 73, pp. 360–368, 1982.

[157] A. L. Dons, "Superstructures in α-Al(Mn,Fe,Cr)Si," *Zeitschrift für Metallkunde*, vol. 76, no. 2, pp. 151–153, 1985.

[158] J. E. Tibballs, J. a. Horst and C. J. Simensen, "Precipitation of α-Al(Fe,Mn) Si from the melt," *Journal of Materials Science*, vol. 36, pp. 937 –941, 2001. DOI: 10.1023/A:1004815621313.

[159] J. Lacaze, L. Eleno and B. Sundman, "Thermodynamic assessment of the aluminum corner of the Al-Fe-Mn-Si system," *Metallurgical and Materials Transactions A*, vol. 41, no. 9, pp. 2208–2215, 2010. DOI: 10.1007/s11661-010-0263-x.

[160] H. Becker, A. Thum, B. Distl, M. J. Kriegel and A. Leineweber, "Effect of Melt Conditioning on Removal of Fe from Secondary Al-Si Alloys Containing Mg, Mn, and Cr," *Metallurgical and Materials Transactions A: Physical Metallurgy and Materials Science*, vol. 49, no. 12, pp. 6375–6389, 2018. DOI: 10.1007/s11661-018-4930-7. [Online]. Available: https://doi.org/10.1007/s11661-018-4930-7.

[161] Á Griger and V. Stefániay, "Equilibrium and non-equilibrium intermetallic phases in Al-Fe and Al-Fe-Si Alloys," *Journal of Materials Science*, vol. 31, no. 24, pp. 6645–6652, 1996. DOI: 10.1007/BF00356274.

[162] P. Donnadieu, G. Lapasset and T. H. Sanders, "Manganese-induced ordering in the α-(Al-Mn-Fe-Si) approximant phase," *Philosophical Magazine Letters*, vol. 70, no. 5, pp. 319–326, 1994. DOI: 10.1080/09500839408240993.

[163] P Orozco-Gonzalez and M. Castro-Román, "Effect of iron addition on the crystal structure of the α-AlFeMnSi phase formed in the quaternary Al-Fe-Mn-Si system phase formed in the quaternary Al-Fe-Mn-Si system," *Revista de Metalurgia*, vol. 47, no. 6, pp. 453–461, 2011. DOI: 10.3989/revmetalm.1068.

[164] A. M. F. Muggerud, Y. Li and R. Holmestad, "Composition and orientation relationships of constituent particles in 3xxx aluminum alloys," *Philosophical Magazine*, vol. 94, no. 6, pp. 556–568, 2014. DOI: 10.1080/14786435.2013.857796.

[165] M. Cooper, "The crystal structure of the ternary alloy α (AlFeSi)," *Acta Crystallographica*, vol. 23, pp. 1106–1107, 1967. DOI: 10.1107/S0365110X67004372.

[166] N. German, V. Bel'skii, T. Yanson and O. Zarechnyuk, "Crystal structure of the compound Fe1.7Al4Si," *Sov. Phys. Crystallogr.*, vol. 34, no. 3, pp. 735–737, 1989.

[167] V. Hansen, B. Hauback, M. Sundberg, C. Rømming and J. Gjønnes, "β-Al4.5FeSi: A Combined Synchrotron Powder Diffraction, Electron Diffraction, High-Resolution Electron Microscopy and Single-Crystal X-ray Diffraction Study of a Faulted Structure," *Acta Crystallographica*, vol. 54, no. 4, pp. 351–357, 1998. DOI: 10.1107/S0108768197017047.

[168] K. Sugiyama, N. Kaji and K. Hiraga, "Crystal structure of rhombohedral λ-AlFeSi," *Journal of Alloys and Compounds*, vol. 368, no. 1-2, pp. 251–255, 2004. DOI: 10.1016/j.jallcom.2003.08.065.

[169] N. German, V. Zavodnik, T. Yanson and O. Zarechnyuk, "Crystal structure of FeAl2Si," *Sov. Phys. Crystallogr.*, vol. 34, no. 3, pp. 738–739, 1989.

[170] T. I. Yanson, M. B. Manyako, O. I. Bodak, N. V. German, O. S. Zarechnyuk, R Cerny, J. V. Pacheco and K Yvon, "Triclinic Fe3Al2Si3 and Orthorhombic Fe3Al2Si4 with New Structure Types," *Acta Crystallographica*, vol. 52, pp. 2964–2967, 1996. DOI: 10.1107/S0108270196008694.

[171] C. Gueneau, C. Servant, F. D'Yvoire and N. Rodier, "FeAl3Si2," *Acta Crystallographica*, vol. 51, no. 2, pp. 177–179, 1995. DOI: 10.1107/s0108270194009030.

[172] ——, "Fe2Al3Si3," *Acta Crystallographica*, vol. 51, no. 12, pp. 2461–2464, 1995. DOI: 10.1107/s0108270195007864.

[173] S. Pontevichi, F. Bosselet, F. Barbeau, M. Peronnet and J. C. Viala, "Solid-liquid phase equilibria in the Al-Fe-Si system at 727°C," *Journal of Phase Equilibria and Diffusion*, vol. 25, no. 6, pp. 528–537, 2004. DOI: 10.1361/15477020421052.

[174] P. Villars and K. Cenzual, Eds., *Fe1.7Al4Si (Fe1.8Al4.4Si0.6 ht) Crystal Structure*. [Online]. Available: https://materials.springer.com/isp/crystallographic/docs/sd{_}1802104.

[175] J. Roger, E. Jeanneau and J. C. Viala, "Crystal structure of the ternary compound γ-Al3FeSi," *Zeitschrift fur Kristallographie*, vol. 226, no. 11, pp. 805–813, 2011. DOI: 10.1524/zkri.2011.1423.

[176] J. Roger, F. Bosselet and J. C. Viala, "X-rays structural analysis and thermal stability studies of the ternary compound α-AlFeSi," *Journal of Solid State Chemistry*, vol. 184, no. 5, pp. 1120–1128, 2011. DOI: 10.1016/j.jssc.2011.03.025.

[177] J. M. Yu, N. Wanderka, G. Miehe and J. Banhart, "Intermetallic phases in high purity Al-10Si-0.3Fe cast alloys with and without Sr modification studied by FIB tomography and TEM," *Intermetallics*, vol. 72, pp. 53–61, 2016. DOI: 10.1016/j.intermet.2016.02.003.

[178] A. L. Dons, "AlFeSi-particles in commercial pure aluminium," *Zeitschrift für Metallkunde*, vol. 75, no. 2, pp. 170–174, 1984.

[179] P. Liu and G. L. Dunlop, "Determination of the crystal symmetry of two AI-Fe-Si phases by convergent-beam electron diffraction," *Journal of Applied Crystallography*, vol. 20, pp. 425–427, 1977. DOI: 10.1002/j.1537-2197.1977.tb15733.x.

[180] L. A. Bendersky, M. J. Kaufman, W. J. Boettinger and F. S. Biancaniello, "Solidification of an "amorphous" phase in rapidly solidified AlFeSi alloys," *Materials Science and Engineering*, vol. 98, no. C, pp. 213–216, 1988. DOI: 10.1016/0025-5416(88)90157-7.

[181] L. A. Bendersky, A. J. McAlister and F. S. Biancaniello, "Phase transformation during annealing of rapidly solidified Al-rich Al-Fe-Si alloys," *Metallurgical Transactions A*, vol. 19, no. 12, pp. 2893–2900, 1988. DOI: 10.1007/BF02647715.

[182] T. Turmezey, V. Stefániay and A Griger, "AlFeSi phases in aluminium," *Key Engineering Materials*, vol. 44-45, pp. 57–68, 1990.

[183] P. Liu and G. L. Dunlop, "Long-range ordering of vacancies in bcc α-AlFeSi," *Journal of Materials Science*, vol. 23, no. 4, pp. 1419–1424, 1988. DOI: 10.1007/BF01154611.

[184] C. M. Allen, K. A. O'Reilly, B. Cantor and P. V. Evans, "Intermetallic phase selection in 1XXX A1 alloys," *Progress in Materials Science*, vol. 43, no. 2, pp. 89–170, 1998. DOI: 10.1016/S0079-6425(98)00003-6.

[185] H. Mehrer, *Diffusion in solids: fundamentals, methods, materials, diffusion-controlled processes*, 2007.

[186] K. A. Dill and S. Bromberg, *Molecular Driving Forces: Statistical Thermodynamics in Biology, Chemistry, Physics, and Nanoscience*, 2011.

[187] A. Paul, T. Laurila, V. Vuorinen and S. V. Divinski, *Thermodynamics, diffusion and the kirkendall effect in solids*, 2014. DOI: 10.1007/978-3-319-07461-0.

[188] A. M. Brown and M. F. Ashby, "Correlations for Diffusion Constants.," *Acta Metallurgica*, vol. 28, no. 8, pp. 1085–1101, 1980. DOI: 10.1016/0001-6160(80)90092-9.

[189] R Pretorius and F. W. Saris, "Use of the effective heat of formation rule for predicting phase formation sequence in Al-Ni systems," *Materials Letters*, vol. 9, no. 12, 1990.

[190] R. Pretorius, A. M. Vredenberg, F. W. Saris and R. De Reus, "Prediction of phase formation sequence and phase stability in binary metal-aluminum thin-film systems using the effective heat of formation rule," *Journal of Applied Physics*, vol. 70, no. 7, pp. 3636–3646, 1991. DOI: 10.1063/1.349211.

[191] R Pretorius, T. Marais and C. Theron, "Thin film compound phase formation sequence: An effective heat of formation model," *Materials Science and Engineering*, vol. 10, pp. 237–274, 1993.

[192] C. Theron, O. Ndwandwe, J. Lombaard and R Pretorius, "First phase formation at interfaces: Comparison between Walser-Bene and effective heat of formation model," *Materials Chemistry and Physic*, vol. 46, pp. 238–247, 1996.

[193] A. A. Kodentsov, G. F. Bastin and F. J. J. V. Loo, "Application of Diffusion Couples in Phase Diagram Determination," in *Methods for Phase Diagram Determination*, Elsevier Ltd, 2007, pp. 222–245. DOI: 10.1016/B978-0-08-044629-5.50006-9. [Online]. Available: http://dx.doi.org/10.1016/B978-0-08-044629-5.50006-9.

[194] J. E. Morral, "Diffusion path theorems for ternary diffusion couples," *Metallurgical and Materials Transactions A: Physical Metallurgy and Materials Science*, vol. 43, no. 10, pp. 3462–3470, 2012. DOI: 10.1007/s11661-011-1026-z.

[195] A. Bahadur and O. N. Mohanty, *Structural studies of hot dip aluminized coatings on mild steel*, 1991. DOI: 10.2320/matertrans1989.32.1053.

[196] M. Akdeniz, A. Mekhrabov and T. Yilmaz, "The role of Si addition on the interfacial interaction in Fe-Al duffusion layer," *Scripta Metallurgica et Materialia*, vol. 3, no. 12, pp. 1723–1728, 1994.

[197] K. Bouché, F. Barbier and A. Coulet, "Intermetallic compound layer growth between solid iron and molten aluminium," *Materials Science and Engineering A*, vol. 249, no. 1-2, pp. 167–175, 1998. DOI: 10.1016/s0921-5093(98)00573-5.

[198] O. W. Gebhardt E, "Reaktionen von festem Eisen mit Schmelzen aus Aluminium und Aluminiumlegierungen," *Zeitschriftfür Metallkunde*, vol. 12, no. 1936, pp. 44–154, 1953.

[199] F. Barbier, D. Manuelli and K. Bouché, "Characterization of aluminide coatings formed on 1.4914 and 316L steels by hot-dipping in molten aluminium," *Scripta Materialia*, vol. 36, no. 4, pp. 425–431, 1997. DOI: 10.1016/S1359-6462(96)00407-1.

[200] N. Takata, M. Nishimoto, S. Kobayashi and M. Takeyama, "Crystallography of Fe2Al5 phase at the interface between solid Fe and liquid Al," *Intermetallics*, vol. 67, pp. 1–11, 2015. DOI: 10.1016/j.intermet.2015.07.011. [Online]. Available: http://dx.doi.org/10.1016/j.intermet.2015.07.011.

[201] Z. Ding, Q. Hu, W. Lu, X. Ge, S. Cao, S. Sun, T. Yang, M. Xia and J. Li, "Microstructural evolution and growth behavior of intermetallic compounds at the liquid Al/solid Fe interface by synchrotron X-ray radiography," *Materials Characterization*, vol. 136, no. December 2017, pp. 157–164, 2018. DOI: 10.1016/j.matchar.2017.12.024.

[202] S. Kobayashi and T. Yakou, "Control of intermetallic compound layers at interface between steel and aluminum by diffusion-treatment," *Materials Science and Engineering A*, vol. 338, no. 1-2, pp. 44–53, 2002. DOI: 10.1016/S0921-5093(02)00053-9.

[203] N. Chen, M. Wang, H. P. Wang, Z. Wan and B. E. Carlson, "Microstructural and mechanical evolution of Al/steel interface with Fe2Al5 growth in resistance spot welding of aluminum to steel," *Journal of Manufacturing Processes*, vol. 34, no. June, pp. 424–434, 2018. DOI: 10.1016/j.jmapro.2018.06.024.

[204] T Heumann and S Dittrich, "Uber die kinetic der reaktion von festem und flussigem aluminium mit eisen," *Zeitschrift für Metallkunde*, vol. 50, no. 10, pp. 617–625, 1959.

[205] W. J. Cheng and C. J. Wang, "Study of microstructure and phase evolution of hot-dipped aluminide mild steel during high-temperature diffusion using electron backscatter diffraction," *Applied Surface Science*, vol. 257, no. 10, pp. 4663–4668, 2011. DOI: 10.1016/j.apsusc.2010.12.118.

[206] A. Bouayad, C. Gerometta, A. Belkebir and A. Ambari, "Kinetic interactions between solid iron and molten aluminium," *Materials Science and Engineering A*, vol. 363, no. 1-2, pp. 53–61, 2003. DOI: 10.1016/S0921-5093(03)00469-6.

[207] D. Naoi and M. Kajihara, "Growth behavior of Fe2Al5 during reactive diffusion between Fe and Al at solid-state temperatures," *Materials Science and Engineering A*, vol. 459, no. 1-2, pp. 375–382, 2007. DOI: 10.1016/j.msea.2007.01.099.

[208] L. Xu, J. D. Robson, L. Wang and P. B. Prangnell, "The Influence of Grain Structure on Intermetallic Compound Layer Growth Rates in Fe-Al Dissimilar Welds," *Metallurgical and Materials Transactions A*, vol. 49, no. 2, pp. 515–526, 2018. DOI: 10.1007/s11661-017-4352-y.

[209] P. Huilgol, K. R. Udupa and K. U. Bhat, "Metastable microstructures at the interface between AISI 321 steel and molten aluminum during hot-dip aluminizing," *Surface and Coatings Technology*, vol. 348, no. March, pp. 22–30, 2018. DOI: 10.1016/j.surfcoat.2018.05.013.

[210] S. B. Lin, J. L. Song, C. L. Yang and G. C. Ma, "Metallurgical and mechanical investigations of aluminium-steel butt joint made by tungsten inert gas welding-brazing," *Science and Technology of Welding and Joining*, vol. 14, no. 7, pp. 636–639, 2009. DOI: 10.1179/136217109X12464549883493.

[211] J. L. Song, S. B. Lin, C. L. Yang and C. L. Fan, "Effects of Si additions on intermetallic compound layer of aluminum-steel TIG welding-brazing joint," *Journal of Alloys and Compounds*, vol. 488, no. 1, pp. 217–222, 2009. DOI: 10.1016/j.jallcom.2009.08.084.

[212] H. Xia, X. Zhao, C. Tan, B. Chen, X. Song and L. Li, "Effect of Si content on the interfacial reactions in laser welded-brazed Al/steel dissimilar butted joint," *Journal of Materials Processing Technology*, vol. 258, pp. 9–21, 2018. DOI: 10.1016/j.jmatprotec.2018.03.010.

[213] H. Azimaee, M. Sarfaraz, M. Mirjalili and K. Aminian, "Effect of silicon and manganese on the kinetics and morphology of the intermetallic layer growth during hot-dip aluminizing," *Surface and Coatings Technology*, vol. 357, no. July 2018, pp. 483–496, 2019. DOI: 10.1016/j.surfcoat.2018.10.035.

[214] W.-J. Cheng and C.-J. Wang, "Observation of high-temperature phase transformation in the Si-modified aluminide coating on mild steel using EBSD," *Materials Characterization*, vol. 61, no. 4, pp. 467–473, 2010. DOI: 10.1016/j.matchar.2010.02.001.

[215] ——, "Effect of chromium on the formation of intermetallic phases in hot-dipped aluminide Cr-Mo steels," *Applied Surface Science*, vol. 277, pp. 139–145, 2013. DOI: 10.1016/j.apsusc.2013.04.015.

[216] B. Lemmens, H. Springer, I. De Graeve, J. De Strycker, D. Raabe and K. Verbeken, "Effect of silicon on the microstructure and growth kinetics of intermetallic phases formed during hot-dip aluminizing of ferritic steel," *Surface and Coatings Technology*, vol. 319, pp. 104–109, 2017. DOI: 10.1016/j.surfcoat.2017.03.040.

[217] J. L. Song et al, "Analysis of intermetallic layer in dissimilar TIG welding–brazing butt joint of aluminium alloy to stainless steel," *Science and Technology of Welding and Joining*, vol. 15, no. 3, pp. 213–218, 2010. DOI: 10.1179/136217110X12665048207610.

[218] W. Jiang, G. Li, Z. Jiang, Y. Wu, Z. Fan and A. Fe, "Effect of heat treatment on microstructures and mechanical properties of Al/Fe bimetal," *Materials Science and Engineering: A*, vol. 0836, 2018. DOI: 10.1080/02670836.2018.1465620.

[219] B. Lemmens, B. Corlu, J. de Strycker and K. Verbeken, "The effect of Si on the intermetallics formation during hot dip aluminizing," *Advanced Materials Research*, vol. 922, pp. 429–434, 2014. DOI: 10.4028/www.scientific.net/AMR.922.429.

[220] B. Lemmens, H. Springer, M. J. Duarte, I. De Graeve, J. De Strycker, D. Raabe and K. Verbeken, "Atom probe tomography of intermetallic phases and interfaces formed in dissimilar joining between Al alloys and steel," *Materials Characterization*, vol. 120, pp. 268–272, 2016. DOI: 10.1016/j.matchar.2016.09.008.

[221] A. Knauschner, "Investigations on Hot Dip Aluminizing of Steel Strip," *Neue Hutte*, vol. 19, no. 7, pp. 398–404, 1974.

[222] S. G. Denner, R. D. Jones and R. J. Thomas, "Hot dip aluminizing of steel strip," *Iron Steel Int.*, vol. 48, no. 3, pp. 241–252, 1975.

[223] G Eggeler, W Auer and H Kaesche, "On the influence of silicon on the growth of the alloy layer during hot dip aluminizing," *Journal of Materials Science*, vol. 21, pp. 3348–3350, 1986. DOI: 0022-2461/86.

[224] D. I. Layner and A. K. Kurakin, "Mechanism of the influence of silicon in aluminium on the reaction diffusion of iron," *Fiz. metal. metalloved.*, vol. 18, no. 1, pp. 145–148, 1964.

[225] A. K. Kurakin, "Mechanism of the influence of silicon on the process of the reaction diffusion of iron in aluminium," *Fiz. metal. metalloved.*, vol. 30, no. 1, pp. 105–110, 1970.

[226] J. E. Nicholls, "Hot-dipped aluminium coatings," *Anti-corrosion methods and materials*, vol. 11, no. 10, pp. 16–21, 1964.

[227] M. V. Akdeniz and A. Mekhrabov, "The effect of substitutional impurities on the evolution of Fe-Al diffusion layer," *Acta Metallurgica*, vol. 46, no. 4, pp. 1185–1192, 1998.

[228] K. Murakami, N. Nishida, K. Osamura, Y. Tomota and T. Suzuki, "Aluminization of high purity iron and stainless steel by powder liquid coating," *Acta Materialia*, vol. 52, no. 8, pp. 2173–2184, 2004. DOI: 10.1016/j.actamat.2004.01.009.

[229] B. Liu, Q. Yang and Y. Wang, "Intereaction and intermetallic phase formation between aluminum and stainless steel," *Results in Physics*, vol. 12, no. November 2018, pp. 514–524, 2019. DOI: 10.1016/j.rinp.2018.11.076.

[230] W. J. Cheng and C. J. Wang, "Characterization of intermetallic layer formation in aluminide/nickel duplex coating on mild steel," *Materials Characterization*, vol. 69, no. 43, pp. 63–70, 2012. DOI: 10.1016/j.matchar.2012.04.007.

[231] J. H. Lee, J. G. Yun, S. Y. Kwak and C. Y. Kang, "Nucleation and growth of intermetallic compounds formed in boron steel hot-dipped in Al-Ni alloy," *Coatings*, vol. 7, no. 11, pp. 1–14, 2017. DOI: 10.3390/coatings7110195.

[232] B. Dangi, T. W. Brown and K. N. Kulkarni, "Effect of silicon, manganese and nickel present in iron on the intermetallic growth at iron - aluminum alloy interface," *Journal of Alloys and Compounds*, vol. 769, pp. 777–787, 2018. DOI: 10.1016/j.jallcom.2018.07.364.

[233] Y. Li, Q. Jia, Z. Zhu, W. Gao and H. Chen, "Growth behaviour of intermetallic layer on stainless steel in aluminium hot-dipping process," *Surface Review and Letters*, vol. 24, no. 4, pp. 1–9, 2017. DOI: 10.1142/S0218625X17500469.

[234] V. I. Dybkov, "Interaction of 18Cr-10Ni stainless steel with liquid aluminium," *Journal of Materials Science*, vol. 25, pp. 3615–3633, 1990.

[235] H. Glasbrenner, J. Konys, K. Stein-Fechner and O. Wedemeyer, "Comparison of microstructure and formation of intermetallic phases on F82H-mod. and MANET II," *Journal of Nuclear Materials*, vol. 258-263, no. PART 2 B, pp. 1173–1177, 1998. DOI: 10.1016/S0022-3115(98)00181-0.

[236] Y. H. Liu, X. Y. Chong, Y. H. Jiang, R. Zhou and J. Feng, "Mechanical properties and electronic structures of Fe-Al intermetallic," *Physica B: Condensed Matter*, vol. 506, no. July 2016, pp. 1–11, 2017. DOI: 10.1016/j.physb.2016.10.032.

[237] R. Borrisutthekul, T. Yachi, Y. Miyashita and Y. Mutoh, "Suppression of intermetallic reaction layer formation by controlling heat flow in dissimilar joining of steel and aluminum alloy," *Materials Science and Engineering A*, vol. 467, no. 1-2, pp. 108–113, 2007. DOI: 10.1016/j.msea.2007.03.049.

[238] R. Hatano, T. Ogura, T. Matsuda, T. Sano and A. Hirose, "Relationship between intermetallic compound layer thickness with deviation and interfacial strength for dissimilar joints of aluminum alloy and stainless steel," *Materials Science & Engineering A*, vol. 735, pp. 361–366, 2018. DOI: 10.1016/j.msea.2018.08.065.

[239] M. Movahedi, A. H. Kokabi, S. M. Seyed Reihani and H. Najafi, "Effect of tool travel and rotation speeds on weld zone defects and joint strength of aluminium steel lap joints made by friction stir welding," *Science and Technology of Welding and Joining*, vol. 17, no. 2, pp. 162–167, 2012. DOI: 10.1179/1362171811Y.0000000092.

[240] H. S. Furuya, Y. T. Sato, Y. S. Sato, H. Kokawa and Y. Tatsumi, "Strength Improvement Through Grain Refinement of Intermetallic Compound at Al/Fe Dissimilar Joint Interface by the Addition of Alloying Elements," *Metallurgical and Materials Transactions A*, vol. 49, no. 2, pp. 527–536, 2018. DOI: 10.1007/s11661-017-4442-x.

[241] Y. peng Zhao, L. feng Chen, S. jie Zhu, Y. feng Sun and S. kang Guan, "Clarifying effect of welding conditions on microstructure and mechanical properties of friction stir spot-welded DH590 automotive high-strength steel plates," *Journal of Iron and Steel Research International*, no. 0123456789, 2020. DOI: 10.1007/s42243-020-00478-x.

[242] R. S. Coelho, A. Kostka, J. F. dos Santos and A. Kaysser-Pyzalla, "Friction-stir dissimilar welding of aluminium alloy to high strength steels: Mechanical properties and their relation to microstructure," *Materials Science and Engineering A*, vol. 556, pp. 175–183, 2012. DOI: 10.1016/j.msea.2012.06.076.

[243] A. Elrefaey, M. Gouda, M. Takahashi and K. Ikeuchi, "Characterization of aluminum/steel lap joint by friction stir welding," *Journal of Materials Engineering and Performance*, vol. 14, no. 1, pp. 10–17, 2005. DOI: 10.1361/10599490522310.

[244] C. Wang, Y. Jiang, J. Xie, D. Zhou and X. Zhang, "Effect of the steel sheet surface hardening state on interfacial bonding strength of embedded aluminum – steel composite sheet produced by cold roll bonding process," *Materials Science & Engineering A*, vol. 652, pp. 51–58, 2016. DOI: 10.1016/j.msea.2015.11.039.

[245] De Graef, Marc, and M. E. McHenry, *Structure of materials: an introduction to crystallography, diffraction and symmetry*, 2012.

[246] D. J. Griffiths, *Introduction to Quantum Mechanics*, 2005.

[247] E. J. Kirkland, *Advanced computing in electron microscopy*, 2010.

[248] C. J. Humphreys, "The scattering of fast electrons by crystals," *Reports on Progress in Physics*, vol. 42, no. 11, pp. 1825–1887, 1979. DOI: 10.1088/0034-4885/42/11/002.

[249] P. D. Nellist and S. J. Pennycook, "The principles and interpretation of annular dark-field Z-contrast imaging," *Advances in Imaging and Electron Physics*, 2000. DOI: 10.1016/S1076-5670(00)80013-0.

[250] R. Erni, *Aberration-corrected imaging in transmission electron microscopy: An introduction*, 2015. DOI: 10.1142/P960.

[251] D. B. Williams and C. Barry Carter, *Transmission Electron Microscopy: Diffraction, imaging, and spectrometry*. Springer, 2016. DOI: DOI10.1007/978-3-319-26651-0_11.

[252] B. Fultz and J. Howe, *Transmission electron microscopy and diffractometry of materials*, 2008.

[253] J. I. Goldstein, D. E. Newbury, J. R. Michael, N. W. M. Ritchie, J. H. J. Scott and D. C. Joy, *Scanning Electron Microscopy and X-Ray Microanalysis*.

[254] R. F. Egerton, *Physical principles of electron microscopy*, 2005.

[255] J. M. Cowley, *Diffraction physics*, 1995.

[256] J. Als-Nielsen and McMorrow, *Elements of modern X-ray physics*, 2011.

[257] Y. Seto, *ReciPro v.4.761*, 2020. [Online]. Available: https://github.com/seto77/ReciPro.

[258] R Vincent and P. Midgley, "Double conical beam-rocking system for measurement of integrated electron diffraction intensities," *Ultramicroscopy*, vol. 53, no. 3, pp. 271–282, 1994. DOI: 10.1016/0304-3991(94)90039-6.

[259] A. S. Eggeman and P. A. Midgley, "Precession electron diffraction," *Advances in Imaging and Electron Physics*, vol. 170, pp. 1–63, 2012. DOI: 10.1016/B978-0-12-394396-5.00001-4.

[260] J. S. Barnard, D. N. Johnstone and P. A. Midgley, "High-resolution scanning precession electron diffraction: Alignment and spatial resolution," *Ultramicroscopy*, vol. 174, no. December 2016, pp. 79–88, 2017. DOI: 10.1016/j.ultramic.2016.12.018.

[261] P. Oleynikov, S. Hovmöller and X. D. Zou, "Precession electron diffraction: Observed and calculated intensities," *Ultramicroscopy*, vol. 107, no. 6-7, pp. 523–533, 2007. DOI: 10.1016/j.ultramic.2006.04.032.

[262] A. S. Ã. Eggeman, T. A. White and P. A. Midgley, "Is precession electron diffraction kinematical? Part II A practical method to determine the optimum precession angle," *Ultramicroscopy*, vol. 110, no. 7, pp. 771–777, 2010. DOI: 10.1016/j.ultramic.2009.10.012. [Online]. Available: http://dx.doi.org/10.1016/j.ultramic.2009.10.012.

[263] K. Gjønnes, "On the integration of electron diffraction intensities in the Vincent-Midgley precession technique," *Ultramicroscopy*, vol. 69, pp. 1–11, 1997.

[264] P. A. Midgley and A. S. Eggeman, "Precession electron diffraction - A topical review," *IUCrJ*, vol. 2, pp. 126–136, 2015. DOI: 10.1107/S2052252514022283.

[265] L. Palatinus, D. Jacob, P. Cuvillier, M. Klementová, W. Sinkler and L. D. Marks, "Structure refinement from precession electron diffraction data," *Acta Crystallographica Section A*, vol. 69, no. 2, pp. 171–188, 2013. DOI: 10.1107/S010876731204946X.

[266] C. Ophus, "Four-Dimensional Scanning Transmission Electron Microscopy (4D-STEM): From Scanning Nanodiffraction to Ptychography and Beyond," *Microscopy and Microanalysis*, no. 2019, pp. 563–582, 2019. DOI: 10.1017/S1431927619000497.

[267] E. Rauch, M Véron, J Portillo, D Bultreys, Y Maniette and S Nicolopoulos, "Automatic crystal orientation and phase mapping in TEM by precession diffraction," *Microscopy and Analysis-UK*, vol. 22, no. 6, S5–S8, 2008.

[268] S. Zaefferer, "A critical review of orientation microscopy in SEM and TEM," *Crystal Research and Technology*, vol. 46, no. 6, pp. 607–628, 2011. DOI: 10.1002/crat.201100125.

[269] E. Rauch, J Portillo, S Nicolopoulos, D Bultreys, S Rouvimov and P Moeck, "Automated nanocrystal orientation and phase mapping in the transmission electron microscope on the basis of precession electron diffraction," *Zeitschrift fur Kristallographie*, vol. 225, no. 2-3, pp. 103–109, 2010. DOI: 10.1524/zkri.2010.1205. arXiv: arXiv:0804.0063.

[270] J. Rouviere, B Armand, Y Martin, T Denneulin and D Cooper, "Improved strain precision with high spatial resolution using nanobeam precession electron diffraction," *Applied Physics Letters*, vol. 103, no. 241913, 2013. DOI: 10.1063/1.4829154.

[271] D. Cooper, T. Denneulin, N. Bernier, A. Béché and J. L. Rouvière, "Strain mapping of semiconductor specimens with nm-scale resolution in a transmission electron microscope," *Micron*, vol. 80, pp. 145–165, 2016. DOI: 10.1016/j.micron.2015.09.001.

[272] I. MacLaren, T. A. MacGregor, C. S. Allen and A. I. Kirkland, "Detectors-The ongoing revolution in scanning transmission electron microscopy and why this important to material characterization," *APL Materials*, vol. 8, no. 11, 2020. DOI: 10.1063/5.0026992.

[273] D. N. Johnstone, P. Crout, J. Laulainen, S. Høgås, B. Martineau, T. Bergh, S. Smeets, S. Collins, J. Morzy, H. W. Ånes, E. Prestat, T. Doherty, T. Ostasevicius, D. Mohsen, E. Opheim, R. Tovey and E. Jacobsen, *Pyxem/pyxem: Pyxem 0.10.1*, 2020. DOI: 10.5281/ZENODO.3667613.

[274] F. de la Peña, E. Prestat, V. T. Fauske, P. Burdet, P. Jokubauskas, M. Nord, T. Ostasevicius, K. E. MacArthur, M. Sarahan, D. N. Johnstone, J. Taillon, J. Lähnemann, V. Migunov, A. Eljarrat, J. Caron, T. Aarholt, S. Mazzucco, M. Walls, T. Slater, F. Winkler, Pquinn-dls, B. Martineau, G. Donval, R. McLeod, E. R. Hoglund, I. Alxneit, D. Lundeby, T. Henninen, L. F. Zagonel and A. Garmannslund, "hyperspy/hyperspy: HyperSpy v1.5.2," *Zenodo*, 2019. DOI: 10.5281/ZENODO.3396791.

[275] S van der Walt, J. Schönberger, J Nunez-Iglesias, F Boulogne, J. Warner, N Yager, E Gouillart, T Yu and T. scikit-image contributors, "scikit-image: image processing in Python," *PeerJ*, vol. 2, no. e453, 2014. DOI: 10.7717/peerj.453.

[276] F Pedregosa, G Varoquaux, A Gramfort, V Michel, B Thirion, O Grisel, M Blondel, P Prettenhofer, R Weiss, V Dubourg, J Vanderplas, A Passos, D Cournapeau, M Brucher, M Perrot and E Duchesnay, "Scikit-learn: Machine Learning in Python," *Journal of Machine Learning Research*, vol. 12, no. 1, pp. 2825–2830, 2011. DOI: 10.1007/s13398-014-0173-7.2. arXiv: arXiv:1011.1669v3.

[277] Y Meng and J. Zuo, "Three-dimensional nanostructure determination from a large diffraction data set recorded using scanning electron nanodiffraction," *IUCrJ*, vol. 3, pp. 300–308, 2016. DOI: 10.1107/S205225251600943X.

[278] S. L. Brunton and J. N. Kutz, *Data-Driven Science and Engineering*, 2019.

[279] M. Keenan and P. Kotula, "Accounting for Poisson noise in the multivariate analysis of ToF-SIMS spectrum images †," *Surface and Interface Analysis*, no. 36, pp. 203–212, 2004. DOI: 10.1002/sia.1657.

[280] J. Shlens, "A Tutorial on Principal Component Analysis," 2014. arXiv: 1404.1100. [Online]. Available: http://arxiv.org/abs/1404.1100.

[281] D. Lee and S Seung, "Learning the parts of objects by non-negative matrix factorization," *Nature*, vol. 401, no. 6755, pp. 788–791, 1999. DOI: 10.1038/44565.

[282] C. Boutsidis and E. Gallopoulos, "SVD based initialization: A head start for nonnegative matrix factorization," *Pattern Recognition*, vol. 41, no. 4, pp. 1350–1362, 2008. DOI: 10.1016/j.patcog.2007.09.010.

[283] A. Eggeman, R Krakow and P. Midgley, "Scanning precession electron tomography for three-dimensional nanoscale orientation imaging and crystallographic analysis," *Nature Communications*, vol. 6, p. 7267, 2015. DOI: 10.1038/ncomms8267.

[284] B. H. Martineau, D. N. Johnstone, A. T. J. van Helvoort, P. A. Midgley and A. S. Eggeman, "Unsupervised machine learning applied to scanning precession electron diffraction data," *Advanced Structural and Chemical Imaging*, vol. 5, no. 1, 2019. DOI: 10.1186/s40679-019-0063-3.

[285] M. Watanabe and D. B. Williams, "The quantitative analysis of thin specimens: A review of progress from the Cliff-Lorimer to the new ζ-factor methods," *Journal of Microscopy*, vol. 221, no. 2, pp. 89–109, 2006. DOI: 10.1111/j.1365-2818.2006.01549.x.

[286] Y. Nan, *Focused ion beam systems: Basics and applications*, 2007. DOI: 10.1017/CBO9780511600302.

[287] S. Lan, X. Liu and J. Ni, "Microstructural evolution during friction stir welding of dissimilar aluminum alloy to advanced high-strength steel," *International Journal of Advanced Manufacturing Technology*, vol. 82, no. 9-12, pp. 2183–2193, 2016. DOI: 10.1007/s00170-015-7531-2.

[288] M. Cooper, "The crystal structure of the ternary alloy α (AlMnSi)," *Acta Crystallographica*, vol. 20, pp. 614–617, 1966. DOI: 10.1107/S0365110X67004372.

[289] S. M. Arbo, "Cold welding of steel and aluminum alloys," Ph.D. dissertation, NTNU, 2020.

[290] J. Chen, B. Shalchi Amirkhiz, R. Zhang and B. Rona, "On the Joint Formation and Interfacial Microstructure of Cold Metal Transfer Cycle Step Braze Welding of Aluminum to Steel Butt Joint," *Metallurgical and Materials Transactions A*, vol. 51, no. 10, pp. 5198–5212, 2020. DOI: 10.1007/s11661-020-05917-8.

[291] C. M. Dinnis, J. A. Taylor and A. K. Dahle, "As-cast morphology of iron-intermetallics in Al-Si foundry alloys," *Scripta Materialia*, vol. 53, no. 8, pp. 955–958, 2005. DOI: 10.1016/j.scriptamat.2005.06.028.

[292] A. Takeuchi and A. Inoue, *Calcualtion of mixing enthalpy and mismatch entropy*, 2000.

[293] A. A. Amenova, N. A. Belov and D. U. Smagulov, "Computation of liquidus of the Al - Fe - Mn - Ni - Si system in the range of aluminum-nickel alloys (nickalins)," *Metal Science and Heat Treatment*, vol. 56, no. 3-4, pp. 137–142, 2014. DOI: 10.1007/s11041-014-9719-8.

[294] A. S. Edelstein, R. K. Everett, G. Y. Richardson, S. B. Qadri, E. I. Altman, J. C. Foley and J. H. Perepezko, "Intermetallic phase formation during annealing of Al/Ni multilayers," *Journal of Applied Physics*, vol. 76, no. 12, pp. 7850–7859, 1994. DOI: 10.1063/1.357893.

[295] K. Barmak, C. Michaelsen and G. Lucadamo, "Reactive phase formation in sputter-deposited Ni/Al multilayer thin films," *Journal of Materials Research*, vol. 12, no. 1, pp. 133–146, 1997. DOI: 10.1557/JMR.1997.0021.

[296] K. J. Blobaum, D. Van Heerden, A. J. Gavens and T. P. Weihs, "Al/Ni formation reactions: Characterization of the metastable Al9Ni2 phase and analysis of its formation," *Acta Materialia*, vol. 51, no. 13, pp. 3871–3884, 2003. DOI: 10.1016/S1359-6454(03)00211-8.

[297] D. Dubaux, Gaudry, M. C. de Weerd, S. Šturm, M. Podlogar, J. Ghanbaja, S. Migot, V. Fournée, M. Sicot and J. Ledieu, "Metastable Al-Fe intermetallic stabilised by epitaxial relationship," *Applied Surface Science*, vol. 533, no. July, 2020. DOI: 10.1016/j.apsusc.2020.147492.

[298] Y.-W. Kim and A. G. Jackson, "Phases and orientation realtionships in a rapidly solidified Al-6Fe-6Ni alloy," *Scripta Metallurgica*, vol. 20, no. 5, pp. 777–782, 1986.

[299] P. Malczyk, C. Weigelt, T. Zienert, N. Brachhold, S. O. Sauke, H. Semrau and C. G. Aneziris, "Investigation of Interfacial Phase Formation During Corrosion of Stainless Steel," *InterCeram: International Ceramic Review*, vol. 69, no. 1, pp. 42–51, 2020. DOI: 10.1007/s42411-019-0070-3.

[300] S. P. Gupta, "Intermetallic compound formation in Fe - Al - Si ternary system: Part I," *Materials Characterization*, vol. 49, pp. 269–291, 2003. DOI: 10.1016/S1044-5803(03)00006-8.

[301] Z. Zhou, Z. Li, Y. Xie, X. Wang, Y. Liu, Z. Long and F. Yin, "Experimental study of the phase relationships in the Al-rich corner of the Al-Si-Fe-Cr quaternary system at 700°C," *International Journal of Materials Research*, vol. 106, no. 5, pp. 470–480, 2015. DOI: 10.3139/146.111202.

[302] Y. Du, Y. A. Chang, B. Huang, W. Gong, Z. Jin, H. Xu, Z. Yuan, Y. Liu, Y. He and F Xie, "Diffusion coefficients of some solutes in fcc and liquid Al: critical evaluation and correlation," *Materials Science and Engineering A*, vol. 363, pp. 140–151, 2003. DOI: 10.1016/S0921-5093(03)00624-5.

[303] C. Zhang, J. D. Robson, S. J. Haigh and P. B. Prangnell, "Interfacial Segregation of Alloying Elements During Dissimilar Ultrasonic Welding of AA6111 Aluminum and Ti6Al4V Titanium," *Metallurgical and Materials Transactions A*, vol. 50, pp. 5143–5152, 2019.

[304] C. R. Werrett, D. R. Pyke and A. K. Bhattacharya, "XPS studies of oxide growth and segregation in aluminium-silicon alloys," *Surface and Interface Analysis*, vol. 25, no. 10, pp. 809–816, 1997. DOI: 10.1002/(SICI)1096-9918(199709)25:10<809::AID-SIA304>3.0.CO;2-M.

[305] F. C. Liu, P. Dong, J. Zhang, W. Lu, A. Taub and K. Sun, "Alloy amorphization through nanoscale shear localization at Al-Fe interface," *Materials Today Physics*, vol. 15, 2020. DOI: 10.1016/j.mtphys.2020.100252.

[306] F. C. Liu and P. Dong, "From thick intermetallic to nanoscale amorphous phase at Al-Fe joint interface: roles of friction stir welding conditions," *Scripta Materialia*, vol. 191, pp. 167–172, 2021. DOI: 10.1016/j.scriptamat.2020.09.031.

[307] S Fukumoto, H Tsubakino, K Okita, M Aritoshi and T Tomita, "Amorphization by friction welding between 5052 aluminium alloy and 304 stainless steel," *Scripta Materialia*, vol. 42, pp. 807–812, 2000.

[308] Y. F. Sun, H. Fujii, N. Takaki and Y. Okitsu, "Microstructure and mechanical properties of dissimilar Al alloy/steel joints prepared by a flat spot friction stir welding technique," *Materials and Design*, vol. 47, pp. 350–357, 2013. DOI: 10.1016/j.matdes.2012.12.007.

[309] L. A. Bendersky and F. Mompiou, "Formation of Al-Fe-Si glass that grows from the melt through a first-order transition," *Journal of Alloys and Compounds*, vol. 536, no. SUPPL.1, S171–S174, 2012. DOI: 10.1016/j.jallcom.2012.01.056.

[310] K. W. Chapman, P. J. Chupas, G. G. Long, L. A. Bendersky, L. E. Levine, F. Mompiou, J. K. Stalick and J. W. Cahn, "An ordered metallic glass solid solution phase that grows from the melt like a crystal," *Acta Materialia*, vol. 62, no. 1, pp. 58–68, 2014. DOI: 10.1016/j.actamat.2013.08.063.

[311] M. Reza-E-Rabby, K. Ross, N. R. Overman, M. J. Olszta, M. McDonnell and S. A. Whalen, "Joining thick section aluminum to steel with suppressed FeAl intermetallic formation via friction stir dovetailing," *Scripta Materialia*, vol. 148, pp. 63–67, 2018. DOI: 10.1016/j.scriptamat.2018.01.026.

[312] V. I. Zheladnov, M. S. Makunin and P. M. Arzhanyi, "Effect of oxygen in iron on the inhibition of diffusion in Al-Fe bimetals," *Metal Science and Heat Treatment*, vol. 18, no. 11, pp. 978–981, 1976.

[313] G. M. Bedford and J. Boustead, "The influence of oxygen and nitrogen on the growth of intermediate phases during the bonding of iron to aluminium," *Journal of Materials Science*, vol. 13, no. 2, pp. 253–260, 1978. DOI: 10.1007/BF00647768.

[314] D. E. Eakins, D. F. Bahr and M. G. Norton, "An in situ TEM study of phase formation in gold-aluminum couples," *Journal of Materials Science*, vol. 39, no. 1, pp. 165–171, 2004. DOI: 10.1023/B:JMSC.0000007741.97288.bd.

[315] H. Xu, I. Qin, H. Clauberg, B. Chylak and V. L. Acoff, "New observation of nanoscale interfacial evolution in micro Cu-Al wire bonds by in-situ high resolution TEM study," *Scripta Materialia*, vol. 115, pp. 1–5, 2016. DOI: 10.1016/j.scriptamat.2015.12.025.

[316] B. Goldstein and J. Dresner, "Growth of MgO films with high secondary electron emission on Al-Mg alloys," *Surface Science*, vol. 71, no. 1, pp. 15–26, 1978. DOI: 10.1016/0039-6028(78)90310-2.

[317] G. R. Wakefield and R. M. Sharp, "The composition of oxides formed on Al-Mg alloys," *Applied Surface Science*, vol. 51, no. 1-2, pp. 95–102, 1991. DOI: 10.1016/0169-4332(91)90065-R.

[318] H. Okamura, K. Aota, M. Sakamoto, M. Ezumi and K. Ikeuchi, "Behaviour of oxides during friction stir welding of aluminium alloy and their effect on its mechanical properties," *Welding International*, vol. 16, no. 4, pp. 266–275, 2002. DOI: 10.1080/09507110209549530.

[319] Y. S. Sato, F. Yamashita, Y. Sugiura, S. H. C. Park and H. Kokawa, "FIB-assisted TEM study of an oxide array in the root of a friction stir welded aluminium alloy," *Scripta Materialia*, vol. 50, no. 3, pp. 365–369, 2004. DOI: 10.1016/j.scriptamat.2003.10.008.

[320] K. Tanaka, M. Kumagai and H. Yoshida, "Dissimilar joining of aluminum alloy and steel sheets by friction stir spot welding," *Journal of Japan Institute of Light Metals*, vol. 56, no. 6, pp. 317–322, 2006.

[321] T. Ogura, Y. Saito, T. Nishida, H. Nishida and T. Yoshida, "Partitioning evaluation of mechanical properties and the interfacial microstructure in a friction stir welded aluminum alloy / stainless steel lap joint," *Scripta Materialia*, vol. 66, no. 8, pp. 531–534, 2012. DOI: 10.1016/j.scriptamat.2011.12.035.

[322] T Ogura, T Nishida, Y Tanaka, H Nishida, S Yoshikawa, M Fujimoto and A Hirose, "Microscale evaluation of mechanical properties of friction stir welded A6061 aluminium alloy / 304 stainless steel dissimilar lap joint," *Science and Technology of Welding and Joining*, vol. 18, no. 2, pp. 108–113, 2013. DOI: 10.1179/1362171812Y.0000000098.

[323] P. Orozco-González, M. Castro-Román, S. Maldonado-Ruíz, S. Haro-Rodríguez, F. Equihua-Guillén, R. Muñiz-Valdez, S. Luna-Álvarez, M. Montoya-Dávila and A. Hernández-Rodríguez, "Nucleation of Fe-Rich Intermetallic Phases on α -Al 2 O 3 Oxide Films in Al-Si Alloys," *Journal of Minerals and Materials Characterization and Engineering*, vol. 3, pp. 15–25, 2015.

[324] P. Orozco, S. Maldonado, R. Muñiz, F. Equihua, S. Luna, J. Oritz, A. García, L. Castruita and A. Hernández, "Effect of oxide films on formation of Fe-rich intermetallic phases in aluminum alloys," *Journal of Thermal Analysis and Calorimetry*, vol. 131, no. 3, pp. 2329–2335, 2017. DOI: 10.1007/s10973-017-6765-7.

[325] E. F. Rauch and L. Dupy, "Rapid spot diffraction patterns identification through template matching," *Archives of Metallurgy and Materials*, vol. 50, no. 1, pp. 87–99, 2005.

[326] L. Li, H. Xia, C. Tan and N. Ma, "Effect of groove shape on laser welding-brazing Al to steel," *Journal of Materials Processing Tech.*, vol. 252, no. June 2017, pp. 573–581, 2018. DOI: 10.1016/j.jmatprotec.2017.10.025.

[327] Y. Meng and J.-M. Zuo, "Improvements in electron diffraction pattern automatic indexing algorithms," *The European Physical Journal Applied Physics*, vol. 80, no. 1, p. 10 701, 2017. DOI: 10.1051/epjap/2017160444.

[328] A. Morawiec, E. Bouzy, H. Paul and J. J. Fundenberger, "Orientation precision of TEM-based orientation mapping techniques," *Ultramicroscopy*, vol. 136, pp. 107–118, 2014. DOI: 10.1016/j.ultramic.2013.08.008.

[329] D. Zhang, P. Oleynikov, S. Hovmoller and X. Zou, "Collecting 3D electron diffraction data by the rotation method," *Zeitschrift fur Kristallographie*, vol. 225, no. 2-3, pp. 94–102, 2010. DOI: 10.1524/zkri.2010.1202.

[330] W. Wan, J. Sun, J. Su, S. Hovmöller and X. Zou, "Three-dimensional rotation electron diffraction: software RED for automated data collection and data processing," *Journal of Applied Crystallography*, vol. 46, no. 6, pp. 1863–1873, 2013. DOI: 10.1107/s0021889813027714.

[331] B. Wang, X. Zou and S. Smeets, "Automated serial rotation electron diffraction combined with cluster analysis: An efficient multi-crystal workflow for structure determination," *IUCrJ*, vol. 6, pp. 854–867, 2019. DOI: 10.1107/S2052252519007681.

[332] I. MacLaren, E. Frutos-Myro, D. McGrouther, S. McFadzean, J. K. Weiss, D. Cosart, J. Portillo, A. Robins, S. Nicolopoulos, E. Nebot Del Busto and R. Skogeby, "A Comparison of a Direct Electron Detector and a High-Speed Video Camera for a Scanning Precession Electron Diffraction Phase and Orientation Mapping," *Microscopy and Microanalysis*, vol. 26, no. 6, pp. 1110–1116, 2020. DOI: 10.1017/S1431927620024411.

[333] J. K. Sunde, S. Wenner and R. Holmestad, "In situ heating TEM observations of evolving nanoscale Al–Mg–Si–Cu precipitates," *Journal of Microscopy*, vol. 00, no. 00, pp. 1–5, 2019. DOI: 10.1111/jmi.12845.

[334] Z. Świątek, A. Gradys, Maj, J. Morgiel, K. W. Marszałek, R. Mania and M. Szlezynger, "XRD and TEM in situ heating of large period Ni/Al multilayer coatings," *Acta Physica Polonica A*, vol. 130, no. 4, pp. 880–883, 2016. DOI: 10.12693/APhysPolA.130.880.

[335] J. Morgiel, M. Szlezynger and R. Mania, "In-situ TEM heating of Ni / Al multilayers," *International Journal of Materials Research*, pp. 703–710, 2015.

[336] U. Gösele and K. N. Tu, "Growth kinetics of planar binary diffusion couples: "Thin-film case" versus "bulk cases"," *Journal of Applied Physics*, vol. 53, no. 4, pp. 3252–3260, 1982. DOI: 10.1063/1.331028.

[337] C Cayron, L Sagalowicz, O Beffort and P. A. Buffat, "Structural phase transition in Al-Cu-Mg-Si alloys by transmission electron microscopy study on an Al-4 wt % Cu-1 wt % Mg-Ag alloy reinforced by SiC particles," *Philosophical Magazine A*, vol. 79, no. 11, pp. 2833–2851, 1999. DOI: 10.1080/01418619908212027.

[338] J. K. Sunde, C. D. Marioara and R. Holmestad, "The effect of low Cu additions on precipitate crystal structures in overaged Al-Mg-Si(-Cu) alloys," *Materials Characterization*, vol. 160, no. November 2019, 2020. DOI: 10.1016/j.matchar.2019.110087.

Part III

Papers

Paper I

Nanocrystal segmentation in scanning precession electron diffraction data

T. Bergh, D.N. Johnstone, P. Crout, S. Høgås, P.A. Midgley, R. Holmestad, P.E. Vullum, A.T.J. van Helvoort

Journal of Microscopy (2020) **279** 158-167

Author contributions

TB, DNJ, and ATJvH sketched the idea and conceptualised the study. AL (acknowledged, not author) prepared the specimen. TB collected the data, wrote code for segmentation and analysed the data. DNJ, ATJvH, PC and SH made significant contributions in relation to the code and data analysis strategy. TB prepared the figures and wrote the manuscript with significant contributions from DNJ and with comments from all authors. ATJvH supervised SH, RH and PEV supervised TB, and PAM supervised DNJ and PC, and all gave comments to the data analysis and to the manuscript.

Nanocrystal segmentation in scanning precession electron diffraction data

T. Bergh[a], D.N. Johnstone[b], P. Crout[b], S. Høgås[a], P.A. Midgley[b], R. Holmestad[a], P.E. Vullum[a,b], A.T.J. van Helvoort[a,*]

[a] *Department of Physics, Norwegian University of Science and Technology (NTNU), Høgskoleringen 5, 7491 Trondheim, Norway*
[b] *Department of Materials Science and Metallurgy, University of Cambridge, Cambridge, United Kingdom.*
[c] *SINTEF Industry, 7034 Trondheim, Norway*

Abstract

Scanning precession electron diffraction (SPED) enables the local crystallography of materials to be probed on the nanoscale by recording a two-dimensional PED pattern at every probe position as a dynamically rocking electron beam is scanned across the specimen. SPED data from nanocrystalline materials commonly contain some PED patterns in which diffraction is measured from multiple crystals. To analyse such data, it is important to perform *nanocrystal segmentation* to isolate both the location of each crystal and a corresponding representative diffraction signal. This also reduces data dimensionality significantly. Here, two approaches to nanocrystal segmentation are presented, the first based on virtual dark-field imaging and the second on non-negative matrix factorisation. Relative merits and limitations are compared in application to SPED data obtained from partly overlapping nanoparticles, and particular challenges are highlighted associated with crystals exciting the same diffraction conditions. It is demonstrated that both strategies can be used for nanocrystal segmentation without prior knowledge of the crystal structures present, but also that segmentation artefacts can arise and must be considered carefully. The analysis workflows associated with this work are provided open-source.

Keywords: scanning precession electron diffraction, nanoparticles, virtual dark-field imaging, watershed segmentation, non-negative matrix factorisation, open-source

1. Introduction

Scanning electron diffraction (SED) is a scanning transmission electron microscopy technique in which a two-dimensional electron diffraction pattern is acquired at each probe position as a nanometre sized electron probe is scanned across a region of interest. Double-conical rocking of the electron probe may also be incorporated to record a precession electron diffraction (PED) pattern [1] at each probe position (SPED) [2]. Analysis of SED and SPED data is typically similar, enabling assessment of local crystallography on the nanoscale by, for instance, crystal phase [3], orientation [4] and strain mapping [5, 6]. S(P)ED data obtained from nanocrystalline materials typically comprise a relatively large number of (P)ED patterns, ca. 100 – 500000,

* Corresponding author
Email address: a.helvoort@ntnu.no (A.T.J. van Helvoort)

recorded from a significantly smaller number of crystals, ca. $10 - 1000$. Such data frequently include some (P)ED patterns that contain scattering from multiple crystals sampled along the beam trajectory. To isolate the diffraction signals from individual crystals that may overlap in projection, *nanocrystal segmentation* can be performed.

Nanocrystal segmentation of S(P)ED data aims to isolate the real space location of each individual crystal in the scan region, as well as a corresponding representative diffraction pattern for each crystal. This is a necessary step in analysing the diffraction from each crystal in a polycrystalline sample and leads to substantial dimensionality reduction. Such segmentation therefore provides a route to overcome limitations associated with two-dimensional phase and orientation mapping in samples where crystal overlap is prominent [7]. Nanocrystal segmentation is also a crucial step in reconstructing the morphology and diffraction pattern of each crystal in a polycrystalline specimen in three dimensions by scanning electron diffraction tomography [8, 9].

Strategies for nanocrystal segmentation based on iterative indexation [10], data matrix factorisation [8, 11], virtual dark-field (VDF) imaging [9] and data clustering [11–13] have been reported for S(P)ED data. Indexation requires knowledge of crystal structures present in the specimen, while clustering typically requires iterative determination of the number of categories. In contrast, VDF imaging and data matrix factorisation approaches can be performed without such *a priori* knowledge, which makes them well suited to the study of unknown phases, and they are therefore the focus of this work. It has also been demonstrated that SPED data is typically more amenable to successful nanocrystal segmentation than SED data [11]. This owes primarily to the integration through crystal bending and the reduction of dynamical oscillations in diffracted intensity as a function of thickness afforded by precession [11]. Hence, the analysis of SPED data is central in the present work.

The VDF imaging approach [9] is based on forming VDF images for numerous different diffraction conditions by plotting the integrated intensity of selected reflections as a function of probe position. The VDF images are compared against each other to identify images that show the same crystal, and such images are merged to yield one real space diffraction contrast image of each crystal. Simultaneously, the information on the associated diffraction conditions used to form each image in a merged set is combined to yield a representative diffraction pattern for that crystal.

The data matrix factorisation approach is a form of unsupervised machine learning where all the (P)ED patterns are stacked as vectors in a data matrix, M, that is factorised into a factor matrix C_P and a loading matrix C_L. Non-negative matrix factorisation (NMF) [14] is one such method that has been applied to S(P)ED data and found to yield factors that resemble (P)ED patterns, so-called component patterns, and loading maps that resemble diffraction contrast images highlighting the associated crystal in the scan region [8, 11].

In this work, VDF imaging and NMF are compared as methods for nanocrystal segmentation. Both approaches are applied to SPED data obtained from a model system composed of partly overlapping magnesium oxide (MgO) nanoparticles, where some crystals excite the same diffraction conditions. This system highlights particular challenges that arise when individual VDF images and individual loading maps are related to multiple crystals, which render the segmentation incomplete. To allow for a more complete nanocrystal segmentation, workflows incorporating image segmentation applied to VDF images or loading maps are developed. Relative merits and limitations of both strategies are discussed, and the associated SPED data [15] and demonstrated

workflows are available open-source [16] for further application and development.

2. Methods

2.1. Specimen preparation

MgO was produced by burning a piece of Mg in air using a gas torch to obtain a smoke containing MgO nanoparticles. TEM grids coated by holey carbon were held in the smoke for ca. 2 s, so that MgO nanoparticles were deposited on the grids.

2.2. Scanning precession electron diffraction

SPED was performed using a JEOL JEM-2100F fitted with a Nanomegas ASTAR system. PED patterns were acquired using an externally mounted Stingray optical camera that imaged the phosphor viewing screen of the microscope. The microscope was operated at 200 kV with a convergence semi-angle of 1.0 mrad and a precession angle of 16 mrad. The precession frequency was 100 Hz and the exposure time at each probe position was 10 ms.

2.3. Data processing and analysis

SPED data were analysed using pyXem [17], an open-source Python library for crystallographic electron microscopy, that builds on scientific Python packages, particularly hyperspy [18], scikit-image [19] and scikit-learn [20]. A notebook including the workflows developed and parameters used [16] and a copy of the associated SPED data [15] have been made available open-source. The raw four-dimensional SPED dataset D_R had dimensions $(2X, 2Y|K_X, K_Y)$, where X and Y refer to the navigation dimensions, i.e. the dimensions of the scanned area, and K_X and K_Y refer to the signal dimensions, i.e. the dimensions of the PED patterns, following the notation used in hyperspy.

2.3.1. Virtual dark-field imaging-based segmentation

The workflow for VDF imaging-based segmentation developed here was an adaption of the VDF imaging-based method proposed in [9]. The main difference was an additional step in which watershed image segmentation [21] was applied to each of the VDF images, so that the method could be used in cases where individual VDF images showed multiple crystals. It should be noted that image segmentation could be achieved using a wide range of established strategies, and application of another strategy may further improve the approach. The complete data processing workflow is illustrated in Fig. 1.

Pre-processing (Fig. 1(a)) included binning D_R in navigation space, which gave $D\,(X, Y|K_X, K_Y)$ that was aligned by shifting the centre of the direct beam to the same coordinates in all PED patterns. The background was removed by performing a difference of Gaussians background subtraction, which gave $D_B\,(X, Y|K_X, K_Y)$, before all diffraction peaks, $P(X, Y)$, were detected in all PED patterns, using a Laplacian of Gaussian blob finder. A clustering routine was employed to identify groups of peaks similar enough in positional coordinates to be considered to belong to the same unique diffraction vector. The unique vectors were filtered by magnitude to exclude the direct beam and diffraction peaks located at the edge of the detector, which resulted in N unique diffraction vectors, $P_U(N|2)$. VDF images were calculated by integrating the intensities within a disk centred at each of the unique peak positions in all PED patterns, which gave N VDF images $V(N|X, Y)$.

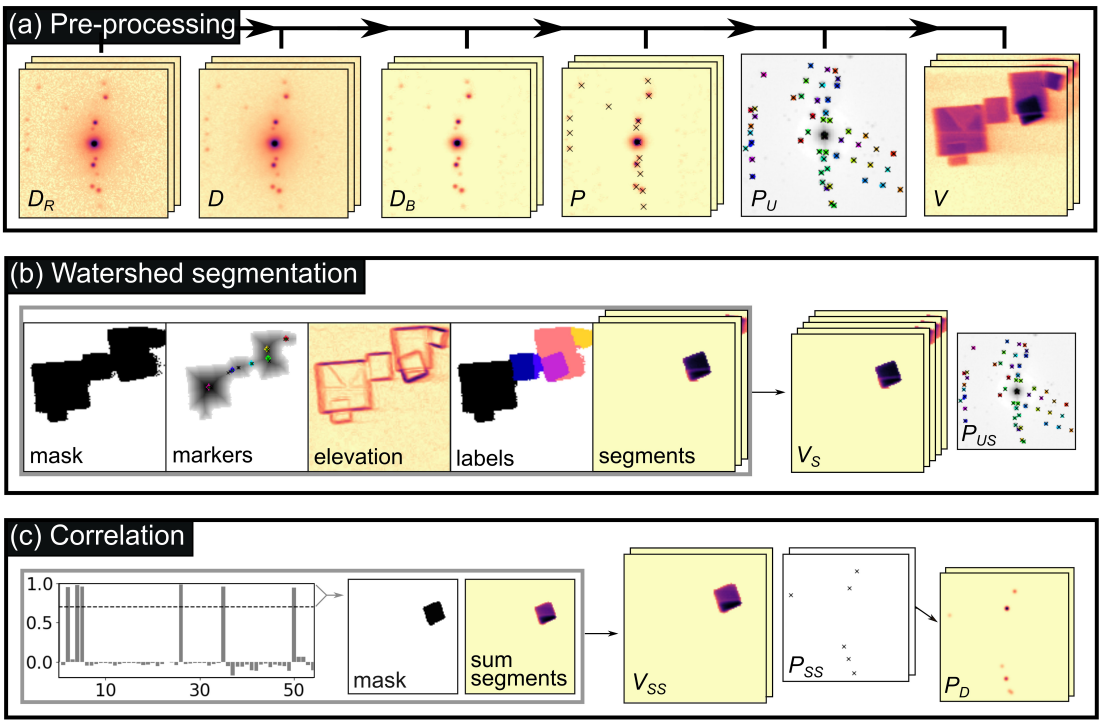

Figure 1: Virtual dark-field (VDF) imaging-based segmentation workflow. **(a)** Pre-processing the raw data (D_R) by binning and alignment (D), before the background is removed (D_B), all peaks are found (P), unique peaks are determined (P_U) and VDF images (V) are formed for all unique peaks. **(b)** Watershed segmentation is performed on each VDF image to yield VDF image segments (V_S) with corresponding peaks (P_{US}). For each VDF image, a mask is formed, markers are determined, and watershed segmentation is performed on the elevation image, leading to labelled regions that are used to define segments. **(c)** Correlation of the VDF image segments, where segments with a correlation exceeding a threshold are summed within a mask, leading to summed VDF image segments (V_{SS}) and corresponding peaks (P_{SS}). Virtual diffraction patterns (P_D) are created to visualise the diffraction spots of each summed segment.

Each VDF image was segmented by the watershed method as depicted in Fig. 1(b). For this, a mask was created by thresholding the VDF image automatically, the distance transform of the mask was calculated, and its maxima were used in determination of markers for watershed. Further, an elevation image was calculated by applying the Sobel filter to the VDF image. The elevation image was segmented by watershed, which resulted in labelled regions. Labelled regions smaller than a user-defined *minimum size* were discarded, before a segment image was created for each labelled region based on the VDF image. Accordingly, applying the watershed segmentation routine to the VDF images yielded a stack of VDF image segments, $V_S(M|X,Y)$, and a corresponding list of unique vectors, $P_{US}(M|2)$, where $M \geq N$.

Cross-correlation was then performed between segments to identify those segments that corresponded to the same crystal, as illustrated in Fig. 1(c). For the case demonstrated here, iterative comparisons of the correlation scores of one segment with the remaining segments were sufficient, although the full correlation matrix may be considered for improved accuracy in other

cases. Segments with a normalised cross-correlation exceeding a user-specified *correlation threshold* were considered. If the number of these segments, which corresponded to the number of associated diffraction vectors, was below a user-specified *vector threshold*, the segments were discarded. Otherwise, a segment mask, defining the region where more segments than a user specified *segment threshold* had intensities above zero, was created, and the corresponding segments were summed within the segment mask. The segment sum was associated with its corresponding list of unique vectors, and each vector was assigned an intensity that was the total intensity of the corresponding single segment image within the segment mask. The correlation step resulted in a stack of summed segments, $V_{SS}\ (L|X,Y)$, and a list of diffraction vectors and intensities, $P_{SS}(L)$, where $L \leq M$. The final step was done for visualisation purposes and consisted of reconstructing virtual diffraction patterns, $P_D\ (L|K_X,K_Y)$, for the summed segments, where Gaussians were used to model the diffraction spots.

2.3.2. Non-negative matrix factorisation-based segmentation

The workflow for NMF-based segmentation is illustrated in Fig. 2. The raw dataset, D_R, was binned and aligned to yield D, as for VDF imaging-based segmentation. D was decomposed by NMF following Poisson noise normalisation [22], as illustrated in Fig. 2(a). The region in the centre of each PED pattern, including the direct beam, was masked prior to performing NMF. This masking improved NMF results by avoiding issues associated with the direct beam saturating the detector and by removing the influence of high intensity variations in the direct beam, which rank highly in the minimised error metrics computed during NMF without being related to the most crystallographically significant features in the data. To estimate the number of components, E, to use for NMF, a scree plot was inspected. The scree plot showed the fraction of total variance explained by each component obtained by singular value decomposition (SVD), after mean-centering of the PED patterns. The NMF decomposition into E components then produced a stack of component patterns, $C_P\ (E|K_X,K_Y)$, and a corresponding stack of loadings, $C_L\ (E|X,Y)$.

Cross-correlation of both the component patterns and loading maps was performed to merge components that originated from the same crystal, since NMF can result in splitting of signal from one crystal into several components. The correlation step is depicted in Fig. 2(b). If the normalised cross-correlation of both the component patterns and loadings exceeded a user-specified *pattern correlation threshold* and a user-specified *loading correlation threshold*, respectively, component patterns and loadings were summed. This correlation step resulted in component patterns, $C_{CP}\ (F|K_X,K_Y)$, and loadings, $C_{CL}\ (F|X,Y)$, where $F \leq E$. After correlation, the loadings were segmented by watershed, as portrayed in Fig. 2(c), using the same approach as for the VDF images described above. Segments were discarded if their maximum intensities were below a user-defined *minimum intensity threshold* or their total sizes were below a user-specified *minimum size*. Each resulting loading segment was associated with its corresponding component pattern, which resulted in component patterns $C_{SP}\ (G|K_X,K_Y)$, and loading segments, C_{SL} $(E|X,Y)$, where $G \geq F$.

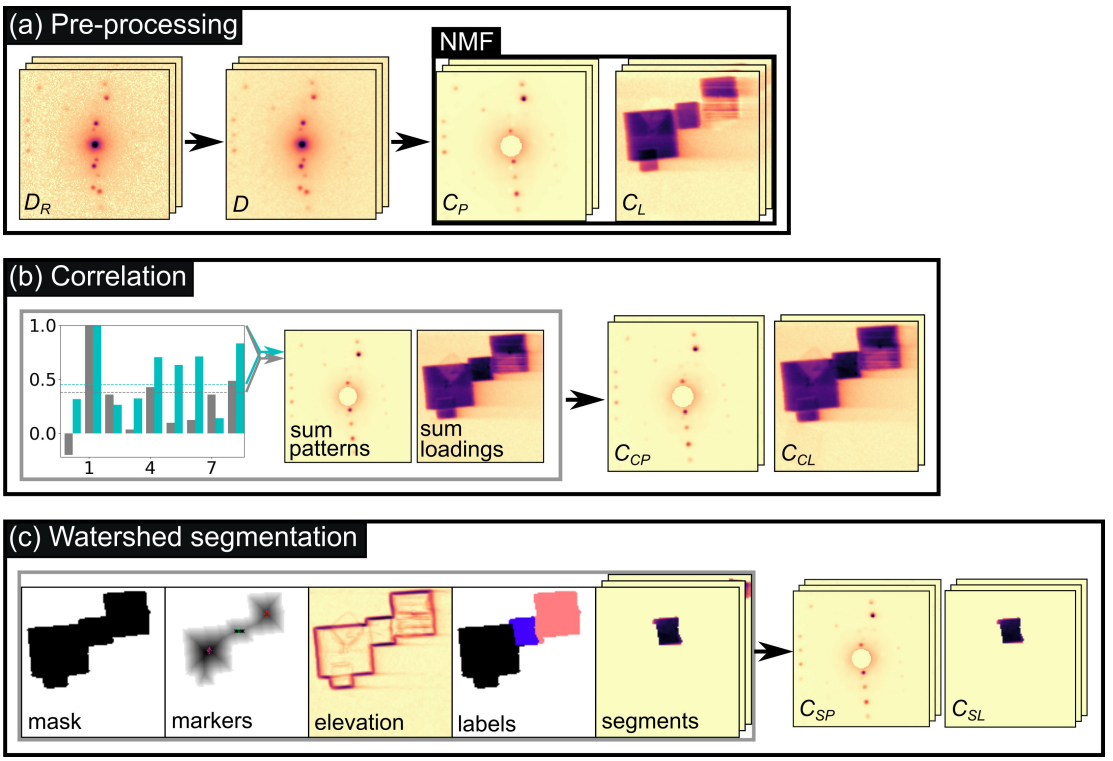

Figure 2: Non-negative matrix factorisation (NMF)-based segmentation workflow. **(a)** Pre-processing where the raw dataset (D_R) is binned and aligned (D). NMF performed on D yields component patterns (C_P) and loadings (C_L). **(b)** Correlation of the component patterns and loadings, where components are summed if the correlations of both patterns and factors exceed threshold values, leading to correlated patterns (C_{CP}) and loadings (C_{CL}). **(c)** Watershed segmentation is performed on each correlated loading to yield loading segments (C_{SL}) with corresponding patterns (C_{SP}). For each loading, a mask is formed, markers are determined, and watershed segmentation is performed on the elevation image, leading to labelled regions that are used to define segments.

3. Results and Discussion

3.1. Scanning precession electron diffraction data inspection

An annular VDF image formed using the demonstration SPED dataset D is shown in Fig. 3(a), where the outline of each of the nine cubic particles, labelled P1-P9, are indicated. Fig. 3(b) shows the sum of PED patterns within a region without overlap for each particle, except for P2 that overlapped significantly with P1. The detected diffraction vectors of P2 are indicated in (b). P3, P4, P6 and P8 had similar orientations, as seen by the morphological similarities in (a) and the similar PED patterns in (b). The sum of the PED patterns of these particles, labelled PΣ, is also shown in (b).

3.2. Virtual dark-field imaging-based segmentation

The results of VDF imaging-based segmentation are shown in Fig. 4. Fig. 4(a) shows summed VDF image segments (V_{SS}), and (b) shows the corresponding virtual diffraction patterns (P_D).

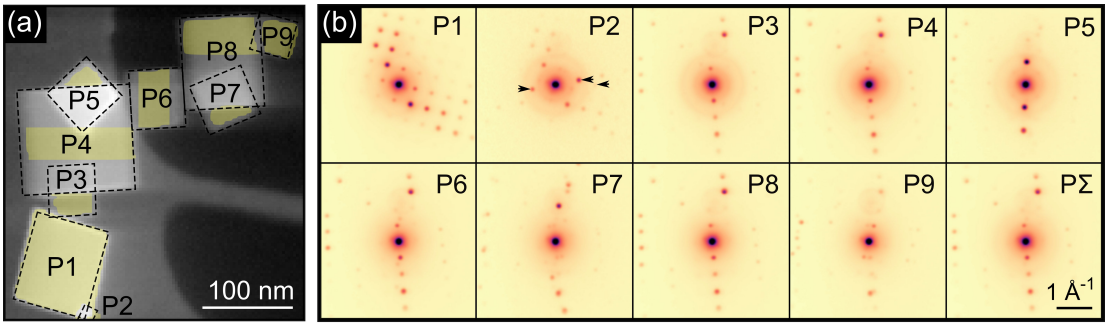

Figure 3: **(a)** Annular virtual dark-field (VDF) image showing nine magnesium oxide (MgO) particles (grey), labelled P1-P9, lying on top of a holey amorphous carbon film (dark grey) or over vacuum (black). The outlines of the MgO particles are indicated by dashed rectangles. **(b)** Sum of PED patterns within the yellow areas in (a). The detected diffraction vectors of P2 are marked by black arrows. PΣ is the sum of P3, P4, P6 and P8.

P1 and P4-P9 were segmented and labelled V1 and V4-V9, respectively. P2 was not included in the segmentation results, since only a few diffraction vectors were detected for this particle (Fig. 3(b)), so that it was excluded by the *vector threshold* criteria. This criteria was incorporated to allow exclusion of segments resulting from noise or from particles not being separated correctly. P3 was not segmented and was included in V4 together with P4 (Fig. 4(a)), since P3 and P4 did not display sufficient differences in their VDF images. These two particles shared the same orientation and had only common diffraction vectors (Fig. 3(b)), which meant that they appeared exclusively in the same VDF images where they always overlapped. Most often, only one marker was defined for both particles (e.g. Fig. 1(b)), which lead to both being included in the same segment after watershed segmentation. Thus, regions were only segmented if they displayed a minimum number of detectable diffraction peaks, and if they displayed sufficient distinctness in the VDF images to allow marker detection and to give clear edges in the elevation images for watershed segmentation.

Fig. 4(c) shows pre-processed PED patterns from regions without overlap where the diffraction vectors found in the virtual diffraction patterns are marked. Fig. 4(d) shows the difference between normalised pre-processed PED patterns and normalised virtual diffraction patterns. Some diffraction vectors were missing in the reconstructed virtual diffraction patterns, and the difference patterns, especially P4-V4, P8-V8 and P9-V9, displayed large residuals where strong peaks were not included fully in the virtual diffraction patterns. Some vectors were left out because of incorrect segmentation in the corresponding VDF images. Incorrect segmentation resulted from inhomogeneous intensity distributions or noise in the VDF images that lead to an inappropriate choice of markers and/or elevation images that did not reflect the particle shapes. In a worst-case scenario, an incorrectly shaped segment could give a sufficiently high correlation score with a correctly shaped segment, giving a false positive result. Furthermore, two diffraction peaks were included in the virtual diffraction patterns at some positions where only one peak was observed in the reference PED pattern, as marked in Fig. 4(c). For these peaks, the virtual apertures overlapped, which meant that intensity from one peak contributed to two VDF images. Another consequence of using a virtual aperture was that the virtual diffraction patterns did not contain any information on the intensity distribution associated with the diffraction vec-

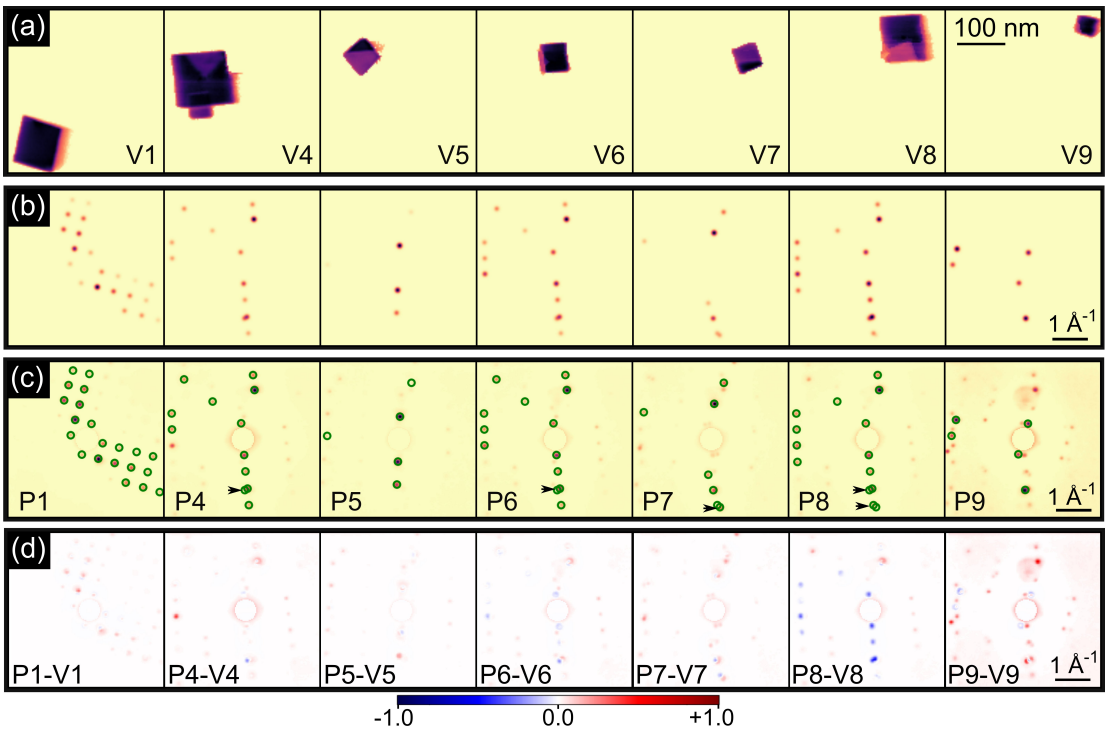

Figure 4: Virtual dark-field (VDF) imaging-based segmentation results. **(a)** Summed VDF image segments (V_{SS}), labelled V1 and V4-V9 according to the particle numbering in Fig. 3, and **(b)** corresponding virtual diffraction patterns (P_D). **(c)** Sum of pre-processed precession electron diffraction (PED) patterns within the regions indicated in Fig. 3(a). The diffraction vectors found in the virtual diffraction patterns ((b)) are encircled in green, and the black arrows indicate positions where the virtual apertures of two vectors overlapped. **(d)** Difference between the pre-processed sum PED patterns ((c)) and the corresponding virtual diffraction patterns ((b)), after normalisation.

tors. This resulted in prominent residuals in the difference patterns near diffraction vectors, e.g. asymmetric annuli in P9-V9.

3.3. Non-negative matrix factorisation-based segmentation

The results obtained by NMF are shown in Fig. 5. For NMF, the number of components, E, was a required parameter. By inspection, eight source signals could be identified in the dataset, i.e. six distinct MgO crystal orientations, amorphous carbon and vacuum (Fig. 3). However, the appropriate number of components for the decomposition could be higher, due to thickness or background intensity variations, strain, bending or crystal defects. In general, the scree plot produced by SVD can be used as a guide to estimate the number of components [11]. Assuming that components describing signals account for the largest fractions of variance in the data, the number of components at which the amount of variance is relatively low and starts to decay slowly is typically considered an appropriate choice, as the components after that point should describe noise. In that case, the scree plot would show an 'elbow' or 'knee' shape. The scree plot associated with SVD of the SPED data is shown in Fig. 5(a), and a notable gap in fraction of variance

can be discerned after 11 components, which was the number of components chosen for NMF.

The component patterns (C_P) and loadings (C_L) obtained by NMF, labelled #0-#10, are shown in Fig. 5(b). Components #1-#3 and #5-#10 were all related to MgO particles, while #0 was related to background and glare from the recording system, and #4 was related to the carbon film. Therefore, components #0 and #4 were discarded prior to the correlation step, which was performed to merge components related to the same crystals. The component patterns and loadings resulting from correlation (C_{CP} and C_{CL}) were labelled C1-C2, C5-C9 and CΣ according to the particle labelling. CΣ resulted from addition of components #2, #6 and #10, which were all related to particles that shared the same orientation; P3, P4, P6 and P8. None of the other components were merged during the correlation step, since they represented individual particles of different orientations and therefore gave low correlation values to the other components. P8 was partly accounted for both by components C8 and CΣ, which indicated that P8 comprised PED patterns that could be grouped mainly into two different diffraction conditions.

After correlation, the loading maps were segmented by watershed, and the resulting loading segments (C_{SL}), labelled CS1-CS7, CS8i-CS8iii and CS9, are shown in Fig. 6(a). CS1, CS5-CS7, CS8iii and CS9 corresponded to the individual particles P1, P5-P7, P8 and P9, respectively. CS2 corresponded to P2, but also included weaker intensities from surrounding regions that were not sufficiently removed by automatic thresholding, but that could have been removed by additional

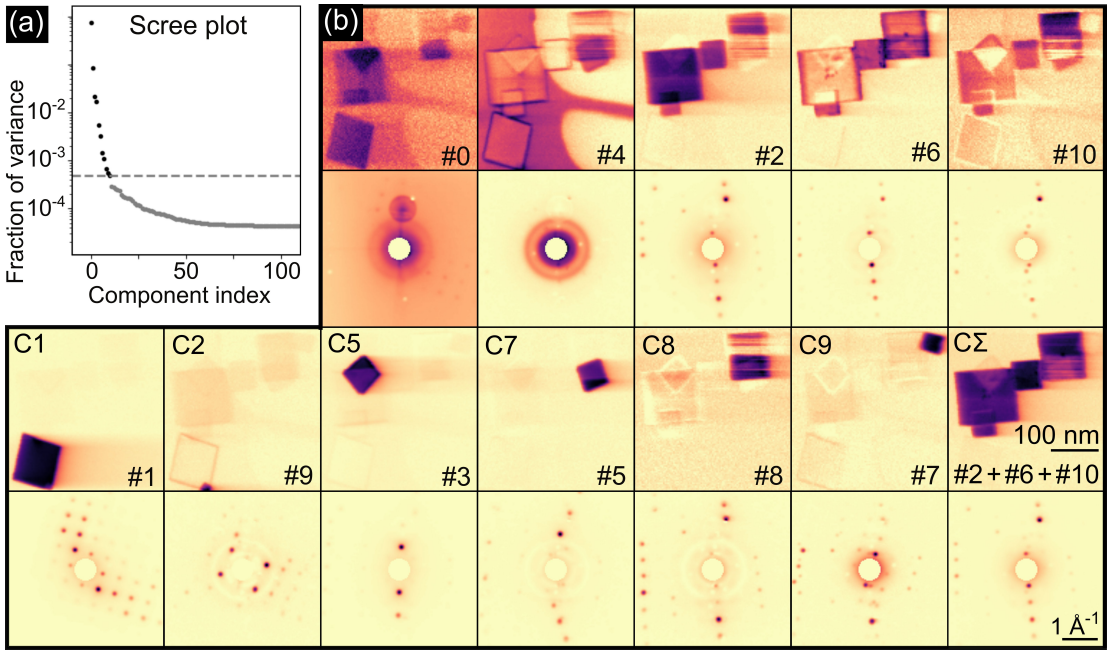

Figure 5: Non-negative matrix factorisation (NMF) results. **(a)** Singular value decomposition (SVD) scree plot showing the fraction of total variance that each component accounted for. The dashed horizontal line indicates that a number of 11 components was used for NMF. **(b)** Component patterns (top) and corresponding loading maps (bottom) obtained by NMF, labelled #0-#10. The component patterns and loadings after correlation are labelled C1-C9, according to the particle labelling in Fig. 3, and CΣ is the sum of components #2, #6 and #10.

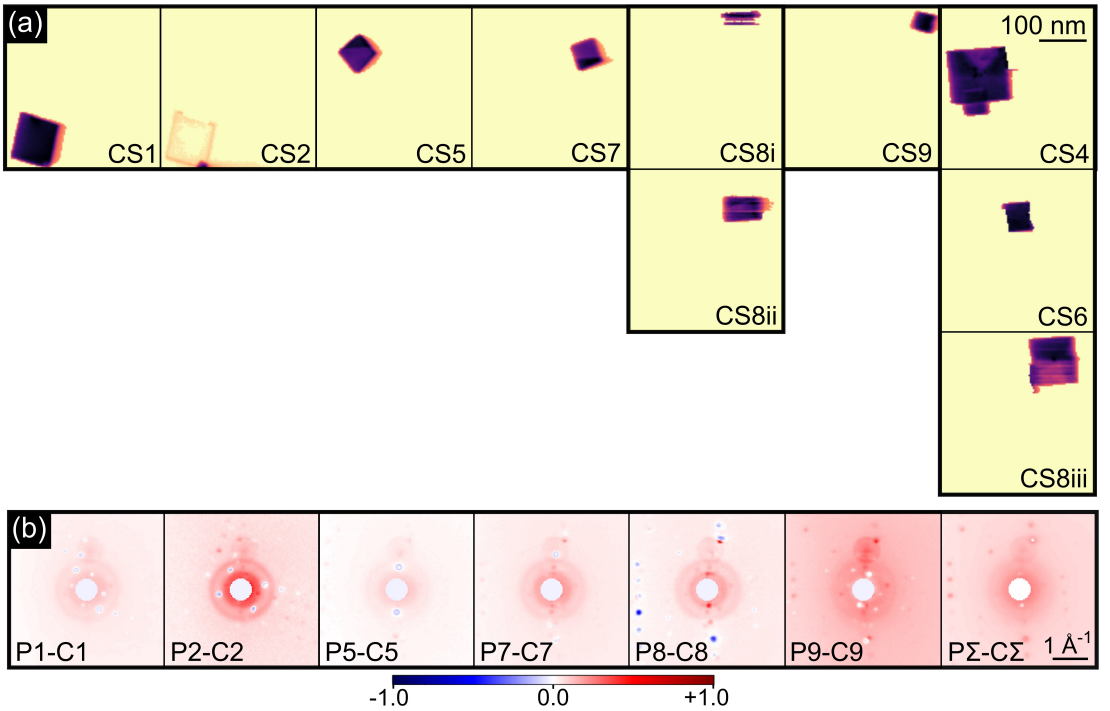

Figure 6: Non-negative matrix factorisation (NMF)-based segmentation results. **(a)** Loading map segments, labelled CS1-CS7, CS8i-CS8iii and CS9 according to the particle labelling (Fig. 3), resulting from watershed segmentation of the correlated component loading maps (Fig. 5(b)). **(b)** Difference between precession electron diffraction (PED) patterns (Fig. 3(b)) and the corresponding component patterns (Fig. 5(b)), after normalisation.

manual thresholding. CS4 contained signals both related to P3 and P4 for the same reason as explained previously for V4. P8 were split into three segments, CS8i-CS8iii, where the first two resulted from C8 and the last from CΣ, since this particle gave rise to more than one unique PED pattern, as mentioned earlier.

Fig. 6(b) shows the difference between the PED patterns (Fig. 3(b)) and the corresponding component patterns (Fig. 5(b)), after normalisation. Pseudo-subtractive intensities, i.e. regions where intensity was apparently missing, could be observed in some component patterns, e.g. #7-#9, similar to observations in [11], which gave positive residuals in the difference patterns, e.g. P2-C2, P8-C8 and P9-C9. Also, the difference patterns showed positive background intensities, since the background was accounted for largely by component #0. Moreover, there were notable residuals related to diffraction vector intensities, even for cases where the PED pattern and the component pattern corresponded to highly similar areas in real space, e.g. negative values $\lesssim$0.06 could be seen in P1-C1.

3.4. Comparison of the two nanocrystal segmentation methods

Comparing the results from the VDF imaging- and the NMF-based segmentation methods (Fig. 4, Fig. 5 and Fig. 6), it is apparent that both approaches resulted in segmentation of par-

ticles P1, P5-P7 and P9. However, P2 was segmented in the NMF-based method and discarded in the VDF imaging-based method (Fig. 4(a) and Fig. 6(a)). This was because the VDF imaging-based method required that each segment displayed a sufficient number of detectable diffraction peaks, while NMF was less restrictive in that all distinct intensities accounting for significant variation in the data could give rise to individual components. That could be advantageous in nanocrystal segmentation as all crystals should be accounted for, given a large enough number of components. On the other hand, it could give complications in physical interpretations, since it is not necessarily diffraction from crystals of distinct orientations that give rise to individual components. Intensities related to individual crystals could be split into several components, which was countered partly in this work by inclusion of a correlation step that enabled summation of similar components. The correlation step lead to summation of components #2, #6 and #10 and subsequent segmentation of P4 and P6. Contrarily, C8, that was related to parts of P8, did not correlate sufficiently with other components, so that contribution from P8 were split into several segments, C8i-C8iii (Fig. 6(a)). Consequently, both segmentation approaches should be used with caution so as to avoid disregarding or oversegmenting crystals.

A major difference between the virtual diffraction patterns and the component patterns (Fig. 4(b) and Fig. 5(b)), was that the component patterns included all major diffraction vectors, while the virtual diffraction patterns were missing some. For VDF imaging-based segmentation, incorrect segmentation happened for some vectors, as mentioned earlier. Moreover, peak finding was done for each pre-processed PED pattern individually, and so relatively weak peaks would either not have been detected or could have resulted in noisy VDF images which could have given incorrect segmentation. NMF was more sensitive in that data redundancy was exploited to pick out even weak, recurring intensities, given a large enough number of components. Furthermore, the virtual diffraction patterns contained no information about the intensity distribution associated with individual diffraction vectors, as opposed to the component patterns. Thus, the need for and the way of creating virtual diffraction patterns should be critically evaluated. Nonetheless, the difference patterns (4(d) and Fig. 6(b)) showed notable residuals near diffraction vector positions for both methods, which indicated that neither the intensities in the component patterns nor the intensities in the virtual diffraction patterns could necessarily be used quantitatively.

The same watershed segmentation procedure was used for both VDF imaging-based and NMF-based segmentation, and it did not enable distinction of P3 from P4, which lead to P3 being included in the segment of P4 for both methods. One way to resolve such issues could be to include morphological prior knowledge as demonstrated in [23], here the fact that the crystals are cubes in projection. An alternative may be to apply contour fitting as a part of the segmentation step, similar to the approach demonstrated in [24]. Such approaches could allow attribution of overlap areas to more than one segment and possibly give segments better reflecting the crystal morphologies.

4. Conclusions

Two methods for nanocrystal segmentation, based on VDF imaging and on NMF respectively, were applied to SPED data obtained from a model system of partly overlapping MgO nanoparticles. This model system contained crystals that excited the same diffraction conditions and emphasised situations where neither of the methods distinguished all crystals. To overcome this issue, a watershed segmentation routine was included in both methods, which allowed segmentation of crystals that had highly similar diffraction patterns. However, the segmentation was

incomplete for a particularly challenging case where crystals that shared the same orientation also overlapped significantly in real space.

The VDF imaging-based segmentation required that each crystal to be segmented exhibited several detectable diffraction peaks, and thus neglected weak peaks and crystals yielding a relatively small number of peaks. Incorrect segmentation happened for some VDF images, so that some diffraction vectors were lacking in the virtual diffraction patterns. Contrary to the virtual diffraction patterns, the component patterns included information on the intensity distribution associated with individual diffraction vectors. Also, the NMF-based segmentation approach required minimal pre-processing and was more sensitive in the sense that no major intensity contribution was neglected and in that subtle intensity variations could be identified. When comparing the original PED patterns with the corresponding component patterns and with the virtual diffraction patterns, notable intensity differences near diffraction peaks were seen for both of the explored methods, which indicated that neither could necessarily be used quantitatively.

Given that they are used with care and that artefacts are considered critically, both VDF imaging- and NMF-based segmentation can be valuable tools for nanocrystal segmentation in SPED data subject to limitations. The workflows developed are available open-source and can be used for analysis of SPED data and as a platform for further developments.

Acknowledgements

Adrian Lervik is acknowledged for MgO specimen preparation, and Håkon Ånes is acknowledged for participating in discussions on unsupervised machine learning. Research Council of Norway: 237900 (SFI Manufacturing) and 197405 (NORTEM); Engineering and Physical Sciences Research Council, UK: EP/R008779/1; European Union's Horizon 2020 research and innovation programme (ESTEEM3): 823717.

References

[1] R Vincent and P. Midgley, "Double conical beam-rocking system for measurement of integrated electron diffraction intensities," *Ultramicroscopy*, vol. 53, no. 3, pp. 271–282, 1994. DOI: 10.1016/0304-3991(94)90039-6.

[2] E. Rauch, J Portillo, S Nicolopoulos, D Bultreys, S Rouvimov, and P Moeck, "Automated nanocrystal orientation and phase mapping in the transmission electron microscope on the basis of precession electron diffraction," *Zeitschrift fur Kristallographie*, vol. 225, no. 2-3, pp. 103–109, 2010. DOI: 10.1524/zkri.2010.1205. arXiv: arXiv:0804.0063.

[3] X Mu, A Kobler, D Wang, V. Chakravadhanula, S Schlabach, D. Szabó, P Norby, and C Kübel, "Comprehensive analysis of TEM methods for $LiFePO_4/FePO_4$ phase mapping: spectroscopic techniques (EFTEM, STEM-EELS) and STEM diffraction techniques (ACOM-TEM)," *Ultramicroscopy*, vol. 170, pp. 10–18, 2016. DOI: 10.1016/j.ultramic.2016.07.009.

[4] S Zaefferer, "A critical review of orientation microscopy in SEM and TEM," *Crystal Research and Technology*, vol. 46, no. 6, pp. 607–628, 2011. DOI: 10.1002/crat.201100125.

[5] J. Rouviere, B Armand, Y Martin, T Denneulin, and D Cooper, "Improved strain precision with high spatial resolution using nanobeam precession electron diffraction," *Applied Physics Letters*, vol. 103, no. 241913, 2013. DOI: 10.1063/1.4829154.

[6] D Cooper, T Denneulin, N Bernier, A Béché, and J.-L. Rouvière, "Strain mapping of semiconductor specimens with nm-scale resolution in a transmission electron microscope," *Micron*, vol. 80, pp. 145–165, 2016. DOI: 10.1016/j.micron.2015.09.001.

[7] A Kobler and C Kübel, "Challenges in quantitative crystallographic characterization of 3d thin films by acom-tem," *Ultramicroscopy*, vol. 173, pp. 84–94, 2017. DOI: 10.1016/j.ultramic.2016.07.007.

[8] A. Eggeman, R Krakow, and P. Midgley, "Scanning precession electron tomography for three-dimensional nanoscale orientation imaging and crystallographic analysis," *Nature Communications*, vol. 6, p. 7267, 2015. DOI: 10.1038/ncomms8267.

[9] Y Meng and J. Zuo, "Three-dimensional nanostructure determination from a large diffraction data set recorded using scanning electron nanodiffraction," *IUCrJ*, vol. 3, pp. 300–308, 2016. DOI: 10.1107/S205225251600943X.

[10] A. Valery, E. Rauch, L Clément, and F Lorut, "Retrieving overlapping crystals information from TEM nano-beam electron diffraction patterns," *Journal of Microscopy*, vol. 268, no. 2, pp. 208–218, 2017. DOI: 10.1111/jmi.12599.

[11] B. Martineau, D. Johnstone, A. van Helvoort, P. Midgley, and A. Eggeman, "Unsupervised machine learning applied to scanning precession electron diffraction data," *Advanced Structural and Chemical Imaging*, vol. 5, no. 1, 2019. DOI: 10.1186/s40679-019-0063-3.

[12] J. Einsle, A. Eggeman, B. Martineau, Z Saghi, S. Collins, R Blukis, P. Bagot, P. Midgley, and R. Harrison, "Nanomagnetic properties of the meteorite cloudy zone," *Proceedings of the National Academy of Sciences of the United States of America*, vol. 115, no. 49, E11436–E11445, 2018. DOI: 10.1073/pnas.1809378115.

[13] M Gallagher-Jones, C Ophus, K. Bustillo, D. Boyer, O Panova, C Glynn, C.-T. Zee, J Ciston, K. Mancia, A. Minor, and J. Rodriguez, "Nanoscale mosaicity revealed in peptide microcrystals by scanning electron nanodiffraction," *Communications Biology*, vol. 2, no. 1, pp. 1–8, 2019. DOI: 10.1038/s42003-018-0263-8.

[14] D. Lee and S Seung, "Learning the parts of objects by non-negative matrix factorization," *Nature*, vol. 401, no. 6755, pp. 788–791, 1999. DOI: 10.1038/44565.

[15] T Bergh, "Scanning precession electron diffraction data of partly overlapping magnesium oxide nanoparticles [data set]," 2019. DOI: 10.5281/zenodo.3382874.

[16] D. Johnstone, P Crout, S Høgås, T Bergh, J Laulainen, and S. Smeets, "Pyxem/pyxem-demos v0.10.0," 2019. DOI: 10.5281/zenodo.3533670.

[17] D. Johnstone, P Crout, J Laulainen, S Høgås, B Martineau, T Bergh, S Smeets, S Collins, J Morzy, H Å nes, E Prestat, T Doherty, T Ostasevicius, M Danaie, and R Tovey, "Pyxem/pyxem v.0.10.0," 2019. DOI: 10.5281/zenodo.3533653.

[18] F de la Peña, E Prestat, V. Fauske, P Burdet, P Jokubauskas, M Nord, T Ostasevicius, K. MacArthur, M Sarahan, D. Johnstone, J Taillon, A. Eljarrat, J Lähnemann, V Migunov, J Caron, S Mazzucco, T Aarholt, M Walls, T Slater, F Winkler, B Martineau, G Donval, R McLeod, E. Hoglund, I Alxneit, D Lundeby, T Henninen, L. F. Zagonel, and A Garmannslund, "Hyperspy/hyperspy v1.4.2," 2019. DOI: 10.5281/zenodo.3249885.

[19] S van der Walt, J. Schönberger, J Nunez-Iglesias, F Boulogne, J. Warner, N Yager, E Gouillart, T Yu, and T. scikit-image contributors, "scikit-image: image processing in Python," *PeerJ*, vol. 2, no. e453, 2014. DOI: 10.7717/peerj.453.

[20] F Pedregosa, G Varoquaux, A Gramfort, V Michel, B Thirion, O Grisel, M Blondel, P Prettenhofer, R Weiss, V Dubourg, J Vanderplas, A Passos, D Cournapeau, M Brucher, M Perrot, and E Duchesnay, "Scikit-learn: Machine Learning in Python," *Journal of Machine Learning Research*, vol. 12, no. 1, pp. 2825–2830, 2011. DOI: 10.1007/s13398-014-0173-7.2. arXiv: arXiv:1011.1669v3.

[21] S Beucher and C Lantuejoul, "Use of watersheds in contour detection," *International Workshop on Image Processing, Rennes, France*, pp. 1–12, 1979.

[22] M. Keenan and P. Kotula, "Accounting for Poisson noise in the multivariate analysis of ToF-SIMS spectrum images," *Surface and Interface Analysis*, no. 36, pp. 203–212, 2004. DOI: 10.1002/sia.1657.

[23] G Hamarneh and X Li, "Watershed segmentation using prior shape and appearance knowledge," *Image and Vision Computing*, vol. 27, no. 1-2, pp. 59–68, 2009. DOI: 10.1016/j.imavis.2006.10.009.

[24] C Jung and C Kim, "Segmenting Clustered Nuclei Using H-minima Transform-Based Marker Extraction and Contour Parameterization," *IEEE Transactions on Biomedical Engineering*, vol. 57, no. 10, pp. 2600–2604, 2010. DOI: 10.1109/tbme.2010.2060336.

Paper II

Microstructural and mechanical characterisation of a second generation hybrid metal extrusion & bonding aluminium-steel butt joint

T. Bergh, L. Sandnes, D.N. Johnstone, Ø. Grong, F. Berto, R. Holmestad, P.A. Midgley, P.E. Vullum

Materials Characterization (2021) **174** 110761

Author contributions

ØG suggested the study, designed the initial idea and supplied the joint. TB performed SEM and prepared the TEM lamellae by FIB, with one lamella prepared by PEV. TB collected TEM data, except for the SED data that were collected by DNJ with significant contributions to the alignments by CSA (acknowledged, not author). TB analysed the TEM data with comments to the analysis strategy and contributions to the interpretation of the results from DNJ, RH and PEV. LS analysed tensile testing data and contributed significantly to interpretation of the mechanical testing data. ØG, LS and FB supervised Mar. Mat. and Mat. Man. (acknowledged, not authors) who performed optical microscopy, and hardness measurements and tensile testing, respectively, and they contributed to understanding of these results. TB prepared the figures and wrote the manuscript with significant contributions from LS, ØG and DNJ, and with comments from all authors. ØG and FB supervised LS, RH and PEV supervised TB, and PAM supervised DNJ, and all made comments to the data interpretation and to the manuscript.

Microstructural and mechanical characterisation of a second generation hybrid metal extrusion & bonding aluminium-steel butt joint

Tina Bergh[a,*], Lise Sandnes[b], Duncan Neil Johnstone[c], Øystein Grong[b], Filippo Berto[b], Randi Holmestad[a], Paul Anthony Midgley[c], Per Erik Vullum[a]

[a] *Department of Physics, Norwegian University of Science and Technology (NTNU), Høgskoleringen 5, 7491 Trondheim, Norway*
[b] *Department of Mechanical and Industrial Engineering, NTNU, Richard Birkelands vei 2b, 7491 Trondheim, Norway*
[c] *Department of Materials Science and Metallurgy, University of Cambridge, 27 Charles Babbage Road, Cambridge, CB3 0FS, UK*

Abstract

Hybrid metal extrusion & bonding (HYB) is a joining method that enables solid-state bonding by combining addition of aluminium filler material through continuous extrusion with pressure exerted by a rotating steel tool. This work presents mechanical and microstructural characterisation of a second generation HYB butt joint of aluminium alloy 6082 and structural steel S355. The ultimate tensile strength was measured to be in the range of 184 – 220 MPa, which corresponds to 60 – 72% joint efficiency. Digital image correlation analysis of the strain development during tensile testing revealed that root cracks formed, before the final fracture ran close to the aluminium-steel interface. A significant amount of residual aluminium was found on the steel fracture surface, especially in regions that experienced higher pressure during joining. Scanning and transmission electron microscopy revealed that the bond strength could be attributed to a combination of microscale mechanical interlocking and a discontinuous nanoscale interfacial Al-Fe-Si intermetallic phase layer. Analysis of scanning electron diffraction data acquired in a tilt series, indicated that the polycrystalline intermetallic phase layer contained the cubic α_c phase. The results give insight into the bonding mechanisms of aluminium-steel joints and into the performance of HYB joints, which may be used to better understand and further develop aluminium-steel joining processes.

Keywords:
aluminium-steel joining, hybrid metal extrusion & bonding, Al-Fe-Si intermetallic phases, transmission electron microscopy, scanning electron diffraction

1. Introduction

Joints between aluminium (Al) alloys and steels have a wide range of applications, especially in the automotive industry, due to the favourable combination of the high strength of steels and the low weight of Al alloys. However, obtaining sound Al-steel joints is challenging by traditional

*Corresponding author
Email address: tina.bergh@ntnu.no (Tina Bergh)

welding processes, due to the large differences in thermo-physical properties. In addition, heat applied or generated during joining may lead to a soft zone on the Al side of the joint, and the formation of brittle interfacial Al-Fe(-Si) intermetallic phases (IMPs) along the bonded interface, that can limit the mechanical properties of the joint [1–4]. Despite these challenges, several joining processes have been adopted to produce sound Al-steel joints [5], e.g. friction stir welding (FSW) [6] and laser welding-brazing [7]. Various innovative hybrid joining techniques that combine valuable aspects of other existing techniques have evolved, including e.g. laser-assisted FSW [8] and the recently developed hybrid metal extrusion & bonding (HYB) process [9].

HYB is a solid state joining method originally developed for butt joining of Al alloy plates [9–11] that has developed into a versatile method for joining of a range of metallic alloys in various configurations [12–14]. The basis of the HYB method is continuous extrusion of a filler material (FM) that is dragged by a rotating steel tool through a non-rotating extruder housing and subsequently squeezed into the weld groove. The addition of FM and the pressure exerted by the rotating tool enable joining at low temperature, which is an advantage for Al-steel joining. By considering the low process temperature and utilising an analytical framework for modelling of Al-Fe interdiffusion, it was found that an IMP layer on the nanoscale was expected for HYB Al-steel joints, which was supported by transmission electron microscopy (TEM) [15]. The first generation of HYB Al-steel joints produced had ultimate tensile strength (UTS) values in the range of 104 – 140 MPa [16]. These joints suffered from a lack of bonding along a significant portion of the bond line. Still, the HYB process holds great potential for Al-steel joining, and more research is needed to optimise the process, explain the underlying bonding mechanisms, and characterise the observed nanoscale IMP layer.

This work presents characterisation of a second generation HYB Al-steel butt joint, produced following improvements of the setup used for the first generation HYB Al-steel joints. By combining mechanical and microstructural characterisation, this study aims to contribute to better understanding of the performance of Al-steel HYB joints and of the underlying bonding mechanisms. This work also provides fundamental insight into solid state Al-steel bonding in general.

2. Materials and methods

2.1. Materials

The FM was a wire of Al alloy 6082 (Ø 1.2 mm), that was manufactured starting with homogenised direct chill cast billets that were hot extruded, quenched and naturally aged, before they were cold drawn and cold shaved. The base materials (BMs) were a plate of rolled Al alloy 6082-T6 and a rolled structural steel S355 (EN 10025-2) plate, both with the following dimensions; length 240 mm, width 120 mm and thickness 4 mm. The nominal alloy compositions are given in Tables 1 and 2. Prior to joining, the edge of the steel plate was machined to obtain a bevelled edge that fitted the shape of the rotating pin. The Al and steel plates were subsequently cleaned with acetone.

Table 1: Nominal compositions of the 6082 Al alloys used as FM and BM in wt.%.

	Si	Mg	Mn	Fe	Cr	Cu	Ti	Zr	Zn	B	Other
Al FM	1.11	0.61	0.51	0.2	0.14	0.002	0.043	0.13	-	0.006	0.029
Al BM	0.9	0.8	0.42	0.45	0.02	0.06	0.02	-	0.05	-	0.02

2.2. Hybrid metal extrusion & bonding

Table 2: Nominal composition of the structural steel S355 BM in wt.%.

Mn	C	Cr	Ni	Al	Cu	Si	Nb	P	Mo	V	S	N	Ti	B
0.69	0.067	0.05	0.05	0.040	0.028	0.02	0.014	0.010	0.009	0.008	0.005	0.005	0.001	0.0001

Schematic illustrations of the HYB process are shown in Figure 1. Prior to joining, the BMs were placed on top of a steel backing and fastened so that a 2 mm root opening formed between them, as shown in Figure 1(a). A HYB PinPoint extruder tool [17] was positioned so that it did not touch the steel plate but was in direct contact with the edge of the Al BM plate. The extruder tool consisted of a steel housing that surrounded a rotating pin equipped with a set of extrusion dies in the bottom end. The steel BM was placed on the advancing side (AS), where the pin rotation was in the same direction as its movement along the weld groove, and oppositely, the Al BM was placed on the retreating side (RS), following the nomenclature used in FSW [18]. During HYB, the extruder travelled along the groove, as illustrated in Figure 1(b), and heavily deformed the edge of the Al BM by digging into and dragging the Al BM around. Simultaneously, the Al FM wire was continuously fed into the extruder where it was dragged around due to the frictional forces acting on it inside the extrusion chamber, i.e. the space in between the rotating pin and the non-rotating steel housing. After meeting an abutment inside the extrusion chamber, the FM was extruded through moving helicoid-shaped dies at the bottom end of the rotating pin. The Al FM was dragged along with the pin before it became deposited in the groove behind the pin. The flow of Al in the groove resulted in bonding and eventually a consolidated joint, as illustrated in Figure 1(c). Further descriptions of the HYB process can be found elsewhere [11, 19, 20].

The joining parameters used were; pin rotation: 400 RPM, welding speed: 6 mm/s

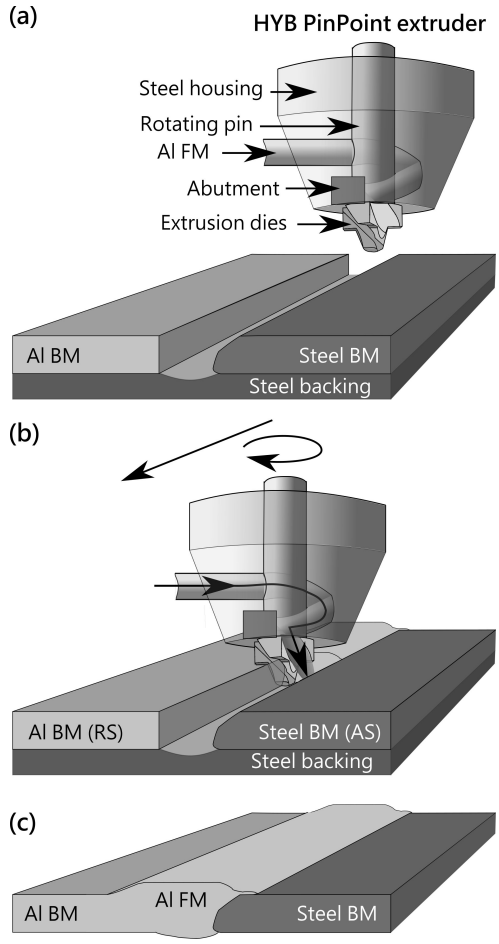

Figure 1: Illustration (not to scale) of **(a)** before, **(b)** during and **(c)** after Al-steel HYB butt joining. Before joining, Al and steel BM plates are clamped onto a steel backing, Al on the retreating side (RS) and steel on the advancing side (AS). During joining, the HYB PinPoint extruder travels along the joint line as the Al FM wire is continuously extruded through extrusion dies in the rotating pin, after meeting an abutment inside the extrusion chamber. The Al FM fills the groove, and a finished joint is produced.

and wire feed rate: 142 mm/s. During joining, the FM inlet in the extruder was cooled by spraying with dry ice supplied at a rate of 160 g/min. The gross heat input during welding was estimated to ~0.27 kJ/mm.

2.3. Hardness measurements

The Vickers hardness of polished cross-sections of the FM wire was measured before joining using an Innovatest Nova 360 instrument and an applied load of 0.5 kg. The hardnesses of the Al and steel BMs were measured before joining on polished specimens using a Mitutoyo micro Vickers hardness testing machine and an applied load of 1.0 kg. The transverse hardness profiles of polished cross-sections of the joint were measured following the same procedure as for the BMs.

2.4. Tensile testing

For tensile testing of the joint, four specimens were prepared with dimensions according to ASTM standard E8/E8M[21], except that the parallel lengths were extended to 36 mm to capture the entire soft zone on the Al side. Two of the specimens, R1 and R2, were tested as-joined with the reinforcement intact. Two other specimens, F1 and F2, were flush-machined prior to testing, in order to remove the excess material at the top (crown) and bottom (root) of the joint. Tensile testing was performed using an Instron 5985 hydraulic test machine equipped with a load cell of 250 kN. During all tensile tests the cross-head speed was set to 1.5 mm/min, which corresponds to a nominal strain rate of ~7e-4 s^{-1}.

Two-dimensional DIC analysis were performed to quantify the strain evolution occurring during tensile testing. Before testing, the specimens were each painted with a fine grained speckle pattern that was monitored during tensile testing with a high-resolution camera recording at ~10 Hz. The images were analysed using the software developed by Fagerholt et al.[22, 23], that is based on calculating the displacements of finite elements in the speckle pattern by cross-correlation. This was done by first adding a mesh onto a reference image of the speckle pattern on the specimen taken before tensile testing, before projecting the mesh onto each image taken during testing. For each element in the mesh, the translation of the speckle pattern was calculated by cross-correlation with respect to the corresponding mesh element in the reference image. The displacement of the speckle pattern was then used to calculate the in-plane principal true strains that were in turn used to calculate the effective strain. The effective strains were finally visualised as two-dimensional strain-field maps.

2.5. Optical microscopy

The macrostructure of Al was imaged in mechanically polished cross-sections that had been leached in a solution of 100 ml H_2O and 1 g NaOH for 3 – 4 min, using an Alicona infinite focus confocal microscope. In order to reveal the Al microstructure, polished cross-sections were anodised by immersion in a solution containing H_2O and 5% HBF_4 (Barker's reagent [24]) for 90 s using a current of 1.0 A and a voltage of 20 V. A Leica MEF4M optical microscope was used to examine the microstructure in polarised light.

2.6. Scanning electron microscopy

Scanning electron microscopy (SEM) studies were conducted on mechanically polished cross-sections of the joint and on original fracture surfaces resulting from tensile testing. The SEM imaging was performed using a FEI Helios G4 dual-beam focused ion beam (FIB)-SEM instrument at acceleration voltages in the range of 3 – 15 kV.

2.7. Transmission electron microscopy

TEM lamellae were prepared from joint cross-sections and fracture surfaces by FIB lift-out. TEM lamellae of improved quality were obtained by rotating each cross-section so that the FIB thinning was performed normal to the Al-steel interface, in order to limit thickness variations due to the difference in milling rates between Al and steel.

TEM, scanning TEM (STEM), and X-ray energy dispersive spectroscopy (EDS) were performed using a JEOL ARM200CF fitted with CEOS spherical aberration correctors in both the probe and image forming optics. The microscope was operated at 200 kV and was equipped with a 100 mm^2 Centurio EDS detector. EDS maps were analysed and visualised using the python library hyperspy [25] to bin and fit the data and to estimate the composition using the Cliff-Lorimer method, as described in detail in Supplementary Information (SI) S1.

Scanning electron diffraction (SED) data were acquired using a JEOL ARM300F (Diamond Light Source, UK) fitted with JEOL spherical aberration correctors in both the probe and image forming optics. The instrument was operated at 200 kV and aligned in an uncorrected nanobeam configuration with a convergence semi-angle of <1 mrad and a diffraction limited probe diameter of ~5 nm. Diffraction patterns were acquired using a Merlin Medipix direct electron detector with an exposure time of 1 ms at each probe position. SED maps were obtained from the same specimen region at a series of specimen tilt conditions covering a range of 30° in steps of 1°.

The SED data were analysed using the python library pyxem [26]. Diffraction contrast images of crystals in the mapped area were produced using virtual dark field (VDF) imaging-based segmentation [27]. VDF images were formed by plotting the intensity within integration windows, positioned to capture measured Bragg diffraction disks, as a function of probe position. Individual crystals in each VDF image were isolated by watershed image segmentation. Further, since several diffraction spots were typically detected for each crystal, VDF image segments associated with the same crystal were identified via cross-correlation and summed.

The crystal structure of observed IMPs was assessed based on diffraction patterns recorded near zone-axis orientations that were selected manually from the SED data. Non-negative matrix factorisation based segmentation [27, 28] was performed using the SED data from a small region of interest including each IMP particle, in order to reduce diffuse scattering and overlapping crystal contributions. Bragg disk positions were then found and the distances between spots in selected rows were calculated. For each selected row, all measured distances between spots ($|\Delta\vec{G}|$) were used to compute an average d-spacing ($\overline{|\Delta\vec{G}|^{-1}}$) and standard deviation. Indexation of the Bragg peaks was then attempted with respect to numerous candidate Al-Fe(-Si) phases, as detailed in SI S2. For this, the two shortest average diffraction spot distances for two non-parallel rows and the angle between these, were considered for each pattern. The phase(s) that best matched with as many patterns as possible was identified. More information on the SED data acquisition and analysis can be found in SI S2.

3. Results

3.1. Mechanical characterisation

To investigate the influence of the joining process on the starting materials, Vickers hardness profiles were measured across joint cross-sections and compared to the hardness of the materials as-received. In the as-received condition, the hardness of the steel BM, Al BM and Al FM were measured to 162.7 ± 4.5 $HV_{1.0}$ (average and standard deviation of 21 measurements), 107.2 ± 1.7

$HV_{1.0}$ (14) and 124.5 ± 2.2 $HV_{0.5}$ (15), respectively. Figure 2(a) presents horizontal and vertical hardness profiles measured across joint cross-sections. Figure 2(b) shows a corresponding optical microscopy image where the location of the hardness profile indents are indicated. By comparing the horizontal profile in Figure 2(a) with the micrograph in (b), it is apparent that the steel showed no decrease in hardness after joining, while Al showed significant softening both inside and outside of the extrusion zone (EZ). The horizontal profile shows a heat affected zone (HAZ) extending 13.5 mm into the Al BM, and the minimum hardness (73.1 $HV_{1.0}$) was found near the EZ-HAZ boarder, 5.5 mm from the weld centre. The vertical profile shows that the hardness decreased from the weld crown at the top towards the weld root region at the bottom.

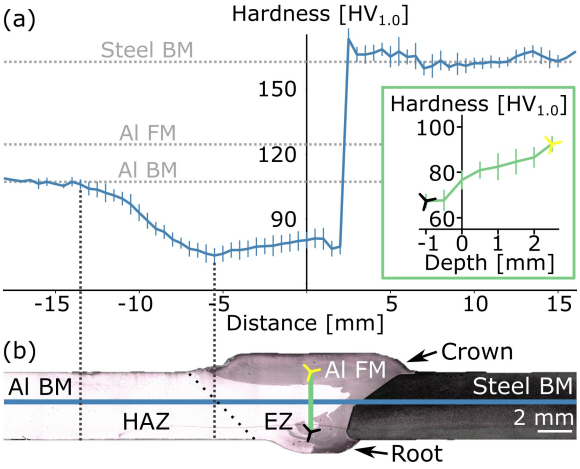

Figure 2: Hardness profiles of joint cross-sections. **(a)** Average horizontal and vertical profiles displayed in blue and green, based on six and five measured profiles, respectively. The error bars show pluas and minus one standard deviation. The horizontal grey lines show the hardness of the steel BM, Al FM and Al BM before joining. The vertical lines at -13.5 mm and -5.5 mm indicate the extent of the soft zone in Al and the minimum value in the horizontal profile, respectively. **(b)** Optical micrograph with coloured lines that mark the positions of the hardness indents. The locations of the root and crown regions, the heat affected zone (HAZ) and the extrusion zone (EZ) are indicated.

The engineering stress-strain curve obtained via tensile testing is shown in Figure 3(a) for specimen R2, while the curves for the other specimens are shown in SI S3. The average UTS was 197 ± 15 MPa, and the average fracture strain was 2.5 ± 0.7%. Considering that the UTS of the Al BM before joining was 307 MPa and that the fracture strain was ~20% [29], the average joint efficiency was 64 ± 5%, and the fracture strain was low. Specimen F1 had the highest UTS of 220 MPa (72%) and R1 and R2 the lowest of 184 MPa (60%). Strain hardening can be observed in Figure 3(a), and the final fracture was brittle with limited necking occurring.

DIC analyses were performed to study the crack initiation and propagation path, as well as the local deformations occurring during tensile testing. Figures 3(b) and (c) show images and strain maps of specimen R2 at different stages (I-IV) during tensile testing. From (b) it can be seen that a crack developed near the interface between steel and Al in the root region (I). With increasing stress, the root crack propagated (II and III), and also a smaller crack became visible in the weld crown region (III). The final fracture occurred close to the Al-steel interface (IV). Figure 3(c) shows strain maps displaying the effective strain. First, strain developed in the soft Al zone and in the vicinity of the root crack (I). As the applied load increased, the deformation increased in both of these regions (II), before the strain became significant also along the Al-steel interface (III). Results from the DIC analysis of specimens R1, F1 and F2 are shown in SI S3. For all tested specimens, the fracture propagated from root flaws and subsequently along the Al-steel interface.

To better understand the fracture path, the fracture surfaces from tensile testing were imaged by SEM. Figures 4(a) and (b) show an optical micrograph together with back-scatter elec-

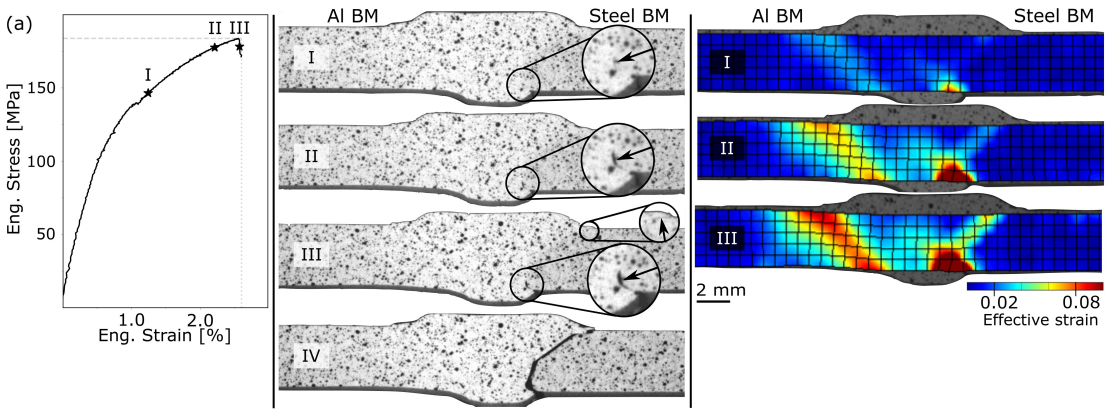

Figure 3: Tensile testing of specimen R2. **(a)** Engineering stress-strain curve where selected points (I-III) are marked. **(b)** Images used for digital image correlation (DIC) analysis at stages I-III and immediately after fracture (IV). The speckle pattern used in the DIC analysis, consisting of black dots painted on top of a light background, can be seen. The insets highlight crack formation. **(c)** Strain maps, resulting from the DIC analysis, showing the effective strain at stages I-III.

tron (BSE) and secondary electron (SE) SEM images of the steel fracture surface of specimen R2. The surface showed two distinct characteristics; i) a flat appearance in the top towards the crown (left side of the blue lines in Figures 4(a) and (b)) and ii) a wavy appearance in the bottom part towards the root region (right side). The flat upper part showed residual Al that had stuck to the steel surface forming thin, elongated chunks. The wavy pattern in the lower region consisted of thick chunks of Al attached to the steel with large bumps and protrusions. The corresponding Al fracture surface showed a wavy pattern with bumps and dimples matching those on the steel surface, as shown in SI S4. The shape of this pattern indicated that it resulted from an impression of the extrusion dies in Al as the rotating pin traversed the weld groove. From both the steel and the Al fracture surfaces, it could be seen that the fracture ran mainly along the Al-steel interface for the upper part, although there was a noticeable amount of residual material. The fracture ran mostly in Al for the lower part, except for the bottom of the root, where the fracture ran close to the Al-steel interface.

3.2. Microstructural characterisation

A micrograph of the joint cross-section is shown in Figure 5(a) (enlarged view of Figure 2(b)), where the Al BM appears brighter than the Al FM. The contrast difference arose after leaching and stemmed from the differences in chemical compositions, which resulted in a difference in overall leaching behaviour for the BM and FM. The top weld region including the crown and the Al region adjacent to steel were predominantly composed of Al FM, while the Al BM was pushed into the centre of the weld groove and into the root region. Figure 5(b) displays the grain structure in the Al region imaged in polarised light after anodisation. Most of the grains in the EZ were smaller than those in the HAZ. The middle region of the EZ comprised fine equiaxed grains, while the bottom region showed larger grains reflecting the Al flow pattern. Series of elliptical features, resembling an onion ring pattern, can be seen in the top weld crown. Figures 5(a) and (b) both indicate that

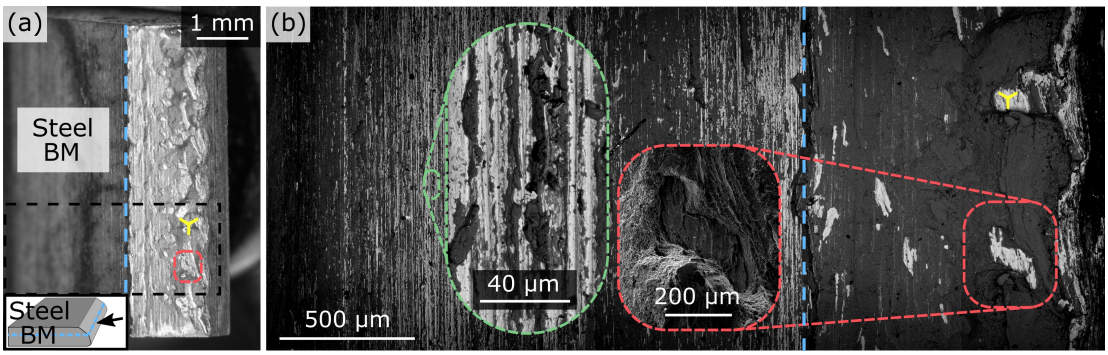

Figure 4: The steel fracture surface resulting from tensile testing of specimen R2. **(a)** Optical micrograph. The bottom inset illustrates the viewing direction, and the blue lines indicate the boarder between the top and the bottom part of the fracture surface. **(b)** BSE SEM image where steel appears light grey and Al dark grey. The inset outlined in green displays a SE SEM image of residual Al found on the upper part of the steel, while that in red shows a SE SEM image of a dent in the residual Al.

the FM flow was directed downward along the steel side of the weld groove and towards the root region, where the FM met the Al BM.

3.2.1. The aluminium-steel interface region

The Al-steel interface region was studied by SEM, as shown in Figure 6. An overview of the weld cross-section is shown in Figure 6(a), where steel fragments of various sizes can be seen in the root region. These steel fragments resulted from the rotating pin coming into contact with the steel surface with enough force to detach steel fragments that were stirred into the EZ. Figures 6(b), (c) and (d) display higher magnification BSE SEM images of the Al-steel interface showing the rough appearance of the interface, which was more pronounced towards the bottom half of the joint. A steel protrusion with dimensions ~20 µm can be seen in Figure 6(c). (d) reveals an interfacial crack in the root region near where crack propagation was observed to initiate in

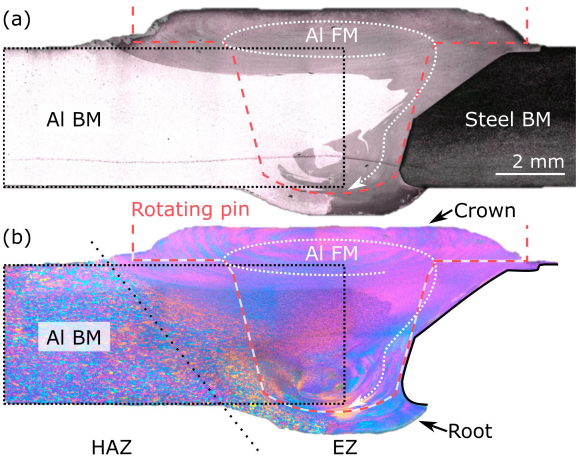

Figure 5: Optical microscopy of joint cross-sections. **(a)** Micrograph where the steel BM appears dark grey, the FM medium grey and the Al BM light grey. The location of the Al BM plate before joining is marked by a black line, the flow of FM during joining is illustrated by a white curved arrow, and the rotating pin during joining is outlined in red. **(b)** Polarised light micrograph showing the Al grain structure. The locations of the root and crown regions, the heat affected zone (HAZ) and the extrusion zone (EZ) are indicated.

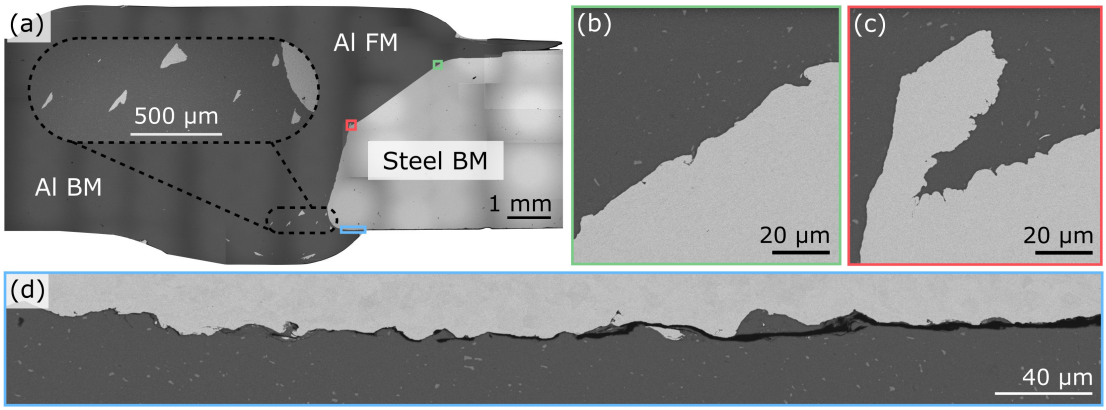

Figure 6: BSE SEM images of the joint cross-section. **(a)** Overview of the weld region where the inset shows steel fragments in the extrusion zone. **(b)**, **(c)** and **(d)** show higher magnification images of the green, red and blue regions marked in (a), respectively. (c) highlights a steel protrusion, while (d) emphasises a root crack.

tensile tests (Figure 3).

More detailed characterisation was performed using (S)TEM of lamellae lifted out using FIB from eight locations along the Al-steel interface, as indicated in Figure 7(a). Three characteristic interface appearances were identified; i) straight (e.g. Figure 7(b)), ii) rough (e.g. Figure 7(c)) and iii) wavy (e.g. Figure 7(d)) interfaces. Straight interfaces were observed in lamellae from the top part of the joint (Lamellae 5 – 8), and these interfaces showed either no signs of an IMP layer (Lamellae 6 and 7) or an IMP layer in only limited parts of the interface (Lamellae 5 and 8). Rough and wavy interfaces were observed in lamellae from the bottom region (Lamellae 1 – 4), and these interfaces were covered by IMP layers that were discontinuous (Lamellae 1 and 2) or continuous (Lamellae 3 and 4). (S)TEM results from all lamellae are shown in SI S5.

Figures 7(b)-(d) show Lamellae 3, 4 and 8 that displayed the three different interface appearances. Figure 7(b) shows an overview bright-field (BF)-TEM image of Lamella 8 that displayed a straight interface. Lamella 8 was lifted out from the steel fracture surface of specimen R2 from a region where a thin and dimpled Al layer covered steel, which explains the top serrated Al surface seen in Figure 7(b). A restricted IMP layer was found covering only a ~0.9 µm wide portion of the Al-steel interface, which is shown in the inset. Figure 7(c) shows an overview BF-TEM image of Lamella 4 where a rough interface with deformed regions of intermixed Al and steel were seen. A ~40 nm thick IMP layer was observed over the whole interface, and the IMP layer grew around the deformed steel fragments near the interface, which can be seen in the insets in (c). In Figure 7(d) an overview BF-TEM image of Lamella 3 is shown, where a slightly wavy Al-steel interface can be seen. The interface was continuously covered by a ~30 nm thick interfacial IMP layer. Further, the number density of dispersoids was observed by visual inspection to be higher close to the steel interface, relative to the number density $\gtrsim$1 µm away from the interface.

3.2.2. The interfacial intermetallic phase layer

The chemical composition of the interfacial IMP layer was investigated by STEM EDS. The ~0.9 µm wide IMP layer in Lamella 8 is shown in Figure 8, and the element maps in (c) reveal

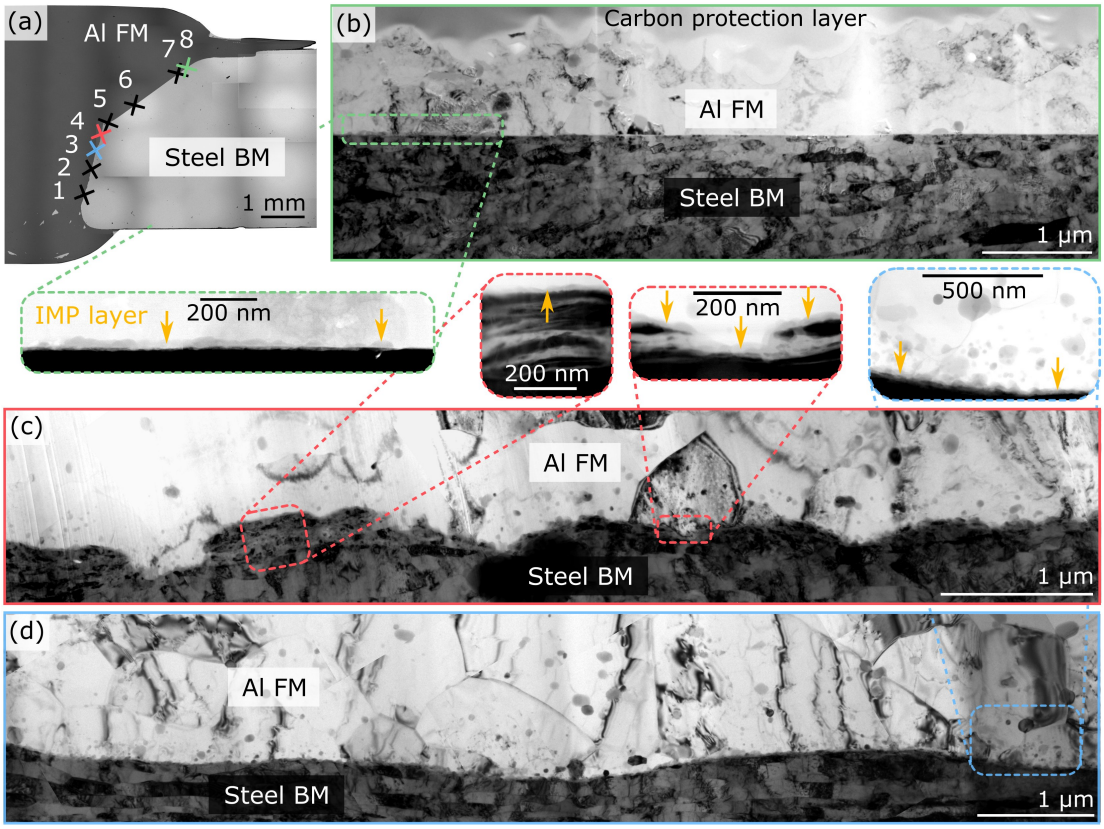

Figure 7: TEM characterisation of the Al-steel interface region. **(a)** BSE SEM image showing the locations from where TEM lamellae were lifted out by FIB. **(b)** BF-TEM image of Lamella 8 showing a straight interface. The inset shows a BF-STEM image of a ~0.9 µm wide IMP layer segment. **(c)** BF-TEM image of Lamella 4 showing a rough interface region. The left-hand inset shows a BF-STEM image of intermixed Al and steel, while the right-hand inset shows an IMP layer growing around deformed steel fragments. **(d)** BF-TEM image of Lamella 3 showing a slightly wavy interface. The BF-STEM image inset shows a relatively large number of small dispersoids close to a continuous IMP layer.

that the major constituents were Al, Fe and Si. In addition, the element maps show a discontinuous interfacial oxide layer, and it can be seen that the Al-Fe-Si layer grew into the Al side and was thicker near the gaps in the oxide layer. Also, some Mn-rich inclusions can be seen in steel, together with some N- and C-rich regions near the steel interface. Apart from the IMP layer segment shown in Figure 8, Lamella 8 showed no signs of any interfacial Al-Fe(-Si) layer, and an interfacial oxide layer covered the remaining part of the interface. This interfacial oxide layer was ~5 nm thick and contained mainly Al, O, Mg and minor amounts of Si, as shown in SI S5.

Lamella 3 that had a continuous IMP layer was also investigated by STEM EDS, as shown in Figure 9. It can be seen that dispersoids located close to the interface were primarily composed of Al-Mg-Si, Al-(Fe, Mn, Cr)-Si or Al-Si-Zr, whereas the IMP layer was composed of Al-Fe-Si-rich phases, as for Lamella 8. In addition, Al-O(-Mg)(-Si) oxide particles were seen near the IMP layer. The interfacial layers in the other lamella were also investigated by STEM EDS, as shown in SI S5.

All showed indications of an interfacial Al-Fe-Si layer and/or of an interfacial Al-O-Mg-Si layer.

The IMP layer composition was estimated using STEM EDS data from Lamellae 3, 4 and 8, by summing spectra inside masked regions corresponding to the IMP layers, and performing model fitting and quantification of the sum spectra, as shown in SI S5. The resulting average relative composition and standard deviation for the major constituents was 59 ± 6 at.% Al, 32 ± 6 at.% Fe and 9 ± 1 at.% Si. These values were subject to considerable errors due to overlap of the IMP layer with both steel and Al to different extent. In addition, absorption of low energy X-rays, i.e. Al-Kα and Si-Kα, caused the proportion of these elements to be systematically underestimated. Nevertheless, this rough estimation suggested that the IMP layer was composed primarily of Al-Fe(-Si) IMP(s) with $\gtrsim$9 at.% Si.

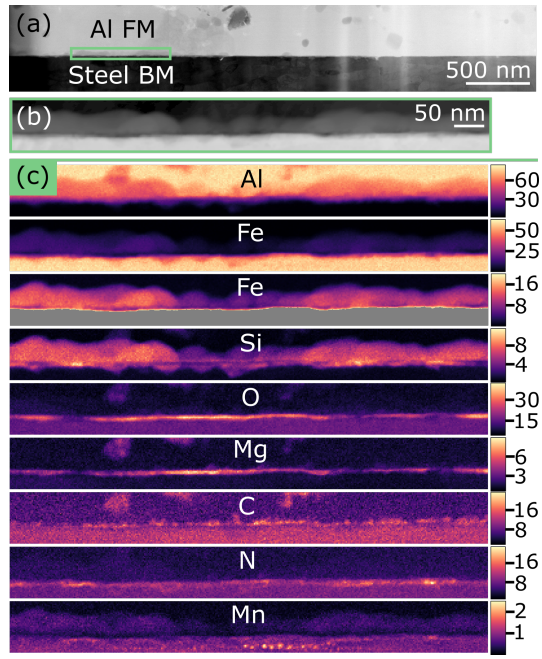

Figure 8: STEM of the restricted IMP layer in Lamella 8. **(a)** BF-STEM overview image. **(b)** HAADF-STEM image and **(c)** element maps (showing at.%) based on STEM EDS of the region highlighted in (a). Note that two Fe maps are shown, and that the bottom one displays only low amounts of Fe (0 – 20 at.%).

The distribution and morphology of IMP crystals, and the crystalline phases present in the IMP layer, were assessed using SED data from an interface region in Lamella 3. Figure 10(a) shows a virtual bright-field (VBF) grayscale image, with overlayed coloured VDF image segments showing the morphologies of some individual interfacial IMP crystals and some dispersoids embedded in Al. Figure 10(b) shows coloured diffraction spots corresponding to the coloured VDF segments in (a), and these are plotted on top of a grayscale pattern that shows the maximum intensity with respect to detector position based on all patterns from the region shown in (a). From Figures 10(a) and (b) it can be seen that the IMP layer was polycrystalline and consisted of crystals with elliptical shapes, some nearly semi-elliptical with the straight side touching steel. The interfacial IMP crystals within the area shown in Figure 10(a) had average dimensions of ~20 nm, including some crystals shorter than ~10 nm and some up to ~40 nm long.

To assess the crystal structure of the IMP crystals, diffraction patterns from individual crystals were extracted from the SED data and compared against expected diffraction from candidate Al-Fe(-Si) crystal structures reported in literature[30–33]. Diffraction patterns recorded near major zone axes would be most useful for such phase categorisation, but in this case the small size of the IMP crystals made orienting individual crystals to such orientations infeasible. SED data were therefore recorded in a tilt series to increase the probability of recording data from some crystals oriented close to zone axes. Inter-vector distances were measured between recorded Bragg

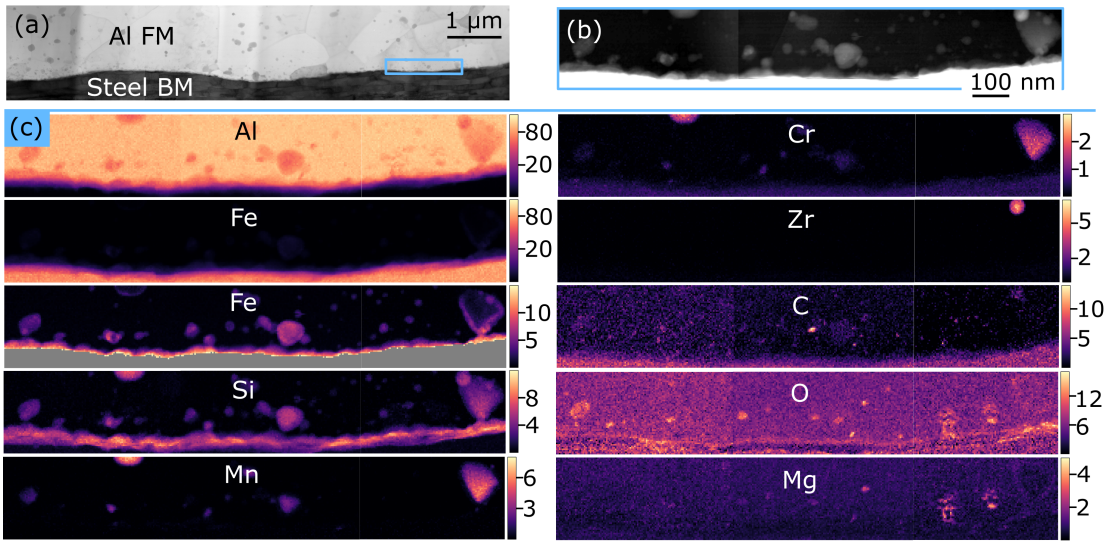

Figure 9: STEM of the interfacial IMP layer in Lamella 3. **(a)** BF-STEM overview image. **(b)** HAADF-STEM image and **(c)** element maps (showing at.%) based on STEM EDS of the region highlighted in (a). Note that two Fe maps are shown, and that the bottom one displays only low amounts of Fe (0 – 15 at.%). All displayed maps comprise results from three datasets acquired individually.

peaks and converted to average d-spacings, which were then compared to calculated values for all candidate Al-Fe(-Si) phases. Crystallographic information for all candidates is given in SI S6. In Figure 10(c), d-spacings are plotted for a subset of the candidate phases, including only Al-rich candidate Al-Fe(-Si) phases reported on Al-steel interfaces [34–36]; θ-Fe_4Al_{13} (also referred to as $FeAl_3$ or $Fe(Al,Si)_3$) [37], cubic α_c-Al-Fe-Si ($Al_{15}(Fe,Mn)_3Si_2$) [38], hexagonal α_h-$Al_{7.1}Fe_2Si$ (τ_5) [39], and β-$Al_{4.5}FeSi$ (τ_6) [40]. Plots that include all candidates and that cover larger ranges of d-spacings are shown in SI S7. The most commonly measured larger d-spacings were ~8.8 Å and ~6.2 Å, which fit several candidates, including in particular the α_c phase (d_{110} = 8.9 Å and d_{200} = 6.3 Å). Based on the measured d-spacings alone, it was not possible to determine the IMP(s) present.

Finally, selected patterns recorded near major crystallographic zone axes were indexed with respect to the candidate Al-Fe(-Si) phases. For each selected pattern, the two longest average d-spacings corresponding to non-parallel rows of spots, together with the angle between them, were considered, and all candidates were checked for possible zone axis giving spots matching these. Several individual patterns could be indexed with respect to the α_c phase, as shown in Figures 10(d)-(f), as could some diffraction patterns from dispersoids embedded in the Al FM. This suggested that the α_c phase was the most probable IMP candidate in the interfacial layer. However, some d-spacings (e.g. 10.8 Å and 7.8 Å), and several individual patterns could not be indexed with respect to this phase, which suggested that additional phase(s) were present. SI S7 shows the considered selected patterns.

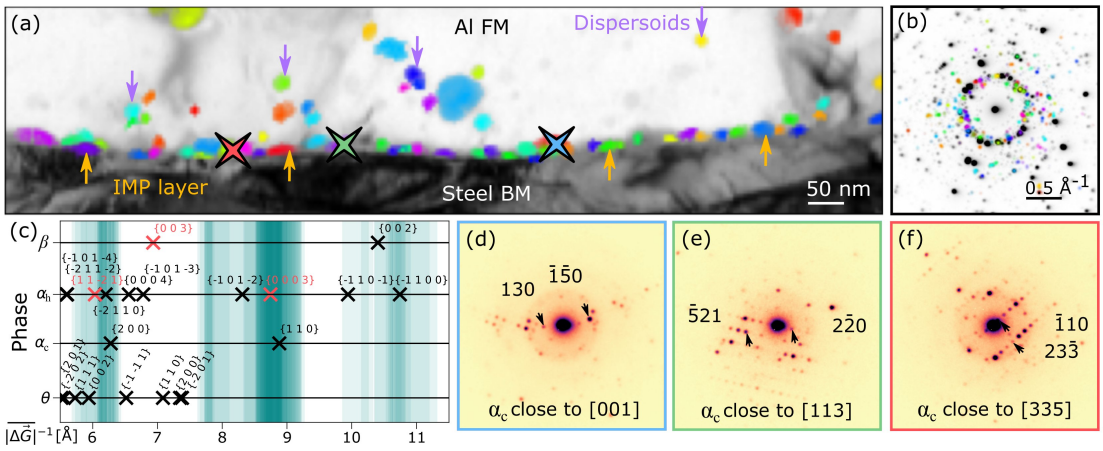

Figure 10: Scanning electron diffraction of an interface region in Lamella 3 (the same as Figure 9). **(a)** Virtual bright field image with overlayed coloured virtual dark field image segments from some individual crystals in the IMP layer and some dispersoids in the Al FM. **(b)** Coloured diffraction spots corresponding to the coloured segments in (a), superimposed on a greyscale pattern that shows the maximum intensity with respect to detector position based on all patterns from the region in (a). **(c)** Measured average d-spacings from selected patterns in the IMP layer plotted in partly transparent turquoise with a line width equal to one standard deviation. On the vertical axis, d-spacings of the phases θ, α_c, α_h and β are shown. Black crosses correspond to kinematically allowed spots, while red crosses correspond to spots possibly seen due to double diffraction. Patterns indexed with respect to the α_c phase from crystals oriented close to **(d)** [001], **(e)** [113] and **(f)** [335] zone axis, located at the positions marked in (a).

4. Discussion

4.1. Joint strength

The UTS of the second generation HYB Al-steel butt joint presented here (184 – 220 MPa) surpassed the UTS of the first generation (104 – 140 MPa [16]). The relatively large spread in these values may be explained by local fluctuations in the FM supply and placement of the pin during joining, which may lead to local variations in bonding conditions. The strength increase may be understood by considering the differences between the setups used for the first and second generation HYB joining, which are illustrated in Figures 11(a) and (b). There are two main differences. Firstly, the shape of the steel groove was different, with the first generation having a half V-form and the second a half Y-form. Secondly, the steel was placed on the RS in the first generation, while on the AS in the second. This change is consistent with the standard practice of placing the hardest material on the AS for FSW butt joints [5, 6]. The material on the AS experiences larger shear forces, which was expected to give better Al-steel bonding.

The Al BM and FM were both notably affected by the joining process. The horizontal hardness profile (Figure 2(a)) showed a typical HAZ with a continuous hardness decrease towards the weld centre. Such a HAZ was expected since the Al BM was artificially aged before joining to reach peak hardness condition that is characterised by a high number density of nanoscale hardening precipitates. Upon heating to $\gtrsim$200°C during joining, coarsening and dissolution of hardening precipitates, possibly accompanied by re-precipitation of non-hardening phases, were expected to leave the Al BM in an overaged state with lower hardness, in accordance with studies of FSW joints of aged 6xxx Al alloys [41–43]. The hardness decrease continued until a minimum was reached

near the EZ-HAZ boarder, which coincided with the strain development in the Al BM during tensile testing (Figure 3(c)). After this point, the horizontal hardness profile showed increasing values towards the weld centre (Figure 2(a)). Such an increase has also been seen in FSW joints, where it was coupled to increasing dissolution of non-hardening precipitates leaving increasing amounts of solutes in solid solution, which in turn gave increasing hardness during natural ageing after cooling [41, 44]. However, a hardness decrease was seen in the vertical profile (Figure 2(a)) moving from the weld crown, that was primarily composed of the harder FM, towards the root region, where mixing of the Al BM and FM occurred (Figure 5(a)). The FM was richer in dispersoid forming elements (Mn, Cr and Zr) and was before joining thermo-mechanically processed to promote work hardening and formation of fine dispersoids. During joining, both the FM and the Al BM in the EZ were subjected to extensive deformation and heating, resulting in a complex microstructure (Figure 5(b)). Small equiaxed grains were seen in the central region and onion-ring structures were seen at the top, both of which are common in FSW joining [18, 43]. However, larger grains reflecting the Al flow were seen towards the root region, which indicated higher heat inputs. Studies focused on the Al region are required for further insight into the precipitation phenomena and microstructural features responsible for the hardness variations in the Al region.

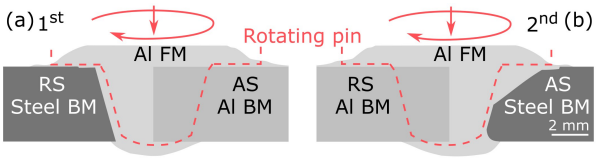

Figure 11: Illustration of the setup used for the production of **(a)** first and **(b)** second generation (this work) HYB Al-steel joints, where the steel BM is placed on the retreating side (RS) or the advancing side (AS), respectively. The outline of the rotating pin during joining is indicated with a red dashed line, and its movement is indicated with red arrows.

Despite the softening on the Al side, cracks in the root region lead to final fracture along the Al-steel interface for all specimens. Poor bonding in the root region was connected to the shape of the steel groove. The very bottom of the bevelled steel edge created a pit filled with FM underneath the steel plate. Considering the Al flow during joining (Figure 5), the forces acting in this region were modest, resulting in poor bonding and formation of root cracks. The forces were also modest for the top part of the steel plate, where the FM flowed outward over the steel plate without meeting any obstacle, giving lack of bonding. However, the fracture surfaces indicated that the Al-steel bonding in the bottom half of the joint was sufficiently strong, except for in the root region. The wavy pattern in the Al on the fracture surfaces (Figure 4), that resembled an impression of the extrusion dies in the pin, suggested that the weakest part in the bottom region was not the Al-steel interface, but rather the bonding between new and previously deposited Al as the pin traversed the weld groove. This indicated that sufficient Al-steel bonding was achieved in regions that experienced high pressure. For development of future generations of HYB Al-steel butt joints, modifying the pin and steel groove shape to increase the pressure in the root region, should be investigated.

The HYB joint performed comparably, in terms of UTS, to sound Al-steel butt joints made with the similar Al alloy 6061 as BM using other joining techniques. For instance, FSW joints have reached ca. 250 MPa [45] and ca. 240 MPa [35], while laser-assisted FSW joints have demonstrated UTS values of ca. 196 MPa [46] and laser welding-brazing joints have demonstrated ca. 208 MPa [47]. Investigations into the bonding mechanisms were crucial to explain the origin of

the considerable bond strength.

4.2. Bonding mechanisms

The Al-steel interface was investigated by SEM and (S)TEM in order to explain the bonding mechanisms induced by HYB. Signs of bonding were seen on both the micro- and nanoscale. On the microscale, SEM studies of the joint cross-section (Figure 6) showed that a significant portion of the interface was rough with small hook-like features. The larger surface area associated with a rough interface is typically beneficial for bond strength. Further, features where one material has flowed into protrusions on the opposing material surface, indicate mechanical interlocking. These micro-interlock features were similar to those observed in FSW Al-steel joints, which were suggested to enhance the bond strength [48]. On the nanoscale, (S)TEM studies uncovered layered intermixed Al-steel regions (Figure 7(c)). These regions were similar to swirl-like intercalated layers reported in FSW joints, that were attributed to the large plastic deformation induced by the stirring of the tool [49].

An interfacial Al-Fe-Si IMP layer (Figures 9 and 10) that was discontinuous and 10–50 nm thick was revealed by (S)TEM investigations. IMP layers may govern the tensile strength of Al-steel joints based primarily on the layer thickness [1–4]. A thicker layer may lead to fracture along the Al-steel interface and a decrease in tensile strength, due to the inherent brittleness of the IMPs and/or due to porosity formed during IMP growth [3]. For instance, one study found that the FSW joint strength decreased exponentially with increasing IMP layer thickness, e.g. the joint strength decreased from 327 MPa to 205 MPa when the IMP layer thickness increased from 0.11 μm to 0.34 μm [2]. In another study on FSW joints, fracture occurred in Al and the tensile strength was $\gtrsim$250 MPa when the IMP layer thickness was below ~0.5 μm, while fracture occurred in the IMP layer yielding a strength of $\lesssim$100 MPa when the IMP layer thickness exceeded ~2 μm [4]. In this context, the 10 − 50 nm thick layer observed here was considered thin. Similar nanoscale IMP layers have been reported in a few other studies. For instance, a 30 nm thick discontinuous IMP layer was found in a FSW joint after post-joining heat treatment at 400°C for 9 min [3], and a polycrystalline non-uniform 40 − 70 nm thick IMP layer with ~5 at.% Si was found in a friction stir dovetail joint [50], which highly resembled the IMP layer found here. Generally, thinner IMP layers form with decreasing heat input, since growth of IMP layers typically is diffusion controlled [51]. The joint temperature during HYB joining has been assumed to reach a maximum of ~400°C, and considering the resulting thermal profile, a nanoscale IMP layer can be expected for HYB joints [15]. Furthermore, the Al FM contained Si, which can be beneficial as it may lead to a reduction of the IMP layer growth rate [34, 36, 52–54]. Thus, it was believed that the low HYB process temperature and favourable Al FM composition, made it possible to avoid excessive IMP growth and to achieve substantial bond strength.

Analysis of SED data indicated that the polycrystalline IMP layer contained the cubic α_c phase (Figure 10). Based on literature, Al-rich IMPs were expected to form first on Al-Fe interfaces, specifically θ-Fe_4Al_{13} for low Si contents, and α_h-$Al_{7.1}Fe_2Si$ and β-$Al_{4.5}FeSi$ for higher Si contents [34, 55]. However, the cubic α_c phase generally forms at the expense of the hexagonal α_h phase in the presence of small amounts of certain transition elements, e.g. Mn and Cr [56–58], and these were contained in the FM used here. The roughly estimated Si content of $\gtrsim$9 at.% (Figure 9) was consistent with Si contents in the range of 6 − 11 at.% previously reported for α_c-Al-(Fe,Mn)-Si crystals [59]. The α_c phase has also been found on Al-steel interfaces in other studies [36, 60], and in an early study a cubic Fe_3SiAl_{12} phase highly similar to α_c was reported to form at $\gtrsim$350°C [53], which further supported the presence of α_c. Al-(Fe, Mn, Cr)-Si dispersoids in the Al FM were

also identified as α_c phases (SI S7). Some regions showed indications of a higher dispersoid number density near the Al-steel interface (Figure 9), which was also reported in another study [50]. Some dispersoids contained increasing amounts of Fe towards their edges (Figure 9), consistent with previous work explaining this based on Fe diffusing more slowly into the dispersoids during prolonged growth [61]. Here it was possible that Fe diffusion across the Al-steel interface during HYB promoted formation of small dispersoids in parallel to growth of already formed dispersoids. However, dispersoid statistics was outside the scope of this study, and future studies of large areas would have to be done to reach valid conclusions. In any case, α_c could not explain all the diffraction recorded from the IMP layer, which indicated that α_c likely co-existed with (an)other Al-Fe(-Si) phase(s) that could not be identified. Further investigations are necessary to fully understand the IMP formation and growth on Al-steel interfaces at nanoscale.

Regions with an interfacial Al-Fe-Si layer demonstrated bonding via interdiffusion. However, some regions showed a ~5 nm thick Al-O-Mg-Si layer (Figure 8 and SI S5). This layer resembled the Al_2O_3 layer, that may also contain Mg and Si, typically found on Al surfaces exposed to air [62–64]. In Al joining, it is generally believed that breaking up the native oxide layer and allowing fresh metal to meet, promotes metallurgical bond formation [65]. Here, Al was heavily deformed and the native surface layer presumably disintegrated and was dragged into the EZ during HYB, similar to in FSW where oxide layer remnants can be found as dispersed particles in the stir zone [66, 67]. The nanoscale Al-O-Mg-Si layer seen on the Al-steel interface supposedly formed as a result of air access during the Al FM extrusion in HYB. Nanoscale Al-O(-Mg)(-Si) oxide films have also been found on extruded Al profiles [68] and at Al-steel interfaces in FSW joints [69–71]. Further, it was seen that the Al-Fe-Si layer may grow thicker into Al where there are gaps in the oxide layer (Figure 8), consistent with the general belief that an oxide film may act as an interdiffusion barrier [72, 73]. Previous studies of Al-steel joints have reported both interfacial oxide layers that were coupled to interfacial fracture [70] or conversely, to high bond strength [69, 71, 73]. Here, interfacial Al-O-Mg-Si layers were also seen in regions where Al stuck to steel after tensile testing, which suggested that limited interface regions covered by interfacial oxides formed during joining not necessarily have detrimental effects on the overall bond strength. Further studies are needed to determine the role of nanoscale interfacial oxides in Al-steel joints made in the solid state.

By combining the findings from the microscopy investigations with those from the mechanical testing, regions with low and high relative bond strength could be identified, as illustrated in Figure 12. The lamellae that showed flat interface appearances with no or only a restricted IMP layer, were predominantly from the top half of the joint. The steel fracture surface (Figure 4) showed less residual Al in this region, which indicated limited bonding. On the other hand, a large amount of residual Al was found on the bottom half of the steel fracture surface, which hinted to stronger Al-steel bonding. Also, the bottom half showed a rougher interface with more interlocking signs, and the TEM lamellae that showed clear signs of a nanoscale IMP layer were also from the same region. Thus, in total the presented characterisation indicated that stronger Al-steel bonding was achieved for interface regions that displayed both a nanoscale IMP layer and more interlocking features. This is supported by another study, where the isolated and combined effects of a large mechanical interlock and a thin IMP layer were investigated, and where it was found that the highest bond strength was achieved when both of these were present simultaneously [50].

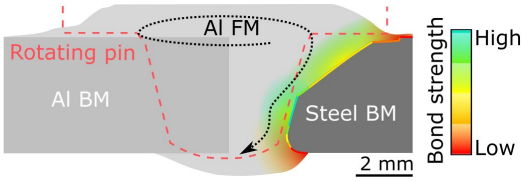

Figure 12: Simplified qualitative illustration of the bond strength in the investigated joint. The Al-steel interface is coloured according to low (red) to high (turquoise) relative bond strength. The position of the Al BM plate before joining is marked by a medium grey rectangle, the flow of FM during joining is illustrated by a black curved arrow, and the rotating pin during joining is indicated by a red line.

5. Summary and conclusions

A second generation Al-steel HYB butt joint was subjected to microstructural and mechanical characterisation, from which the main findings can be summarised as follows.

i Transverse hardness profiles showed a heat affected zone that extended 13.5 mm into Al, while steel was unaffected.

ii The ultimate tensile strength (UTS) was measured to be in the range of 184 – 220 MPa, corresponding to 60 – 72% joint efficiency.

iii Digital image correlation (DIC) analysis of the strain development during tensile testing showed that although strain developed in the soft zone in Al, cracks in the root region were severe. The final fracture propagated from root cracks and ran close to the Al-steel interface.

iv Scanning electron microscopy (SEM) of the fracture surfaces revealed significant portions of residual Al on the steel fracture surface, which indicated sufficient Al-steel bond strength, especially on the bottom half of the steel that experienced larger pressure during joining.

v SEM and transmission electron microscopy (TEM) investigations revealed signs of microscale mechanical interlocking, showed that the Al-steel interface was rough, especially on the bottom half of the steel, and showed some intermixed Al-steel regions.

vi TEM characterisation showed an interfacial discontinuous 10 – 50 nm thick intermetallic phase (IMP) layer. Quantification by X-ray energy dispersive spectroscopy (EDS) indicated that the layer was mainly composed of Al, Fe and Si with a relative Si content roughly estimated to $\gtrsim$9 at.%. Some regions showed ~5 nm thick interfacial oxide layers mainly composed of Al, O and Mg with minor amounts of Si.

vii Analysis of scanning electron diffraction (SED) data acquired in a tilt series indicated that the IMP layer was polycrystalline with nanocrystals of the cubic α_c phase. The α_c phase could not explain all the diffraction patterns from the Al-Fe-Si layer, and further investigations are needed to fully understand the Al-Fe(-Si) phase formation at the nanoscale in Al-steel joints.

In short, the Al-steel HYB butt joint showed considerable bond strength that was attributed to a combination of microscale mechanical interlocking and a nanoscale interfacial Al-Fe-Si layer.

Acknowledgements

Matteo Manfrotto is acknowledged for performing tensile testing. Marie Mathiasson is acknowledged for performing optical microscopy of the joint cross-section. Dr. Christopher S. Allen is acknowledged for performing alignments and for technical assistance in relation to the scanning electron diffraction experiments. The authors acknowledge financial support from

the Research Council of Norway to SFI Manufacturing [237900], NORTEM [197405] and NorFab [245963/F50], from the NTNU Aluminium Product Innovation Center (NAPIC) and from HyBond AS. PAM acknowledges the Engineering Physical Sciences Research Council (EPSRC), UK, [EP/R008779/1]. The authors thank Diamond Light Source for access and support in the use of the electron Physical Science Imaging Centre (ePSIC) [EM20527].

Supplementary information

SI has been made available with this publication.

Data availability

The raw SED data have been made available [74].

References

[1] R. Borrisutthekul, T. Yachi, Y. Miyashita, and Y. Mutoh, "Suppression of intermetallic reaction layer formation by controlling heat flow in dissimilar joining of steel and aluminum alloy," *Materials Science and Engineering A*, vol. 467, no. 1-2, pp. 108–113, 2007. DOI: 10.1016/j.msea.2007.03.049.

[2] T. Tanaka, T. Morishige, and T. Hirata, "Comprehensive analysis of joint strength for dissimilar friction stir welds of mild steel to aluminum alloys," *Scripta Materialia*, vol. 61, no. 7, pp. 756–759, 2009. DOI: 10.1016/j.scriptamat.2009.06.022.

[3] H. Springer, A. Kostka, J. F. dos Santos, and D. Raabe, "Influence of intermetallic phases and Kirkendall-porosity on the mechanical properties of joints between steel and aluminium alloys," *Materials Science and Engineering A*, vol. 528, no. 13-14, pp. 4630–4642, 2011. DOI: 10.1016/j.msea.2011.02.057.

[4] R. Hatano, T. Ogura, T. Matsuda, T. Sano, and A. Hirose, "Relationship between intermetallic compound layer thickness with deviation and interfacial strength for dissimilar joints of aluminum alloy and stainless steel," *Materials Science & Engineering A*, vol. 735, pp. 361–366, 2018. DOI: 10.1016/j.msea.2018.08.065.

[5] W. Cai, G. Daehn, A. Vivek, J. Li, H. Khan, R. S. Mishra, and M. Komarasamy, "A state-of-the-art review on solid-state metal joining," *Journal of Manufacturing Science and Engineering, Transactions of the ASME*, vol. 141, no. 3, pp. 1–35, 2019. DOI: 10.1115/1.4041182.

[6] K. Kimapong and T. Watanabe, "Friction stir welding of aluminum alloy to steel," *Welding Journal (Miami, Fla)*, vol. 83, no. 10, pp. 277–282, 2004, ISSN: 00432296.

[7] H. Laukant, C. Wallmann, M. Müller, M. Korte, B. Stirn, H. G. Haldenwanger, and U. Glatzel, "Fluxless laser beam joining of aluminium with zinc coated steel," *Science and Technology of Welding and Joining*, vol. 10, no. 2, pp. 219–226, 2005. DOI: 10.1179/174329305X37051.

[8] M Merklein and A Giera, "Laser assisted Friction Stir Welding of drawable steel-aluminium tailored hybrids," *International Journal of Material Forming*, vol. 1, pp. 1299–1302, 2008. DOI: 10.1007/s12289-008-0141-x.

[9] Ø. Grong, "Recent Advances in Solid-State Joining of Aluminum," *Welding Journal*, vol. 91, no. 1, pp. 26–33, 2012.

[10] U. R. Aakenes, "Industrialising of the Hybrid Metal Extru usion & Bonding (HYB) method – from prototype towards commercial process," Ph.D. dissertation, Norwegian University of Science and Technology, 2013, ISBN: 9788247148198.

[11] U. R. Aakenes, Ø. Grong, and T. Austigard, "Application of the Hybrid Metal Extrusion & Bonding (HYB) method for joining of AA6082-T6 base material," *Materials Science Forum*, vol. 794-796, pp. 339–344, 2014. DOI: 10.4028/www.scientific.net/MSF.794-796.339.

[12] J. Blindheim, T. Welo, and M. Steinert, "First demonstration of a new additive manufacturing process based on metal extrusion and solid-state bonding," *International Journal of Advanced Manufacturing Technology*, vol. 105, no. 5-6, pp. 2523–2530, 2019. DOI: 10.1007/s00170-019-04385-8.

[13] J. Blindheim, Ø. Grong, T. Welo, and M. Steinert, "On the mechanical integrity of AA6082 3D structures deposited by hybrid metal extrusion & bonding additive manufacturing," *Journal of Materials Processing Technology*, vol. 282, 2020. DOI: 10.1016/j.jmatprotec.2020.116684.

[14] Ø. Grong, L. Sandnes, and F. Berto, "A status report on the hybrid metal extrusion & bonding (HYB) process and its applications," *Material Design & Processing Communications*, vol. 1, no. 2, e41, 2019. DOI: 10.1002/mdp2.41.

[15] Ø. Grong, L. Sandnes, T. Bergh, P. E. Vullum, R. Holmestad, and F. Berto, "An analytical framework for modelling intermetallic compound (IMC) formation and optimising bond strength in aluminium-steel welds," *Material Design & Processing Communications*, no. February, e57, 2019. DOI: 10.1002/mdp2.57.

[16] F. Berto, L. Sandnes, F. Abbatinali, O. Grong, and P. Ferro, "Using the Hybrid Metal Extrusion & Bonding (HYB) Process for Dissimilar Joining of AA6082-T6 and S355," *Procedia Structural Integrity*, vol. 13, pp. 249–254, 2018. DOI: 10.1016/j.prostr.2018.12.042.

[17] Ø. Grong, "Method and devices for joining of metal components, particularly light metal components," US patent: US 7131567 B2, 2006.

[18] P. L. Threadgilll, A. J. Leonard, H. R. Shercliff, and P. J. Withers, "Friction stir welding of aluminium alloys," *International Materials Reviews*, vol. 54, no. 2, pp. 49–93, 2009. DOI: 10.1179/174328009X411136.

[19] Ø. Grong, L. Sandnes, and F. Berto, "Progress in solid state joining of metals and alloys," *Procedia Structural Integrity*, vol. 17, pp. 788–798, 2019. DOI: 10.1016/j.prostr.2019.08.105.

[20] F. Leoni, Ø. Grong, L. Sandnes, T. Welo, and F. Berto, "Finite element modelling of the filler wire feeding in the hybrid metal extrusion & bonding (HYB) process," *Journal of Advanced Joining Processes*, vol. 1, no. November 2019, p. 100 006, 2020. DOI: 10.1016/j.jajp.2020.100006.

[21] ASTM International, "ASTM E8/E8M - 16a Standard test methods for tension testing of metallic materials," 2016. DOI: 10.1520/E0008_E0008M-16A.

[22] E. Fagerholt, E. Østby, T. Børvik, and O. S. Hopperstad, "Investigation of fracture in small-scale SENT tests of a welded X80 pipeline steel using Digital Image Correlation with node splitting," *Engineering Fracture Mechanics*, vol. 96, pp. 276–293, 2012. DOI: 10.1016/j.engfracmech.2012.08.007.

[23] E. Fagerholt, T. Borvik, and O. S. Hopperstad, "Measuring discontinuous displacement fields in cracked specimens using digital image correlation with mesh adaptation and crack-path optimization," *Optics and Lasers in Engineering*, vol. 51, no. 3, pp. 299–310, 2013. DOI: 10.1016/j.optlaseng.2012.09.010.

[24] L. J. Barker, "Revealing the grain structure of common aluminium alloy metallographic specimens," *Transactions of the A.S.M.*, vol. 42, pp. 347–356, 1950.

[25] F. de la Peña, E. Prestat, V. T. Fauske, P. Burdet, P. Jokubauskas, M. Nord, T. Ostasevicius, K. E. MacArthur, M. Sarahan, D. N. Johnstone, J. Taillon, J. Lähnemann, V. Migunov, A. Eljarrat, J. Caron, T. Aarholt, S. Mazzucco, M. Walls, T. Slater, F. Winkler, Pquinn-dls, B. Martineau, G. Donval, R. McLeod, E. R. Hoglund, I. Alxneit, D. Lundeby, T. Henninen, L. F. Zagonel, and A. Garmannslund, "hyperspy/hyperspy: HyperSpy v1.5.2," 2019. DOI: 10.5281/ZENODO.3396791.

[26] D. N. Johnstone, P. Crout, J. Laulainen, S. Høgås, B. Martineau, T. Bergh, S. Smeets, S. Collins, J. Morzy, H. W. Ånes, E. Prestat, T. Doherty, T. Ostasevicius, D. Mohsen, E. Opheim, R. Tovey, and E. Jacobsen, "Pyxem/pyxem: Pyxem 0.10.1," 2020. DOI: 10.5281/ZENODO.3667613.

[27] T. Bergh, D. N. Johnstone, P. Crout, S. Høgås, P. A. Midgley, R. Holmestad, P. E. Vullum, and A. T. van Helvoort, "Nanocrystal segmentation in scanning precession electron diffraction data," *Journal of Microscopy*, vol. 279, no. 3, pp. 158–167, 2020. DOI: 10.1111/jmi.12850.

[28] B. H. Martineau, D. N. Johnstone, A. T. J. van Helvoort, P. A. Midgley, and A. S. Eggeman, "Unsupervised machine learning applied to scanning precession electron diffraction data," *Advanced Structural and Chemical Imaging*, vol. 5, no. 1, 2019. DOI: 10.1186/s40679-019-0063-3.

[29] L. Sandnes, Ø. Grong, J. Torgersen, T. Welo, and F. Berto, "Exploring the hybrid metal extrusion and bonding process for butt welding of Al–Mg–Si alloys," *International Journal of Advanced Manufacturing Technology*, vol. 98, no. 5-8, pp. 1059–1065, 2018. DOI: 10.1007/s00170-018-2234-0.

[30] C. M. Allen, K. A. O'Reilly, B. Cantor, and P. V. Evans, "Intermetallic phase selection in 1XXX A1 alloys," *Progress in Materials Science*, vol. 43, no. 2, pp. 89–170, 1998. DOI: 10.1016/S0079-6425(98)00003-6.

[31] N. Krendelsberger, F. Weitzer, and J. C. Schuster, "On the Reaction Scheme and Liquidus Surface in the Ternary System Al-Fe-Si," *Metallurgical and Materials Transactions A*, vol. 38, no. August, 2007. DOI: 10.1007/s11661-007-9182-x.

[32] G. Ghosh, "Aluminim-Iron-Silicon (Iron Systems, Part 1)," *SpringerMaterials Landolt-Börnstein - Group IV Physical Chemistry 11D1*, pp. 1–83, 2008. DOI: 10.1007/978-3-540-69761-9_11.

[33] M. C. J. Marker, B. Skolyszewska-Kühberger, H. S. Effenberger, C. Schmetterer, and K. W. Richter, "Intermetallics Phase equilibria and structural investigations in the system Al-Fe-Si," *Intermetallics*, vol. 19, no. 12, pp. 1919–1929, 2011. DOI: 10.1016/j.intermet.2011.05.003.

[34] H. Springer, A. Kostka, E. J. Payton, D. Raabe, A. Kaysser-Pyzalla, and G. Eggeler, "On the formation and growth of intermetallic phases during interdiffusion between low-carbon steel and aluminum alloys," *Acta Materialia*, vol. 59, no. 4, pp. 1586–1600, 2011. DOI: 10.1016/j.actamat.2010.11.023.

[35] T. Chen, "Process parameters study on FSW joint of dissimilar metals for aluminum-steel," *Journal of Materials Science*, vol. 44, no. 10, pp. 2573–2580, 2009. DOI: 10.1007/s10853-009-3336-8.

[36] L. A. Jacome, S. Weber, A. Leitner, E. Arenholz, J. Bruckner, H. Hackl, and A. R. Pyzalla, "Influence of Filler Composition on the Microstructure and Mechanical Properties of Steel - Aluminum Joints Produced by Metal Arc Joining," *Advanced Engineering Materials*, vol. 11, no. 5, pp. 350–358, 2009. DOI: 10.1002/adem.200800319.

[37] J. Grin, U. Burkhardt, M. Ellner, and K. Peters, "Refinement of the Fe4Al13 structure and its relationship to the quasihomological homeotypical structures," *Zeitschrift fur Kristallographie*, vol. 209, no. 6, pp. 479–487, 1994. DOI: 10.1524/zkri.1994.209.6.479.

[38] M. Cooper, "The crystal structure of the ternary alloy α (AlFeSi)," *Acta Crystallographica*, vol. 23, pp. 1106–1107, 1967. DOI: 10.1107/S0365110X67004372.

[39] R. N. Corby and P. J. Black, "The Structure of α-(AlFeSi) by Anomalous-Dispersion Methods," *Acta Crystallographica*, vol. B33, pp. 3468–3475, 1977. DOI: 10.1107/S0567740877011224.

[40] V. Hansen, B. Hauback, M. Sundberg, C. Rømming, and J. Gjønnes, "β-Al4.5FeSi: A Combined Synchrotron Powder Diffraction, Electron Diffraction, High-Resolution Electron Microscopy and Single-Crystal X-ray Diffraction Study of a Faulted Structure," *Acta Crystallographica Section B Structural Science*, vol. 54, no. 4, pp. 351–357, 1998. DOI: 10.1107/S0108768197017047.

[41] O. R. Myhr and Ø. Grong, "Process modelling applied to 6082-T6 aluminium weldments II. Applications of model," *Acta Metallurgica Et Materialia*, vol. 39, no. 1, pp. 2703–2708, 1991.

[42] Y. S. Sato, H. Kokawa, M. Enomoto, and S. Jogan, "Microstructural evolution of 6063 aluminum during friction-stir welding," *Metallurgical and Materials Transactions A*, vol. 30, no. 9, pp. 2429–2437, 1999. DOI: 10.1007/s11661-999-0251-1.

[43] L.-E. Svensson, L. Karlsson, H. Larsson, B. Karlsson, M. Fazzini, and J. Karlsson, "Microstructure and Mechanical Properties of Friction Stir Welded 5083 and 7075 Aluminum Alloys," *Science and Technology of Welding and Joining*, vol. 5, pp. 285–296, 2000. DOI: 10.1007/s11665-017-2543-8.

[44] Ø. Frigaard, Ø. Grong, and O. T. Midling, "A process model for friction stir welding of age hardening aluminum alloys," *Metallurgical and Materials Transactions A*, vol. 32, no. 5, pp. 1189–1200, 2001. DOI: 10.1007/s11661-001-0128-4.

[45] E. Taban, J. E. Gould, and J. C. Lippold, "Dissimilar friction welding of 6061-T6 aluminum and AISI 1018 steel: Properties and microstructural characterization," *Materials and Design*, vol. 31, no. 5, pp. 2305–2311, 2010. DOI: 10.1016/j.matdes.2009.12.010.

[46] X. Fei, X. Jin, Y. Ye, T. Xiu, and H. Yang, "Effect of pre-hole offset on the property of the joint during laser-assisted friction stir welding of dissimilar metals steel and aluminum alloys," *Materials Science and Engineering A*, vol. 653, pp. 43–52, 2016. DOI: 10.1016/j.msea.2015.11.101.

[47] H. Xia, X. Zhao, C. Tan, B. Chen, X. Song, and L. Li, "Effect of Si content on the interfacial reactions in laser welded-brazed Al/steel dissimilar butted joint," *Journal of Materials Processing Technology*, vol. 258, pp. 9–21, 2018. DOI: 10.1016/j.jmatprotec.2018.03.010.

[48] S. Lan, X. Liu, and J. Ni, "Microstructural evolution during friction stir welding of dissimilar aluminum alloy to advanced high-strength steel," *International Journal of Advanced Manufacturing Technology*, vol. 82, no. 9-12, pp. 2183–2193, 2016. DOI: 10.1007/s00170-015-7531-2.

[49] W.-B. Lee, M. Schmuecker, A. Mercardo, G. Biallas, and S.-B. Jung, "Interfacial reaction in steel-aluminum joints made by friction stir welding," *Scripta Materialia*, vol. 55, pp. 355–358, 2006. DOI: 10.1016/j.scriptamat.2006.04.028.

[50] M. Reza-E-Rabby, K. Ross, N. R. Overman, M. J. Olszta, M. McDonnell, and S. A. Whalen, "Joining thick section aluminum to steel with suppressed FeAl intermetallic formation via friction stir dovetailing," *Scripta Materialia*, vol. 148, pp. 63–67, 2018. DOI: 10.1016/j.scriptamat.2018.01.026.

[51] S. Kobayashi and T. Yakou, "Control of intermetallic compound layers at interface between steel and aluminum by diffusion-treatment," *Materials Science and Engineering A*, vol. 338, no. 1-2, pp. 44–53, 2002. DOI: 10.1016/S0921-5093(02)00053-9.

[52] D. I. Layner and A. K. Kurakin, "Mechanism of the influence of silicon in aluminium on the reaction diffusion of iron," *Fiz. metal. metalloved.*, vol. 18, no. 1, pp. 145–148, 1964.

[53] A. K. Kurakin, "Mechanism of the influence of silicon on the process of the reaction diffusion of iron in aluminium," *Fiz. metal. metalloved.*, vol. 30, no. 1, pp. 105–110, 1970.

[54] J. L. Song, S. B. Lin, C. L. Yang, and C. L. Fan, "Effects of Si additions on intermetallic compound layer of aluminum-steel TIG welding-brazing joint," *Journal of Alloys and Compounds*, vol. 488, no. 1, pp. 217–222, 2009. DOI: 10.1016/j.jallcom.2009.08.084.

[55] W.-J. Cheng and C.-J. Wang, "Observation of high-temperature phase transformation in the Si-modified aluminide coating on mild steel using EBSD," *Materials Characterization*, vol. 61, no. 4, pp. 467–473, 2010. DOI: 10.1016/j.matchar.2010.02.001.

[56] D Munson, "A clarification of the phases occurring in aluminium-rich aluminium-iron-silicon alloys, with particular referanse to the ternary α-AlFeSi," *Journal of the institute of metals*, vol. 95, pp. 217–219, 1967.

[57] C. Y. Sun and L. F. Mondolfo, "A clarification of the phases occurring in aluminium-rich aluminium-iron-silicon alloys," *Journal of the institute of metals*, vol. 95, p. 384, 1967.

[58] H. Becker, T. Bergh, P. E. Vullum, A. Leineweber, and Y. Li, "Effect of Mn and cooling rates on α-, β- and δ-Al–Fe–Si intermetallic phase formation in a secondary Al–Si alloy," *Materialia*, vol. 5, 2019. DOI: 10.1016/j.mtla.2018.100198.

[59] A. L. Dons, "Superstructures in α-Al(Mn,Fe,Cr)Si," *Zeitschrift für Metallkunde*, vol. 76, no. 2, pp. 151–153, 1985.

[60] S. M. Arbo, T. Bergh, H. Solhaug, I. Westermann, and B. Holmedal, "Influence of thermomechanical processing sequence on properties of AA6082-IF steel cold roll bonded composite sheet," *Procedia Manufacturing*, vol. 15, pp. 152–160, 2018. DOI: 10.1016/j.promfg.2018.07.189.

[61] A. M. F. Muggerud, Y. Li, and R. Holmestad, "Composition and orientation relationships of constituent particles in 3xxx aluminum alloys," *Philosophical Magazine*, vol. 94, no. 6, pp. 556–568, 2014. DOI: 10.1080/14786435.2013.857796.

[62] B. Goldstein and J. Dresner, "Growth of MgO films with high secondary electron emission on Al-Mg alloys," *Surface Science*, vol. 71, no. 1, pp. 15–26, 1978. DOI: 10.1016/0039-6028(78)90310-2.

[63] G. R. Wakefield and R. M. Sharp, "The composition of oxides formed on Al-Mg alloys," *Applied Surface Science*, vol. 51, no. 1-2, pp. 95–102, 1991. DOI: 10.1016/0169-4332(91)90065-R.

[64] C. R. Werrett, D. R. Pyke, and A. K. Bhattacharya, "XPS studies of oxide growth and segregation in aluminium-silicon alloys," *Surface and Interface Analysis*, vol. 25, no. 10, pp. 809–816, 1997. DOI: 10.1002/(SICI)1096-9918(199709)25:10<809::AID-SIA304>3.0.CO;2-M.

[65] D. R. Cooper and J. M. Allwood, "The influence of deformation conditions in solid-state aluminium welding processes on the resulting weld strength," *Journal of Materials Processing Technology*, vol. 214, no. 11, pp. 2576–2592, 2014. DOI: 10.1016/j.jmatprotec.2014.04.018.

[66] H. Okamura, K. Aota, M. Sakamoto, M. Ezumi, and K. Ikeuchi, "Behaviour of oxides during friction stir welding of aluminium alloy and their effect on its mechanical properties," *Welding International*, vol. 16, no. 4, pp. 266–275, 2002. DOI: 10.1080/09507110209549530.

[67] Y. S. Sato, F. Yamashita, Y. Sugiura, S. H. C. Park, and H. Kokawa, "FIB-assisted TEM study of an oxide array in the root of a friction stir welded aluminium alloy," *Scripta Materialia*, vol. 50, no. 3, pp. 365–369, 2004. DOI: 10.1016/j.scriptamat.2003.10.008.

[68] S. Kumari, S. Wenner, J. C. Walmsley, O. Lunder, and K. Nisancioglu, "Progress in Understanding Initiation of Intergranular Corrosion on AA6005 Aluminum Alloy with Low Copper Content," *Journal of The Electrochemical Society*, vol. 166, no. 11, pp. C3114–C3123, 2019. DOI: 10.1149/2.0211911jes.

[69] K. Tanaka, M. Kumagai, and H. Yoshida, "Dissimilar joining of aluminum alloy and steel sheets by friction stir spot welding," *Journal of Japan Institute of Light Metals*, vol. 56, no. 6, pp. 317–322, 2006.

[70] T. Ogura, Y. Saito, T. Nishida, H. Nishida, and T. Yoshida, "Partitioning evaluation of mechanical properties and the interfacial microstructure in a friction stir welded aluminum alloy / stainless steel lap joint," *Scripta Materialia*, vol. 66, no. 8, pp. 531–534, 2012. DOI: 10.1016/j.scriptamat.2011.12.035.

[71] T Ogura, T Nishida, Y Tanaka, H Nishida, S Yoshikawa, M Fujimoto, and A Hirose, "Microscale evaluation of mechanical properties of friction stir welded A6061 aluminium alloy / 304 stainless steel dissimilar lap joint," *Science and Technology of Welding and Joining*, vol. 18, no. 2, pp. 108–113, 2013. DOI: 10.1179/1362171812Y.0000000098.

[72] V. I. Zheladnov, M. S. Makunin, and P. M. Arzhanyi, "Effect of oxygen in iron on the inhibition of diffusion in Al Fe bimetals," *Metal Science and Heat Treatment*, vol. 18, no. 11, pp. 978–981, 1976.

[73] G. M. Bedford and J. Boustead, "The influence of oxygen and nitrogen on the growth of intermediate phases during the bonding of iron to aluminium," *Journal of Materials Science*, vol. 13, no. 2, pp. 253–260, 1978. DOI: 10.1007/BF00647768.

[74] T. Bergh, D. N. Johnstone, and C. S. Allen, "Scanning electron diffraction tilt series data of an aluminium-steel interface region [dataset]," *Zenodo*, 2020. DOI: 10.5281/zenodo.3938899.

Supplementary information

Microstructural and mechanical characterisation of a second generation hybrid metal extrusion & bonding aluminium-steel butt joint

Tina Bergh[a,*], Lise Sandnes[b], Duncan Neil Johnstone[c], Øystein Grong[b], Filippo Berto[b], Randi Holmestad[a], Paul Anthony Midgley[c], Per Erik Vullum[a]

[a] *Department of Physics, Norwegian University of Science and Technology (NTNU), Høgskoleringen 5, 7491 Trondheim, Norway*
[b] *Department of Mechanical and Industrial Engineering, NTNU, Richard Birkelands vei 2b, 7491 Trondheim, Norway*
[c] *Department of Materials Science and Metallurgy, University of Cambridge, 27 Charles Babbage Road, Cambridge, CB3 0FS, UK*

Abstract

Hybrid metal extrusion & bonding (HYB) is a joining method that enables solid-state bonding by combining addition of aluminium filler material through continuous extrusion with pressure exerted by a rotating steel tool. This work presents mechanical and microstructural characterisation of a second generation HYB butt joint of aluminium alloy 6082 and structural steel S355. The ultimate tensile strength was measured to be in the range of 184 – 220 MPa, which corresponds to 60 – 72% joint efficiency. Digital image correlation analysis of the strain development during tensile testing revealed that root cracks formed, before the final fracture ran close to the aluminium-steel interface. A significant amount of residual aluminium was found on the steel fracture surface, especially in regions that experienced higher pressure during joining. Scanning and transmission electron microscopy revealed that the bond strength could be attributed to a combination of microscale mechanical interlocking and a discontinuous nanoscale interfacial Al-Fe-Si intermetallic phase layer. Analysis of scanning electron diffraction data acquired in a tilt series, indicated that the polycrystalline intermetallic phase layer contained the cubic α_c phase. The results give insight into the bonding mechanisms of aluminium-steel joints and into the performance of HYB joints, which may be used to better understand and further develop aluminium-steel joining processes.

Keywords: aluminium-steel joining, hybrid metal extrusion & bonding, Al-Fe-Si intermetallic phases, transmission electron microscopy, scanning electron diffraction

*Corresponding author
Email address: tina.bergh@ntnu.no (Tina Bergh)

S1. X-ray energy dispersive spectroscopy data analysis

The X-ray energy dispersive spectroscopy (EDS) data analysis was performed using the python library hyperspy[1]. Each dataset was analysed using the same workflow. The dataset was first binned in the spatial axes, if needed, to achieve at least ~2k total counts per individual spectrum. Further, a model was created that comprised a polynomial of order six to model the continuous X-ray background, and one Gaussian per X-ray line. The sum spectrum was inspected to determine the X-ray lines present. Most often, lines from Al, C, Cr, Cu, Fe, Ga, Mg, Mn, O and Si, could be seen, and in some scans lines from Zr, N, Cl and/or Mo could also be seen. The dataset was model fitted with the amplitude of each Gaussian as a free parameter, and the X-ray line intensities were extracted from the model fitted Gaussians. The intensities of the Kα-lines were used for relative quantification by the Cliff-Lorimer method. The k-factors used were calculated k-factors extracted from the JEOL EDS software Analysis Station version 3.8.0.34. The quantification results were used to create element maps showing the relative composition in at.%. Note that the lamellae were thinned by focused ion beam (FIB), which resulted in a notable Ga content in Al, especially near grain boundaries. Further, most lamellae were fastened on Cu grids (Lamellae 1, 3, 5, 7 and 8), which resulted in notable Cu stray radiation, while two lamellae were fastened on Si-based grids (Lamellae 2 and 6), and one on a Mo grid (Lamella 4).

For selected datasets acquired from interface regions including intermetallic phase (IMP) layers, masks were created that comprised the IMP layers. Each mask was created by thresholding the Si map, typically to >5 at.%, optionally followed by hole filling and removal of small disconnected segments. The raw spectra inside the mask were summed, and the sum spectrum was model fitted and quantified, using the same approach as explained previously. Overlap of the IMP layer with both Al and steel to different extent, the use of un-calibrated k-factors and the lack of absorption correction, made it impossible to obtain an accurate composition by the method used. The performed quantification was therefore only intended to give a rough estimate for the IMP layer composition.

Figure S1 illustrates the data analysis workflow for one selected dataset. Figure 9 shows element maps from Lamella 3, and the displayed maps comprise 3 datasets that were acquired individually, which was necessary to ensure that each mapped region was in focus due to slight specimen bending. Figure S1 displays the dataset acquired from the region located in the middle of the maps shown in Figure 9. Figure S1(a) shows the sum spectrum, and (b) shows a high angle annular dark field scanning TEM (HAADF-STEM) image of the mapped region. Figure S1(c) shows three individual spectra; 1 from Al, 2 from the IMP layer and 3 from steel. The spectra were binned 2×2 in the spatial axes, so that each spectrum was the sum of four raw spectra. A model was created comprising a polynomial background component and Gaussians for each of the X-ray lines from the elements Al, C, Cr, Cu, Ga, Mg, Mn, O, Si and Zr. The model fitting results are shown in Figure S1(c) for the three selected spectra. The intensities of the Kα-lines obtained by the model fitting were used for Cliff-Lorimer quantification, in order to create element maps. Maps for Al, Fe and Si are shown in Figure S1(d), and the other maps can be seen in Figure S11. A mask for the IMP layer is shown in Figure S1(e), and Figure S1(f) shows the sum spectrum and the model fitting result. Quantification yielded for this region a relative composition of: Al: 49, O: 6, Cu: 5, Si: 6, Ga: 1, C: 1, Fe: 31, Mg: <1, Mn: <1, Cr<0.1 and Zr: <0.1 at.%. Considering the major elements only, the relative composition was 57 at.% Al, 36 at.% Fe and 7 at.% Si.

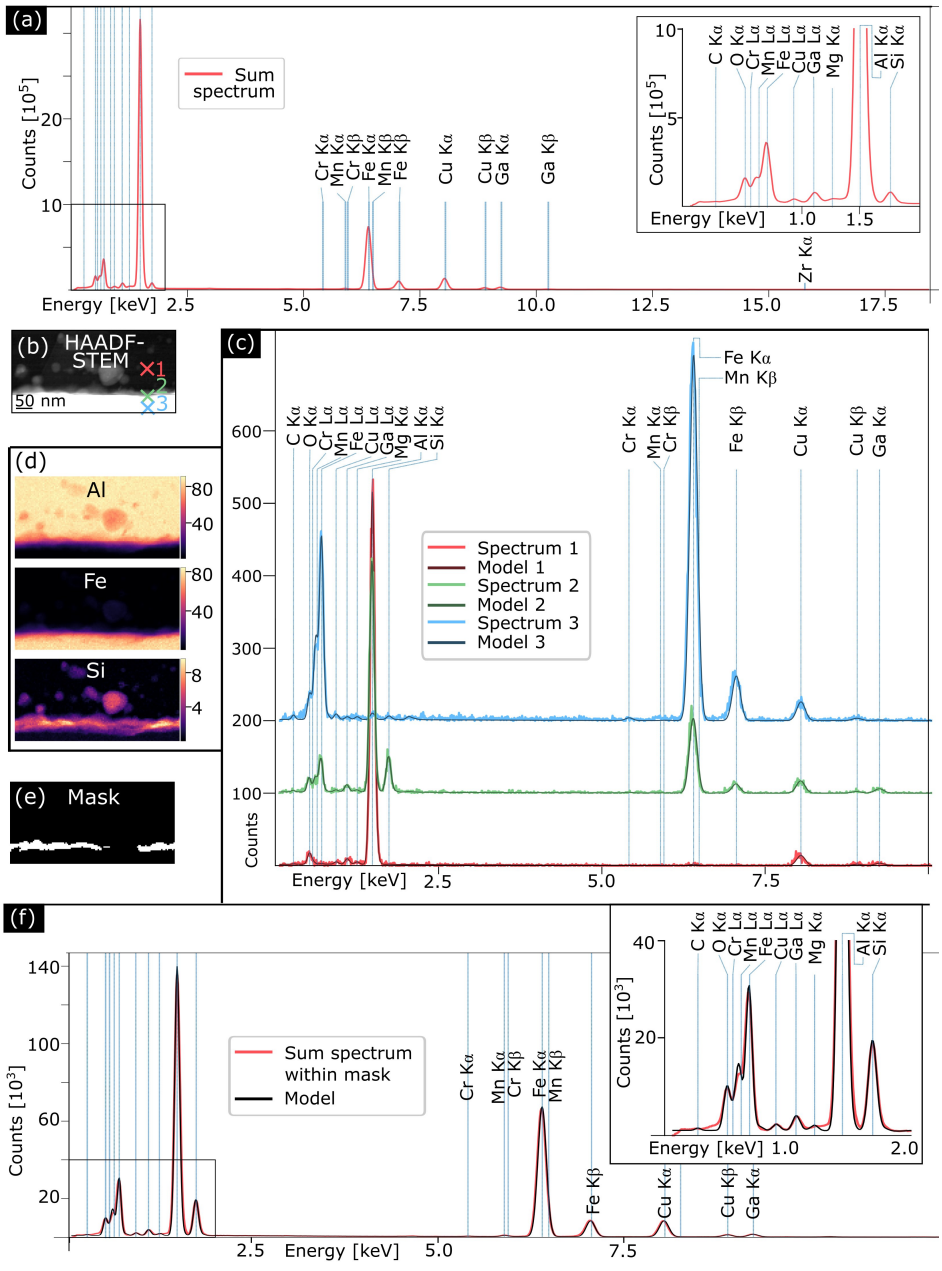

Figure S1: Data analysis of one EDS map of an interface region in Lamella 3. **(a)** Sum spectrum, where X-ray lines are marked. **(b)** HAADF-STEM image of the mapped region. Three locations are marked; 1 in Al, 2 in the IMP layer and 3 in steel. **(c)** Individual spectra and model fitting results from the three locations marked in (b). **(d)** Element maps of Al, Fe and Si showing the relative composition in at%. **(e)** Mask comprising the IMP layer, made by thresholding the Si map to >5 at.% following hole filling and removal of small segments. **(f)** Sum spectrum of the spectra within the mask in (e) and the model fitting result.

S2. Scanning electron diffraction data acquisition, visualisation and analysis

S2.1. Acquisition

Scanning electron diffraction (SED) data were acquired using a JEOL ARM300F (Diamond Light Source, UK) fitted with a cold field emission gun, a high-resolution pole piece and JEOL spherical aberration correctors in both the probe and image forming optics. The instrument was operated at 200 kV and aligned in an uncorrected nanobeam configuration using a 10 μm condenser aperture to obtain a convergence semi-angle of <1 mrad and a diffraction limited probe diameter of ~5 nm. SED data were acquired with a scan step size of 5.1 nm and a camera length of 12 cm. A Merlin Medipix direct electron detector was used to record diffraction patterns of dimensions 256×256 pixels. The exposure time was 1 ms at each probe position. SED maps were obtained from the same region at a series of specimen tilt conditions over a range of 30° in steps of 1°.

The SED data were analysed using the python library pyxem[2]. The real and reciprocal scales were calibrated based on SED data from a polycrystalline gold cross grating specimen acquired during the same session using the same experimental conditions.

S2.2. Visualisation

In order to visualise the morphologies of individual crystals comprising the IMP layer, virtual dark field (VDF) imaging-based segmentation[3] was applied to the dataset acquired at zero tilt. This approach aimed at overcoming crystal overlap and creating one isolated VDF image for each individual crystal. Figure S2(a) shows a virtual bright field (VBF) image of the interface region in this dataset.

First, centering of the direct beam was performed. A Difference of Gaussians peak finding method was employed to detect diffraction spots in all diffraction patterns in the dataset, before the unique spot positions were found using a clustering routine. Figure S2(b) shows the detected unique peaks. For each unique spot identified, a VDF image was created by integrating and plotting the intensity within a circular region centred on the spot, i.e. a virtual aperture, with respect to probe position. Since visualisation was aimed at disclosing crystals in the IMP layer and dispersoids in Al, a mask was created that included the Al and the IMP layer regions, but excluded steel. The mask was applied to the VDF images, so that they had zero intensity in the steel region. The mask is shown in Figure S2(c), and one example VDF image is shown in Figure S2(d).

Since one VDF image could contain intensity associated with more than one crystal, each of the VDF images were segmented by watershed segmentation to isolate the contributions from different crystals. The result from watershed segmentation on the VDF image shown in Figure S2(d) is shown in Figure S2(e). Further, since each crystal was associated with several diffraction spots, each crystal gave rise to several VDF image segments. Segments originating from the same crystal were identified, by considering the normalised cross-correlation (NCC) between segments, and subsequently summed. A clustering routine was employed to reveal the segment membership, that considered the correlation distances between the segments, given by $NCC - 1$. In contrast to the cited work[3], where an iterative list comparison of the NCC scores was used to determine the segment groups, the full NCC matrix between all segments was considered at once in this work. This was done to eliminate the possibility that the previous summation of VDF segments during the iterative comparison could influence the subsequent summation, which could

be important when considering numerous similar crystals. Lastly, diffraction spots were recreated for each sum segment by letting Gaussians model each of the diffraction spots associated with the segment sum.

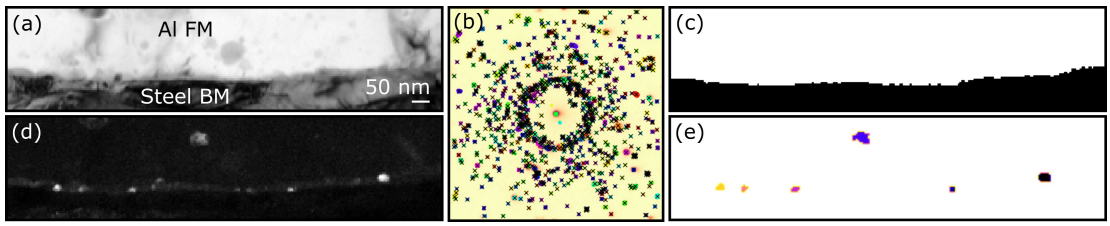

Figure S2: Visualisation of the IMP crystals in the scanning electron diffraction dataset acquired at zero tilt, by virtual dark field (VDF) imaging-based segmentation. **(a)** Vritual bright field image. **(b)** Peak finding to detect the unique diffraction spots in the region shown in (a). Unique spot positions are marked by black crosses, and coloured circles show positions of detected peaks, with one colour signifying one cluster. The underlying image shows a diffraction pattern where the maximum intensity with respect to detector position is plotted, based on all the individual diffraction patterns in the region shown in (a). **(c)** Mask for the IMP layer and Al region applied to the VDF images. **(d)** and **(e)** one VDF image and the corresponding watershed segmentation result showing individual VDF image segments plotted in different colours, respectively.

S2.3. Analysis

For assessment of the crystal structure(s) of the IMP(s), diffraction patterns showing systematic rows were selected by visual inspection from data acquired at different tilt conditions. Since the IMP crystals were small compared to the lamella thickness, they often overlapped with other crystals. Figures S3(a) and (b) show single diffraction patterns from one selected IMP crystal, where partial overlap with another crystal is particularly prominent in (b). In order to reduce or remove contributions from other partly overlapping crystals and background intensities from the selected patterns, non-negative matrix factorisation (NMF)-based segmentation[3, 4] was used. The segmentation was performed individually for each selected crystal, considering a cropped dataset only comprising the selected crystal and adjacent crystals. Figure S3(c) shows such a cropped dataset comprising one selected crystal. For each selected crystal, NMF was performed on the cropped dataset, following centering of the direct beam if needed. The region including and surrounding the central beam was masked out and not considered for NMF, in order to avoid components associated with variations in the high intensity direct beam. The singular value decomposition scree plot, which showed the fraction of total variance that each component accounted for, was investigated to determine the number of components. NMF resulted in factor components resembling average diffraction patterns and loading components resembling diffraction contrast images of the probed area. The component pattern most similar to the diffraction pattern recorded from the selected crystal was identified manually. If there were other components similar to the selected component, the NCC scores of both the factors and loadings were considered in order to identify components associated with the same crystal, and these components were summed. This was done since NMF could result in splitting of the signal from one crystal into several components. Figures S3(d) and (e) show the loading map and factor pattern resulting from NMF-based segmentation of the example selected crystal. The loading map associated with the selected component pattern was thresholded to create a real space mask for

the selected crystal, and the raw diffraction patterns within this mask were summed. Figure S3(f) shows the pattern sum within the loading map shown in Figure S3(d). This enabled a qualitative comparison of the NMF-based segmentation result to the summed raw data. The selected factor pattern (optionally a sum of similar factor patterns) that resembled a summed diffraction pattern was considered in the subsequent analysis.

For each selected pattern, all diffraction spots were found by Laplacian of Gaussian peak finding, and the spot positions were refined by a local Gaussian method. Figure S3(g) shows the factor pattern of the example selected crystal and the detected peaks. Systematic rows in the patterns were selected for further analysis. For each selected row, all measured distances between spots ($|\Delta\vec{G}|$), i.e. $\frac{1}{2}N(N-1)$ lengths for N peaks, were used to compute an average d-spacing ($\overline{|\Delta\vec{G}|}^{-1}$) and standard deviation. Figure S3(h) shows detected spots along selected rows and the corresponding measured average d-spacings and standard deviations.

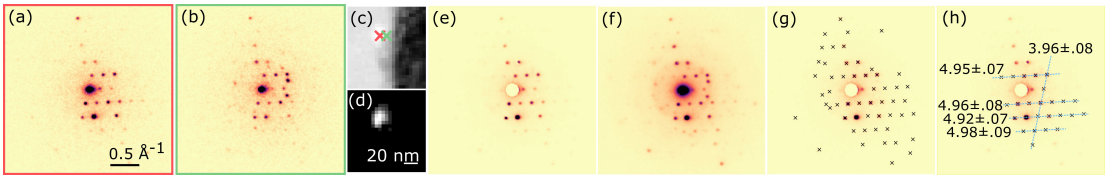

Figure S3: Analysis of the diffraction recorded from one selected crystal in the IMP layer, acquired at a specific specimen tilt condition. **(a)** and **(b)** single diffraction patterns of the selected crystal from the locations marked by red and green in (c). **(c)** Virtual bright field image of a cropped dataset comprising the selected crystal and adjacent crystals, where steel appear dark grey, aluminium light grey and IMP crystals light to medium grey. **(d)** and **(e)** thresholded loading map and factor pattern resulting from NMF-based segmentation of the cropped dataset. **(f)** Sum pattern of all the raw diffraction patterns from the region within the loading map in (d). **(g)** The pattern in (e) with crosses that mark the position of identified diffraction spots. **(g)** The pattern in (e) where the calculated average inverse inter-spot distances and standard deviations are given in Å for selected rows.

Lastly, individual selected patterns were indexed. None of the selected crystals were oriented exactly to zone axis, which made the indexation more challenging. The indexation was performed not to obtain the correct orientation of the shown patterns, but to determine close low-index zone axes. For each of the selected patterns, the two shortest non-parallel reciprocal vectors, corresponding to the two longest average d-spacings, and the angle between them, were considered. Each candidate phase was checked for potential zone axes with visible spots that matched the magnitudes and angle found experimentally. For this purpose, a code was written that was partly based on pyxem[2] and that enabled a systematic check of the magnitudes and angles between all reciprocal lattice points in all candidate phases. Simulated electron diffraction patterns corresponding to the identified zone axes were produced using ReciPro[5], employing a kinematical diffraction model with a parallel incident beam, to allow for visual qualitative comparisons.

S3. Tensile testing

Figures S4, S5 and S6 show engineering stress-strain curves, images and strain maps of specimens R1, F1 and F2 at different stages during tensile testing, respectively. Note that for both R1 and F1, an extensometer was placed on the Al side of the joint, which compromised the strain analysis in the soft zone in Al.

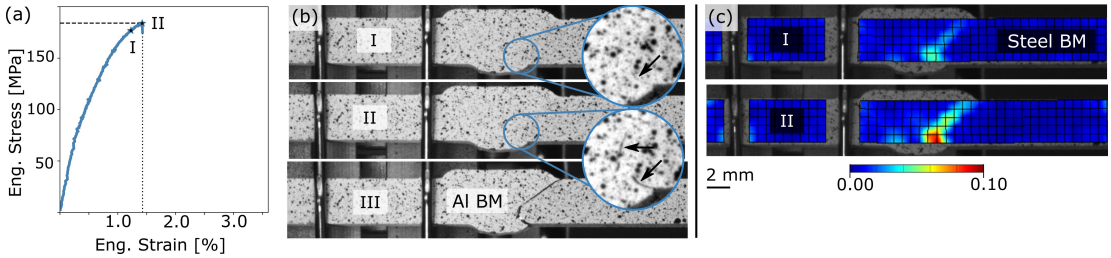

Figure S4: Tensile testing of specimen R1. **(a)** Engineering stress-strain curve. **(b)** Images used for digital image correlation analysis at different stages (I-III) during tensile testing, where III is immediately after final fracture. Cracks in the root region are pinpointed by arrows in the insets in I and II. **(c)** Strain maps showing the effective strain at stage I and II during tensile testing. Note that an extensometer placed on the Al side of the joint compromised the strain analysis in the soft zone in Al.

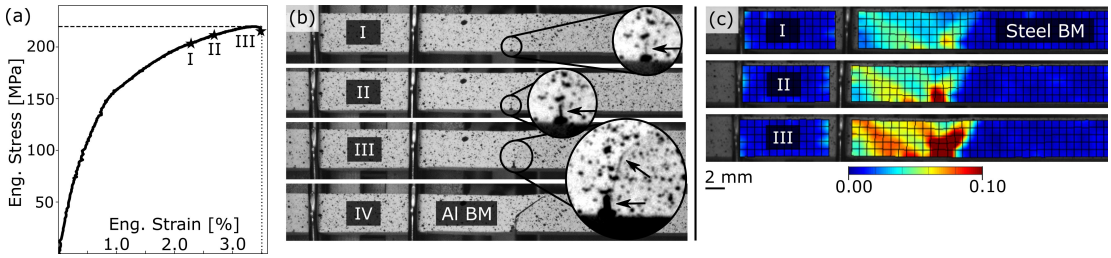

Figure S5: Tensile testing of specimen F1. **(a)** Engineering stress-strain curve. **(b)** Images used for digital image correlation analysis at different stages (I-IV) during tensile testing, where IV is immediately after final fracture. In I-III the insets show cracks in the root region, pinpointed by arrows. **(c)** Strain maps showing the effective strain at stages I-III during tensile testing. Note that an extensometer placed on the Al side of the joint compromised the strain analysis in the soft zone in Al.

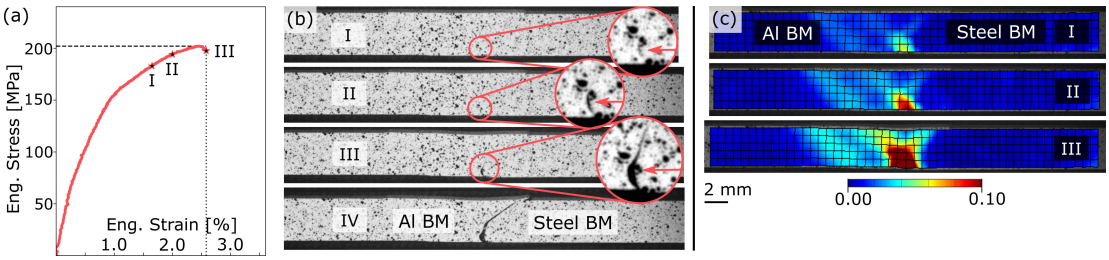

Figure S6: Tensile testing of specimen F2. **(a)** Engineering stress-strain curve. **(b)** Images used for digital image correlation analysis at different stages (I-IV) during tensile testing, where IV is immediately after final fracture. In I-III the insets show cracks in the root region, pinpointed by arrows. **(c)** Strain maps showing the effective strain at stages I-III during tensile testing.

S4. Fracture surfaces

Figure S7 shows optical microscopy and SEM images of the steel and Al fracture surfaces of specimen R2. Figure S7(a) and (b) show the same images of the steel fracture surface as Figure 4, while Figure S7(c) and (d) show the corresponding Al fracture surface of specimen R2. On the Al fracture surface, a wavy pattern with bumps and dimples matching those on the steel surface could be seen. Figure S7(d) shows a back-scatter electron (BSE) SEM image of the Al fracture surface, where residual steel pieces in the form of elongated flakes could be seen on the flat part (left side of the blue lines in Figures S7(c) and (d)). For the wavy part of the surface (right side), some steel flakes with flat appearance were attached to the Al fracture surface. Such a steel flake that stuck out of the Al surface is highlighted with the inset framed in red that shows a secondary electron (SE) SEM image corresponding to that shown in the red inset in Figure S7(b). At the locations where steel flakes were attached to the Al fracture surface, the steel fracture surface showed corresponding flat steel regions with no residual Al.

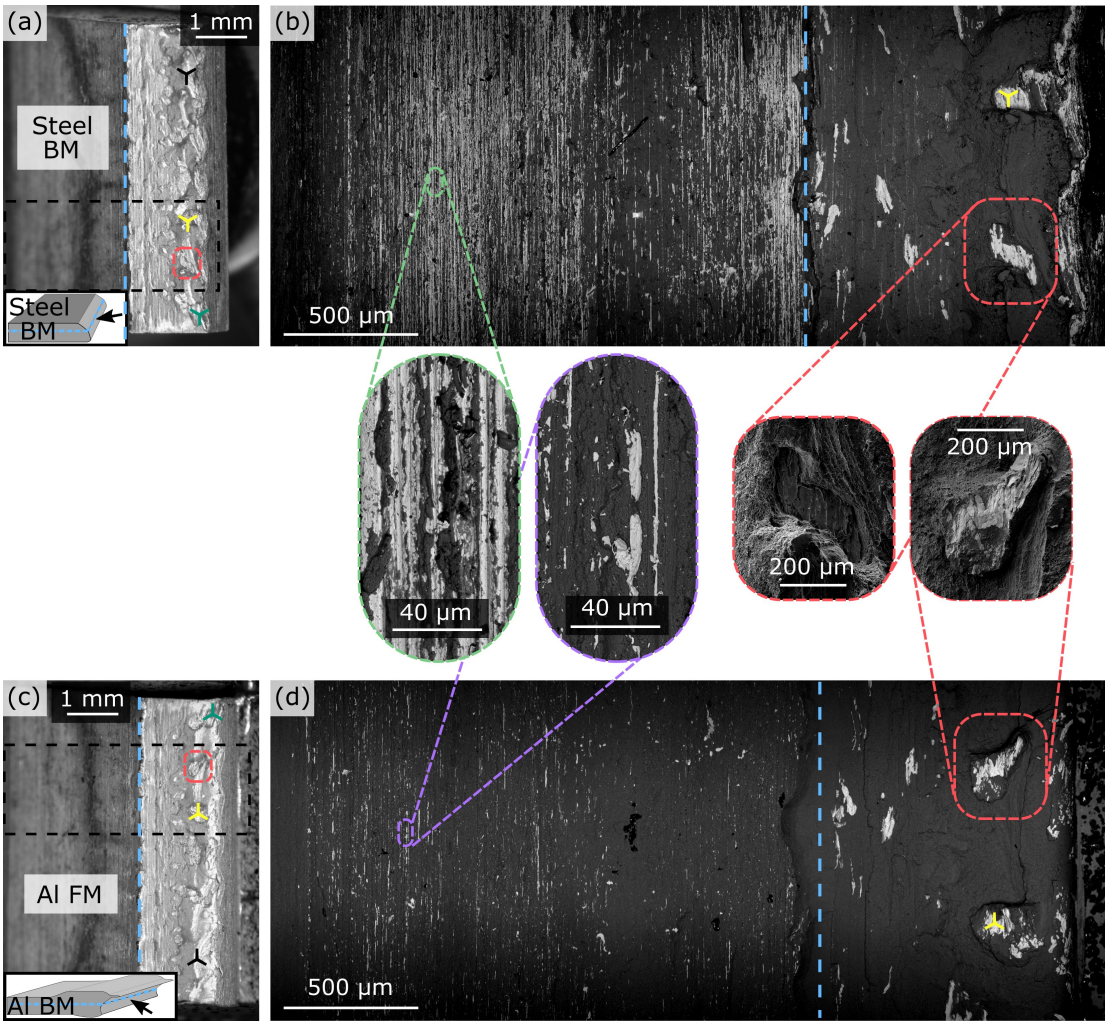

Figure S7: The Al and steel fracture surfaces resulting from tensile testing of specimen R2. Optical microscopy images of **(a)** the steel and **(c)** the Al fracture surface. The bottom insets illustrate the viewing directions. The dashed blue lines indicate the boarder between the top and bottom part of the fracture surfaces. **(b)** BSE SEM image of the steel fracture surface. The inset outlined in green displays a higher magnification image of the residual Al found on the upper part of the steel. **(d)** BSE SEM image of the Al fracture surface, where the inset outlined in blue shows residual steel fragments. In both (b) and (d), the insets outlined in red show SE SEM images of a dimple in the residual Al on the steel fracture surface and correspondingly a bulge covered by steel sticking out on the Al fracture surface. In all images, the coloured icons indicate corresponding locations on the two fracture surfaces.

S5. Overview of the aluminium-steel interface region

In this section, (S)TEM images and element maps based on STEM EDS are presented from each of the 8 lamellae investigated from the Al-steel interface region. Table S1 summarises the interface characteristics identified for each lamella.

Table S1: Characteristics of the interface regions in the investigated lamellae numbered $1-8$ as in Figure 7(a). The interface appearance was straight, slightly wavy or rough with deformed steel grains. In some lamellae, no interfacial IMP layer was observed, while in other lamella interfacial IMP layers were observed that were either continuous over the Al-steel interface in the lamella, discontinuous or restricted, i.e. covered only a narrow part of the Al-steel interface in the lamella.

Lamella	1	2	3	4	5	6	7	8
Interface appearance								
straight					x	x	x	x
slightly wavy	x		x					
rough		x		x				
Interfacial IMP layer								
not observed						x	x	
restricted					x			x
discontinuous	x	x						
continuous			x	x				

S5.1. Lamella 1

Figure S8 shows STEM images and element maps of Lamella 1 that had a slightly wavy interface and a discontinuous IMP layer. The location of where Lamella 1 was lifted out from the joint is shown in Figure S8(a). Figures S8(b)-(d) show BF-STEM images of the interface region. A high number of steel fragments and dispersoids were seen on the Al side of the interface, and more so closer to the interface. Figures S8(e) shows element maps based on STEM EDS of the interface region. A thin discontinuous Al-Fe-Si layer could be seen, together with a high number of dispersoids close to the interface.

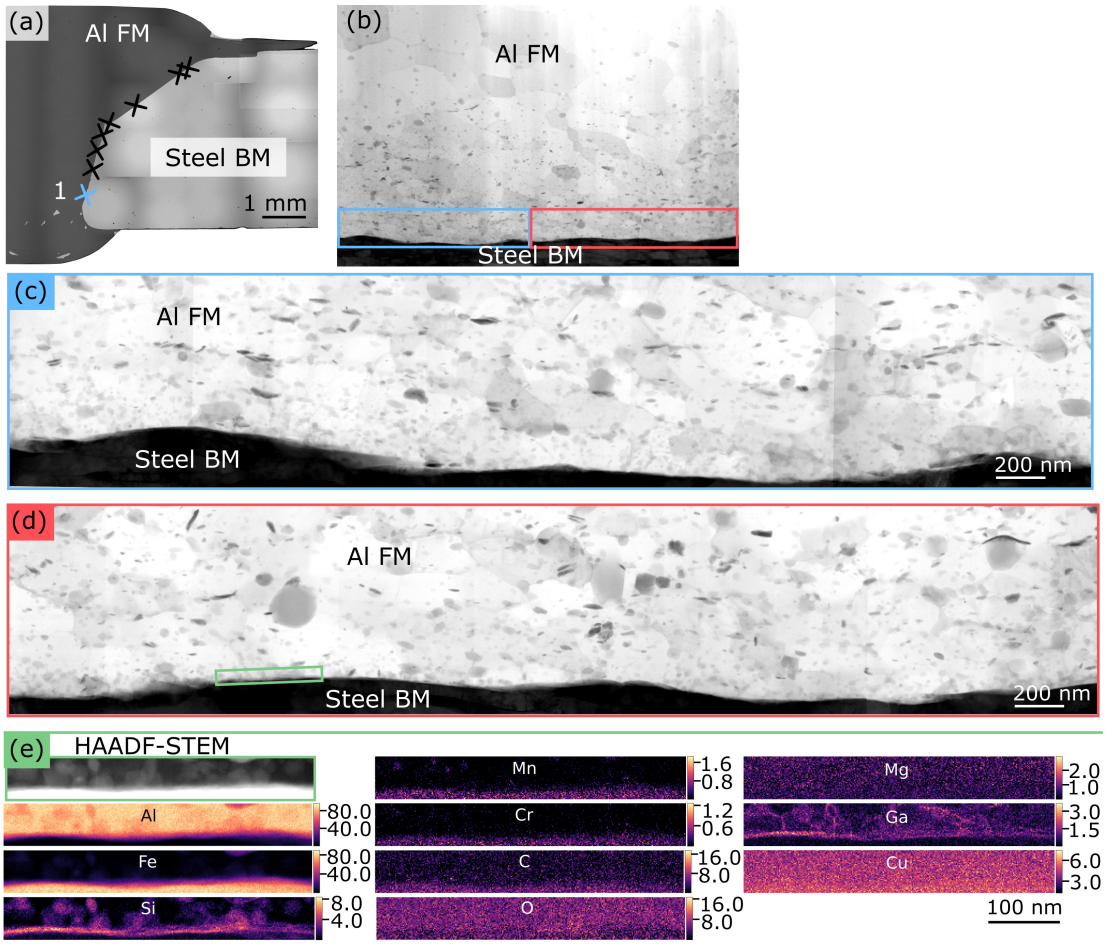

Figure S8: TEM characterisation of Lamella 1 that had a slightly wavy interface and a discontinuous IMP layer. **(a)** BSE SEM image of the Al-steel interface, where the blue cross indicates the location of where the lamella was lifted out. **(b)** BF-STEM overview image. **(c)** and **(d)** BF-STEM images of the interface regions marked by blue and red in (b), respectively. **(e)** HAADF-STEM image from the region marked by green in (d), and element maps based on STEM EDS showing the relative composition in at%.

S5.2. Lamella 2

Figure S9 shows (S)TEM images and element maps of Lamella 2 that had a rough interface with deformed steel grains and a discontinuous IMP layer. The location of where Lamella 2 was lifted out from the joint is shown in Figure S9(a), while (b) shows a BF-TEM image of the interface region, and (c) shows element maps. A discontinuous interfacial Al-Fe-Si IMP layer could be seen, and the interface was irregular with deformed steel regions. Note that the lamella was first thinned while fastened to a Cu grid, before it was transferred and fastened to a grid partly covered by amorphous silicon nitride, so that stray Si signal was expected in the element maps. Also, the transfer resulted in some Cu redeposition, which could be seen in the maps.

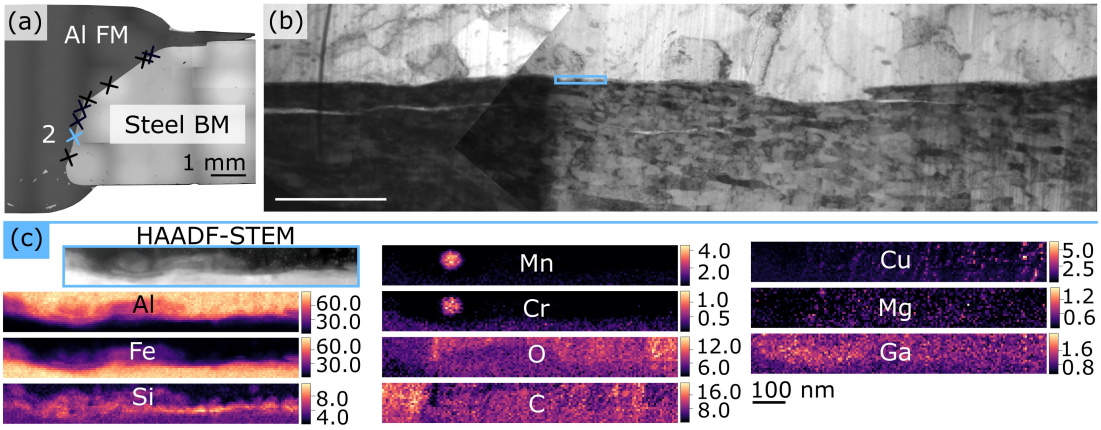

Figure S9: TEM characterisation of Lamella 2 had a rough interface and a discontinuous IMP layer. **(a)** BSE SEM image of the Al-steel interface, where the blue cross indicates the location of where the lamella was lifted out. **(b)** BF-TEM overview image of the interface region. **(c)** HAADF-STEM image from the interface region marked by blue in (b), and element maps based on STEM EDS showing the relative composition in at%.

S5.3. Lamella 3

Figures S10-S12 show (S)TEM images and element maps of Lamella 3 that had a continuous IMP layer and a slightly wavy interface. The location of where Lamella 3 was lifted out from the joint is shown in Figure S10(a), while (b) shows a BF-TEM image of the interface region, and (c) shows element maps based on STEM EDS of the IMP layer. Figure S10(d) shows the sum spectrum within the mask in (c), and model fitting and quantification of this spectrum yielded for the major constituents a relative composition of 59 at.% Al, 30 at.% Fe and 11 at.% Si.

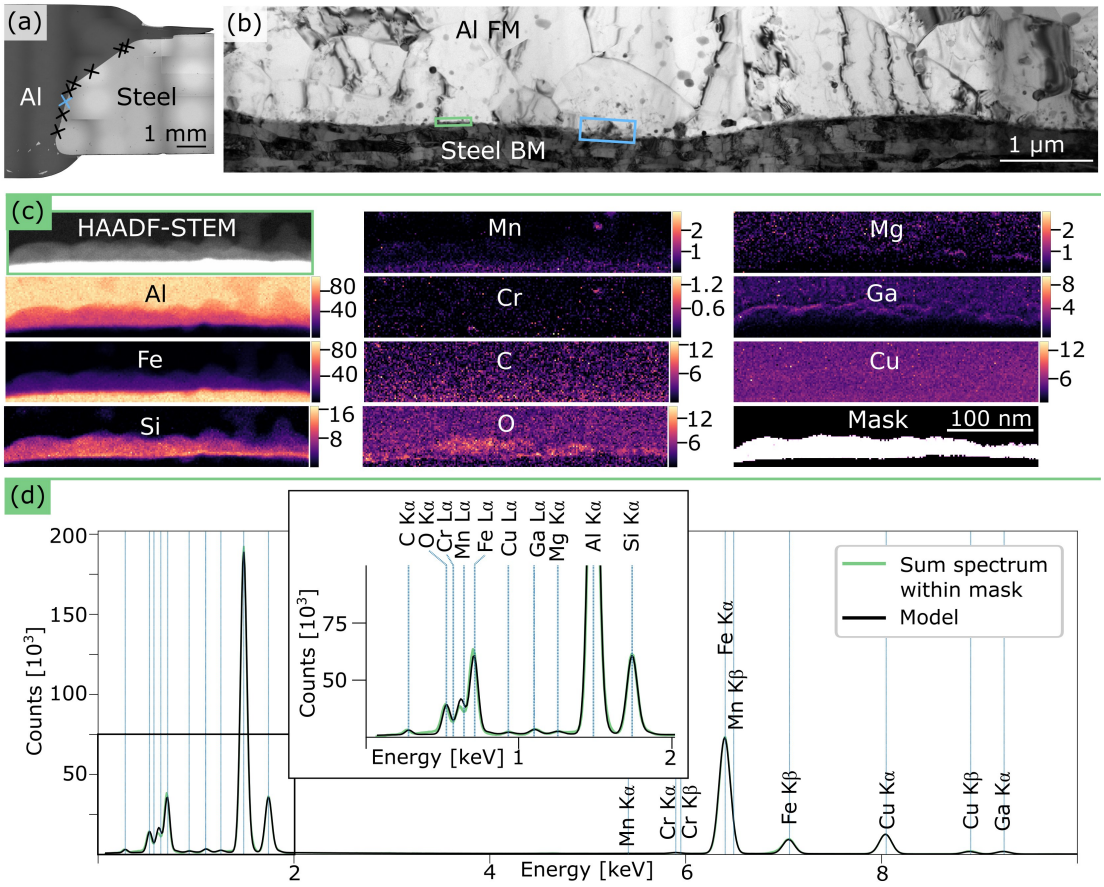

Figure S10: TEM characterisation of Lamella 3 that had a slightly wavy interface and a continuous interfacial Al-Fe-Si IMP layer. **(a)** BSE SEM image of the Al-steel interface, where the blue cross indicates the location of where the lamella was lifted out. **(b)** BF-TEM overview image of the interface region. **(c)** HAADF-STEM image from the interface region marked by green in (b), element maps showing the relative composition in at%, and a mask for the Al-Fe-Si IMP layer. **(d)** Sum spectrum from the region within the mask and the model fitting result.

Figure S11 shows STEM EDS results of another interface region in Lamella 3. Figure S11 (a) shows element maps, together with a HAADF-STEM image and a mask of the IMP layer. Figure S11(b) shows the sum spectrum within the mask in (a), and model fitting and quantification of this spectrum yielded a relative composition of 54 at.% Al, 38 at.% Fe and 8 at.% Si.

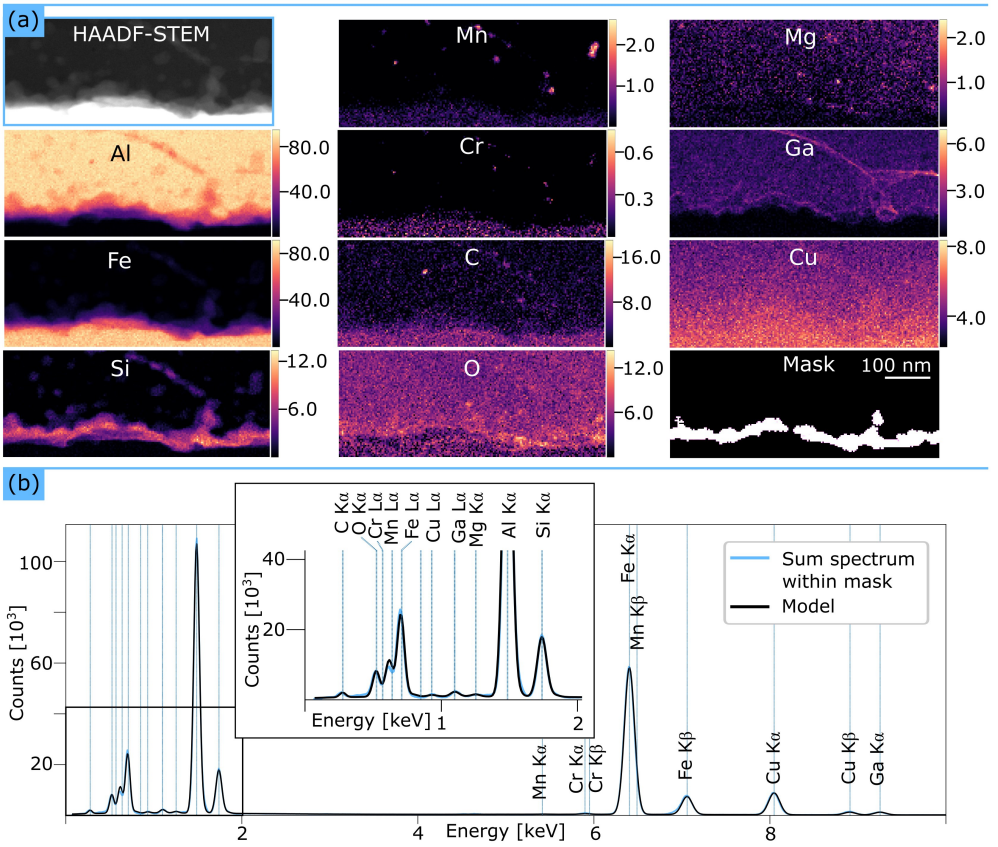

Figure S11: TEM characterisation of Lamella 3 that had a slightly wavy interface and a continuous interfacial Al-Fe-Si IMP layer. **(a)** HAADF-STEM image from the interface region marked by blue in Figure S10(b), element maps showing the relative composition in at%, and a mask for the Al-Fe-Si IMP layer. **(b)** Sum spectrum from the region within the mask and the model fitting result.

Figure S12 shows the same images as Figure 9 in addition to further TEM images and STEM EDS results. Figure S12(a) and (b) show a BF-STEM and a HAADF-STEM image of the interface region, respectively, while (c) shows a mask of the IMP region. Figure S12(c) shows element maps based on STEM EDS, while (d) shows the total sum spectrum. Note that the shown maps are composed of three individually acquired maps, which was necessary to ensure correct specimen height over the mapped area, as mentioned earlier. Figure S12(f) shows the sum spectrum within the mask in (c), together with the model fitting result, which gave for the major constituents a relative composition of 55 at.% Al, 37 at.% Fe and 8 at.% Si.

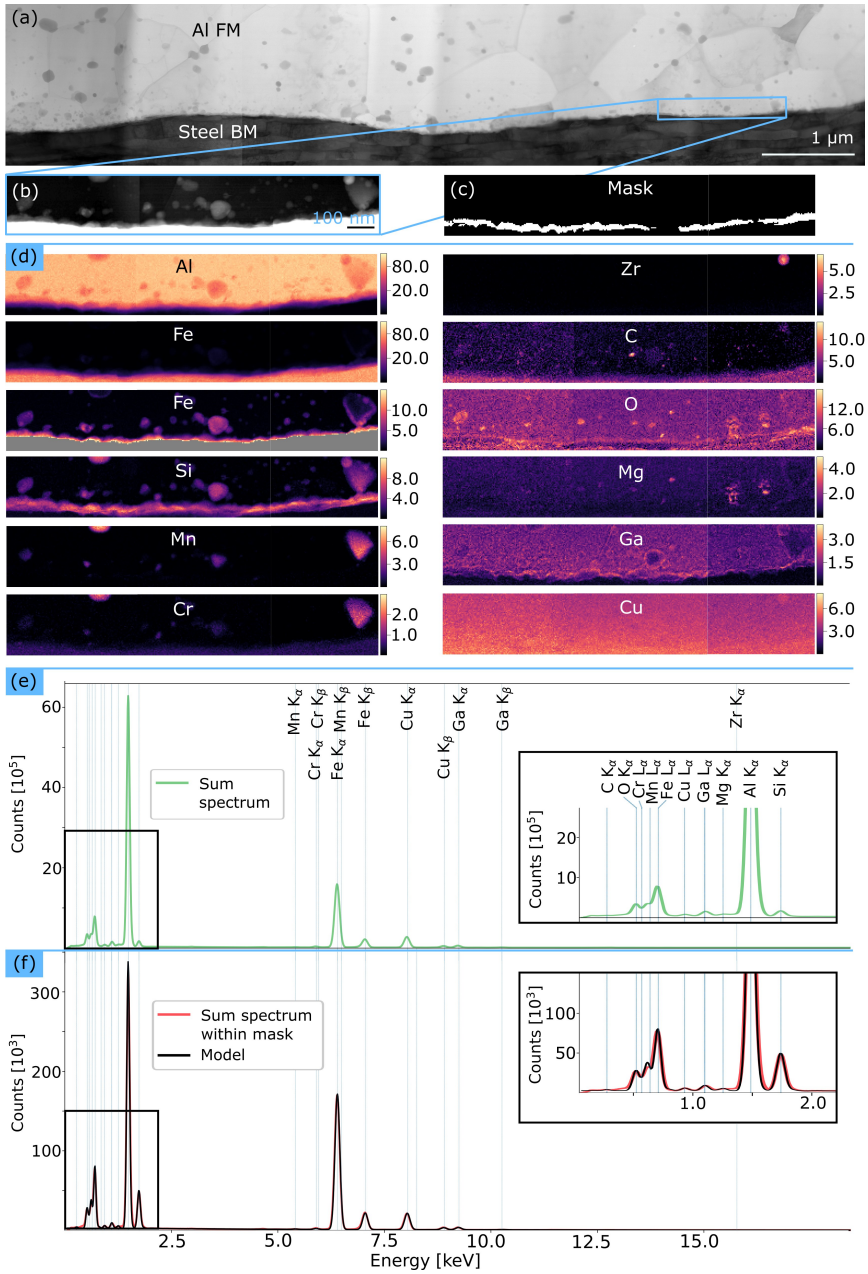

Figure S12: TEM characterisation of Lamella 3 that had a slightly wavy interface and a continuous interfacial Al-Fe-Si IMP layer. **(a)** BF-STEM image showing an overview of the interface region. **(b)** HAADF-STEM image of the region marked by blue in (a). **(c)** Mask for the IMP layer created from the Si map in (d). **(d)** Element maps based on STEM EDS showing the relative composition in at%. **(e)** Total sum spectrum. **(f)** Sum spectrum from the region within the mask in (c) and the model fitting result.

S5.4. Lamella 4

Figures S13 and S14 show (S)TEM images and element maps of Lamella 4 that had a continuous IMP layer and a rough interface with deformed steel grains. The location of where Lamella 4 was lifted out from the joint is shown in Figure S13(a), while (b) and (c) show a BF-TEM image and a BF-STEM image of the interface region, respectively. Figure S13(c) shows element maps of an intermixed Al-steel interface region, where an Al-Fe-Si IMP layer can be seen at the Al-Fe interface adjacent to the Al side of the interface.

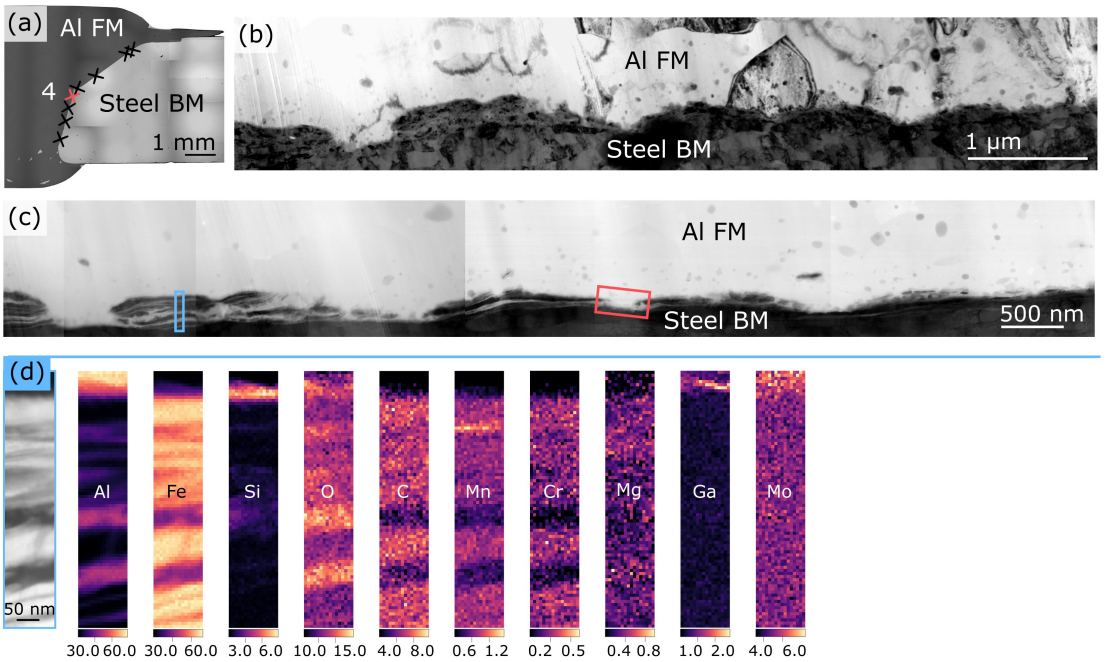

Figure S13: TEM characterisation of Lamella 4 that had a rough interface and a continuous interfacial Al-Fe-Si IMP layer. **(a)** BSE SEM image of the Al-steel interface, where the blue cross indicates the location of where the lamella was lifted out. **(b)** BF-TEM image showing an overview of the interface region. **(b)** BF-STEM image of the interface region. **(d)** Element maps based on STEM EDS of the intermixed Al-Fe interface region marked by blue in (c), showing the relative composition in at%.

Figure S14(a) shows a HAADF-STEM image and element maps of another interface region, where an Al-Fe-Si IMP layer enclosed steel fragments near the interface. A mask for the IMP layer is also shown, and Figure S14(b) shows the sum spectrum within the mask in (a). Model fitting and quantification of this spectrum yielded a relative composition for the major constituents of 61 at.% Al, 31 at.% Fe and 8 at.% Si.

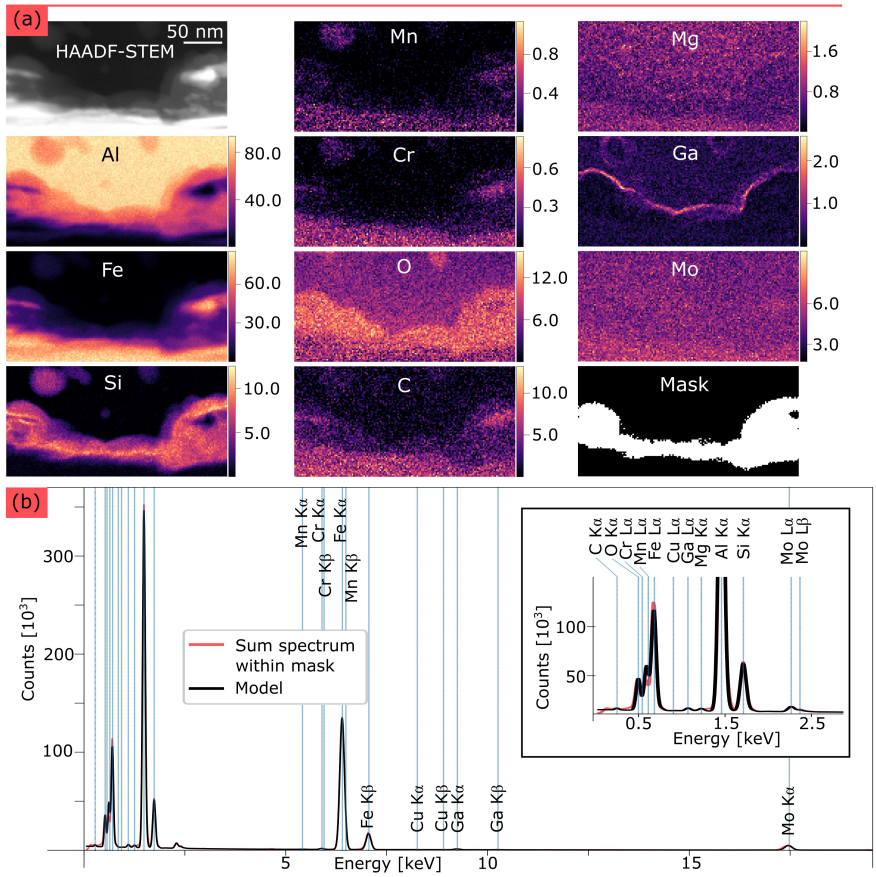

Figure S14: TEM characterisation of Lamella 4 that had a rough interface and a continuous interfacial Al-Fe-Si IMP layer. **(a)** HAADF-STEM image of the region marked by red in Figure S13(c), element maps showing the relative composition in at%, and a mask for the IMP layer created from the Si map. **(b)** Sum spectrum from the region within the mask in (a) and the model fitting result.

S5.5. Lamella 5

Figure S15 shows (S)TEM images and element maps of Lamella 5 that had a straight interface and a restricted IMP layer. The location of where Lamella 5 was lifted out from the joint is shown in Figure S15(a). Figure S15(b) shows a BF-STEM overview image of the interface region, while (c) shows a BF-STEM image of the restricted IMP layer that only covered one ~0.9 µm long portion of the interface. Figure S15(d) shows element maps based on STEM EDS of the restricted IMP layer, where oxides could also be seen close to the interface.

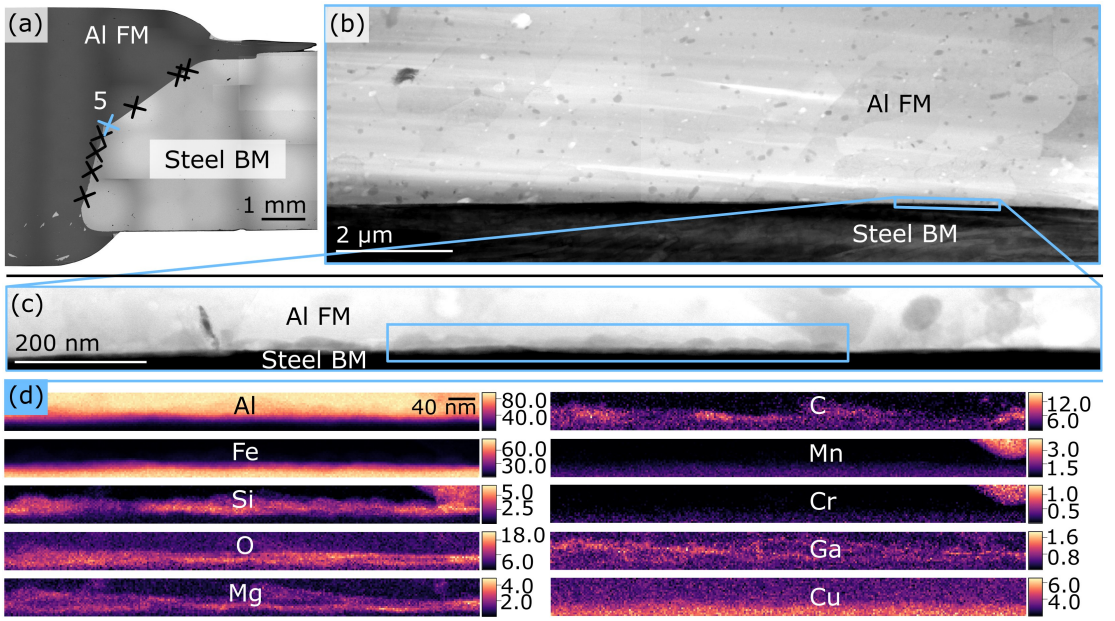

Figure S15: TEM characterisation of Lamella 5 that had a straight interface and a restricted interfacial Al-Fe-Si IMP layer. **(a)** BSE SEM image of the Al-steel interface, where the blue cross indicates the location of where the lamella was lifted out. **(b)** BF-STEM image showing an overview of the interface region. **(b)** BF-STEM image of the interface region with a restricted IMP layer that covered one ~0.9 µm wide portion of the interface. **(d)** Element maps based on STEM EDS of the interface region marked by blue in (c), showing the relative composition in at%.

S5.6. Lamella 6

Figure S16 shows TEM images and EDS maps of Lamella 6 that had a straight interface with no observed IMP layer. The location of where Lamella 6 was lifted out from the joint is shown in Figure S16(a). Lamella 6 was lifted out from the steel fracture surface of tensile specimen R2, from a region where a thin Al layer covered the steel. Figures S16(b) and (c) show BSE SEM images of the location where Lamella 6 was lifted out. Figures S16(d) shows a SE SEM image taken after initial FIB milling of the cross-section that was to become Lamella 6, which was subsequently lifted-out, thinned on a Cu grid and fastened on a Si-based grid. Figure S16(e) shows a BF-TEM overview image of the interface region, while (f) shows a HAADF-STEM image of an interface region. Figure S16(e) shows element maps based on STEM EDS of the region in (f). Note that this lamella had a poorer surface quality with considerable content of C, O and Ga. No IMP layer could be observed.

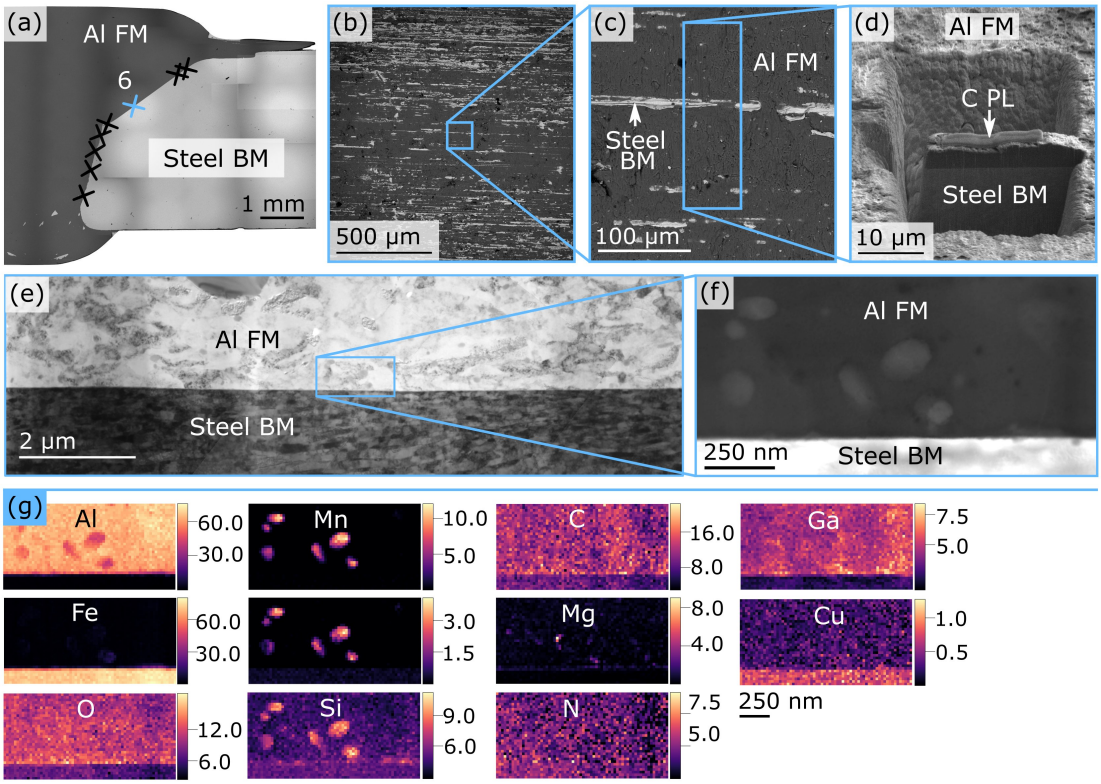

Figure S16: TEM characterisation of Lamella 6 that had a straight interface with no observed IMP layer. **(a)** BSE SEM image of the Al-steel interface, where the blue cross indicates the location of where the lamella was lifted out. **(b)** and **(c)** BSE SEM images of the location where the lamella was lifted out from the steel fracture surface of tensile specimen R2. **(d)** SE SEM image after initial FIB milling of the cross-sectional specimen, where the C protection layer (C PL) and milled trenches can be seen. **(e)** BF-TEM image showing an overview of the interface region. **(f)** HAADF-STEM image of an interface region. **(g)** Element maps based on STEM EDS of the interface region shown in (f), showing the relative composition in at%.

S5.7. Lamella 7

Figure S17 shows TEM images and element maps of Lamella 7 that had a straight interface with no observed IMP layer. The location of where Lamella 7 was lifted out from the joint is shown in Figure S17(a). Figure S17(b) shows a BF-STEM overview image of the interface region, while (c) shows a HAADF-STEM image of an interface region. Figure S17(d) shows element maps based on STEM EDS where no IMP layer, but instead an interfacial oxide layer could be observed. The oxide layer was composed mainly of Al, O and Mg, with minor amounts of Si.

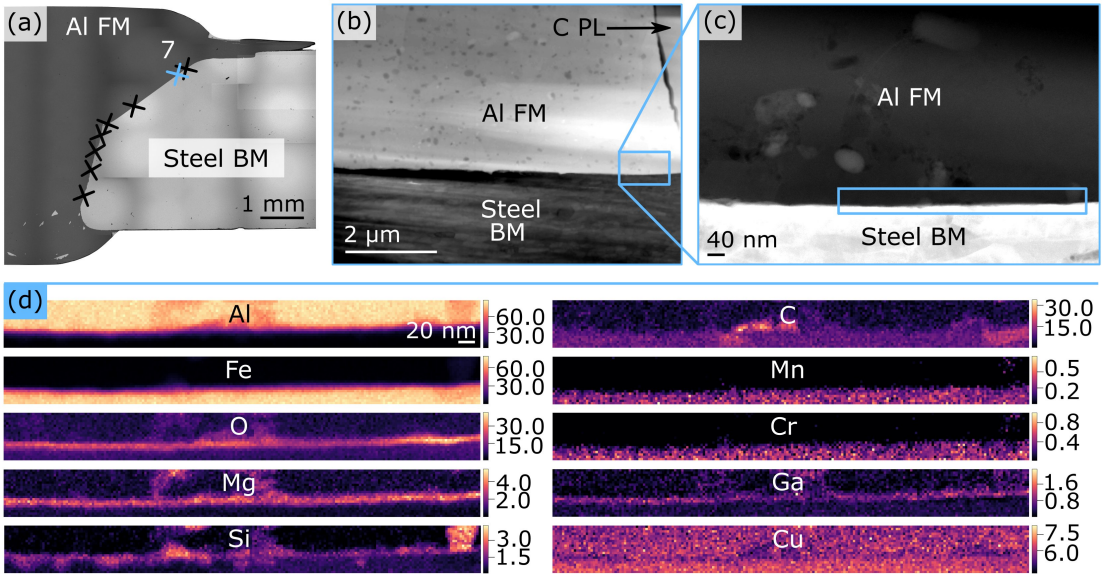

Figure S17: TEM characterisation of Lamella 7 that had a straight interface with no observed IMP layer. **(a)** BSE SEM image of the Al-steel interface, where the blue cross indicates the location of where the lamella was lifted out. **(b)** BF-STEM image showing an overview of the interface region. **(c)** HAADF-STEM image of an interface region. **(d)** Element maps based on STEM EDS of the interface region marked by blue in (c), showing the relative composition in at%.

S5.8. Lamella 8

Lamella 8 was lifted out from the steel fracture surface of tensile specimen R2 from a region where a thin Al layer covered steel. Figures S18(a)-(d) shows SEM images taken during the FIB preparation of the lamella.

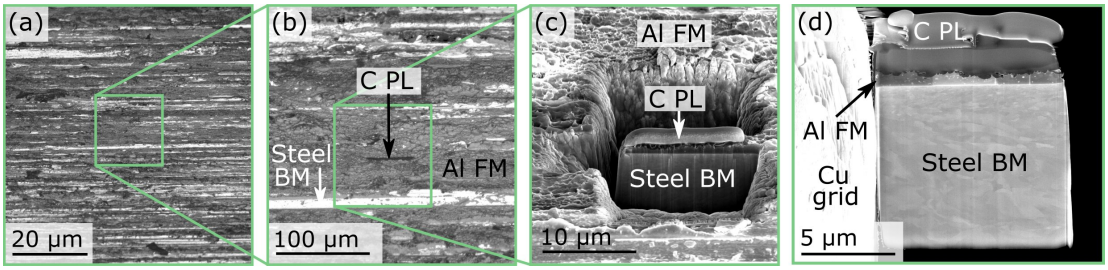

Figure S18: FIB preparation of Lamella 8. **(a)** and **(b)** BSE SEM images of the location where the lamella was lifted out from the steel fracture surface of tensile specimen R2. **(c)** SE SEM image after initial FIB milling of the cross-sectional specimen, where the C protection layer (C PL) and milled trenches can be seen. **(c)** SE SEM image of the lamella fastened to a Cu grid, prior to final thinning.

Figure S19 shows TEM images and element maps of Lamella 8 that had a straight interface with a restricted IMP layer. The location of where Lamella 8 was lifted out from the joint is shown in Figure S19(a). Figure S19(b) shows a BF-STEM overview image of the interface region. Figure S19(c) shows a HAADF-STEM image and element maps of the interface region with the restricted IMP layer that covered one ~1.3 µm wide portion of the interface. A mask for the IMP layer is also shown, and Figure S19(d) shows the sum spectrum within the mask in (c). Model fitting and quantification of this spectrum yielded for the major constituents a relative composition of 72 at.% Al, 19 at.% Fe and 9 at.% Si. Figure S19(e) shows EDS maps of an interface region without IMP layer, where instead an interfacial oxide layer ~5 nm thick could be seen that was mainly composed of Al, O and Mg with minor amounts of Si. Note that the Al region shown in (e) was thinner than other regions shown here (relative thickness $\frac{t}{\lambda} = 0.2 - 0.4$ measured by electron energy loss spectroscopy, where t is the thickness and λ is the inelastic mean free path), which resulted in a relatively large amount of Cu stray signal.

S6. Crystallography of intermetallic Al-Fe(-Si) phases

Crystallographic information for known Al-Fe(-Si) IMPs considered as candidate phases in this work is listed in Table S2. Although the Al-rich Al-Fe(-Si) system has been investigated extensively[6–8], several metastable phases and superstructure modifications have been discovered[9, 10] and several crystal structures have not been determined fully. Crystallographic information for Al-Fe(-Si) intermetallic phases that were considered as candidate phases in this work, but for which the structure has not been fully determined, is listed in Table S3. Several superstructures of the α_c phase have been proposed, including α_T, α' and α'', which are also included in Table S3.

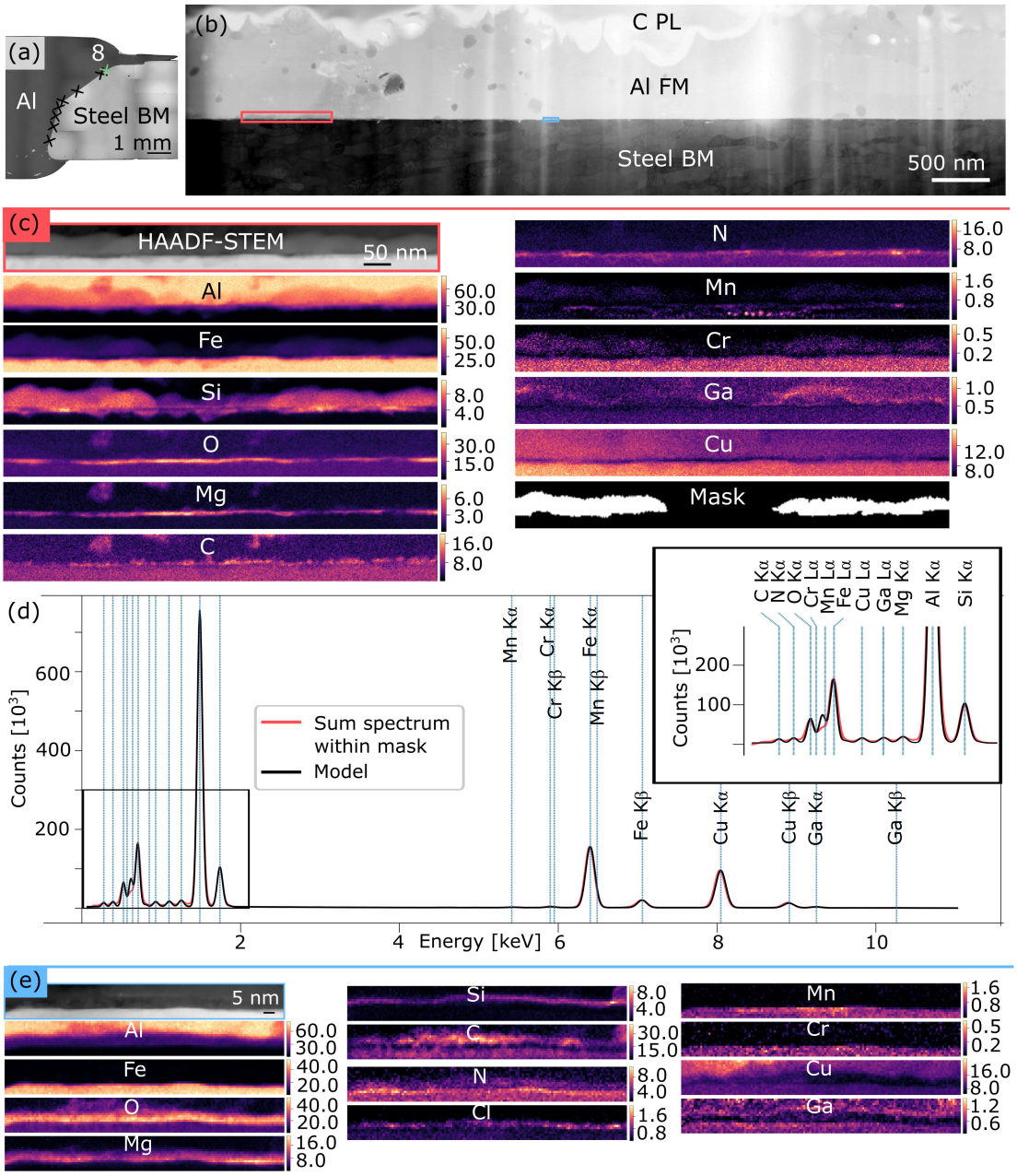

Figure S19: TEM characterisation of Lamella 8 that had a straight interface and a restricted interfacial Al-Fe-Si IMP layer. **(a)** BSE SEM image of the Al-steel interface, where the blue cross indicates the location of where the lamella was lifted out. **(b)** BF-STEM image showing an overview of the interface region. **(c)** HAADF-STEM image and element maps of the interface region marked by red in (c) with the restricted IMP layer, showing the relative composition in at%. A mask for the IMP layer created from the Si map is also shown. **(d)** Sum spectrum from the region within the mask in (c) and the model fitting result. **(e)** HAADF-STEM image and element maps of the interface region marked by blue in (c), showing the relative composition in at%.

Table S2: Crystallographic information for the known Al-Fe(-Si) intermetallic phases considered as candidate phases in this work. Note that various phase names are used in literature, and that the first phase name listed is used in this work. Note that in the column named 'Si content', Si contents are given as reported in the cited studies, which do not (necessarily) correspond to the homogeneity range of Si, and so these numbers should only be regarded as an indication of possible Si contents.

Phase	**Lattice parameters *a; b; c* [Å] ($\alpha;\beta;\gamma$ [°])**	**Crystal System**	**Space Group (#)**	**Si content** [at.%]	**Comments**	**Ref.**
ζ, $FeAl_2$	$a = 4.8745; b = 6.4545; c = 8.7361$ $\alpha = 87.93; \beta = 74.396; \gamma = 83.062$	Triclinic	$P1$ (1)	0.14[11]		[12]
η, Fe_2Al_5	$a = 7.6559; b = 6.4154; c = 4.2184$	Orthorhombic	$Cmcm$ (63)	0 – 2.2[7]	Low temperature modifications	[13]
η', Fe_3Al_8	$a = 11.3212; b = 6.3731; c = 8.6352$ $\beta = 104.43;$	Monoclinic	$C2/c$ (15)		of η include η', η'', η''' and η^m[14–16].	[14]
θ, Fe_4Al_{13}	$a = 15.492; b = 8.078; c = 12.471$ $\beta = 107.69$	Monoclinic	$C2/m$ (12)	0 – 4.4[11]		[17]
Fe_2Al_9	$a = 6.2406; b = 6.2993; c = 8.5992$ $\beta = 95.129$	Monoclinic	$P2_1/c$ (14)	< 1[18]		[19]
$FeAl_m$	$a = b = 8.84; c = 21.60$	Tetragonal	$I\bar{4}2m$ (121)	0 – 2.1[20]	m~4.	[21]
$FeAl_6$	$a = 6.464; b = 7.440; c = 8.779;$	Orthorombic	$Cmc2_1$ (36)	0 – 1.9[20]		[22]
α_c, α-AlFeSi	$a = b = c = 12.56$	Cubic	$Im\bar{3}$ (204)	5.9-11.1[23]	Transition elements M (e.g. Mn, Cr)	[24]
α_{sc}, α-AlMnSi	$a = b = c = 12.68$	Cubic	$Pm\bar{3}$ (200)		are interchangeable with Fe. α_{sc} forms for high M/Fe-rato and α_c for low.	[24]
α_h, τ_5, $Al_{7.1}Fe_2Si$	$a = b = 12.404; c = 26.234$	Hexagonal	$P6_3/mmc$ (194)	8.0[8] – 13.1[25]		[26]
τ_{11}, Al_5Fe_2Si, $Al_4Fe_{1.7}Si$	$a = b = 7.509; c = 7.594$	Hexagonal	$P6_3/mmc$ (194)	9.2 – 11.8[7]		[27]
β, τ_6, $FeAl_{4.5}Si$	$a = 6.1676; b = 6.1661; c = 20.8093;$ $\beta = 91.00$	Monoclinic	$A12/a1$ (15)	14.7 – 18.9[28]	Polytypes of β have been described[28], including an	[29]
β_{ABCD}	$a = b = 6.168; c = 41.618;$	Tetragonal	$I4_1/acd$ (142)		ABCD polytype (β_{ABCD}).	[28]
λ, γ, τ_2, Al_3FeSi [a]	$a = b = 10.222; c = 19.668;$ alt.: $a = 8.821; \alpha = 70.82;$	Trigonal	$R\bar{3}$ (148)	14.9[34] – 26.1[32]		[31]
τ_{12}, Al_3Fe_2Si	$a = b = c = 10.806$	Cubic	$Fd\bar{3}m$ (227)	15.4 – 16.0		[7]
τ_3 Al_2FeSi	$a = 7.995; b = 15.162; c = 15.221;$	Orthorhombic	Cmma (67)	18.9 – 23.0[7]		[35]
τ_1, τ_9, $Al_2Fe_3Si_3$	$a = 4.6512; b = 6.326; c = 7.499;$ $\alpha = 101.38; \beta = 105.923; \gamma = 101.237$	Triclinic	$P\bar{1}$ (2)	20.8 – 41.2[7]		[36]
δ, τ_4, Al_3FeSi_2	$a = b = 6.06; c = 9.525$	Tetragonal	$I4/mcm$ (140)	27 – 43	Can intergrow with β[28].	[37]
τ_7, $Al_3Fe_2Si_3$	$a = 7.179; b = 8.354; c = 14.455$ $\beta = 93.80$	Monoclinic	$P2_1/c$ (14)	27.3[7]-37.5[38]		[38]
τ_8, $Al_2Fe_3Si_4$	$a = 3.6687; b = 12.385; c = 10.147$	Orthorhombic	$Cmcm$ (63)	37.3 – 42.3[7]		[36]

[a] First, Munson described the γ-AlFeSi phase to be C-face-centred monoclinic with $a = 17.78; b = 10.25; c = 8.90$; [Å] and $\beta = 132.17°$[30]. Much later, Sugiyama et. al[31] determined the structure of the phase λ-AlFeSi, a rhombohedral phase ($R\bar{3}$, 148) with $a = b = 10.222$; $c = 19.668$ [Å] and with a composition close to that of γ. Afterwards, Roger et. al[32] determined the structures of two γ-Al_3FeSi phase crystals; one Si-poor ($Al_{80}Fe_{25}Si_{18}$) and one Si-rich ($Al_{79}Fe_{26}Si_{18}$), and described them as trigonal crystals ($R\bar{3}$, 148) with $a = b = 10.2223(2)$; $c = 19.6781(4)$ [Å] for the Si-poor crystal and with $a = b = 10.1987(2)$; $c = 19.5320(3)$ [Å] for the Si-rich crystal. Thereafter, Yu et. al[33] determined the lattice parameters of τ_2-$Al_{4.5}FeSi$ (γ) and described it as a trigonal R-centred crystal with $a = b = 10.34(5)$; $c = 19.83(8)$ [Å]. In this work, the structure reported by Sugiyama et al. was used.

Table S3: Crystallographic information for the reported Al-Fe(-Si) intermetallic phases considered as candidate phases in this work, for which the crystal structure has not been fully determined. Note that in the column named 'Si content', Si contents are given as reported in the cited studies, which do not (necessarily) correspond to the homogeneity range of Si, and so these numbers should only be regarded as an indication of possible Si contents.

Phase	**Lattice parameters** ***a; b; c*** **[Å]** $(\alpha;\beta;\gamma\ [^\circ])$	**Crystal System**	**Space Group (#)**	**Si content** [at.%]	**Comment**	**Ref.**
Al_xFe	$a = 21.6; b = 9.3; c = 9.05$ $\beta = 94.0;$	Monoclinic		0 – 1.9[20]	x∼5. Incommensurate and defective structure. Reported structure not consistent with all data.	[39]
Al_pFe	$a = b = c = 10.3$	Cubic	I		p∼4.	[40]
q_2	$a = 12.5; b = 12.3; c = 19.3$ $\beta = 109;$	Monoclinic	Pm (6)	3.8		[40, 41]
q_1	$a = 12.7; b = 36.2; c = 12.7$	Orthorhombic	$Cmmm$ (65)	4.1[40] – 4.7[20]		[40, 41]
α_v	$a = 8.47; b = 6.35; c = 6.10$ $\beta = 93.4;$	Monoclinic		4.5 – 10.5	Similar to Fe_2Al_9, but with higher Si content and with shorter a- and c–axes.	[42]
α', α_R	$a = b = c = 20.82; \alpha = 95.2$ alt: $a = b = 30.76; c = 32.6$	Trigonal Hexagonal	$R\bar{3}$ (148)	3.8	α_c superstructure. Possibly the same phase as α_T.	[43, 44]
α''	$a = b = 17.76; c = 10.88$	Trigonal	$P\bar{3}$(147)	3.8	α_c superstructure.	[43, 44]
α_T	$a = 27.950; b = 30.619; c = 20.729$ $\beta = 97.79;$	Monoclinic	C-centred	5.9 – 8.6	α_c superstructure.	[23]
β^*	$a = 8.9; b = 4.9; c = 41.6$ $\beta = 92$	Monoclinic				[45]
τ_{10}, $Al_4Fe_{1.7}Si$	$a = b = 15.518; c = 7.297$	Hexagonal		15.5		[8]

S7. Scanning electron diffraction of intermetallic phases

Figures S22-S24 show measured average spot distances converted to average d-spacings based on selected patterns from the IMP layer, and these show an enlarged version of Figure 10(c). Figure S22 show an overview image of all measured d-spacings and calculated values for all phases in the interval of 4.8 – 18.5 Å. Measured and calculated d-spacings in the range of 4.8 – 11.5 Å are shown in Figures S23 and S24 for the candidate Al-Fe-Si phases listed in Tables S2 and S3, respectively.

Figure S20 shows a VBF image where the locations of selected IMP crystals, numbered 1 – 34, are indicated. These crystals gave diffraction patterns with at least two non-parallel systematic rows at specific tilt settings and were selected for further investigations. Note that some of these numbers might indicate the same crystal, since it was not determined which patterns were recorded from the same crystal at different tilt conditions.

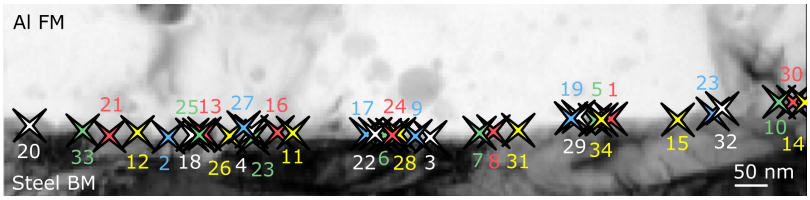

Figure S20: Virtual bright field image of the interfacial region mapped by SED, where the locations of selected interfacial Al-Fe-Si crystals are indicated by white, green, red, yellow and blue crosses numbered 1 – 34.

Figures S25-S27 show selected diffraction patterns, and both the summed diffraction patterns and patterns resulting from NMF-based segmentation are shown. For each pattern, spot distances were measured, and the two longest average d-spacings corresponding to non-parallel rows of spots, together with the angle between them, were used as a basis for indexation. Average measurements are given in the figures. For each pattern, all candidate phases were investigated for possible zone axes with spots matching these measurements. In total, the phase that fit best with most of the experimental patterns was α_c. In Figures S25-S27, patterns that fit with α_c are framed in black and are indexed with respect to this phase. Figure S28 shows simulated kinematic patterns of α_c corresponding to the zone axes found from the patterns in Figures S25-S27. However, there were also patterns that could not be indexed with respect to α_c, and such patterns are framed in dark blue in Figures S25-S27. Some of these contained spots at distances corresponding to average d-spacings of e.g. 16 ± 1 Å, 10.8 ± 0.5 Å and 7.8 ± 0.3 Å, which could not be described by α_c.

Some selected patterns from dispersoids embedded in the Al matrix were also investigated. Several of these patterns were consistent with α_c, and Figures S21(a)-(c) show three such patterns.

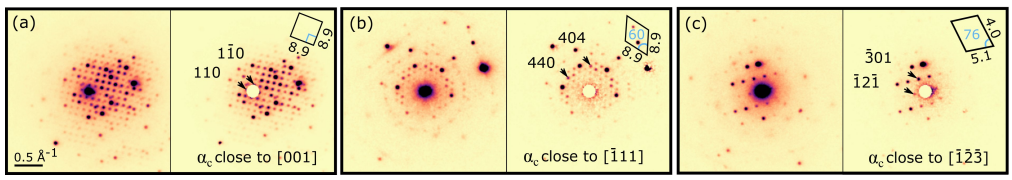

Figure S21: Selected summed diffraction patterns (left) and patterns resulting from NMF-based segmentation (right) from dispersoids embedded in the Al matrix indexed with respect to α_c for the zone axis **(a)** [001], **(b)** [$\bar{1}$11], and **(c)** [$\bar{1}\bar{2}\bar{3}$]. The insets illustrate average measured inverse spot distances in Å and measured angles in degrees.

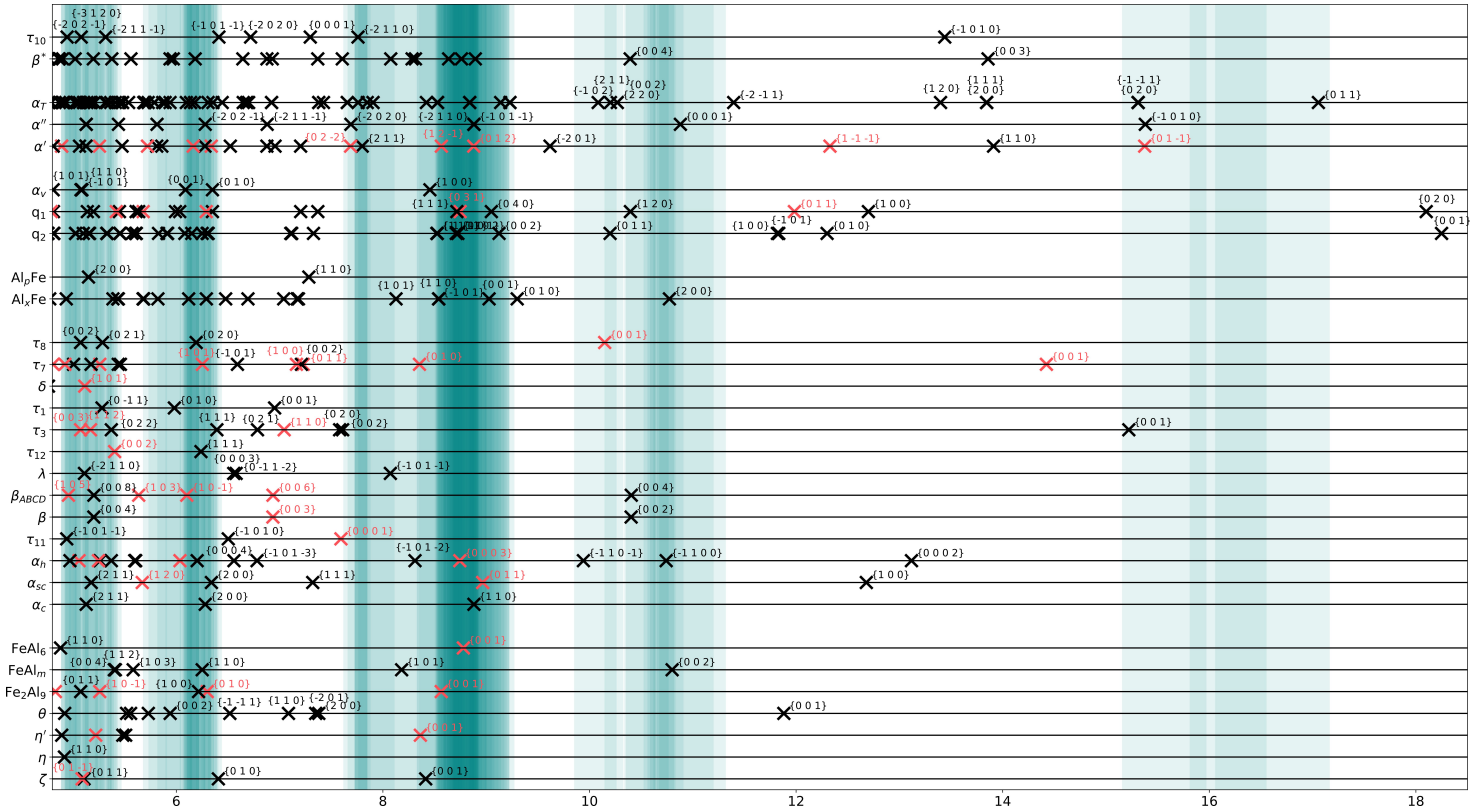

Figure S22: d-spacings of the IMP layer. Measured average d-spacings ($\overline{|\Delta\vec{G}|^{-1}}$) from selected patterns in the IMP layer are plotted in partly transparent turquoise with a line width equal to one standard deviation. On the vertical axis, d-spacings of the Al-Fe(-Si) phases listed in Tables S2 and S3 are shown for comparison. Crosses in black correspond to kinematically allowed spots, while crosses in red correspond to spots possibly seen due to double diffraction. For clarity, only some of the hkl indices are given.

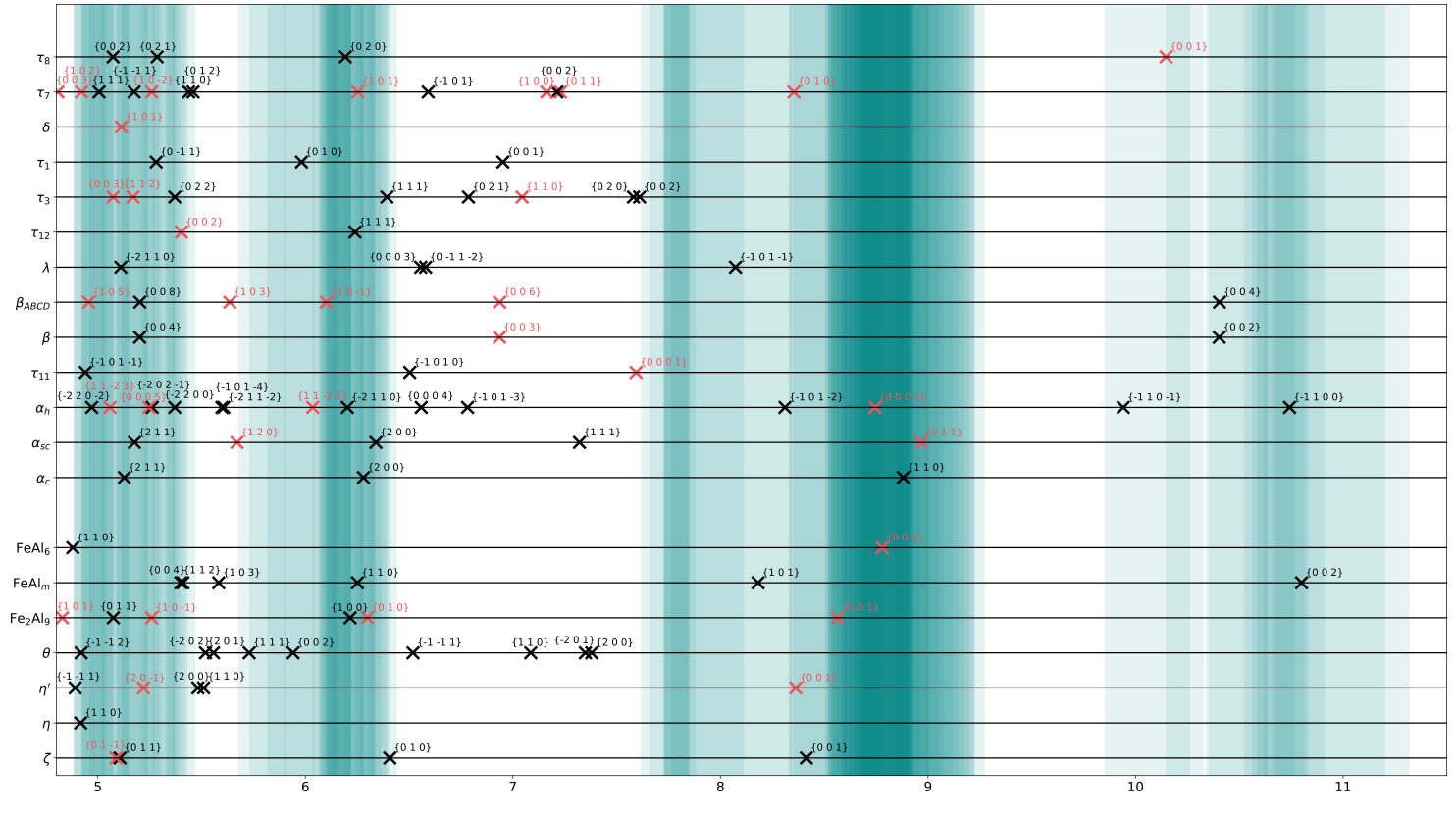

Figure S23: d-spacings of the IMP layer. Measured average d-spacings ($\overline{|\Delta\vec{G}|^{-1}}$) from selected patterns in the IMP layer are plotted in partly transparent turquoise with a line width equal to one standard deviation. On the vertical axis, d-spacings of the Al-Fe(-Si) phases listed in Table S2 are shown for comparison. Crosses in black correspond to kinematically allowed spots, while crosses in red correspond to spots possibly seen due to double diffraction.

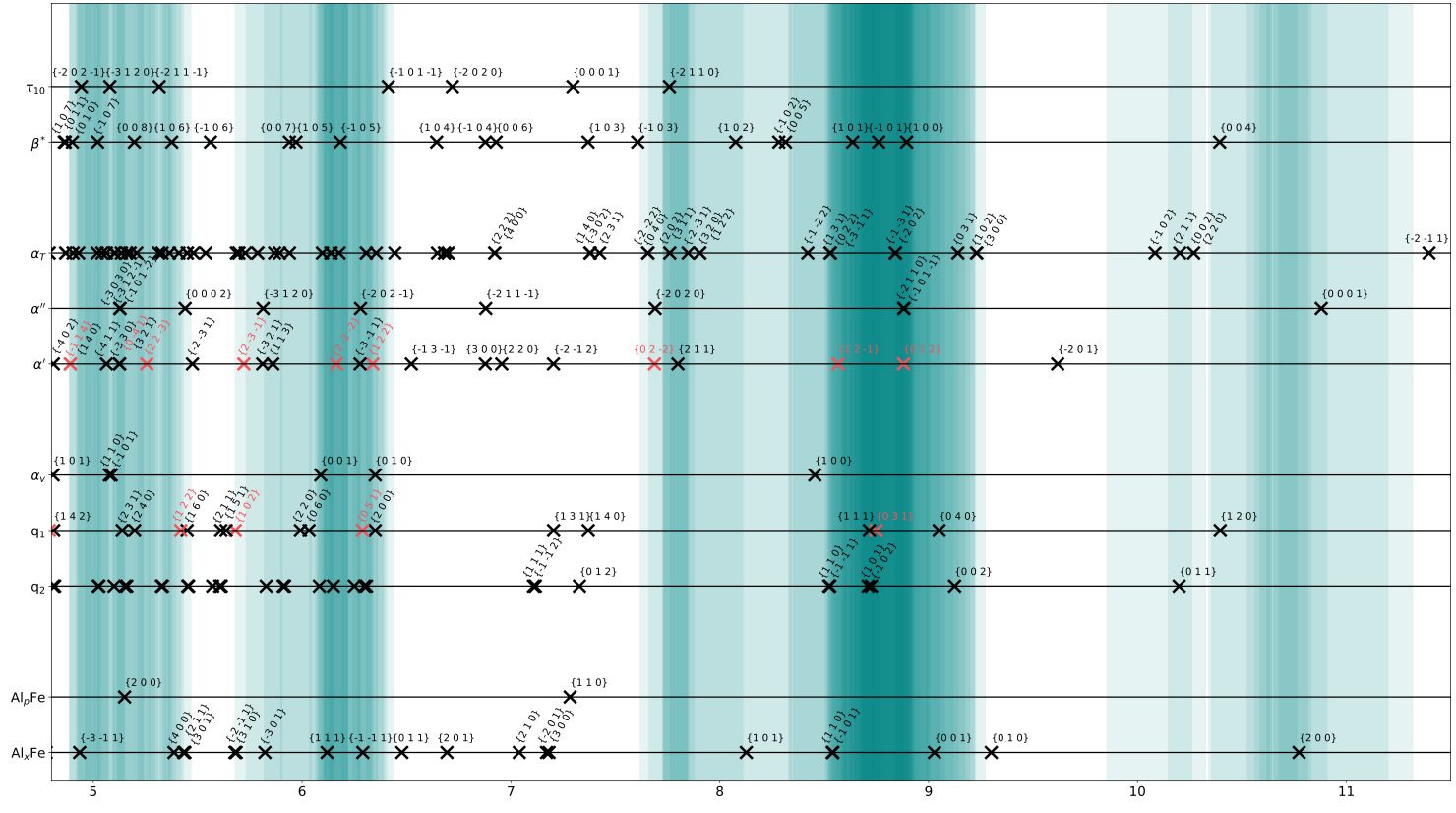

Figure S24: d-spacings of the IMP layer. Measured average d-spacings ($\overline{|\Delta\vec{G}|}^{-1}$) from selected patterns in the IMP layer are plotted in partly transparent turquoise with a line width equal to one standard deviation. On the vertical axis, d-spacings of the Al-Fe(-Si) phases listed in Table S3 are shown for comparison. Crosses in black correspond to kinematically allowed spots, while crosses in red correspond to spots possibly seen due to double diffraction. For clarity, only some of the *hkl* indices are given for q_2 and α_T.

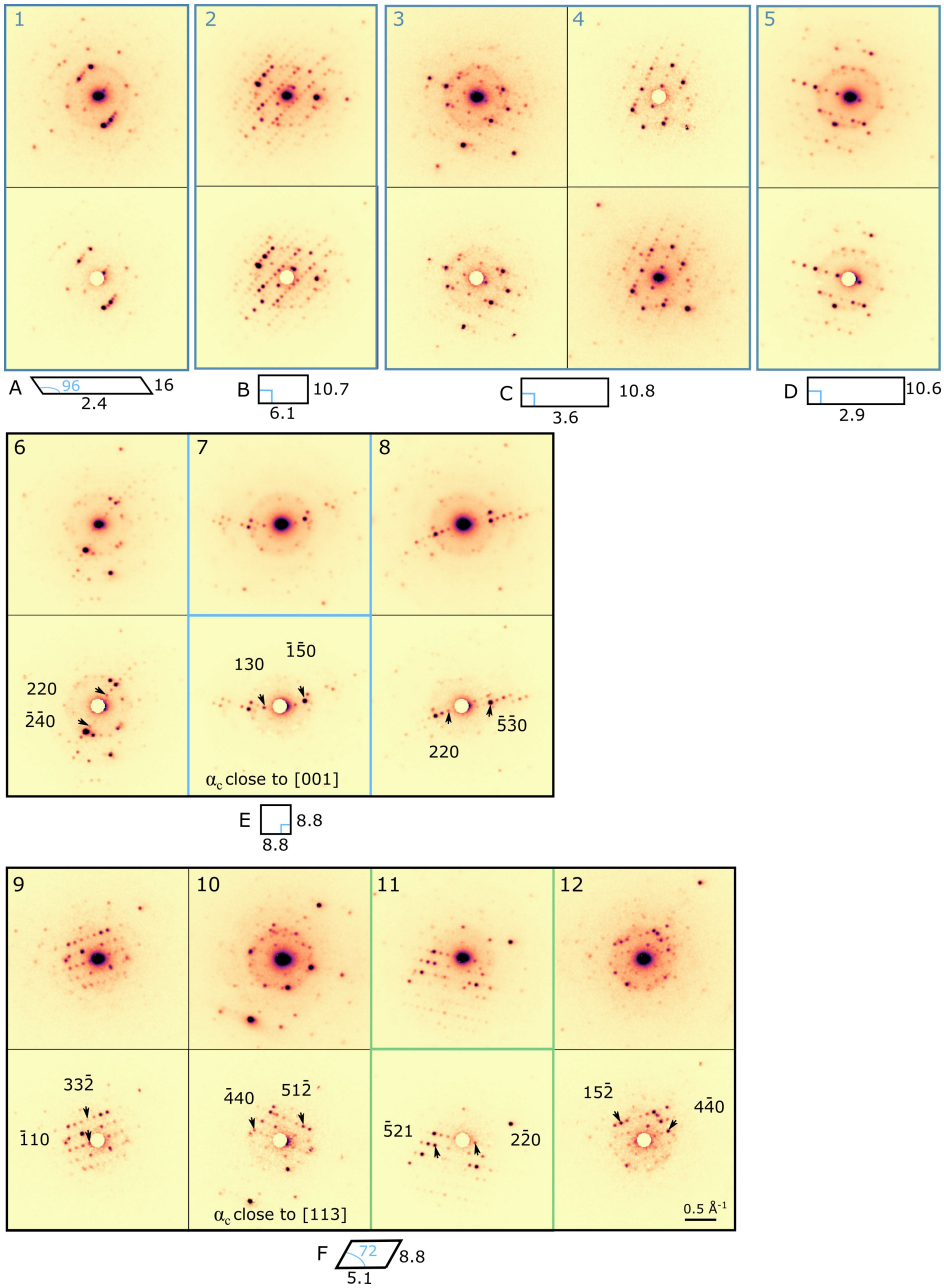

Figure S25: Selected patterns from interfacial Al-Fe-Si crystals from the locations marked by 1 – 12 in Figure S20. For each crystal, the top pattern shows summed diffraction patterns, while the bottom pattern resulted from NMF-based segmentation. Patterns outlined in black are indexed with respect to α_c, while patterns outlined in dark blue could not be indexed with respect to this phase. The patterns outlined in light blue and green are also shown in Figures 10(d) and (e), respectively. The bottom insets, marked by $A - F$, illustrate average measured inverse spot distances in Å and measured angles in degrees.

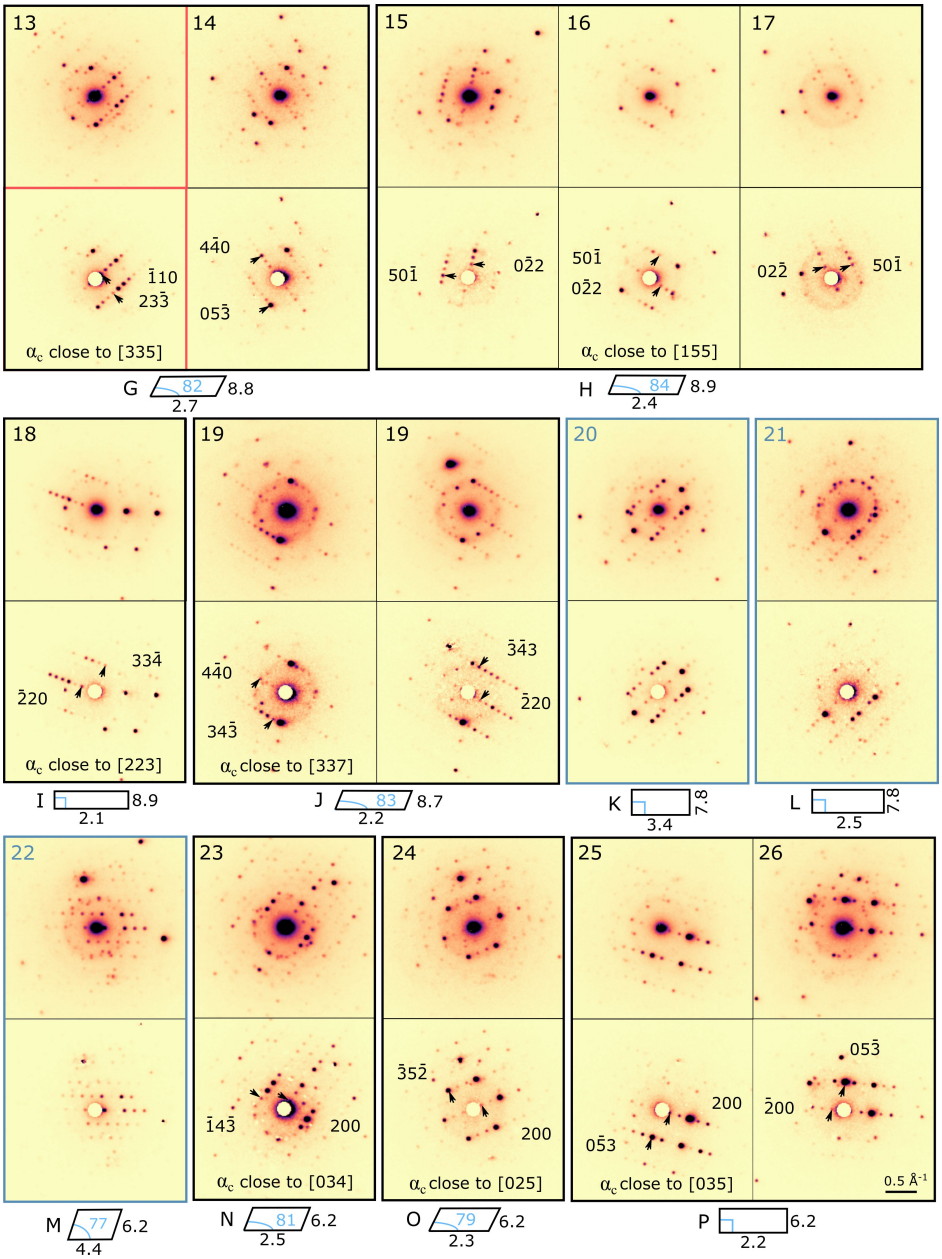

Figure S26: Selected patterns from interfacial Al-Fe-Si crystals from the locations marked by 13 – 26 in Figure S20. For each crystal, the top pattern shows summed diffraction patterns, while the bottom pattern resulted from NMF-based segmentation. Patterns outlined in black are indexed with respect to α_c, while patterns outlined in dark blue could not be indexed with respect to this phase. The pattern outlined in red is also shown in Figure 10(f). The bottom insets, marked by $G - P$, illustrate average measured inverse spot distances in Å and measured angles in degrees. Note that the two patterns marked by 19 were recorded from the same crystal at two different tilt conditions differing only by 1°.

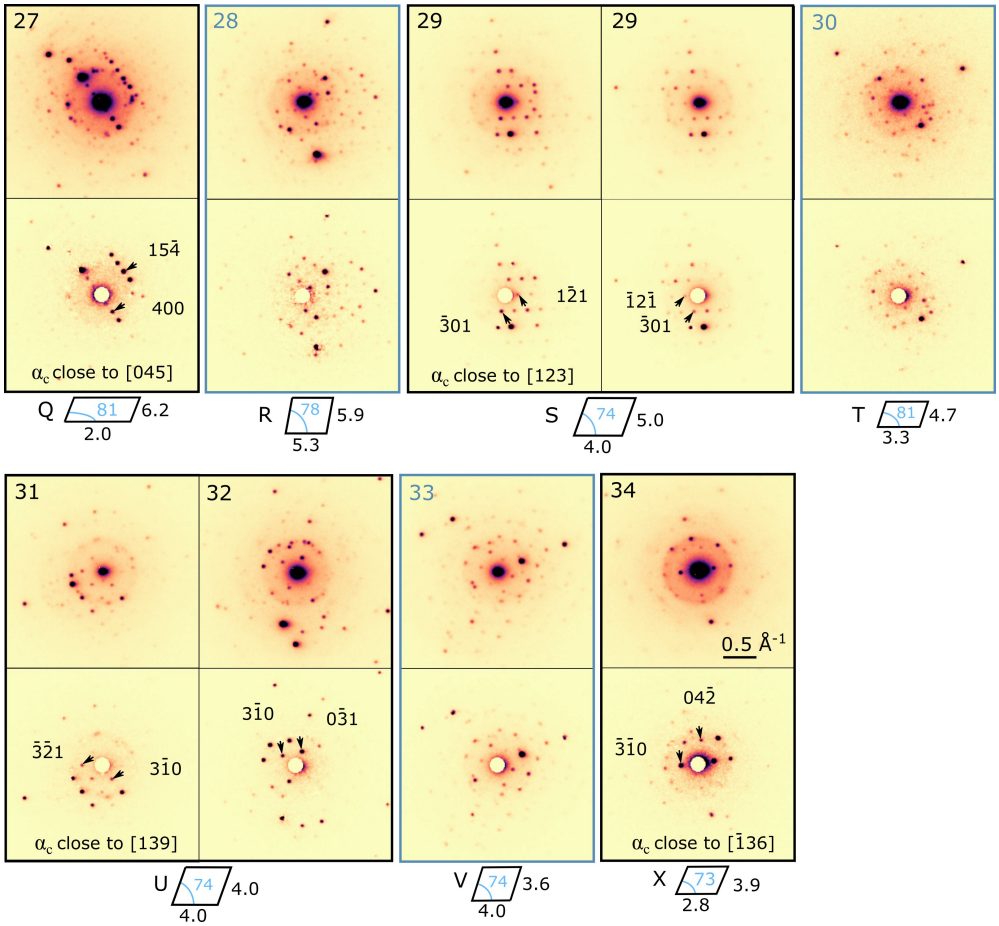

Figure S27: Selected patterns from interfacial Al-Fe-Si crystals from the locations marked by 27 – 34 in Figure S20. For each crystal, the top pattern shows summed diffraction patterns, while the bottom pattern resulted from NMF-based segmentation. Patterns outlined in black are indexed with respect to α_c, while patterns outlined in dark blue could not be indexed with respect to this phase. The bottom insets, marked by $Q - X$, illustrate average measured inverse spot distances in Å and measured angles in degrees. Note that the two patterns marked by 29 were recorded from the same crystal at two different tilt conditions differing only by 1°.

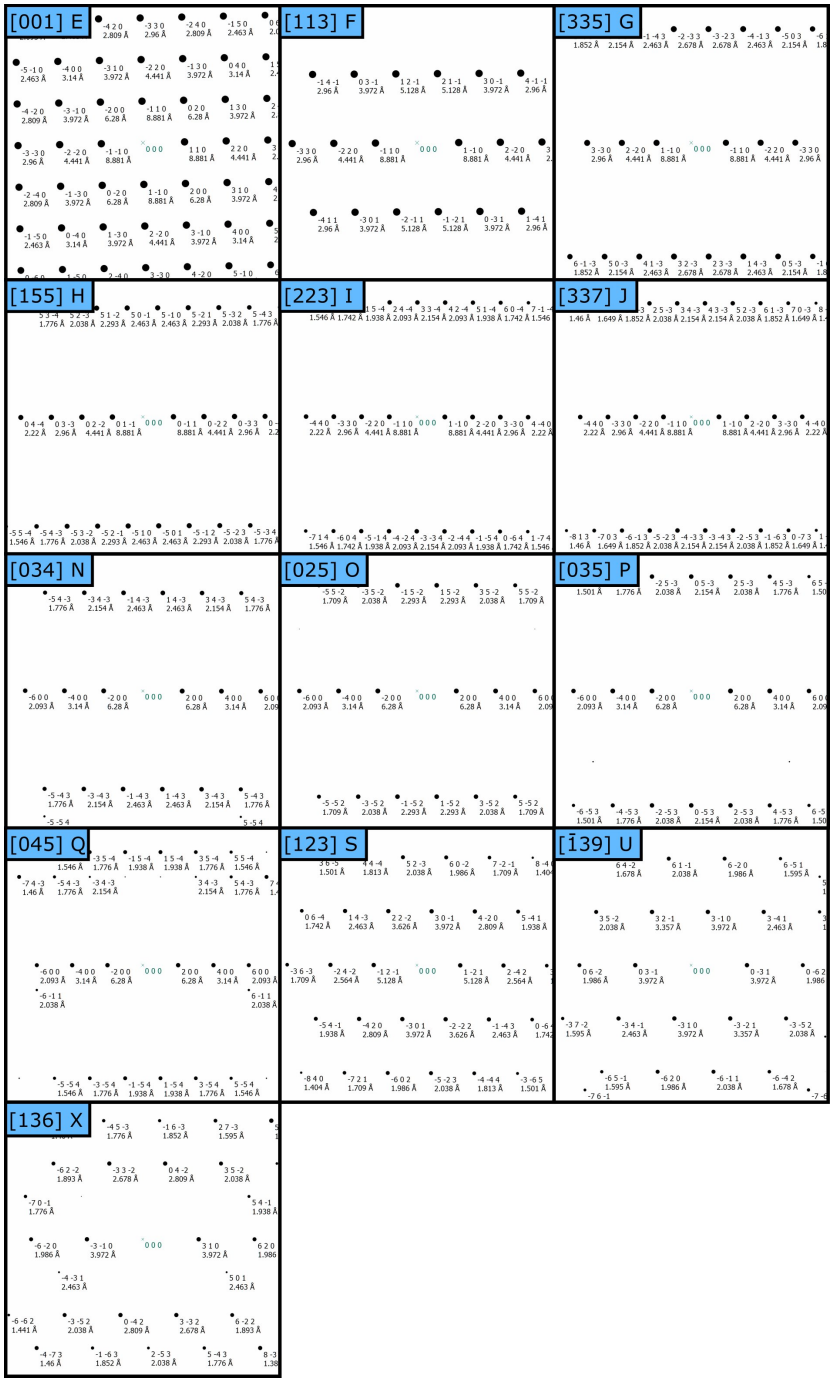

Figure S28: Simulated kinematic zone axis patterns for α_c, produced using ReciPro, where the *hkl* indices and *d*-spacings [Å] are given. The patterns are marked by zone axis and a letter denoting the corresponding experimental patterns in Figures S25-S27.

References

[1] F. de la Peña, E. Prestat, V. T. Fauske, P. Burdet, P. Jokubauskas, M. Nord, T. Ostasevicius, K. E. MacArthur, M. Sarahan, D. N. Johnstone, J. Taillon, J. Lähnemann, V. Migunov, A. Eljarrat, J. Caron, T. Aarholt, S. Mazzucco, M. Walls, T. Slater, F. Winkler, Pquinn-dls, B. Martineau, G. Donval, R. McLeod, E. R. Hoglund, I. Alxneit, D. Lundeby, T. Henninen, L. F. Zagonel, and A. Garmannslund, "hyperspy/hyperspy: HyperSpy v1.5.2," 2019. DOI: 10.5281/ZENODO.3396791.

[2] D. N. Johnstone, P. Crout, J. Laulainen, S. Høgås, B. Martineau, T. Bergh, S. Smeets, S. Collins, J. Morzy, H. W. Ånes, E. Prestat, T. Doherty, T. Ostasevicius, D. Mohsen, E. Opheim, R. Tovey, and E. Jacobsen, "Pyxem/pyxem: Pyxem 0.10.1," 2020. DOI: 10.5281/ZENODO.3667613.

[3] T. Bergh, D. N. Johnstone, P. Crout, S. Høgås, P. A. Midgley, R. Holmestad, P. E. Vullum, and A. T. van Helvoort, "Nanocrystal segmentation in scanning precession electron diffraction data," *Journal of Microscopy*, vol. 279, no. 3, pp. 158–167, 2020. DOI: 10.1111/jmi.12850.

[4] B. H. Martineau, D. N. Johnstone, A. T. J. van Helvoort, P. A. Midgley, and A. S. Eggeman, "Unsupervised machine learning applied to scanning precession electron diffraction data," *Advanced Structural and Chemical Imaging*, vol. 5, no. 1, 2019. DOI: 10.1186/s40679-019-0063-3.

[5] Y. Seto, *ReciPro v.4.761*, 2020. [Online]. Available: https://github.com/seto77/ReciPro.

[6] X. Li, A. Scherf, M. Heilmaier, and F. Stein, "The Al-Rich Part of the Fe-Al Phase Diagram," *Journal of Phase Equilibria and Diffusion*, vol. 37, no. 2, pp. 1–12, 2016. DOI: 10.1007/s11669-015-0446-7.

[7] M. C. J. Marker, B. Skolyszewska-Kühberger, H. S. Effenberger, C. Schmetterer, and K. W. Richter, "Intermetallics Phase equilibria and structural investigations in the system Al-Fe-Si," *Intermetallics*, vol. 19, no. 12, pp. 1919–1929, 2011. DOI: 10.1016/j.intermet.2011.05.003.

[8] N. Krendelsberger, F. Weitzer, and J. C. Schuster, "On the Reaction Scheme and Liquidus Surface in the Ternary System Al-Fe-Si," *Metallurgical and Materials Transactions A*, vol. 38, no. August, 2007. DOI: 10.1007/s11661-007-9182-x.

[9] G. Ghosh, "Aluminim-Iron-Silicon (Iron Systems, Part 1)," *SpringerMaterials Landolt-Börnstein - Group IV Physical Chemistry 11D1*, pp. 1–83, 2008. DOI: 10.1007/978-3-540-69761-9_11.

[10] C. M. Allen, K. A. O'Reilly, B. Cantor, and P. V. Evans, "Intermetallic phase selection in 1XXX A1 alloys," *Progress in Materials Science*, vol. 43, no. 2, pp. 89–170, 1998. DOI: 10.1016/S0079-6425(98)00003-6.

[11] W.-J. Cheng and C.-J. Wang, "Observation of high-temperature phase transformation in the Si-modified aluminide coating on mild steel using EBSD," *Materials Characterization*, vol. 61, no. 4, pp. 467–473, 2010. DOI: 10.1016/j.matchar.2010.02.001.

[12] I. Chumak, K. W. Richter, and H. Ehrenberg, "Redetermination of iron dialuminide, FeAl2," *Acta Crystallographica*, vol. 66, no. 9, pp. 87–88, 2010. DOI: 10.1107/S0108270110033202.

[13] U. Burkhardt, Y. Grin, M. Ellner, and K. Peters, "Structure refinement of the iron–aluminium phase with the approximate composition Fe2Al5," *Acta Crystallographica*, vol. 50, no. 3, pp. 313–316, 1994. DOI: 10.1107/S0108768193013989.

[14] N. L. Okamoto, J. Okumura, M. Higashi, and H. Inui, "Crystal structure of η'-Fe3Al8; low-temperature phase of η-Fe2Al5 accompanied by an ordered arrangement of Al atoms of full occupancy in the c -axis chain sites," *Acta Materialia*, vol. 129, pp. 290–299, 2017. DOI: 10.1016/j.actamat.2017.02.060.

[15] H. Becker and A. Leineweber, "Atomic channel occupation in disordered η-Al5Fe2 and in two of its low-temperatures phases, η" and η"'," *Intermetallics*, vol. 93, no. August 2017, pp. 251–262, 2018. DOI: 10.1016/j.intermet.2017.09.021.

[16] H. Becker, L Amirkhanyan, J Kortus, and A. Leineweber, "Powder X-ray diffrcation analysis of the crystal structure of the η'-Al8Fe3 (η'-Al2.67Fe) phase," *Journal of Alloys and Compounds*, vol. 721, pp. 691–696, 2017. DOI: 10.1016/j.jallcom.2017.05.336.

[17] J. Grin, U. Burkhardt, M. Ellner, and K. Peters, "Refinement of the Fe4Al13 structure and its relationship to the quasihomological homeotypical structures," *Zeitschrift fur Kristallographie*, vol. 209, no. 6, pp. 479–487, 1994. DOI: 10.1524/zkri.1994.209.6.479.

[18] C. J. Simensen and R Vellasamy, "Determination of phases present in cast material of an Al-0.5Wt.% Fe-0.2 Wt.% Si alloy," *Zeitschrift für Metallkunde*, pp. 428–431, 1977.

[19] I. Chumak, K. W. Richter, and H. Ipser, "The Fe-Ni-Al phase diagram in the Al-rich (>50 at.% Al) corner," *Intermetallics*, vol. 15, no. 11, pp. 1416–1424, 2007. DOI: 10.1016/j.intermet.2007.04.012.

[20] W. Khalifa, F. H. Samuel, and J. E. Gruzleski, "Iron intermetallic phases in the Al corner of the Al-Si-Fe system," *Metallurgical and Materials Transactions A: Physical Metallurgy and Materials Science*, vol. 34, no. 13, pp. 807–825, 2003. DOI: 10.1007/s11661-003-1009-9.

[21] J. Gjønnes, V. Hansen, B. S. Berg, P. Runde, Y. F. Cheng, K. Gjønnes, D. L. Dorset, and C. J. Gilmore, "Structure Model for the Phase AlmFe Derived from Three-Dimensional Electron Diffraction Intensity Data Collected by a Precession Technique. Comparison with Convergent-Beam Diffraction," *Acta Crystallographica*, vol. A54, no. 3, pp. 306–319, 1998. DOI: 10.1107/S0108767397017030.

[22] L. K. Walford, "The structure of the intermetallic phase FeAl6," *Acta Crystallographica*, vol. 18, no. 2, pp. 287–291, 1965. DOI: 10.1107/S0365110X65000610.

[23] A. L. Dons, "Superstructures in α-Al(Mn,Fe,Cr)Si," *Zeitschrift für Metallkunde*, vol. 76, no. 2, pp. 151–153, 1985.

[24] M. Cooper, "The crystal structure of the ternary alloy α (AlFeSi)," *Acta Crystallographica*, vol. 23, pp. 1106–1107, 1967. DOI: 10.1107/S0365110X67004372.

[25] S. Pontevichi, F. Bosselet, F. Barbeau, M. Peronnet, and J. C. Viala, "Solid-liquid phase equilibria in the Al-Fe-Si system at 727°C," *Journal of Phase Equilibria and Diffusion*, vol. 25, no. 6, pp. 528–537, 2004. DOI: 10.1361/15477020421052.

[26] R. N. Corby and P. J. Black, "The Structure of α-(AlFeSi) by Anomalous-Dispersion Methods," *Acta Crystallographica*, vol. B33, pp. 3468–3475, 1977. DOI: 10.1107/S0567740877011224.

[27] N. German, V. Bel'skii, T. Yanson, and O. Zarechnyuk, "Crystal structure of the compound Fe1.7Al4Si," *Sov. Phys. Crystallogr.*, vol. 34, no. 3, pp. 735–737, 1989.

[28] H. Becker, T. Bergh, P. E. Vullum, A. Leineweber, and Y. Li, "β- and δ-Al-Fe-Si intermetallic phase, their intergrowth and polytype formation," *Journal of Alloys and Compounds*, vol. 780, pp. 917–929, 2019. DOI: 10.1016/j.jallcom.2018.11.396.

[29] V. Hansen, B. Hauback, M. Sundberg, C. Rømming, and J. Gjønnes, "β-Al4.5FeSi: A Combined Synchrotron Powder Diffraction, Electron Diffraction, High-Resolution Electron Microscopy and Single-Crystal X-ray Diffraction Study of a Faulted Structure," *Acta Crystallographica Section B Structural Science*, vol. 54, no. 4, pp. 351–357, 1998. DOI: 10.1107/S0108768197017047.

[30] D Munson, "A clarification of the phases occurring in aluminium-rich aluminium-iron-silicon alloys, with particular referanse to the ternary α-AlFeSi," *Journal of the institute of metals*, vol. 95, pp. 217–219, 1967.

[31] K. Sugiyama, N. Kaji, and K. Hiraga, "Crystal structure of rhombohedral λ-AlFeSi," *Journal of Alloys and Compounds*, vol. 368, no. 1-2, pp. 251–255, 2004. DOI: 10.1016/j.jallcom.2003.08.065.

[32] J. Roger, E. Jeanneau, and J. C. Viala, "Crystal structure of the ternary compound γ-Al3FeSi," *Zeitschrift fur Kristallographie*, vol. 226, no. 11, pp. 805–813, 2011. DOI: 10.1524/zkri.2011.1423.

[33] J. M. Yu, N. Wanderka, G. Miehe, and J. Banhart, "Intermetallic phases in high purity Al-10Si-0.3Fe cast alloys with and without Sr modification studied by FIB tomography and TEM," *Intermetallics*, vol. 72, pp. 53–61, 2016. DOI: 10.1016/j.intermet.2016.02.003.

[34] J. Roger, F. Bosselet, and J. C. Viala, "X-rays structural analysis and thermal stability studies of the ternary compound α-AlFeSi," *Journal of Solid State Chemistry*, vol. 184, no. 5, pp. 1120–1128, 2011. DOI: 10.1016/j.jssc.2011.03.025.

[35] N. German, V. Zavodnik, T. Yanson, and O. Zarechnyuk, "Crystal structure of FeAl2Si," *Sov. Phys. Crystallogr.*, vol. 34, no. 3, pp. 738–739, 1989.

[36] T. I. Yanson, M. B. Manyako, O. I. Bodak, N. V. German, O. S. Zarechnyuk, R Cerny, J. V. Pacheco, and K Yvon, "Triclinic Fe3Al2Si3 and Orthorhombic Fe3Al2Si4 with New Structure Types," *Acta Crystallographica*, vol. 52, pp. 2964–2967, 1996. DOI: 10.1107/S0108270196008694.

[37] C. Gueneau, C. Servant, F. D'Yvoire, and N. Rodier, "FeAl3Si2," *Acta Crystallographica*, vol. 51, no. 2, pp. 177–179, 1995. DOI: 10.1107/s0108270194009030.

[38] ——, "Fe2Al3Si3," *Acta Crystallographica*, vol. 51, no. 12, pp. 2461–2464, 1995. DOI: 10.1107/s0108270195007864.

[39] R. M. K. Young and T. W. Clyne, "An Al-Fe intermetallic phase formed during controlled solidification," *Scripta Metallurgica*, vol. 15, pp. 1211–1216, 1981.

[40] P. Liu, T Thorvaldsson, G. L. Dunlop, and G. L. Dunlop, "Formation of intermetallic compounds during solidification of dilute Al-Fe-Si alloys," *Materials Science and Technology*, vol. 2, no. 10, pp. 1009–1018, 1986. DOI: 10.1179/mst.1986.2.10.1009.

[41] P. Liu and G. L. Dunlop, "Determination of the crystal symmetry of two AI-Fe-Si phases by convergent-beam electron diffraction," *Journal of Applied Crystallography*, vol. 20, pp. 425–427, 1977. DOI: 10.1002/j.1537-2197.1977.tb15733.x.

[42] A. L. Dons, "AlFeSi-particles in commercial pure aluminium," *Zeitschrift für Metallkunde*, vol. 75, no. 2, pp. 170–174, 1984.

[43] L. A. Bendersky, A. J. McAlister, and F. S. Biancaniello, "Phase transformation during annealing of rapidly solidified Al-rich Al-Fe-Si alloys," *Metallurgical Transactions A*, vol. 19, no. 12, pp. 2893–2900, 1988. DOI: 10.1007/BF02647715.

[44] T. Turmezey, V. Stefániay, and A Griger, "AlFeSi phases in aluminium," *Key Engineering Materials*, vol. 44-45, pp. 57–68, 1990.

[45] H Westengen, "Formation of intermetallic compounds during DC casting of a commercial purity Al-Fe-Si alloy," *Zeitschrift für Metallkunde*, vol. 73, pp. 360–368, 1982.

Paper III

Microstructure and tensile properties of a multi-material aluminium-copper-steel-titanium butt joint made in one pass by hybrid metal extrusion & bonding

T. Bergh, H. Fyhn, L. Sandnes, J. Blindheim, Ø. Grong, R. Holmestad, F. Berto, P.E. Vullum

To be submitted

This article is not yet published and is therefore not included.

Paper IV

On intermetallic phases formed during interdiffusion between aluminium alloys and stainless steel

T. Bergh, S.M. Arbo, A.B. Hagen, J. Blindheim, J. Friis, M.Z. Khalid, I. Ringdalen, R. Holmestad, I. Westermann, P.E. Vullum

To be submitted

This article is not yet published and is therefore not included.

Paper V

On interfacial intermetallic phase layers in cold metal transfer aluminium-steel joints made with an Al-Si-Mn alloy as filler material

T. Bergh, H.W. Ånes, R. Aune, S. Wenner, R. Holmestad, X. Ren, P.E. Vullum

Unpublished work

This article is not yet published and is therefore not included.

ISBN 978-82-326-6011-7 (printed ver.)
ISBN 978-82-326-5276-1 (electronic ver.)
ISSN 1503-8181 (printed ver.)
ISSN 2703-8084 (online ver.)

NTNU

Norwegian University of
Science and Technology